

Designing quantum states by artificially constructed atom arrays with proximity-induced superconductivity

Dissertation

zur Erlangung des Doktorgrades
am Fachbereich Physik der Universität
Hamburg

vorgelegt von

Khài That Tôn

aus Minden

- Hamburg, 2024 -

GUTACHTER DER DISSERTATION:

Prof. Dr. Roland Wiesendanger

PD Dr. Jens Wiebe

MITGLIEDER DER PRÜFUNGSKOMMISSION:

Prof. Dr. Roland Wiesendanger

PD Dr. Jens Wiebe

Prof. Dr. Michael Potthoff

Prof. Dr. Philip Moll

Prof. Dr. Alexander Lichtenstein

DATUM DER DISPUTATION:

24.01.2025

VORSITZENDER DER PRÜFUNGSKOMMISSION:

Prof. Dr. Michael Potthoff

VORSITZENDER DES
FACH-PROMOTIONS-AUSSCHUSSES PHYSIK:

Prof. Dr. Wolfgang J. Parak

LEITER DES FACHBEREICHS PHYSIK:

Prof. Dr. Markus Drescher

DEKAN DER FAKULTÄT MIN:

Prof. Dr.-Ing Norbert Ritter

Abstract

In topological quantum material research, the search for Majorana bound states (MBSs) has spurred the field of topological superconductivity. Their use in quantum computation may revolutionize current quantum computing approaches due to their topological protection. The ingredients for a topological superconductor are Rashba spin-orbit coupling (SOC), superconductivity, and magnetism. One approach to finding a system with all these properties is to create it artificially. Following this approach, proximity-superconductivity can be used to induce superconductivity into systems that were originally not superconducting. This can lead to the formation of new states of quantum matter, as we will explore in this thesis. To this end, the methods of scanning tunneling microscopy (STM) and scanning tunneling spectroscopy (STS) are used, providing the ability to build, manipulate, and probe these quantum systems atom by atom. The main focus of this thesis is a systematic investigation of the above ingredients of topological superconductivity one by one and how they interact with each other.

For this thesis, Nb(110) is used as a superconducting substrate, where Nb is the elemental superconductor with the highest T_c .

Thin Ag(111) islands were grown on the substrate, exhibiting the characteristic Ag(111) surface state. Quantum corrals are built on the surface by assembling non-magnetic atoms to confine the Ag(111) surface state. The energetic positions of the corral eigenmodes can be tuned by resizing the corral. Spectroscopic mea-

surements inside the corral reveal a superconducting gap, where in-gap states occur whenever a corral state is tuned into the superconducting gap. This gap spectrum is interpreted as a system with two superconducting gaps, one originating from the strongly proximitized bulk electrons of the Ag island and one that is explained by weaker proximitized surface state electrons. The superconductivity induced in the surface state system, which is normally strongly decoupled from the bulk, is explained by a coupling mediated through scattering processes with the quantum corral walls.

These Ag(111) corrals are furthermore studied in combination with single Fe-atoms, which induce Yu-Shiba-Rusinov (YSR)-states on the proximitized Ag islands. A single Fe-impurity is placed inside of the corrals, inducing a long-range excitation at the same energetic position as the YSR-states of the Fe-atom, which extends over several tens of nanometers. This effect, dubbed YSR-mirage, is explained by an indirect coupling between the Fe-atom and the corral state mediated by the superconducting bulk. The YSR-mirage is studied as a function of the corral size. It is found that the intensity of the YSR-mirage state oscillates as a function of corral size such that the particle-hole composition of the mirage is inverted with respect to that of the original YSR-state whenever an eigenmode is at the Fermi energy. This particle-hole inversion is less pronounced for the corral with multiple YSR-impurities forming parts of the corral walls; in addition to that, it is investigated whether a long-range interaction between multiple YSR-impurities can be mediated by using the YSR-mirage.

With the deposition of Bi-atoms onto Ag(111), a BiAg₂ surface alloy is grown on the superconducting substrate. Topographic and spectroscopic measurements of the surface are conducted to confirm the result. The spectroscopic measurements of the quasiparticle interference (QPI) patterns on the BiAg₂ hint towards a hybridization between the Rashba-split band structure of the BiAg₂ surface state and quantum well states of the Ag bulk. Lastly, STS-measurements in the low energy regime are performed on the sample as a function of the temperature, confirming the proximity-induced superconductivity on the surface.

Finally, Fe-atoms are deposited onto the proximitized BiAg₂ substrate. The adsorption sites of Fe on BiAg₂ and the associated spectral properties are investigated. Two different adsorption sites are identified for Fe (hollow and bridge sites). YSR-states can be found on Fe-atoms of both sites. Furthermore, hollow-site Fe-atoms show a pair of YSR-states located close to the Fermi energy, which is especially interesting for creating topological superconductivity. The Fe adatoms are arranged in pairs as a function of distance and orientation, and hybridization effects between the Fe hollow-site atoms are studied. The magnetic atoms are then used to build YSR chains on the BiAg₂ substrate. Scanning tunneling spectroscopy techniques are used to probe the spectral properties of these chains and yield excitations at zero energy localized at both ends of the chains. The topological properties of these YSR chains are checked in perturbation experiments.

Zusammenfassung

Im Forschungsfeld der topologischen Quantenmaterialien hat die Suche nach den Majorana-Zuständen das Interesse an topologischen Supraleitern stark angefacht. Bei der Verwendung im Bereich des Quantencomputing könnten sie aufgrund ihres topologischen Schutzes die Konzepte zum Bau von Quantencomputer revolutionieren. Die Zutaten zur Erzeugung eines solchen topologischen Supraleiters sind Rashba-Spin-Bahn-Wechselwirkung, Supraleitung und Magnetismus. Eine Möglichkeit um diese Systeme zu finden besteht darin, sie künstlich zu erzeugen. Ein wesentlicher Bestandteil hierbei ist der Proximity-Effekt, der es erlaubt Supraleitung in Systemen zu induzieren, die von Natur aus nicht supraleitend wären. So können neuartige Phasen in Quantensystemen erzeugt werden, wie in dieser Arbeit demonstriert wird. Zur Bearbeitung dieser Fragestellungen wird auf die Methoden der Rastertunnelmikroskopie und -spektroskopie zurückgegriffen, die den Bau, die Manipulation und die Charakterisierung dieser Quantensysteme auf atomarer Skala erlauben. Diese Arbeit legt den Fokus auf die systematische Untersuchung der oben genannten Zutaten, erst im Einzelnen und anschließend im Zusammenspiel.

Für diese Arbeit wird Nb(110) als supraleitendes Substrat gewählt. Das Element Nb ist weithin bekannt als der elementare Supraleiter mit der höchsten Sprungtemperatur T_c .

Dünne Ag(111)-Inseln mit dem charakteristischen Ag(111)-Oberflächenzustand werden auf dem Nb-Substrat gewachsen. Nichtmagnetische Atome werden auf der Oberfläche verschoben und

zu Quantenpferchen arangiert, die die Moden des Ag(111)-Oberflächenzustandes einsperren. Diese Moden lassen sich in der Energie, durch das Verkleinern/Vergrößern der Quantenpferche, verschieben. Spektroskopiemessungen im Inneren der Quantenpferche zeigen, dass sich Zustände innerhalb der Energielücke des Supraleiters (in-gap states) bilden, sobald eine der Quantenpferchmoden energetisch in die Energielücke verschoben wird. Die innerhalb des Quantenpferches gemessenen Spektren werden als Zeichen für ein System mit zwei verschiedenen Arten von Supraleitung und daher zwei supraleitenden Energielücken interpretiert. Die erste Lücke wird den Bulk-Elektronen zugeschrieben, die aufgrund des Proximity-Effektes supraleitend werden. Die zweite Lücke wird auf eine schwächer induzierte Supraleitung im Oberflächenzustand zurückgeführt. Die Supraleitung im Oberflächenzustand wird durch eine Kopplung an den Bulk durch Streuung an den Quantenpferchwänden erklärt.

Die gleichen Quantenpferche werden nun in Kombination mit einzelnen Eisenatomen untersucht, die durch die Wechselwirkung mit dem darunterliegenden Supraleiter sogenannte Yu-Shiba-Rusinov (YSR)-Zustände erzeugen. Ein einzelnes Eisenatom wird im Inneren des Quantenpferches platziert. Es werden langreichweitige Anregungen bei den YSR-Zustandsenergien gemessen, die sich über den ganzen Quantenpferch erstrecken (im Bereich von mehreren 10 Nanometern). Dieses Phänomen wird "YSR-Mirage" genannt und entsteht durch eine indirekte Kopplung zwischen dem Eisenatom und der Quantenpferchmode, die durch den supraleitenden Bulk vermittelt wird. Das YSR-Mirage wird als Funktion der Pferchgröße untersucht. Es wird festgestellt, dass die YSR-Mirage-

intensität in Abhängigkeit von der Pferchgröße oszilliert und dass die Teilchen-Loch-Symmetrie invertiert zu der des YSR-Zustands des Eisenatoms ist, wenn eine Quantenpferchmode die supraleitende Lücke durchquert. Dieses invertierte Verhalten wird nicht für einen Quantenpferch beobachtet, bei dem Teile der inneren Wände durch Eisenatome ersetzt wurden. Zuletzt wird untersucht, ob das YSR-Mirage genutzt werden kann, um zwei Atome im Inneren des Quantenpferches zu koppeln.

Durch das Aufdampfen von Bi-Atomen auf die Ag(111)-Oberfläche wird eine BiAg₂-Oberflächenlegierung auf dem supraleitenden Substrat gewachsen. Es werden topographische und spektroskopische Messungen zur Bestätigung der korrekten Oberfläche durchgeführt. Weitere Aufnahmen von QPI-Mustern weisen auf eine Hybridisierung zwischen den Rashba-Bändern und Quantentopfzuständen aus dem Bulk hin. Zuletzt wird die supraleitende Energielücke auf der BiAg₂-Oberfläche geprüft. Durch temperaturabhängige Messungen wird bestätigt, dass die Oberfläche supraleitend ist.

Als letztes werden Eisenatome auf die supraleitende BiAg₂-Oberfläche aufgedampft. Die Eisenatome werden auf ihre möglichen Adsorptionsplätze und die damit zusammenhängenden Spektren untersucht. Es werden zwei Adsorptionsplätze gefunden (hollow und bridge). Auf beiden Plätzen werden YSR-Zustände gefunden. Weiterhin werden für Eisenatome auf Hollowplätzen YSR-Zustände nahe der Fermienergie gefunden, was sie für den Bau eines topologischen Supraleiters interessant macht. Eisenatome werden in Paaren auf der Oberfläche arrangiert. Die Hybridisierung der YSR-Zustände wird als Funktion der Entfernung und der rel-

ativen Orientierung gemessen. Die magnetischen Atome werden dann zum Bau von YSR-Ketten genutzt. Untersuchungen der Ketten mithilfe von Rastertunnelspektroskopie zeigen Zustände bei Nullenergie an den Kettenenden. In Störungsexperimenten werden die topologischen Eigenschaften dieser YSR-Zustände untersucht.

Contents

1	Introduction	17
2	Theoretical foundations	23
2.1	Surface states in noble metal systems	24
2.2	Superconductivity	27
2.2.1	Superconductors in magnetic fields	27
2.2.2	BCS-theory	29
2.2.3	Proximity effect	34
2.2.4	Magnetic impurities in superconductors . . .	37
2.3	Rashba spin-orbit coupling (SOC)	40
2.4	Kitaev model	42
3	Experimental methods and setup	49
3.1	Scanning tunneling microscopy	49
3.2	Fundamentals of scanning tunneling spectroscopy .	52
3.3	Modes of operation in STM and STS	55
3.4	Tunneling between superconducting electrodes . . .	59
3.5	Experimental setups	66
3.5.1	The 4.2 K/1 K SPECS setup	66
3.5.2	The 300 mK home-built system	70
4	Proximity induced superconductivity in artificial quantum dots: experimental discovery of Machida-Shibata states	73
4.1	Noble metal system growth on a superconductor . .	77
4.2	Artificially constructed quantum dots	94
4.3	Machida-Shibata theory on resonance scattering and superconductors	120

4.4	Conclusion	134
5	Realization of the YSR quantum mirage	137
5.1	YSR-states of Fe on Ag(111)/Nb(110)	141
5.2	YSR-mirage effect in elliptical corrals	149
5.3	Tuning YSR-mirages in rectangular corrals	162
5.4	Oscillations in the YSR-mirage intensity	174
5.5	Multiple impurity corral	202
5.6	Conclusion	214
6	Bottom up constructed YSR-chains on a superconducting Rashba surface	217
6.1	Topographic and spectroscopic properties of BiAg ₂ on Ag(111)/Nb(110)	220
6.2	Scattering patterns on the BiAg ₂ surface	227
6.3	Quantum well states	237
6.4	Proximity induced superconductivity on BiAg ₂	243
6.5	Single Fe-atoms on BiAg ₂	249
6.6	Hybridization between YSR-states on BiAg ₂	263
6.7	YSR-chains on superconducting BiAg ₂	273
6.8	Perturbing the edge states of a YSR-chain	284
6.9	Conclusion	299
7	Conclusion and outlook	303

Acronyms

FP	focal point
qubit	quantum bit
MZM	Majorana zero mode
MBS	Majorana bound state
BCS	Bardeen-Cooper-Schrieffer
YSR	Yu-Shiba-Rusinov
MS	Machida-Shibata
MSS	Machida-Shibata state
dGSJ	de Gennes-Saint James
SIS	superconductor-insulator-superconductor
JT	Joule-Thomson
AES	Auger electron spectroscopy
LEED	low-energy electron diffraction
QD	quantum dot
QPT	quantum phase transition
ML	monolayer
DL	double-layer
BZ	Brillouin zone
QWS	quantum well state
SC	superconductor
PMZM	precursor Majorana zero mode
ac	alternating current
dc	direct current
ARPES	angle-resolved photoemission spectroscopy
DOS	density of states
fcc	face-centered cubic

Contents

FFT	fast Fourier transformation
LDOS	local density of states
QPI	quasi-particle interference
SOC	spin-orbit coupling
STM	scanning tunneling microscopy
STS	scanning tunneling spectroscopy
UHV	ultra-high vacuum
vHS	van Hove singularity
MAR	multiple Andreev reflection
N	normal metal

1 Introduction

Quantum computing promises to significantly enhance the ability to solve complex problems currently intractable by classical computers [1]. The most prominent examples are Grover's algorithm for searching unsorted databases [2] and Shor's algorithm for factoring large numbers. After decades of research, quantum computers are now beginning to demonstrate quantum advantage [3] over classical computers for several use cases [4–7]. However, one of the most significant issues that quantum computers face is decoherence [8], which might lead to loss of information during the computational process. To prevent that, error-correcting measures are used, such as storing the information redundantly on multiple quantum bits (qubits) [9, 10]. This, on the other hand, increases the complexity of the quantum computer without increasing its calculational power. To build a universal quantum computer that can run Shor's or Grover's algorithm, the number of qubits would have to be much larger, complicating the situation even further [11].

The field of topological quantum computation provides a different solution to this problem [12, 13]. Topological quantum computation proposes using topologically protected quasiparticles, the Majorana zero modes (MZMs). MZMs are categorized as non-Abelian anyons with their own quantum statistics. If two anyons are interchanged with each other, they acquire a phase [14]. One can use this property to perform logical operations, known as braiding operation [12].

The first description of these MZMs was given by Kitaev in his Kitaev chain model [15]. This oversimplified model describes a tight-binding model for a superconducting 1D chain consisting of spinless particles where neighboring lattice sites are coupled. The model demonstrates that the Hamiltonian gets into a topological phase, leading to topological edge states for specific parameters. These states appear at both ends of the chain, located at zero energy, and were shown to have properties of MZMs. The model is, therefore, an example of a topological superconductor. Unfortunately, the realization of the Kitaev chain Hamiltonian in a real solid-state system is a challenging task since superconductors are usually comprised of spinful electrons.

The motivation to find the MZMs has spurred efforts and ideas to create systems behaving similarly to the Kitaev chain [16–21]. All these proposals have in common that they unite the following three ingredients: magnetism, Rashba SOC, and superconductivity [22]. Materials in which all of these properties exist together are sparse. For this reason, artificially combining materials, where each material contributes one of the ingredients, is required to form the desired system.

The experimental platforms for the realization of MZMs can be roughly categorized into two groups:

1. The semiconductor-superconductor heterostructure approach involves using semiconducting nanowires such as InAs or InSb with large SOC [18, 23–25]. By depositing superconducting material onto these wires, proximity-superconductivity can be induced into the system. When large external mag-

netic fields are applied along the wire, the occurrence of MZMs at the ends of the wire is predicted.

2. In magnet-superconductor hybrids, magnetic textures with high Rashba SOC or spin spirals are grown/assembled on a superconducting surface [26]. The spin textures can be created either in 1D [27–29] or 2D [30–32].

For the investigation of magnet-superconductor hybrids, STM can be the perfect instrument as it can characterize these systems and be used to tailor systems with atomical precision, thereby tuning specific parameters of the sample to the needs of the experimentalist. Majorana physics and STM, therefore, is a perfect fit as testified by numerous works in this area [26–30, 33–39].

By this time, the complexity of the investigated systems has gradually increased. While in the first works, superconducting sample surfaces were investigated where self-assembled magnetic chains were deposited [28], later works added a layer of complexity by building magnetic chains artificially using atom manipulation techniques [27, 29]. Another level of complexity has been added when additional layers of materials have been grown on top of a superconductor to tune specific properties of the sample [40, 41] before spins are deposited. The superconductivity is provided by an underlying superconducting substrate, which proximitizes the layers grown on top.

To choose the materials systematically, following a bottom-up approach where the interplay between the different ingredients is investigated separately would be helpful, which would be led by

the following questions: How is the superconductivity induced into the sample surface by proximity? What is the interplay between a proximitized surface state and a magnetic impurity? How can Rashba SOC be added to the system?

After this introductory chapter, **Chapter 2** introduces the reader to the theoretical foundations of surface state systems, superconductivity, Rashba SOC, and the Kitaev chain, which are required to follow and understand the experiments and results later in the thesis.

Next, **Chapter 3** introduces the experimental techniques used throughout this thesis, focusing on the basics of STM and STS techniques. Then, we will take a look at the specific experimental setups that have been used in the thesis.

Starting with **Chapter 4**, we will delve into the experimental results, where we used a Nb(110) crystal surface to grow Ag(111) islands on top. We will use the Ag(111) surface state and non-magnetic atoms to build quantum corrals out of it, allowing us to study one of the simplest quantum systems: a single, non-magnetic quantum level. In this basic setting, we will observe whether and, if yes, how proximity-superconductivity is induced into this quantum state.

Chapter 5 continues the investigations on the corrals from the last chapter and combines the proximity-superconductivity with magnetic impurities, which leads to so-called Yu-Shiba-Rusinov (YSR) states. We will examine the interactions between a YSR-state and the quantum corral eigenstates.

The sample preparation from the last chapters serves as a base for **Chapter 6**. We grow a BiAg₂ surface alloy by depositing Bi-atoms onto the Ag(111) islands. BiAg₂ is well-known for its large Rashba SOC. With that, we can study how superconductivity is induced into this strongly spin-orbit coupled surface state. Then we look at a system where all the ingredients are combined, forming a potential candidate system for topological superconductivity. We will take the BiAg₂ surface, evaporate Fe-atoms onto it, and build chains. With this, all the ingredients for topological superconductivity are combined in one system. We will investigate whether such a system shows indications for topological superconductivity and MZMs.

In the last chapter (**Chapter 7**), I will give a conclusion on the main results that have been presented throughout this thesis and provide an outlook for further ideas for investigations to advance the field.

2 Theoretical foundations

In this chapter, I will introduce the reader to the theoretical foundations necessary to follow the ideas of the experiments and discussions of the results presented throughout the thesis. We begin by exploring the theory behind surface states, examining their origin and how their properties are altered by introducing Rashba-type SOC.

We will then delve into the fundamentals of superconductivity, covering the Bardeen-Cooper-Schrieffer (BCS)-theory and Andreev reflections and their relevance to the proximity effect. Next, we will examine systems where superconductivity and magnetism are combined, leading to the emergence of YSR-states. Finally, we will touch upon the topic of topological superconductivity. We will employ a simple toy model to demonstrate the concept of topology in the context of condensed matter physics. This section will also discuss how SOC, superconductivity, and magnetism can create a topological superconductor.

2.1 Surface states in noble metal systems

Bloch-waves describe the electronic states inside of a crystal with periodic boundary conditions. In this derivation, the crystal is approximated by an infinitely large periodic lattice. The time-independent Schrödinger equation for an electron in the crystal is given by:

$$\left[-\frac{\hbar^2}{2m} \nabla^2 + V(\mathbf{r}) \right] \psi(\mathbf{r}) = E\psi(\mathbf{r}), \quad (2.1)$$

where \hbar is the reduced Planck constant, m_e^* is the electron mass, $V(\mathbf{r})$ is the periodic potential inside the crystal, and $\psi(\mathbf{r})$ is the wave function of the electron [42, 43]. The periodicity of the crystal leads to the formation of electronic bands, which describe the properties of the electrons inside the crystal.

This periodic boundary condition is no longer given at the system's surface. Consequently, the lattice potential $V(\mathbf{r})$ has a relatively abrupt jump to the vacuum level. Therefore, under special conditions, new solutions to the Schrödinger equation (Eq. 2.1) are possible, which will be discussed in the following.

The solutions in the one-dimensional case can be classified into two categories as depicted in Figure 2.1A. The first kind of solution refers to the bulk states (grey and blue), which extend in the direction of the crystal bulk but decay exponentially into the vacuum. The second state shows a decaying behavior in the vacuum and the bulk. Consequently, the electronic states are strongly localized at that surface. Due to this, the first kind is referred to as

bulk state, while the second is called surface state.

The first to derive the existence of surface states for systems with weakly interacting electrons was William Shockley [44]. Hence, these states are also referred to as Shockley surface states. Even though these states are confined along the direction perpendicular to the surface, they show a dispersive behavior in the directions parallel to the surface plane. A depiction of that can be seen in Figure 2.1B. Here, the dispersion relation of the surface state is shown in red. The dispersion relations of the bulk bands can be projected onto the surface as depicted by the blue and grey shaded areas. The comparison between the energetic locations of the bands reveals another characteristic property of surface states. They can only exist in a gap formed by the projection of all bulk bands onto the surface since the hybridization with the bulk bands would prohibit the confinement to the surface. Note that this is only a necessary condition, but not a sufficient one for the existence of surface states. It is furthermore required that the Fourier coefficient of the lattice periodic potential $V(\mathbf{r})$ has the correct sign at the location of the surface [45].

Over the past decades, Shockley-states in noble metal systems such as Ag, Cu, and Au [46–48] have been the subject of many investigations in surface science.

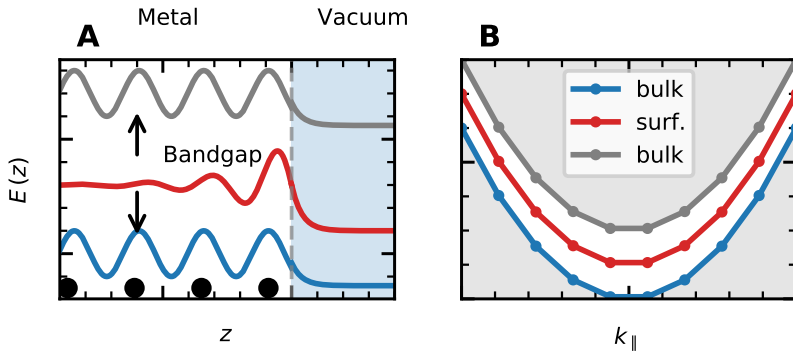


Figure 2.1: Schematic representation of the surface state formation. (A) At the interface between the metal and the vacuum, the crystal's translational symmetry is broken, possibly leading to the formation of intrinsic surface states as depicted by the red line, which decay into the vacuum and the bulk of the crystal. (B) Schematic representation of the band structure of a metal. The grey-shaded areas represent bulk states. The surface state forming at the surface of the metal is located inside the surface-projected bulk band gap.

2.2 Superconductivity

Superconductivity is a quantum mechanical phenomenon observed in some metals when cooled below a specific temperature, known as the critical temperature T_c . Heike Kamerlingh Onnes first discovered this phenomenon in 1911 [49]. He found out that mercury's electrical resistance drops to zero when cooled below 4.2 K. The term *superconductor* refers to this property. In 1933, Walther Meissner and Robert Ochsenfeld discovered another characteristic property of superconductors [50]. They noticed that when a superconductor is cooled below T_c and placed in a magnetic field, it expels the magnetic field inside, acting like a perfect diamagnet. This effect was named after its discoverers and is known as the Meissner-Ochsenfeld effect. It took more than 40 years after its discovery to develop a theory that could provide a microscopic understanding of superconductivity. Today, this theory is known as BCS-theory, named after its developers, John Bardeen, Leon Neil Cooper, and John Robert Schrieffer. It was reported in 1957 [51] and was honored with the Nobel Prize in Physics in 1972.

2.2.1 Superconductors in magnetic fields

At first glance, one might be tempted to explain the occurrence of the Meissner effect by considering Lenz's law. When a magnetic field is applied to the superconductor, currents are induced inside the superconductor. One could argue that these currents will cause another magnetic field, which counteracts the magnetic

fields that they were caused by. This might play a role in the scenario where the magnetic field is turned on after the superconductor has been cooled below T_c . However, in the scenario where the magnetic field is applied first, and the superconductor is cooled afterward, the same perfect diamagnetism is observed. The superconductor does not care whether the magnetic field is applied before or after the cooldown. It will repel the magnetic field regardless. Therefore, it is considered that this is an inherent property of the superconductor. When the applied magnetic field is increased further, it will eventually reach a critical value, at which the superconductivity is quenched. The relation between critical field and temperature follows an empirical law given by

$$H_c(T) = H_c(0) \left[1 - \left(\frac{T}{T_c} \right)^2 \right] \quad (2.2)$$

with $H_c(0)$ being the critical field at $T = 0$. For some superconductors, two of these critical magnetic fields are found. These are called *Type-II superconductors*, while the first ones are called *Type-I superconductors*. In Type-II superconductors, the law for the critical field only applies to the first critical field $H_{c,1}$. After $H_{c,1}$, a Type-II superconductor will show magnetic vortices in which the magnetic field begins penetrating the superconductor. When the field is increased, we see that the number of vortices increases, and in the end, when a second critical field $H_{c,2}$ is reached, the superconductivity breaks down completely.

2.2.2 BCS-theory

In their theory, Bardeen, Cooper, and Schrieffer explain the zero-resistance of a superconductor with the help of a small attractive force between electrons with opposing momentum \mathbf{k} and spin σ [51]. This attractive force is mediated by electron-phonon coupling, where one electron moving through the lattice distorts the lattice locally, creating a phonon mode. The phonon travels through the lattice and couples to another electron, effectively mediating an attractive force between the two electrons. The coupled electrons form a new quasi-particle known as a Cooper pair. Cooper pairs are bosonic particles that allow the coupled electrons to fall into the ground state of a system, forming a condensate. In the ground state, the only way to excite the Cooper pairs is to break them up, requiring the binding energy Δ . Consequently, any interaction between the Cooper pair electrons with the environment that involves energies below Δ is forbidden. Therefore, as long as the current is below a critical value, the electrons can travel through the material without dissipating energy to the crystal lattice or defects.

To start, we consider a tight-binding Hamiltonian with an attractive pairing term, which couples electrons with opposing spins and momenta \mathbf{k} with each other [52].

$$H = \sum_{\mathbf{k},\sigma} \epsilon_{\mathbf{k}} c_{\mathbf{k}\sigma}^\dagger c_{\mathbf{k}\sigma} - \sum_{\mathbf{k},\mathbf{k}'} V_{\mathbf{k},\mathbf{k}'} c_{\mathbf{k}'\uparrow}^\dagger c_{-\mathbf{k}'\downarrow}^\dagger c_{-\mathbf{k}\downarrow} c_{\mathbf{k}\uparrow} \quad (2.3)$$

Here $\epsilon_{\mathbf{k}}$ is the electron energy, $c_{\mathbf{k},\sigma}^\dagger$ and $c_{\mathbf{k},\sigma}$ are the creation and

2 Theoretical foundations

annihilation operators for electrons with wave vector \mathbf{k} and spin σ , and $V_{\mathbf{k},\mathbf{k}'}$ represents the attractive interaction potential.

The first sum represents the metal's quasi-free electron dispersion relation, while the second is the weak interaction mediated via electron-phonon coupling. While the first term is already written in the diagonalized form, the second term has to be simplified to solve the Hamiltonian. To do this, we approximate the interaction term using a mean-field approach. This leaves us with an effective Hamiltonian, which has only quadratic terms in creation and annihilation operators:

$$H_{\text{eff}} = \sum_{\mathbf{k},\sigma} \epsilon_{\mathbf{k}} c_{\mathbf{k}\sigma}^\dagger c_{\mathbf{k}\sigma} - \Delta^* \sum_{\mathbf{k}} c_{-\mathbf{k}\downarrow} c_{\mathbf{k}\uparrow} - \Delta \sum_{\mathbf{k}'} c_{\mathbf{k}'\uparrow}^\dagger c_{-\mathbf{k}'\downarrow}^\dagger + \frac{|\Delta|^2}{V} \quad (2.4)$$

with

$$\Delta = V \sum_{\mathbf{k}} \langle c_{-\mathbf{k}\downarrow} c_{\mathbf{k}\uparrow} \rangle \quad \Delta^* = V \sum_{\mathbf{k}} \langle c_{\mathbf{k}\uparrow}^\dagger c_{-\mathbf{k}\downarrow}^\dagger \rangle. \quad (2.5)$$

and the assumption that the pairing potential is constant for a small energy window around E_F :

$$V_{\mathbf{k},\mathbf{k}'} = V \quad \text{for} \quad |\epsilon_{\mathbf{k}} - \epsilon_{\mathbf{k}'}| < \hbar\omega_D \quad (2.6)$$

with the Debye-frequency of the phonon ω_D .

For the diagonalization of the Hamiltonian, the Bogliubov transformation can be used [53, 54], where we rewrite the electron creation and annihilation operators in a new set of fermionic opera-

tors:

$$\begin{aligned}\alpha_{\mathbf{k}} &= u_{\mathbf{k}}c_{\mathbf{k}\uparrow} - v_{\mathbf{k}}c_{-\mathbf{k}\downarrow}^\dagger & \alpha_{\mathbf{k}}^\dagger &= u_{\mathbf{k}}^*c_{\mathbf{k}\uparrow}^\dagger - v_{\mathbf{k}}^*c_{-\mathbf{k}\downarrow} \\ \beta_{\mathbf{k}} &= u_{\mathbf{k}}c_{-\mathbf{k}\downarrow} + v_{\mathbf{k}}c_{\mathbf{k}\uparrow}^\dagger & \beta_{\mathbf{k}}^\dagger &= u_{\mathbf{k}}^*c_{-\mathbf{k}\downarrow}^\dagger + v_{\mathbf{k}}^*c_{\mathbf{k}\uparrow}\end{aligned}\quad (2.7)$$

In order to fulfill the fermionic commutation relations, the coefficients $u_{\mathbf{k}}$ and $v_{\mathbf{k}}$ must satisfy:

$$|u_{\mathbf{k}}|^2 + |v_{\mathbf{k}}|^2 = 1 \quad (2.8)$$

We can find that this is given for:

$$u_{\mathbf{k}}^2 = \frac{1}{2} \left(1 + \frac{\epsilon_{\mathbf{k}}}{\sqrt{\epsilon_{\mathbf{k}}^2 + |\Delta|^2}} \right) \quad v_{\mathbf{k}}^2 = \frac{1}{2} \left(1 - \frac{\epsilon_{\mathbf{k}}}{\sqrt{\epsilon_{\mathbf{k}}^2 + |\Delta|^2}} \right) \quad (2.9)$$

The transformation yields the new Hamiltonian, which is bilinear in all creation and annihilation operators:

$$H_{\text{eff}} = \sum_{\mathbf{k},\sigma} E_{\mathbf{k}}(\alpha_{\mathbf{k}}^\dagger\alpha_{\mathbf{k}} + \beta_{\mathbf{k}}^\dagger\beta_{\mathbf{k}}) + \sum_{\mathbf{k}}(\epsilon_{\mathbf{k}} - E_{\mathbf{k}}) + \frac{|\Delta|^2}{V} \quad (2.10)$$

with

$$E_{\mathbf{k}} = \pm\sqrt{\epsilon_{\mathbf{k}}^2 + |\Delta|^2} \quad (2.11)$$

By introducing the new fermionic operators, we could break the problem down to a single-particle problem. The new fermionic operators represent quasiparticles, the Bogoliubov-quasiparticles (Bogoliubons).

In Figure 2.2, the coefficients (A) and the energy (B) of the Bogoli-

2 Theoretical foundations

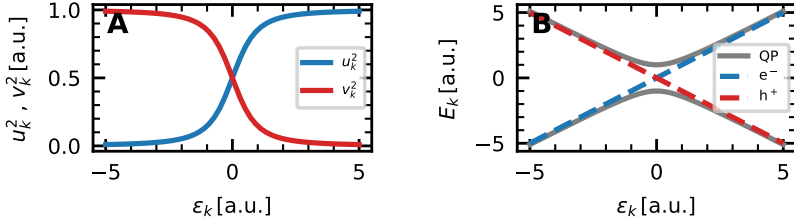


Figure 2.2: Properties of the Bogoliubov quasiparticles. (A) Evolution of the particle and hole coefficients as a function of energy. **(B)** Bogoliubon energy as a function of the electron energy.

ubon are plotted as a function of ϵ_k (given by Eq. 2.9 and 2.11). Panel (A) shows, that for $\epsilon_k < 0$, the amplitude of v_k is much larger. As we get to $\epsilon_k = 0$ the amplitudes are equal. For $\epsilon_k > 0$ the relation between v_k and u_k is inverted. The interpretation of these coefficients shows an essential property of the Bogoliubons, the particle-hole symmetry in energy. Bogoliubons are a superposition of a particle (electron) and an antiparticle (hole). Depending on the energy, it shows a more hole-like ($E \ll E_F$) or a more electron-like character ($E \gg E_F$).

In panel (B), we can see how the quasiparticle energy E_k behaves as a function of the free electron energy ϵ_k . The grey lines depict the relation from Eq. 2.11, while the dashed lines represent the energies of an electron or hole. Here, we can see that the Bogoliubons behave like electrons or holes for energies far away from 0 (E_F). However, when ϵ_k approaches 0, the Bogoliubon energy deviates more and more from the usual electron/hole behavior. We can see that it approaches $|\Delta|$. Here, we realize the real meaning of

the order parameter Δ , which we introduced in the model above. It represents an energy gap inside the superconductor's dispersion, in which no quasiparticle states are present. This becomes even more apparent when we plot the density of states (DOS) of the BCS superconductor given by:

$$\begin{aligned}
 N(E) &= \sum_{\mathbf{k}} \delta(E - E_{\mathbf{k}}) \\
 &= \int_{-\infty}^{+\infty} N(E - \mu) \delta(E - \sqrt{\epsilon^2 + \Delta^2}) d\epsilon \quad (2.12) \\
 &= 2N_0 \int_0^{+\infty} \delta(E - \sqrt{\epsilon^2 + \Delta^2}) d\epsilon
 \end{aligned}$$

where we plugged in Eq. 2.11 in the first step and assumed that the metallic DOS around E_F is constant (N_0), which is valid for small energy ranges around E_F . The integration leads to:

$$N(E) = \begin{cases} 2N_0 \frac{E}{\sqrt{E^2 - \Delta^2}} & \text{for } E > \Delta, \\ 0 & \text{for } E < \Delta, \end{cases} \quad (2.13)$$

For a realistic system, the quasiparticles have a finite lifetime. We reflect this by adding a broadening factor Γ to the equation leading to:

$$N(E) = 2N_0 \text{Re} \left[\frac{E + i\Gamma}{\sqrt{(E + i\Gamma)^2 - \Delta^2}} \right]. \quad (2.14)$$

The function is plotted in Figure 2.3. We can see that a gap is opened up with the value of 2Δ . Inside of this interval, no quasiparticle states are present. Large local density of states (LDOS) peaks, known as coherence peaks, appear at both borders of these

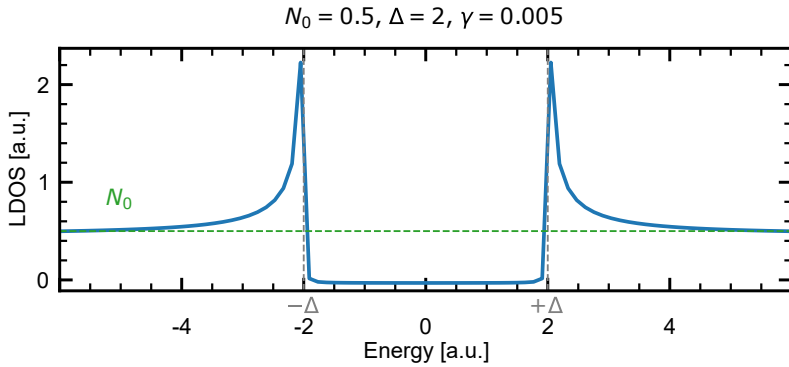


Figure 2.3: Plot of the Dynes function. The superconducting gap energies at negative and positive bias ranges are marked by the grey dashed, vertical lines. The green horizontal line depicts the value of N_0 .

gapped regions. For energies outside of the gapped regions of the superconductor, the spectrum resembles that of a simple metallic electrode.

2.2.3 Proximity effect

The proximity effect refers to the phenomenon in which normal conducting metals are brought into the vicinity of a superconductor. By that, superconducting correlations inside the normal metal are induced. This way, a material that is originally metallic can be made into a superconductor. The proximity effect allows us to design novel electron phases by pairing superconductors (SCs) with other interesting materials that were originally non-superconducting. One of the most prominent applications is given

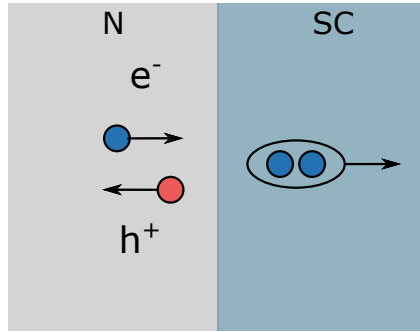


Figure 2.4: Schematic representation of the Andreev reflection process. The blue circle (e^-) represents an electron inside the N approaching the N-SC interface. The Cooper pair resulting from the Andreev reflection process is represented by the two circles in the SC. The red circle represents the reflected hole (h^+).

in the field of topological superconductivity, where the proximity effect is used to create non-trivial phases of superconductivity by a combination with magnetism [31, 55, 56].

The basic mechanism behind the proximity effect is Andreev reflection. Andreev reflections can be found at interfaces between a normal metal (N) and a SC. The process is depicted in Figure 2.4. When an electron inside of the N reaches the boundary to the SC, it can either cross the SC if its energy $E > \Delta_{SC}$ or be reflected if $E < \Delta_{SC}$. Due to the missing energy, the electron cannot enter the SC. Instead, it can form a Cooper pair with another electron to enter the SC while simultaneously creating a hole reflected into the N. The hole has the opposite spin and momentum, which results in spin and momentum conservation throughout the process.

2 Theoretical foundations

The Andreev reflection process produces a phase shift $\delta\phi$ between the ingoing electron and the outgoing hole. This phase shift is given by:

$$\delta\phi = \Phi + \arccos\frac{\epsilon}{\Delta} \quad (2.15)$$

where Φ is the phase of the superconductor, ϵ is the energy of the ingoing electron and Δ is the superconducting gap. This induced phase correlation leads to the superconducting correlations in the normal metal. As a measure for the spatial extent of this induced phase, the coherence length ξ_N can be used given by [57, 58]:

$$\xi_N \approx \frac{\hbar v_F}{2\pi k_B T} \quad (2.16)$$

with the Fermi-velocity of the normal metal v_F and the temperature T . However, one should note that the upper equation only applies to sample systems within the clean limit, where the defect rates inside the metal and at the interface are small. In this case, the transport through the material is considered to be in the ballistic limit.

Another type of mechanism leading to proximitized superconductivity can be found in very clean crystalline thin metallic film systems (N) with a few tens of nanometers thicknesses brought into the proximity of a superconductor (SC). Typically, the N has one interface to the superconductor (N/SC) and an interface to the vacuum. These interfaces can serve as reflective barriers where electrons and holes can scatter. Due to the comparably short distances between the interfaces, electrons/holes can coherently scatter multiple times via Andreev reflection at the N/SC interface

and specular reflection at the vacuum boundary. As a result, the DOS of the N is gapped out around E_F . The multiple Andreev reflections can be measured as peaks at the ends of the gapped region and are known as de Gennes-Saint James (dGSJ)-states [59, 60]. Due to their resemblance to the coherence peaks of normal superconductors, they are often referred to as the "coherence peaks" of the proximitized metal.

2.2.4 Magnetic impurities in superconductors

As the Meissner-Ochsenfeld shows on a macroscopic level, magnetism and superconductivity tend to be competing interactions. L. Yu, H. Shiba, and A. I. Rusinov [61–63] were the first to theoretically describe the influence of single magnetic impurities on a superconductor. The presence of a magnetic impurity in a superconducting host material breaks time-reversal symmetry and can locally disrupt the superconducting order parameter. This leads to excitations located inside the host's superconducting gap. These excitations are known as Yu-Shiba-Rusinov states (YSR-states) [64, 65]. They are quasiparticles that are spatially bound to the magnetic impurity. For the case of $3d$ transition metal atoms coupled to a SC when the Cooper pairs are in the s-bands of the material, the origin of the YSR-states is the exchange interaction, which couples the s-orbitals of the conduction electrons with the magnetic d-orbitals of the magnetic impurity. One can handwavingly explain the YSR-states by the exchange field of the magnetic impurity, which destabilizes the Cooper pairs by misaligning the spins of the paired electrons. As a result, it takes less energy to break up

the Cooper pair, leading to excitations at energies smaller than Δ . The Anderson impurity model can be used as a starting point to describe the YSR-states. The conduction electrons are described by the effective BCS-Hamiltonian (Eq. 2.10), and the magnetic impurity is modeled as a classical spin \mathbf{S} , which interacts with the spin of the delocalized conduction electrons $\boldsymbol{\sigma}$. The strength of the interaction is given by the exchange coupling J :

$$H = H_{\text{eff}} - \frac{J}{2N} \sum_{\mathbf{k}, \mathbf{k}'} c_{\mathbf{k}}^{\dagger} \boldsymbol{\sigma} c_{\mathbf{k}'} \cdot \mathbf{S}, \quad (2.17)$$

Another term that considers the Coulomb scattering between the impurity and the substrate can be used to extend this equation. In the spectrum, this interaction leads to a particle-hole asymmetry in the peak intensities. For 3d metal atoms, each orbital can induce a pair of YSR-states where the spatial shape reflects the orbital.

With the above equation, the energy of the YSR-states is then given by:

$$E_{\text{YSR}} = \pm \Delta \frac{1 - (\pi N_0 J S)^2}{1 + (\pi N_0 J S)^2}, \quad (2.18)$$

where Δ is the superconducting gap and N_0 is the normal metal's density of states at the Fermi level.

The YSR-state is usually localized around the magnetic impurity. Unique properties of the underlying substrate, such as strong confinement along the surface [66] or the anisotropic shape of the substrate's Fermi surface [67], can lead to long-ranged patterns of the YSR-states.

In any case, the amplitudes of the particle- and hole components of the YSR-state decay with the distance from the impurity with the following relation:

$$u_r, v_r \propto \frac{\sin(k_F r + \delta^\pm)}{k_F r} \exp\left(-\frac{r}{\xi_0}\right), \quad (2.19)$$

with the Fermi-wavevector of the substrate k_F , the scattering phase shift δ and the coherence length of the superconductor ξ_0 . Please note that in this equation, the Coulomb scattering is also implicitly included.

When two YSR-states are placed near each other, hybridization effects between them can occur. This leads to a splitting or shifting of the original YSR-states. The hybridization strength depends on factors such as the spatial extent of the YSR-state or the distance between the YSR-impurities, or the strength and direction of the magnetic moments [68–70]. This can even be extended to chains or arrays of YSR-impurities. In this case, the hybridization between the YSR-states will lead to the formation of bands called YSR-bands. In this thesis, I will refer to a 1D chain system built this way as YSR-chain.

2.3 Rashba spin-orbit coupling (SOC)

Rashba spin-orbit coupling (SOC) occurs at the surface of a crystal [71]. It can be explained by relativistic effects, where the change to the reference frame leads to a coupling between the momentum of an electron and its spin. At the surface of a crystal, the inversion symmetry is broken. This leads to an electric field at the surface region. If an electron moves along the surface of the crystal, it will be influenced by this surface electric field. From its reference frame, the movement within the surface electric field effectively induces a magnetic field coupling to the electron's spin. The strength and direction of the magnetic field seen by the electron depend on its momentum and direction of movement as well as on the strength of the surface electric field. This effectively leads to a coupling between the electron's momentum and its spin alignment. To describe this phenomenon, we can make use of the Rashba-Hamiltonian:

$$H_R = \alpha_R (\boldsymbol{\sigma} \times \mathbf{k}_{\parallel}) \cdot \hat{\mathbf{Z}}, \quad (2.20)$$

where α_R is the Rashba coupling constant, and $\hat{\mathbf{Z}}$ is the unit vector perpendicular to the surface plane. It is perpendicular to $\boldsymbol{\sigma}$, the spin of the electron, and \mathbf{k}_{\parallel} , the momentum component of the electron parallel to the surface. If we assume a quasi-free electron model for the electrons residing at the surface, with dispersion

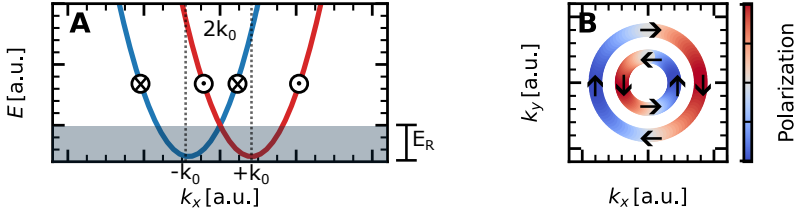


Figure 2.5: Rashba-split dispersion relation. (A) Cut of the Rashba-split dispersion relation along k_x -direction. The color and symbols (\otimes/\odot) depict the spin-polarization of the subbands. (B) Cut of the dispersion relation along the (k_x, k_y) -plane. The arrows depict the k -dependent spin orientation. The color depicts the spin polarization along the y -direction.

$\frac{\hbar^2 k_{\parallel}^2}{2m_e^*}$, the resulting dispersion relation is given by:

$$E = \frac{\hbar^2 k_{\parallel}^2}{2m^*} \pm \alpha_R k_{\parallel} \quad (2.21)$$

where m^* is the effective mass of the electrons and α_R refers to the Rashba-parameter indicating the strength of the interaction [72, 73]. From this equation, one can extract the Rashba-energy E_R , which is given by:

$$E_R = 2\alpha_R k_0, \quad (2.22)$$

Moreover, the momentum splitting of the bands is given by

$$2k_0 = \Delta k_R = 2\alpha_R m^* / \hbar^2, \quad (2.23)$$

When plotting these energy bands as a function of k_x , i.e., one component of \mathbf{k}_{\parallel} , we can see the typical Rashba-split band struc-

ture (Figure 2.5A). Here, the subbands are spin-polarized as given by the colors of the two dispersion branches. The Rashba interaction lifts the spin-degeneracy. Due to the coupling between the spin and the direction of movement, the Rashba interaction introduces a chiral structure, as visible in Figure 2.5B. With this coupling, an electron's spin can be aligned (e.g., by a magnetic field) to influence its direction of movement or vice versa.

2.4 Kitaev model

The Kitaev model was first introduced by Alexei Kitaev in 2001 [15] and describes a one-dimensional chain of spinless fermions in which phases emerge that can be categorized according to their topology. The Kitaev model is particularly known for its prediction of MZMs in the solid state system, which will be localized at the ends of the chain. This concept is of great interest for topological quantum computation [12].

In its usual form, the Kitaev chain is a spinless one-dimensional tight-binding model, which considers an onsite energy, a hopping term, and a pairing potential between neighboring sites [74]:

$$H = -\mu \sum_{j=1}^N c_j^\dagger c_j - \sum_{j=1}^{N-1} \left(t c_j^\dagger c_{j+1} + \Delta_p c_j c_{j+1} + \text{h.c.} \right), \quad (2.24)$$

Here c_j^\dagger and c_j are the creation and annihilation operators for electrons at site j , μ is the chemical potential, t is the hopping amplitude, and Δ_p is the p-wave pairing potential. Note that Δ_p is not

the same as the order parameter used throughout the thesis for the superconductivity of the substrates. Unlike s-wave superconductivity, which involves coupling electrons with opposite spins, the Kitaev model is a spinless system.

To illustrate the topological properties of this model, we can express the annihilation and creation operators c and c^\dagger by a superposition of new operators [75]:

$$c_j = \frac{1}{2}(\gamma_{2j-1} + i\gamma_{2j}) \quad c_j^\dagger = \frac{1}{2}(\gamma_{2j-1} - i\gamma_{2j}) \quad (2.25)$$

γ_{2j-1} and γ_{2j} are so-called Majorana operators, with the characteristic property:

$$\gamma_i = \gamma_i^\dagger, \quad (2.26)$$

making the particle its own antiparticle. This representation can be rationalized in the following way. With the normal electronic operators c , we depict each lattice site by its index j . There can either be an electron or none for each lattice site. The new representation splits up each site into two. Therefore, the number of sites has doubled. In the new representation, each lattice site is addressed by the indices given by $2j - 1$ and $2j$.

We rewrite the Hamiltonian in Eq. 2.24 in terms of the Majorana operators and obtain:

$$H = -i\frac{\mu}{2} \sum_{j=1}^N \gamma_{2j-1}\gamma_{2j} + i\frac{t + \Delta_p}{2} \sum_{j=1}^N \gamma_{2j}\gamma_{2j+1} + i\frac{-t + \Delta_p}{2} \sum_{j=1}^N \gamma_{2j-1}\gamma_{2j+2}. \quad (2.27)$$

By considering different limits in the parameter space between μ ,

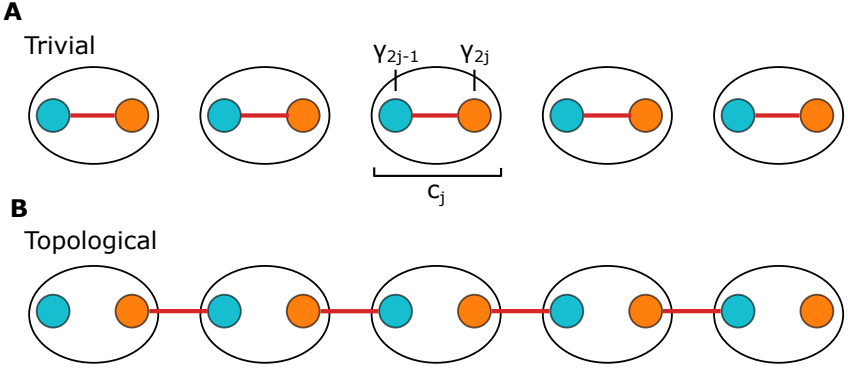


Figure 2.6: Topologically trivial and non-trivial phase of the Kitaev chain. Schematic illustrating the coupling between the Majorana operators γ_j in the trivial (A) and the topological phase (B). The black circles represent the electronic lattice sites c_j . In the Majorana representation, each electron comprises two Majorana operators, γ_{2j-1} and γ_{2j} . The red lines depict the couplings between the Majorana operators.

t , and Δ_p , the new representation gives an insight into the distinction between the topological and the trivial phases.

In the limit $|\mu| > 2|t|$, Eq. 2.27 reduces to

$$H = -\mu \frac{i}{2} \sum_{j=1}^N \gamma_{2j-1} \gamma_{2j}. \quad (2.28)$$

Interestingly, this Hamiltonian no longer couples the Majorana operators from the same electronic sites to each other; instead, it couples Majorana operators from neighboring electronic lattice sites. This phase is, therefore, known as the topologically nontrivial phase.

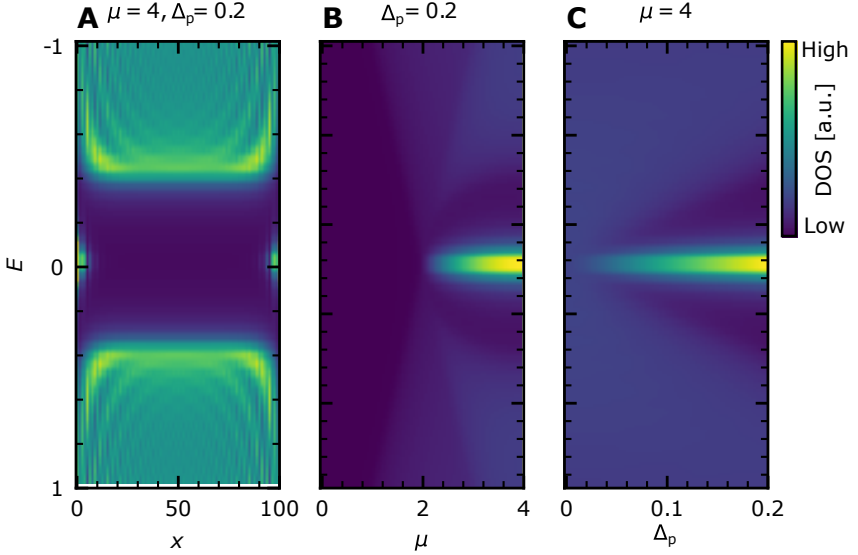


Figure 2.7: MZMs as a function of parameter space. (A) LDOS of a Kitaev chain with 100 sites as a function of the energy E and position x for fixed values of μ and Δ_p . (B) LDOS at the edge of the chain as a function of E for varying μ and fixed Δ_p . (C) Same as in (B) but with a fixed μ and a varying Δ_p . The calculation was done with a Python toolkit for tight-binding calculations [76]. For each panel, $t = 1$. The LDOS and the color scale are given in arbitrary units.

Figure 2.6 gives a pictorial representation of the two phases. In this picture, it becomes evident that the Majorana-quasiparticles at the ends of the chain remain unpaired in the topological phase.

We can calculate the LDOS of the chain numerically. Figure 2.7 shows the calculation for a chain with 100 sites. As seen in panel (A), a gap is opened due to the pairing potential Δ_p . However, at the ends of the chain, we can see states appearing at $E = 0$.

This is the MZM. To see how this mode behaves for different sets of parameters of the Kitaev chain, we can look at panels (B) and (C), where the spectrum is taken on the edge sites of the chain for different values of μ (B) and Δ_p (C). Here, the other parameters are kept constant. In (B), one can see that no MZM can be found for the value of $\mu < 2$. For $\mu > 2$, a mode appears at $E = 0$, which stays constantly at this energy. In panel (C), we can see that as soon as $\Delta_p > 0$, a state can be found at zero energy as long as μ has the correct value. For small Δ_p , we can see that the intensity of the MZM becomes smaller due to its delocalization along the chain.

MZMs or MBSs obey non-Abelian exchange statistics, which makes them candidates for implementing topological quantum bits [12, 13, 77–79]. Due to their topological nature, MZMs are inherently stable against perturbations smaller than the gap Δ_p . Therefore, they inherently solve the problem of decoherence that usual quantum bits have [8, 80].

This has sparked an enormous interest in the experimental realization of the Kitaev model. However, finding a system that shows the properties the model proposes is still tricky. The most challenging aspect is the spinless pairing term. This mechanism could be realized by coupling a p-wave superconductor (which is based on spin triplet coupling) to a magnet. However, p-wave superconductivity has not yet been found to occur in any (not artificially designed hybrid) material, and the most prominent candidate for p-wave superconductivity, Sr_2RuO_4 is still under dispute [81, 82].

On the other hand, elemental superconductors, which can be de-

scribed by BCS theory, rely on an s-wave pairing mechanism involving an antiparallel alignment of the electrons' spins. One workaround is to consider completely spin-polarized systems. If the whole system does not show any differences in the observable, one can also treat it as if this observable does not exist. Therefore, the system behaves effectively spinless, at least within one of the spin-polarized bands. The idea could now be to use such a system and proximitize it with a superconductor to induce pairing correlations. However, magnetism and conventional superconductivity usually have a rivaling relationship with each other (see Section 2.2.1). Therefore, a spin-polarized system would usually not allow s-wave pairing to occur. One way out of this dilemma is the involvement of SOC. SOC can tilt the spins of the Cooper pair electrons out of their original plane, thereby inducing a component to the correlation, which is not of s-wave but of p-wave nature. In other words, SOC inside an s-wave superconductor can mix in p-wave correlations. In contrast to the s-wave correlations, p-wave correlations are not challenged by spin-polarized systems. Consequently, p-wave superconductivity induced in a spin-polarized system could realize the Kitaev-chain model [15, 83].

Circling back to the original question, we can say that in order to realize the Kitaev chain model, there are three ingredients to consider: magnetism, s-wave superconductivity, and Rashba SOC (see Section 2.3).

One promising platform, which possibly combines all of these interactions, is based on magnetic chains proximitized by a super-

conductor [19, 27–29, 38]. In this approach, magnetic impurities are placed on a superconductor. As mentioned above, the resulting YSR-states already combine two (magnetism and superconductivity) of the three ingredients. The atoms can be used to form chains of YSR-states, thereby creating YSR-bands. Depending on the substrate choice, SOC can also be included, which is the topic of Chapter 6.

3 Experimental methods and setup

In this chapter, I will introduce the reader to the scanning tunneling microscopy (STM) and scanning tunneling spectroscopy (STS) methods used throughout the thesis. I will start with the general principle and then move on to the STM's various operational modes. Then, I will continue with the actual setups used to acquire the measurements presented in the results chapters.

3.1 Scanning tunneling microscopy

Heinrich Rohrer and Gerd Binnig developed STM in 1982 [84], for which they were awarded the Nobel Prize in Physics in 1986. STM/STS are powerful methods extensively used in surface science for investigating conducting surfaces with atomic resolution [85–88].

To construct a scanning tunneling microscope, an atomically sharp tip is needed, which acts as one electrode. The sharp metallic tip is placed above the conducting sample, which acts as the second electrode, with a bias voltage V_{bias} between them. Because the electrodes are very close together, a relatively narrow tunneling barrier is created. This allows electrons to jump between the electrodes even when the applied bias voltage is smaller than the vertical height of the tunneling barrier. This phenomenon is known as the *tunneling effect* [89]. As a result, a small electrical current

3 Experimental methods and setup

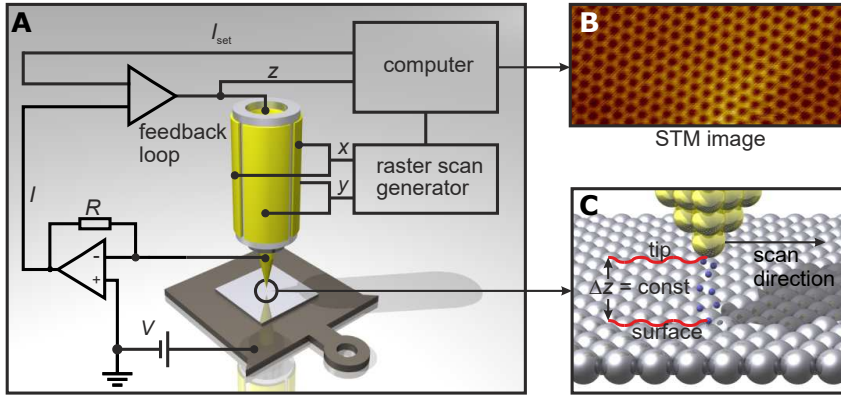


Figure 3.1: Illustration of STM. (A) Components of a STM setup. (B) Example of a constant current STM image. (C) Schematic of the STM tip above the sample surface. Taken from Ref. [90].

can be detected between the electrodes, which depends on various factors such as the electrical properties of the electrodes, the applied bias voltage, and the height of the tunneling barrier. As a first approximation, the relation between the tunneling probability P and tip-sample distance d is given by:

$$P \propto e^{-2\kappa d} \quad (3.1)$$

where κ is a factor determined by the electrodes' work functions, electron energy, and bias voltage V_{bias} . The tunneling probability scales exponentially with decreasing d , which, together with the relative sharpness of the tip with respect to the flat sample surface, is the reason for the high spatial resolution of the STM.

While ideally operated under ultra-high vacuum (UHV) condi-

tions, STM can also function with less precision and more frequent tip changes under ambient conditions. As depicted in Figure 3.1, the precise movements of the tip are typically controlled by electronic parts constructed from piezoelectric materials [91]. When a high voltage is applied to these materials, they expand or contract depending on their polarity. In modern STM setups, the tip and tip holder are embedded into a piezoelectric tube, also known as a tube scanner. It consists of a piezoelectric tube with radial polarization and five electrodes arranged like four concentrically aligned sheets on its sides and one in the interior of the tube. By applying a bias voltage between opposite-facing electrodes, the tube flexes in one direction, allowing precise movement of the tip in the x - y plane in the subnanometer range. To move the tip in the z -direction, the same voltage is applied to each of the four outer electrodes with respect to the innermost electrode, causing a motion in the z -direction. Depending on the STM design, the bias voltage V_{bias} can be applied to either the sample or the tip side. In our setup, V_{bias} is applied to the sample. Thereby, a positive V_{bias} means that electrons tunnel from the tip to the sample, while a negative V_{bias} implies that electrons tunnel from the sample to the tip. The tunneling current generated by the scanning tunneling microscope is on the order of pA to nA and susceptible to errors. To address this, the tunneling current is fed into a preamplifier, which converts it into a voltage signal and amplifies it. Subsequently, the signal is split into two paths: one to the data acquisition electronics for recording and saving the data and the other to the feedback loop, which regulates the distance between the tip and sample. This feedback loop operates in constant-current

mode, where a setpoint current I_{set} is maintained by varying the vertical position z of the tip.

One can raster the sample surface in the x - and y -directions while recording the vertical position z of the tip at each point. This results in a 2D matrix of values that can be displayed on a computer, providing the sample surface's topographic information. Depending on the mode of operation, the tunnel current can also be recorded.

3.2 Fundamentals of scanning tunneling spectroscopy

The basic theory of the tunneling process is part of the undergraduate courses on quantum mechanics and can be found in various quantum mechanics textbooks [92]. If we consider a particle with the energy E and mass m , the probability for it to tunnel through a barrier with height V_0 and width d is approximately determined by the proportionality:

$$T \propto e^{-\frac{2d}{\hbar} \sqrt{2m(V_0-E)}} \quad (3.2)$$

In the case of STM, the tunneling barrier refers to the vacuum region between the tip and the sample, with d being the distance between them. The applied V_{bias} gives the electron its energy. In this strongly simplified picture, the electronic structures of the tip and sample are neglected.

John Bardeen gave a more detailed approach to this problem, which is only outlined in the following (please refer to Ref. [93] for the detailed description). In Bardeen's tunneling theory, the tip and the sample are viewed as distinct quantum mechanical systems modeled by their respective wavefunctions. A tunneling matrix describes the tunneling probabilities between the tip and sample electrode. The elements of this matrix can be calculated by a perturbative approach. Using Fermi's golden rule, one can now obtain the transition rates between the electrodes.

As stated by Tersoff and Hamann, the expression for the tunneling current can be simplified. The approach is to approximate the tip electrode by an *s*-wave function. This is justified because most of the tunneling current goes through the tip apex, which usually consists of a single atom [94]. Under this assumption for the tip state, one gets:

$$I(V, T, x, y) = \frac{4\pi e}{\hbar} \int_{-\infty}^{\infty} \rho_s(E - E_F, x, y) \rho_t(E - E_F + eV) \mathcal{T}(E, V, T) (f(E - E_F + eV, T) - f(E - E_F, T)) dE \quad (3.3)$$

Here, $\rho_{s/t}$ are the LDOS of the sample/tip measured at position (x, y) , V is the bias voltage, \mathcal{T} is the transmission coefficient, and f is the temperature (T)-dependent Fermi-function. In our picture, tunneling electrons can only tunnel from occupied to unoccupied states. The bias voltage can alter the Fermi level difference in the electrodes, determining between which states the electrons can tunnel. When, for example, a positive bias voltage is applied between the tip and the sample, the Fermi level in the sample is

3 Experimental methods and setup

lowered relative to the tip. Electrons can now tunnel from occupied states of the tip into unoccupied states of the sample that are at the same energy. In a real system thermal effects have to be taken into account. Due to these, electrons can be thermally excited into unoccupied states, smearing out the occupation number of the electron states near the Fermi levels. Mathematically, this is taken into account by the temperature-dependent Fermi function:

$$f(\epsilon, T) = \frac{1}{e^{\epsilon/k_B T} + 1} \quad (3.4)$$

with $\epsilon = E - E_F$.

As one can see from Eq. 3.3, the tunneling current depends on the LDOS $\rho_S(E - E_F, x, y)$ of the sample. Therefore, we can use this relation to get insights into the sample's LDOS using a measurement of I . To do this, we take the derivative of Eq. 3.3:

$$\begin{aligned} dI/dV(V, T, x, y) \propto & \\ \int_{-\infty}^{\infty} \left[\rho_S(E - E_F, x, y) \frac{\partial \rho_t(E - E_F + eV)}{\partial V} (f(E - E_F + eV, T) \right. & (3.5) \\ \left. - f(E - E_F, T)) + \rho_t(E - E_F + eV) \frac{\partial f(E - E_F + eV, T)}{\partial V} \right] dE. & \end{aligned}$$

Here, the transmission coefficient has been left out as it can be approximated by a constant value when the applied bias voltages are sufficiently small.

With the assumption that ρ_t only changes slowly as a function of the energy E , which is true for small energy windows (meV), we

can simplify the above equation to:

$$dI/dV(V, T, x, y) \propto \int_{-\infty}^{\infty} \rho_t(E - E_F + eV) \frac{\partial f(E - E_F + eV, T)}{\partial V} dE \quad (3.6)$$

We can further simplify the equation if the temperature is low enough ($k_B T \ll eV$):

$$dI/dV(V, T, x, y) \propto \rho_s(E - E_F = eV, x, y) \quad (3.7)$$

This way, STS provides direct access to the sample's LDOS below the tip apex's location (x, y) .

3.3 Modes of operation in STM and STS

Despite its basic principle, the scanning tunneling microscope operates in various modes to gather specific information about the sample. The different modes of operation take advantage of the fact that the tunneling current in STM depends on the tip-sample distance and the electronic properties of the tip and the sample.

Constant-current mode

In constant-current mode, the tunneling current is kept constant while a feedback loop controls the tip's z -position. This loop adjusts the tip-sample distance by retracting the tip from the sample if the current exceeds a setpoint value I_{set} , and approaching it if the tunneling current falls below this value.

Specroscopy modes

Apart from the topographic information, STM can also provide information on the spectral properties of the sample. We can deduce the sample's LDOS if we know the tip's DOS or make reasonable assumptions about this DOS.

As shown in Eq. 3.7, the LDOS of the sample is directly related to the differential conductance tunneling, which the STM can measure. The differential conductance is obtained by recording the tunneling current as a function of V_{bias} and subsequently calculating the derivative of the tunneling current with respect to V_{bias} .

However, in modern STM setups, the lock-in technique is commonly used to measure the dI/dV -signal. This technique enables an almost instantaneous measurement of the differential conductance tunneling signal and enhances the signal-to-noise ratio through internal filtering instead of numerically deriving the tunneling current. In this method, a lock-in amplifier introduces a small voltage signal V_{mod} with a high frequency f (typically in the ranges of a few kHz) to the direct current (dc) bias voltage signal. The voltage modulation induces a response in the tunneling current with the same frequency. This signal is fed into the lock-in amplifier, where it is multiplied by a reference signal with the same frequency and phase and integrated over a time τ to isolate the alternating current (ac) response from the rest of the input. This part of the response represents the change in the tunneling current for a small change in the bias voltage. It is, therefore, directly proportional to the dI/dV value of the tunneling junction.

For the measurements presented in this thesis, f was chosen to be 1097.1 Hz (for the SPECS setup, see Subsec. 3.5.1) or 4142 Hz (for the 300 mK setup, see Subsec. 3.5.2). τ was chosen to be 10 ms for bias-spectroscopy measurements (see more on the operation mode below) and mostly 3 ms for spectroscopic maps (depending on the scanning speed and number of data points).

Bias-spectroscopy measurements

In the bias-spectroscopy measurement mode, the tip is stabilized above a chosen location using a stabilization current I_{stab} and a stabilization bias voltage V_{stab} . Then, the feedback is turned off. During the measurement, V_{bias} is ramped inside a defined sweep range, while the tunneling current and the dI/dV -signal are recorded as described above. The dI/dV -signal then gives information on the LDOS of the sample at the location of the tip and as a function of energy ($E = E_F + eV_{\text{bias}}$). It is also possible to conduct this measurement along a line or inside a grid with multiple measurement points. For each point, the bias spectroscopy measurement is repeated. In the case of the line, we would call this measurement a spectroscopic line profile. In the case of the grid, I will refer to this measurement as grid spectroscopy measurement or spectroscopic grid.

Recording spectroscopic maps

Spectroscopic information on the sample can also be obtained while scanning the surface in a similar fashion to the topographic imaging mode. In contrast to the bias spectroscopy mode, the sample is scanned with a constant bias voltage applied. Thereby, the LDOS at energy $E = E_F + eV_{\text{bias}}$ can be measured using the lock-in amplifier technique. This measurement can be done with or without feedback to prevent artifacts from stabilization effects.

A similar mode used throughout the thesis is the so-called constant contour mode. In this case, the sample is first scanned in constant-current mode to record the topography of the sample. Afterward, the feedback is turned off, and the bias voltage is set to a specific value. Then, the recorded topography is followed, while the dI/dV -signal is recorded.

Atom manipulation

Atom manipulation is the last mode used very heavily in this thesis. With this technique invented by Don Eigler [95], the STM tip can be used to move around single atoms or even larger objects on the surface. Atom manipulation can be done vertically or horizontally [96]. During this thesis, only horizontal manipulation has been used. To do this, a high tunneling resistance is set by switching to high I_{set} and low V_{bias} . When the tip gets near the single atom, the potential of the tip causes the atom to bind partially to the tip. This allows for dragging the atom to a location of choice.

When the atom is placed in the desired location, the tip can be retracted again by switching to the normal parameters I_{set} and V_{bias} used for scanning.

3.4 Tunneling between superconducting electrodes

The spectroscopy measurements shown throughout this thesis have been done with a superconducting tip. The reason for that can be understood by considering Eq. 3.5. Thermal effects, which are considered by the Fermi function, lead to an energetic broadening of features in the LDOS. In other words, finite temperatures reduce the energy resolution of the spectroscopy measurements. This problem can be solved by using superconducting tips. Mathematically, the tunneling current is a convolution between the tip's DOS and the sample's LDOS. The convolution of a function $f(x)$ with a delta function $\delta(x)$ will result in $f(x)$ [97]. Shifting the delta function by a value a ($\delta(x - a)$) will yield the same result but with a shift of the signal in the x-axis by the value a , i.e., $f(x - a)$. To make use of this effect, the coherence peaks provided by a superconducting tip can be used as an approximation of the delta function. With this method, the energy resolution can be increased beyond the limit given by the Fermi function [98].

The tunneling process for a superconductor-insulator (vacuum) - superconductor tunnel barrier is depicted in Figure 3.2. In this illustrated case, a superconducting tip with a gap of Δ_t and a super-

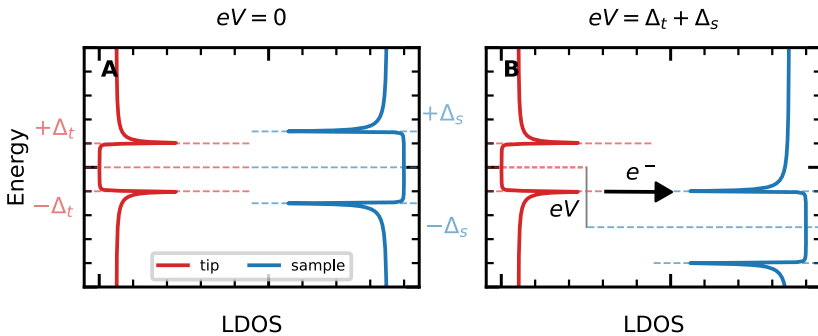


Figure 3.2: Illustration of tunneling processes in SIS-junctions. Tunneling processes between a superconducting tip electrode's LDOS (red) and a superconducting sample electrode's LDOS without V_{bias} (A) and with $V_{\text{bias}} = \Delta_t + \Delta_s$ applied between tip and sample (B). The gap parameters of the tip (Δ_t) and the sample electrode (Δ_s) are depicted by the dotted line at the coherence peaks. The dashed lines between the respective coherence peaks illustrate E_F of the respective electrodes. The applied bias voltage in (B) leads to a relative shift between E_F of the tip and the sample. Consequently, an electron current flows, depicted by the black arrow in (B).

3.4 Tunneling between superconducting electrodes

conducting sample with a gap of Δ_s are considered. The dashed lines mark the coherence peaks labeled $\pm\Delta_t$ ($\pm\Delta_s$). Dashed lines between the respective coherence peak pairs mark E_F . Panel (A) illustrates the case for $V_{\text{bias}} = 0$. The Fermi energies of both electrodes are aligned to each other. No current flows because no bias voltage is applied. If $V_{\text{bias}} \neq 0$ is applied, the Fermi energies of the electrodes are shifted with respect to each other. We first assume zero temperature $T = 0$. Since both electrodes are gapped for voltages $|eV| < |\Delta_s + \Delta_t|$, there is no current flow between the electrodes for V_{bias} in this range. A current begins to flow at $eV = \pm(\Delta_s + \Delta_t)$. This scenario is depicted in panel (B). In this case, the tip electrode's occupied coherence peak overlaps with the sample's unoccupied coherence peak, leading to an electron current flowing from the tip electrode to the sample electrode. A sharp tunneling current onset can be measured due to the sharp LDOS at both electrodes. The same is true for a bias voltage of $eV = -(\Delta_s + \Delta_t)$. However, the current flows opposite, from the sample to the tip. We now consider a non-zero temperature $T > 0$. Then, the tunneling can already occur when a bias voltage of $eV = \pm(\Delta_s - \Delta_t)$ is applied. This would apply to the cases where either the thermally depopulated coherence peaks below E_F or the thermally populated coherence peaks above E_F of the electrodes are aligned with each other. Thereby, additional tunneling processes are caused by finite temperature effects. This leads to small peaks in the spectrum located close to E_F if $\Delta_t \approx \Delta_s$.

When using a superconducting tip to measure in-gap states (e.g., YSR-states), the interpretation of the spectra becomes more difficult because each in-gap feature gets shifted by $\pm\Delta_t$. On top of

that, when measuring at elevated temperatures, the thermal peaks lead to an additional layer of complexity since every in-gap state will also introduce a thermal resonance at values between $-\Delta_t$ and $+\Delta_t$. To account for this, the information on Δ_t is added to each spectrum shown throughout this thesis.

Modelling the SIS-spectra

In order to interpret features in spectra taken with a SC tip, the SIS-spectra can be modeled using the tunneling current equation (Eq. 3.3). The LDOS of the superconducting tip and the superconducting samples are modeled using Dynes functions (Eq. 2.14).

Suppose we insert these into the tunneling current Eq. 3.3 and take its derivative, we get the current and the STS-spectrum shown in Figure 3.3. We can see a spectrum with intense coherence peaks appearing at $\pm(\Delta_s + \Delta_t)$ (C). Furthermore, we can see thermal peaks around $V_{\text{bias}} \approx 0$. By comparison to the measured spectra, we can extract the values for Δ_s and Δ_t as done throughout this thesis. Due to the use of superconducting tips at $T \approx 4.54$ K, every feature of the sample can be seen doubled and shifted by the value of the tip gap. This is why, to relate the energies measured in the SIS-spectra back to a normal spectrum, we mark the tip gap values, which indicate the bias voltage at which the samples' E_F can be found. The regions in between $\pm\Delta_t$ show redundant information. For this reason, we often grey out this area or cut it out to focus on the real features. This thesis will deal with in-gap states, such as YSR-states. When we want to model such states, we add

3.4 Tunneling between superconducting electrodes

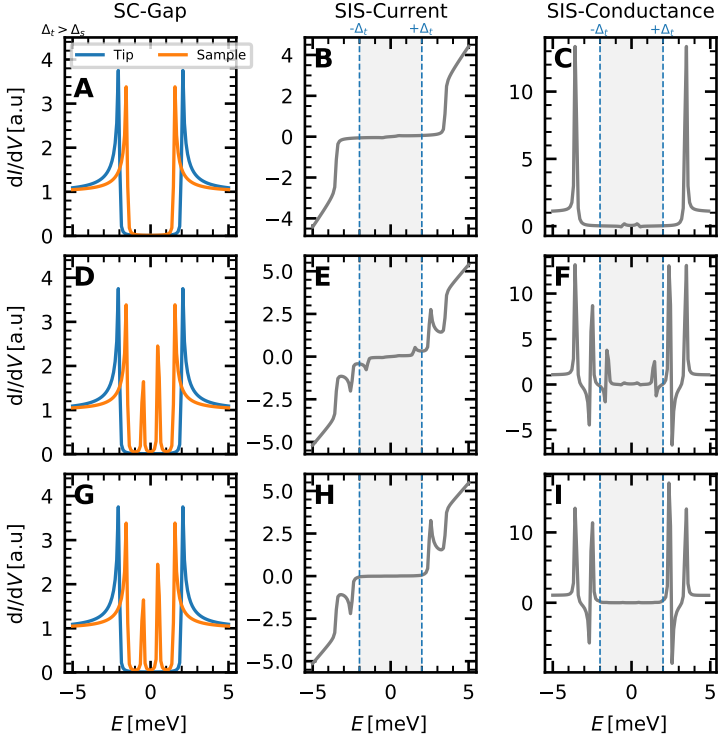


Figure 3.3: Modelling of the SIS-spectra. (A, D, G) Modelled gaps of the tip (blue) and the sample (orange) for a sample without in-gap states (A) and a sample with in-gap states (D, G) as explained in the text. (B, E, H) Tunneling current simulated from the LDOS shown in (A) for the case of a clean gap (B), a gap with in-gap states at $T = 4.54$ K (E) and at $T = 0.32$ K (H). (C, F, I) STS-spectrum calculated from the tunneling current shown in (B), (E) and (H) for the case of a clean gap (C) a gap with in-gap states at $T = 4.54$ K (F) and at $T = 0.32$ K (I). Parameters: $N_{0,\text{tip}} = 1 \text{ meV}^{-1} \text{ m}^{-3}$, $N_{0,\text{sample}} = 1 \text{ meV}^{-1} \text{ m}^{-3}$, $\Delta_t = 2 \text{ meV}$, $\Delta_s = 1.5 \text{ meV}$, $\gamma_{\text{sample}} = \gamma_{\text{tip}} = \gamma_{\text{YSR}} = 0.02 \text{ meV}$, (A-I), $I_1 = 0.2 \text{ meV}^{-1} \text{ m}^{-3}$, $I_2 = 0.3 \text{ meV}^{-1} \text{ m}^{-3}$, $\epsilon_{\text{YSR},1} = 0.5 \text{ meV}$, $\epsilon_{\text{YSR},2} = 0.5 \text{ meV}$ (D-I) $T = 4.54$ K (A-F), $T = 320$ mK (G-I).

3 Experimental methods and setup

additional Lorentzian peaks into the LDOS of the sample as given by (panels (D-F)):

$$L(\epsilon, I_0, \epsilon_0) = \frac{I_0 \gamma^2}{\gamma^2 + (\epsilon - \epsilon_0)^2} \quad (3.8)$$

where I_i is the height, ϵ_i is the energetic location of the peak, and γ is the peak broadening parameter. This results in the sample's overall LDOS:

$$N_s(E) = 2N_0 \text{Re} \left[\frac{E + i\Gamma}{\sqrt{(E + i\Gamma)^2 - \Delta^2}} \right] + \sum_{i=0}^n L(\epsilon, I_{0,i}, \epsilon_{0,i}) \quad (3.9)$$

where the summation runs over each in-gap peak of the sample LDOS. The simulated SIS-spectrum in panel (F) shows that the in-gap states are energy-shifted by $\pm\Delta_i$. Furthermore, tunneling at elevated temperatures leads to thermal copies of those states inside the redundant energy region (grey, shaded bias voltage range). To prevent the occurrence of these thermal excitations, the experiment can be done at lower temperatures. The panels (G-I) demonstrate what to expect in this case. Please note that in the actual experiment, decreasing the temperature from $T = 4.54$ K to 320 mK will also affect Δ_t and Δ_s . However, we only vary the temperatures between (D) and (G) while keeping the rest of the parameters constant for demonstration purposes. In panel (H), we can see that the decreased temperature leads to the disappearance of the thermal peaks. This is more clearly seen in the dI/dV -signal in panel (I). While the thermal peaks disappear, the peak of the YSR-states increases in intensity.

Tip preparation

The measurements presented in this thesis have all been done using superconducting Nb tips. These tips were made from a high-purity Nb-wire, which was mechanically cut and sharpened. The tip was subsequently prepared under UHV conditions, where it was flashed to ≈ 1500 K to remove residual contaminants and oxide layers on the surface of the tip. To prepare a tip with a large and clean superconducting gap Δ_t during measurements, the tip was coated with further superconducting material by indenting it into the superconducting substrate with a high voltage applied. To induce small changes in the tip's spectroscopic properties or reshape the tip apex's microscopic shape, the tip was mildly indented into the sample (usually with a few hundred pm) without applying voltage pulses.

3.5 Experimental setups

This thesis has utilized two different low-temperature UHV STM setups. The first setup is a commercially available system manufactured by the company SPECS [99]. The second setup is a home-built STM system capable of operating at temperatures as low as 300 mK [100]. Both STM setups are equipped with UHV preparation chambers, which will be detailed in the following sections.

3.5.1 The 4.2 K/1 K SPECS setup

The primary measurement setup used in this thesis is shown in Figure 3.4 [99]. This setup was used for conducting STM and STS measurements presented in Chapters 4, 5, and parts of Chapter 6. The diagram in panel (A) shows the three separate chambers. The first chamber, shown in blue, is the Joule-Thomson (JT)-chamber, which contains a JT-cryostat with a scanning tunneling microscope. The system was produced commercially by *SPECS* and *CryoVac*. The cryostat includes a liquid nitrogen (LN_2) reservoir to pre-cool the system to liquid nitrogen temperatures of 77 K and a liquid helium bath cryostat, which is thermally connected to the microscope, cooling it to a base temperature of 4.2 K. Utilizing the JT cooling mechanism, the microscope can be cooled to a base temperature of 1.1 K. However, further discussion is omitted as the JT-cooling was not utilized in this work due to a blockage in the impedance capillary. The JT-chamber, located inside the cryostat, houses evaporation ports that enable the depo-

sition of single atoms onto the sample surface while it is cooled to $T \approx 4.2$ K. Adjacent to the JT-chamber is the first preparation chamber, highlighted in green, interconnected via a UHV gate valve. This chamber incorporates multiple evaporation ports, a pyrolytic boron nitride resistive heating stage, and a combined low-energy electron diffraction (LEED)- and Auger electron spectroscopy (AES)-system. The second preparation chamber, marked in orange, is linked to the first preparation chamber through a UHV gate valve. It houses an e-beam stage and a sputter gun. Each chamber has an ion getter pump and a Ti-sublimation pump, ensuring UHV conditions during operation. Furthermore, both preparation chambers are linked to turbo pumps for pumping during preparation. Under normal operational conditions, the background pressure within the system typically remains in the range of 10^{-10} mbar.

To prepare the samples presented in this thesis, we used preparation chamber 2 to sputter anneal and flash Nb(110) crystals. After this step, the Ag islands presented in Chapters 4 and 5 were grown in the preparation chamber 1. For the BiAg₂ surface presented in Chapter 6, the Bi-evaporator in the preparation chamber 1 was used. Finally, to evaporate individual atoms onto the cold surface, such as the Fe-atoms presented in Chapters 5 and 6, a triple evaporator manufactured by the company *Focus* was used.

3 Experimental methods and setup

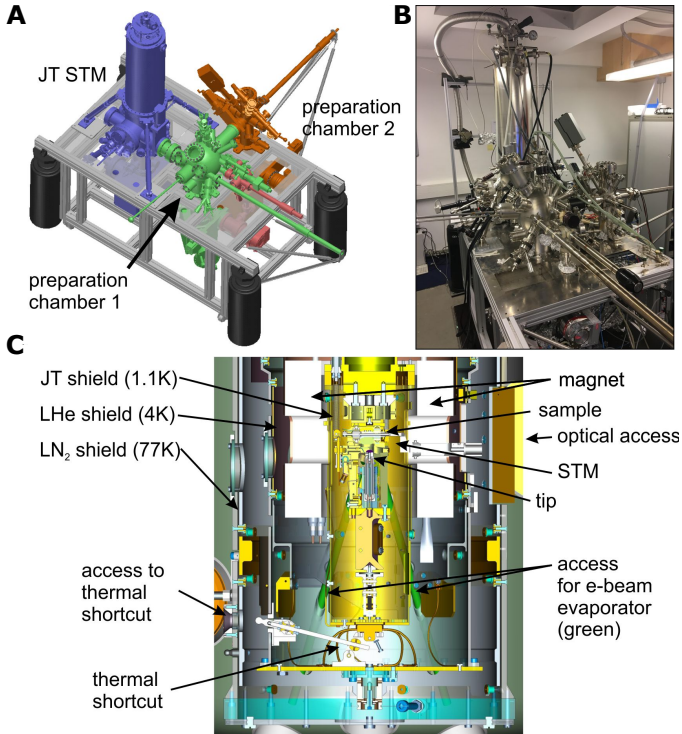


Figure 3.4: The JT-SPECS setup. (A) Schematic of the STM setup, with the JT-STM chamber (blue) and the preparation chambers attached to it (green and orange). (B) Photograph of the system; (C) Cross-section of the design showing the lower part of the JT-chamber with the STM and the magnet taken from Ref. [101].

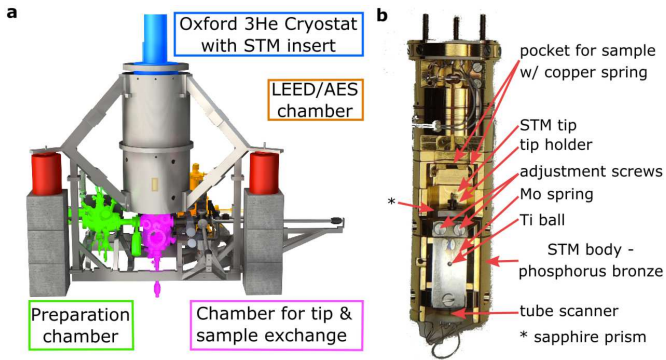


Figure 3.5: 300 mK UHV STM setup. (A) Schematic of the 300 mK UHV STM setup consisting of the cryostat with the scanning tunneling microscope and the magnet (blue), the mechanical noise damping system, the preparation chamber (green), the chamber for sample and tip exchange (pink) and the LEED/AES chamber (orange). Note that the LEED/AES was not used during this thesis. (B) Close-up image of the STM head embedded inside of the cryostat shown in (A). The image was taken from Ref. [102].

3.5.2 The 300 mK home-built system

The second STM setup utilized for a portion of the measurements within this thesis is a home-built low-noise UHV system operating at approximately 300 mK (see Figure 3.5). The system was designed and constructed by J. Wiebe and A. Wachowiak, and it is extensively detailed in Ref. [100]. The STM system features a base temperature of around 315 mK and can be broken down into two main components: the cryogenic system, which includes the cryostat and the ^3He cooling mechanism, and the UHV multi-chamber system. Turbo pumps are attached to the chambers to establish and maintain UHV conditions during sample preparation and bake-outs. The preparation chamber (green) houses the e-beam stage for flashing samples, a sputter gun setup, and multiple evaporators to deposit atoms on a warm sample. During measurements, the STM-head is located inside the cryostat. However, the microscope can be brought into the tip/sample exchange chamber below the cryostat for a tip or a sample exchange. Furthermore, the chamber has an evaporation port with a triple evaporator manufactured by Focus attached to it, which can be used to deposit single atoms onto a cold surface. Titanium sublimation pumps and ion-getter pumps are utilized to maintain UHV during measurements. Superconducting magnets allow applying magnetic fields in the out-of-plane direction of the sample up to 12 T. The ^3He is used in a closed cycle to cool the STM-head below the liquid helium temperature down to 315 mK with a hold time of ≈ 20 h.

For the preparation of the BiAg_2 on $\text{Nb}(110)$ presented in Chap-

ters 6, the preparation chamber was used. The Nb(110) crystal was sputter-annealed and flashed in multiple cycles. The evaporators mounted onto the preparation chamber were used to deposit Ag- and Bi-atoms for the growth of BiAg₂ on Nb(110). To deposit magnetic atoms, the sample was put into the STM-head, which was lowered into the tip/sample-exchange chamber. Here, the sample was cooled, and atoms were evaporated onto it.

4 Proximity induced superconductivity in artificial quantum dots: experimental discovery of Machida-Shibata states

This chapter deals with the investigation of artificially constructed quantum dots and their superconducting properties when being proximitized by a superconductor. To do this, we grow Ag(111) islands on the superconducting surface of a Nb(110) crystal. We examine the surface state of Ag(111) and how it behaves under the influence of the underlying superconducting substrate. Using atom manipulation, we will build quantum corrals to also laterally confine the Ag(111) surface state, creating a quantum dot with spin-degenerate energy levels. With this, we will address the question of what happens to the eigenmodes when it is coupled to a superconductor. The results of this chapter will shed light on the first ingredient of topological superconductivity, the proximity effect. During the time of my thesis, parts of the results of this chapter have been published in the following works:

4 Proximity induced superconductivity in artificial quantum dots: experimental discovery of Machida-Shibata states

Lucas Schneider, Khai That Ton, Ioannis Ioannidis, Jannis Neuhaus-Steinmetz, Thore Posske, Roland Wiesendanger and Jens Wiebe

Proximity superconductivity in atom-by-atom crafted quantum dots

Nature **621**, 60–65 (2023)

Lucas Schneider, Christian von Bredow, Howon Kim, Khai That Ton, Torben Hänke, Jens Wiebe and Roland Wiesendanger

Scanning tunneling spectroscopy study of proximity superconductivity in finite-size quantized surface states

Phys. Rev. B **110**, L100505 (2024)

Experimental and theoretical work sharing

Dr. Lucas Schneider and I conducted and analyzed the measurements presented in this chapter. For the data analysis, we used self-written Mathematica and Python scripts. Ioannis Ioannidis derived the resonance scattering model under the supervision of Dr. Thore Posske. Dr. Lucas Schneider used self-written Mathematica scripts to simulate the particle-in-a-box model.

Introduction

Inducing superconductivity in systems, which are initially non-superconducting, can lead to the formation of physical systems with non-trivial properties [16, 55, 103–105]. In the research field of topological superconductivity, for example, many proposals incorporate the idea of using the proximity effect to induce superconductivity onto magnetic systems with non-trivial spin-textures [30, 31, 106]. For hybrid systems between a normal metal and a superconductor, the proximitized superconductivity depends on the interface's transparency. For the clean limit, proximity-superconductivity in the normal metal can still be observed for normal metal film thicknesses of up to 45 nm [107]. However, inducing superconductivity into the surface state of the material requires a more thorough understanding of the proximity effect since the surface state is known to be well decoupled from the bulk. In the field of STM, creating designer quantum states of matter by atom manipulation often involves the confinement of surface state electrons [108–110]. Experiments in this field range from the creation of artificial topologically non-trivial lattice systems [111, 112] to the creation of artificial molecular orbitals [113–115]. Understanding how to induce superconductivity in such systems would open up new possibilities for emulating superconducting systems.

Experimental procedures

The measurements in this chapter were taken with a superconducting tip, made from a high purity mechanically cut Nb wire,

4 Proximity induced superconductivity in artificial quantum dots: experimental discovery of Machida-Shibata states

which was flashed to ≈ 1500 K as also described in Section 3.4. In the spectra, we mark the V_{bias} value corresponding to the tip gap energy $\pm\Delta_t$ by dashed lines with the respective label. In some of the measurements, we cut the V_{bias} -interval between $-\Delta_t/e$ and $+\Delta_t/e$ to leave out the redundant information of the spectra and focus on the relevant features.

4.1 Noble metal system growth on a superconductor

This section deals with the growth of Ag(111) on Nb(110). The procedures described here will lay the foundation for the works on the quantum corrals in the sections hereafter.

Wetting layer growth of Ag

We begin our investigations by growing clean Ag(111) surfaces on top of Nb(110). To achieve this, we use a Nb-crystal cut in the (110)-direction and clean the crystal by flashing it to approximately $T \approx 2000$ K. This process leaves us with the typical reconstructed NbO_x surface. The characteristic disordered striped pattern covers the surface [116].

On the reconstructed Nb(110) surface, we deposit Ag from a high-purity rod using an e-beam evaporator. The deposition rate is approximately 0.1 MLs per minute while heating the sample to about 600 K.

After deposition, we observe a coverage of approximately $\approx 15\%$, where the deposited atoms mostly form small Ag islands. An example of that can be seen in panel (A) of Figure 4.1. The Ag island is marked by a blue cross, while the reconstructed NbO_x surface is marked by an orange cross. The islands on the substrate exhibit heights of about 500-540 pm, corresponding to 2 MLs of Ag. Since the Ag does not fully cover the surface, we can still see the

4 Proximity induced superconductivity in artificial quantum dots: experimental discovery of Machida-Shibata states

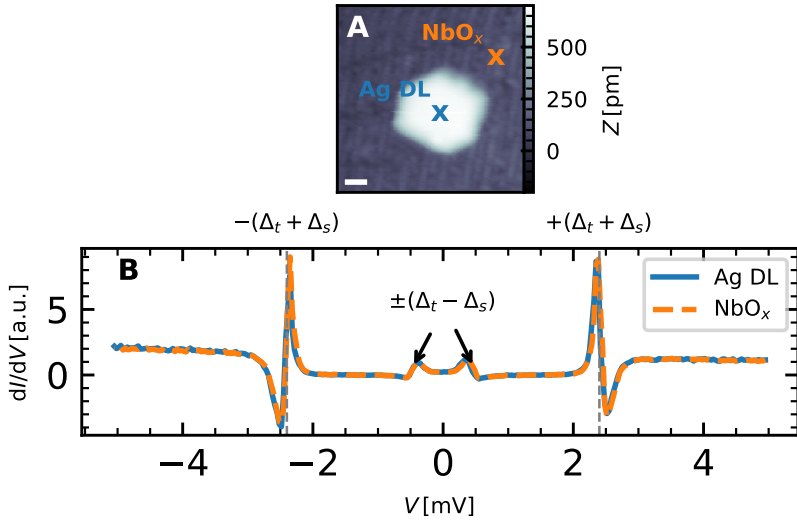


Figure 4.1: Growth of 2 MLs islands of Ag on Nb(110). (A) Constant-current STM image of a thin Ag island grown on oxygen-reconstructed Nb(110). The apparent height of the island equals 540 pm, indicating that the Ag grows in DLs. The white bar corresponds to 2 nm. (B) dI/dV -spectra measured on the Ag DL and the oxidized Nb(110) substrate; the sharp peaks at bias voltages corresponding to $\pm(\Delta_t + \Delta_s)$ are marked by grey, dashed lines and the ones at $\pm(\Delta_t - \Delta_s)$ are marked by black arrows. Parameters: $V_{\text{bias}} = 5 \text{ mV}$, $I_{\text{set}} = 1 \text{ nA}$ (A), $I_{\text{stab}} = 1 \text{ nA}$, $V_{\text{stab}} = 5 \text{ mV}$ and $V_{\text{mod}} = 50 \mu\text{V}$ (B).

reconstructed $\text{NbO}_x/\text{Nb}(110)$ substrate.

Next, we compare bias-spectroscopy measurements taken on the island with those taken on the Nb-substrate (marked by the blue and orange "x" in Figure 4.1A). The spectra can be seen in panel (B), with the orange line corresponding to the NbO_x substrate and the blue curve corresponding to the Ag island. The result shows the typical spectrum for SIS-tunneling (see Section 3.4). The sharp peaks observed at $V_{\text{bias}} = \pm 2.35$ mV can be assigned to tunneling between the coherence peaks of sample and tip given by $\pm(\Delta_t + \Delta_s)$. In contrast, the two peaks at $V_{\text{bias}} = \pm 0.36$ mV correspond to thermally activated tunneling processes between the coherence peaks of the sample and tip given by $\pm(\Delta_t - \Delta_s)$. By measuring the spectrum with different microtips, we determine a sample gap of $\Delta_s = 1.35$ meV [117].

Even though we did not clean the Nb(110) surface from the oxygen reconstruction, comparing the spectrum measured on the Ag wetting layer and the one measured directly on the Nb-substrate yields almost no differences. The fully opened gap proposes that the oxide interface between the Nb-substrate and the Ag-film does not influence the proximity-induced superconductivity on the surface of the Ag DL.

In the next step, we zoom in on the surface of the Ag DL island, as presented in Figure 4.2. Panel (A) shows the constant-current STM image at normal imaging parameters. The surface is covered with impurities of unknown chemical composition. We scan the same area with larger tunneling currents and lower bias voltages to uncover the surface's atomic structure, as presented in panel

4 Proximity induced superconductivity in artificial quantum dots: experimental discovery of Machida-Shibata states

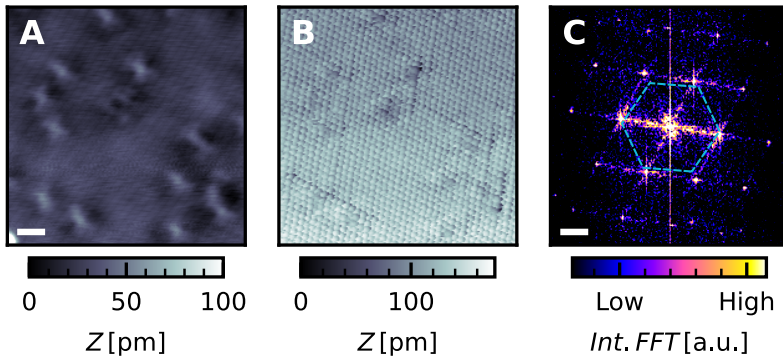


Figure 4.2: Zoom-in on the Ag DL surface. (A) Zoom-in on the DL, exhibiting atomically flat areas of Ag and several twofold symmetric defects of unknown origin. The white bar corresponds to 1 nm. (B) Atomically resolved constant-current STM image of the same area shown in panel (A). (C) Fourier transform of the atomic-resolution image in (B), showing Bragg spots incompatible with a hexagonal lattice (a perfect hexagon is overlaid in blue) but with a pseudomorphic growth on the bcc(110) surface of clean Nb. The white line corresponds to 1.92 nm^{-1} . Parameters: $V_{\text{bias}} = 1 \text{ V}$, $I_{\text{set}} = 0.1 \text{ nA}$ (A), $V_{\text{bias}} = 2.5 \text{ mV}$, $I_{\text{set}} = 10 \text{ nA}$ (B).

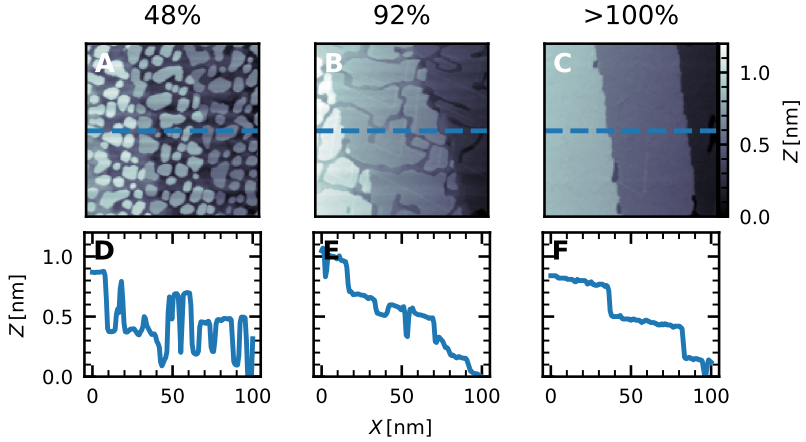


Figure 4.3: Closing of the Ag-wetting layer. (A-C) Constant-current STM image of Ag grown on NbO_x/Nb(110) at different coverages indicated by the labelling above. (D-F) Line cuts through the measurements shown in (A-C) as indicated by the blue dashed lines. Parameters: $V_{\text{bias}} = 1.0 \text{ V}$, $I_{\text{set}} = 0.02 \text{ nA}$ (A), $V_{\text{bias}} = 100.0 \text{ mV}$, $I_{\text{set}} = 0.2 \text{ nA}$ (B), $V_{\text{bias}} = 100.0 \text{ mV}$, $I_{\text{set}} = 0.5 \text{ nA}$ (C).

(B). This measurement reveals a pseudomorphic growth on the underlying Nb(110) surface: The scanned area's fast Fourier transformation (FFT) shows a 2-fold symmetric structure, with peaks at the corners of a distorted hexagon (C).

A similar growth behavior has been reported for Au on reconstructed V(100) [118]. According to the authors, the oxygen atoms in the V substrate become mobile upon heating the sample. When the Au atoms are deposited onto the surface, they replace the oxygen atom, forming a relatively clean layer of Au.

4 Proximity induced superconductivity in artificial quantum dots: experimental discovery of Machida-Shibata states

When the amount of deposited material increases, the Ag-atoms form larger DL islands on top of the Nb-substrate until a closed Ag DL is formed. Figure 4.3 illustrates the surface for different degrees of coverage, with a line cut through the scan in the respective panel below. At 48% coverage, panel (A), individual DL islands cover the surface with a height of around 500 pm. We can discern the different step edges of the Nb-substrate below the Ag islands. At a coverage of 92%, panel (B), the individual islands merge and begin to form almost fully closed layers. Panel (C) shows the surface for a preparation where the Ag DL is completely closed. Here, the observed height differences mostly stem from the step edges of the Nb-substrate. Only then, for even larger amounts of deposited material, thicker islands are formed (see below). So, the growth mode of Ag on Nb(110) is a Stranski-Krastanov growth mode with a wetting layer of two layers of Ag [119].

Epitaxial growth of thicker Ag islands

In a three-step process, we deposit Ag-atoms to grow thicker epitaxial Ag(111) islands on the Nb-surface. In the first step, we deposit 2 MLs of Ag at 600 K to form a closed wetting layer. After a closed wetting layer is created, thicker islands begin to grow on it. We decrease the temperature of the sample to 400 K and continue depositing 2 MLs of Ag. The lowered temperature decreases the mobility of Ag-atoms deposited on the wetting layer, leading to the formation of nucleation centers for the thicker islands. In the last step, we increase the temperature to 600 K and deposit an ad-

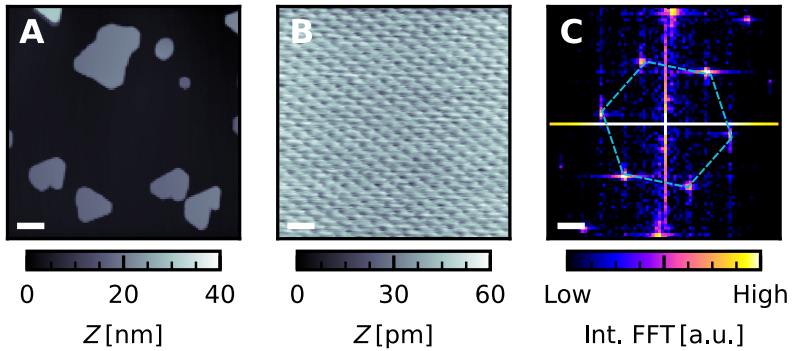


Figure 4.4: Growth of thicker Ag(111) islands on Nb(110). (A) Large-scale constant-current STM image of a sample with nominal Ag coverage of 8 MLs. The DL thick Ag wetting layer covers the Nb-surface. The additional amount of Ag forms thicker Ag(111) islands. The white bar corresponds to 500 nm. (B) Atomically resolved constant-current STM image of a thick Ag island. The white bar corresponds to 0.5 nm. (C) FFT of the image, showing Bragg spots in good agreement with a hexagonal fcc(111) growth. The white bar corresponds to 1.52 nm^{-1} . Parameters: $V_{\text{bias}} = 1 \text{ V}$, $I_{\text{set}} = 100 \text{ pA}$ (A), $V_{\text{bias}} = 100 \text{ mV}$, $I_{\text{set}} = 1 \text{ nA}$ (B).

ditional 3 MLs of Ag. The increased temperature helps anneal the surface and create a flat surface on top of the thicker Ag islands.

The result of this sample preparation is presented in Figure 4.4. In panel (A), a large-scale overview of the surface is shown. The Nb(110) substrate is fully covered with the 2 MLs thin wetting layer. On top of the wetting layer, Ag islands with thicknesses of 20 nm to 40 nm are observed. We can see a clean surface when zooming onto the island surface. Panel (B) shows an atomically resolved image of such an island, revealing an atomically well-ordered lattice. The surface atoms are ordered in a hexagonal lattice. The FFT of the atomically resolved image is shown in panel (C) to quantify this further. Here, we can see six points around the coordinate system's origin, forming the corners of an equilateral hexagon. We conclude that the pseudomorphic growth of the Ag(110) wetting layer has been followed by the growth of 3D Ag islands exhibiting a (111) surface orientation and that the morphology of those islands is already like that of bulk Ag.

This result coincides with what has been reported in Ref. [107], where the Stranski-Krastanov growth mode for Ag on Nb(110) has been observed.

Spectroscopy measurements on thicker Ag(111) islands

Next, we look at the spectral properties of the thicker Ag(111) islands grown on the Nb-substrate. Our measurements aim to elucidate two primary aspects. Firstly, we delve into the Shockley-type surface state of Ag(111), a topic previously discussed in Chapter 2.1. It can serve as additional proof that the surface is, in fact, the Ag(111) surface. Secondly, we will look at spectra in the low-energy regime around E_F . This will allow us to determine whether superconductivity is induced into the Ag(111) surface state.

The Shockley-type surface state of the Ag(111) surface can be probed by observing interference patterns in dI/dV -maps resulting from the scattering of surface state electrons at defects on the surface, also known as QPI. These defects can be point-like impurities or one-dimensional step edges. Figure 4.5 provides an example of a step edge on one of the Ag(111) islands (see panel (A)). In addition to the step edge, single impurities on the surface serve as additional scatterers. The dI/dV -maps of the same area were acquired for different V_{bias} , shown in panels (B-D) and (H-J). These maps reveal wavy interference patterns across the surface. In the measurement at -20 mV (B), for instance, a comparison with the topography in (A) shows that these waves originate from the scattering centers. The respective FFT of the map (E) displays an isotropic scattering pattern, indicated by the ring-shaped feature. As V_{bias} increases, the wavelength of the interference patterns becomes smaller, panels (C, D, H-J), which is further illustrated by the corresponding FFTs shown in the respective panels below (F,

4 Proximity induced superconductivity in artificial quantum dots: experimental discovery of Machida-Shibata states

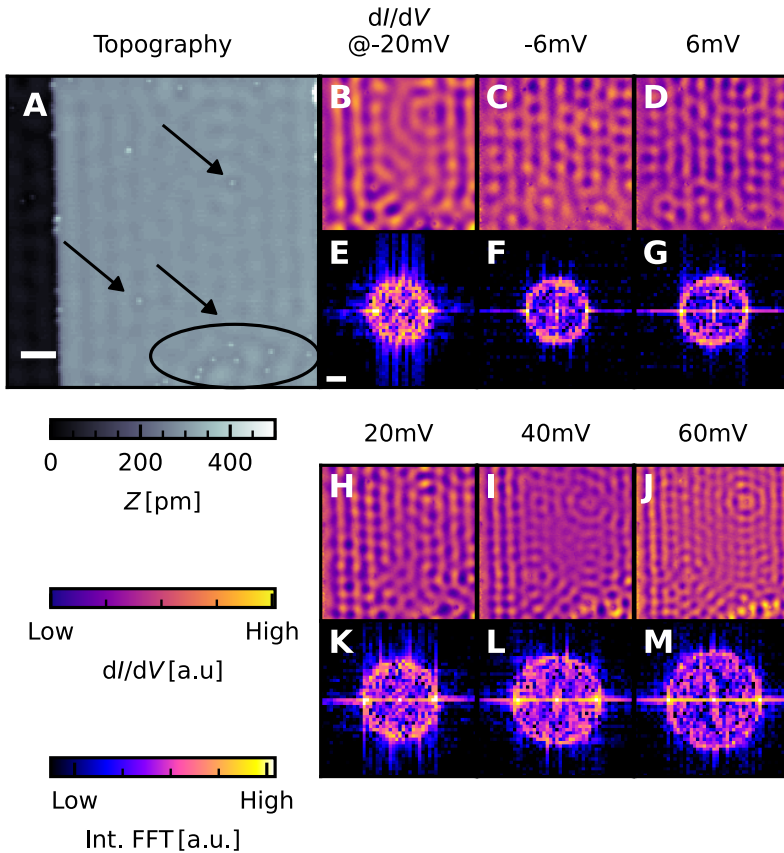


Figure 4.5: Scattering pattern of the Ag(111) surface state. (A) Constant-current STM image of a Ag(111) terrace with a step edge. The white line corresponds to 4 nm. Examples of defects are marked by the black arrows. (B-D), (H-J) dI/dV -maps of the Ag(111) surface taken at different bias voltages as indicated on top of each image. (E-G), (K-M) FFT image of the respective dI/dV -measurement above. The white line in (E) corresponds to 0.12 nm^{-1} . Parameters: $I_{\text{set}} = 200 \text{ pA}$, $V_{\text{bias}} = 5 \text{ mV}$ (A); $I_{\text{set}} = 200 \text{ pA}$, $V_{\text{mod}} = 50 \text{ } \mu\text{V}$, feedback: on (B-D), (H-J).

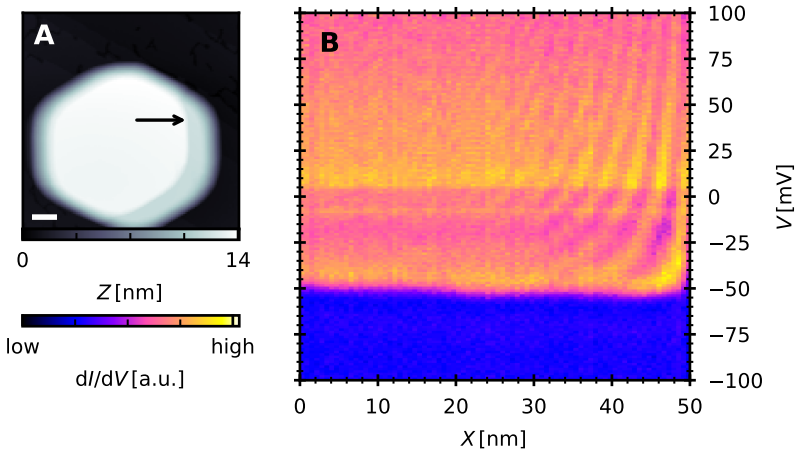


Figure 4.6: Spectroscopic line profile on the Ag(111) island over a large bias range. (A) Constant-current STM image of the Ag(111) island. The white line corresponds to 20 nm. (B) Spectroscopic line profile over a wide bias range, measured along the line depicted by the black arrow in (A). Parameters: $I_{\text{set}} = 100 \text{ pA}$, $V_{\text{bias}} = 100 \text{ mV}$ (A); $I_{\text{stab}} = 1 \text{ nA}$, $V_{\text{stab}} = 100 \text{ mV}$, $V_{\text{mod}} = 5 \text{ mV}$ (B).

G, K-M). The circles' radii in the FFTs increase with V_{bias} , corresponding to the decreasing wavelength of the interference patterns. Note that the horizontal line is an artifact resulting from the FFT process. Apart from these artifacts, the circle's presence as the only sharp feature in the FFT suggests that the scattering in one electron band predominantly causes the observed patterns.

A spectroscopic line profile was acquired to investigate how the surface state behaves as a function of energy along a line on the surface (see Figure 4.6). Please note that the topographic image

4 Proximity induced superconductivity in artificial quantum dots: experimental discovery of Machida-Shibata states

of the island in panel (A) shows a double tip feature on the right. Therefore, we limit the spectroscopic line profile to the topmost terrace. The measurement was taken along the black arrow in panel (A).

The spectroscopic line profile in panel (B) was taken over a wide bias range from -100 mV to 100 mV. The measurements taken on the terraces show the typical spectrum for Ag(111): From the negative to positive value of V_{bias} , we observe that between -100 mV and approximately -55 mV the signal is at a low level and constant as a function of energy. At about -55 mV, we see a step-like increase in the onset of the surface state band. On closer inspection of the spectra taken on the flat terraces, we can observe an oscillation of the dI/dV signal as a function of X for voltages between the step at -55 mV and 100 mV. Note that the wavelength of this oscillation decreases as the bias voltage V_{bias} increases. Furthermore, these oscillations are most apparent near the boundary to the step and lose intensity as we move toward the island's interior.

The scattering patterns in the spectroscopic line profile can be used to extract the dispersion relation for the Ag(111) surface band. We take the FFT for each spectroscopic line profile energy slice. This way, we end up with an intensity map as a function of the scattering vector q and the energy given by eV_{bias} shown in Figure 4.7. This dispersion can be fitted by using the quasi-free electron model. The dispersion relation of the quasi-free electron model is

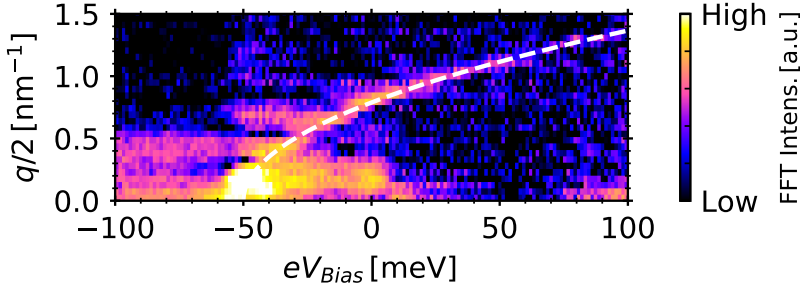


Figure 4.7: Ag(111) surface-band dispersion relation. The values were obtained by Fourier transforming the spectroscopic line profile shown in Fig. 4.6 for each energy line by line. The white dashed line depicts the fitted dispersion of a quasi-free-electron gas using Eq. 4.1. Fitting parameters: $m_{\text{eff}} = 0.47m_e$, $E_0 = -50$ meV

given by [120]:

$$E(k_{\parallel}) = \frac{\hbar^2 k_{\parallel}^2}{2m_{\text{eff}}} + E_0 \quad (4.1)$$

with the electron energy E , the wavevector parallel to the surface k_{\parallel} , the effective mass m_{eff} and the surface band onset E_0 . In our case, k_{\parallel} is given by $k_{\parallel} = q/2$ since q describes a scattering vector from a state at $-k_{\parallel}$ to $+k_{\parallel}$ or vice versa. For large energies, it has been reported that the band dispersion relation deviates from a parabolic relation [121]. In that case, using a tight-binding modeling approach would lead to better results. However, in our case, the quasi-free electron is sufficient to model our system.

The fitted values can be seen in Figure 4.7 as a white dashed line, where $m_{\text{eff}} = 0.47m_e$ and $E_0 = -50$ meV. The value for m_{eff} is in accordance with what has been reported in the literature

4 Proximity induced superconductivity in artificial quantum dots: experimental discovery of Machida-Shibata states

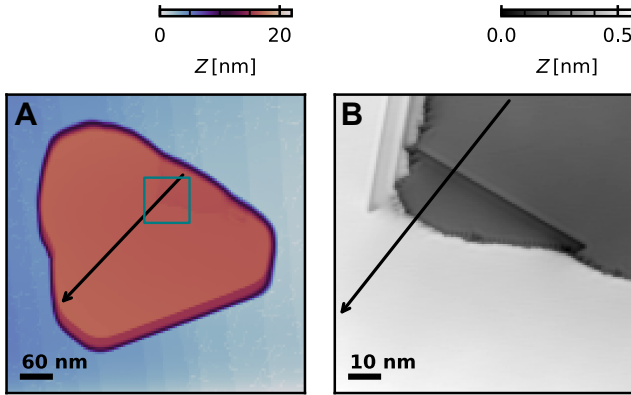


Figure 4.8: Ag(111) island with step edges. (A) Constant-current STM image of the Ag(111) island with multiple step edges. (B) Zoom-in on the region marked by the blue square with step edges in panel (A). Parameters: $I_{\text{set}} = 50 \text{ pA}$, $V_{\text{bias}} = 1 \text{ V}$ (A); $I_{\text{set}} = 1 \text{ nA}$, $V_{\text{bias}} = 100 \text{ mV}$ (B).

($m_{\text{eff}} = 0.41m_e$ [122], $m_{\text{eff}} = 0.42m_e$ [123]). However, a more notable discrepancy exists between our E_0 and the one reported in Ref. [122] ($E_0 = -65 \text{ meV}$). One reason could be the strain in the Ag island, stemming from the lattice mismatch between the Nb(110) surface and the Ag(111) crystal structure, which can shift the surface bands onset to higher energies [124].

Next, we take a closer look at the superconducting properties of the Ag(111) island surfaces. The measurements were taken on the Ag(111) island shown in Figure 4.8A. The island has a thickness of approximately 55 MLs. On this island, one can find a region with multiple step edges (panel (B)). In Figure 4.9A, a low-bias spectroscopic line profile is presented, which was taken along the arrow

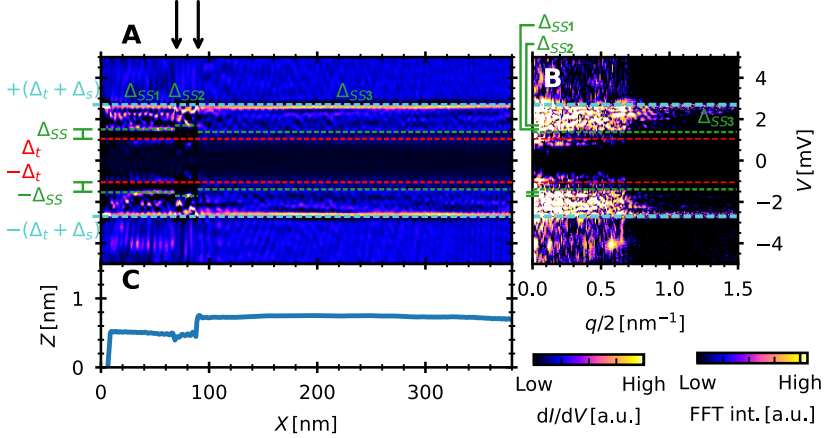


Figure 4.9: Spectroscopic line profile on the Ag(111) island over a small bias range and FFT. (A) Spectroscopic line profile in the low-bias regime measured along the Ag(111) islands shown in Figure 4.8, where the arrow in Figure 4.8A depicts the position of the line profile. The values of the tip gap $\pm\Delta_t$ (red) and the sum of the tip and sample gap value $\pm(\Delta_t + \Delta_s)$ (cyan) are marked by the dashed lines and labeled respectively. The energy interval between $\pm\Delta_t$ and the green dashed lines depict the induced gaps of the surface state $\Delta_{SS,i}$. The black arrows on the top mark the edges of terraces. **(B)** FFT of panel (A). **(C)** Topographic line profile of the step edge corresponding to panel (A). See also supplementary Fig. 5 in Ref. [117] for more information on the island. Parameters: $I_{\text{stab}} = 1 \text{ nA}$, $V_{\text{stab}} = 5 \text{ mV}$, $V_{\text{mod}} = 50 \mu\text{V}$ (A).

4 Proximity induced superconductivity in artificial quantum dots: experimental discovery of Machida-Shibata states

in Figure 4.8. The spectra range from $V_{\text{bias}} = -5 \text{ mV}$ to 5 mV to highlight features around the superconducting gap. As mentioned at the beginning of the chapter, the spectra were obtained using a superconducting tip, which shifts all features inside and outside the gap by $\pm\Delta_t$ with respect to their original energetic position relative to E_F . The energetic positions of $\pm\Delta_t$ are marked by red dashed lines, while the cyan dashed lines indicate $\pm(\Delta_t + \Delta_s)$. In the energy range between $-\Delta_t$ and $+\Delta_t$, we observe the thermally excited replica of the in-gap features at energies above $\pm\Delta_t$. For the measurements taken on the terraces, multiple states are visible between Δ_t ($-\Delta_t$) and $+(\Delta_t + \Delta_s)$ ($-(\Delta_t + \Delta_s)$). Interestingly, these in-gap states are strongly quenched when measuring at the step edge.

As described in Section 2.2.3 and in Ref. [60], the proximity-induced superconductivity inside of a metal as a function of thickness is given by the coherence length of the metal. For a noble metal like Ag, we extracted a coherence length of $\xi_N = 270 \text{ nm}$ (see details in Ref. [125]). Given that our island's thickness $d \approx 14 \text{ nm}$ is well below the coherence length, we would expect to see a proximitized gap on the surface. However, when measuring the spectrum on the Ag(111) surface, we observe that multiple in-gap states dominate the gap, and only a very small gap Δ_{SS} opens on the large Ag(111) terrace. Interestingly, we can see that the number of in-gap states and the size of Δ_{SS} differs between the individual terraces. Most importantly, we see that $\Delta_{SS,1}$ and $\Delta_{SS,2}$, which correspond to locations with the same island thickness, differ strongly.

This contradicts the interpretation in Ref. [107], where it has been

4.1 Noble metal system growth on a superconductor

stated that the superconductivity induced into the Ag-surface state will get stronger as the islands get thinner. So, the suggestion is that proximitized superconductivity in the surface state is not determined by the island thickness but rather by something else, as we will see later in this chapter (Section 4.3).

4.2 Artificially constructed quantum dots

In the previous experiments, we investigated the surface state of Ag(111) using bias spectroscopy measurements. We also examined the superconducting gap and observed that the sample gap is filled with in-gap states distributed across the Ag(111) surface. However, given that the thickness of the island is well below the coherence length of the proximitized Ag, we would expect to see some level of proximitized superconductivity. One possible explanation for the lack of a clear proximitized gap is that the Ag island might need to be more transparent. However, the observation of an almost fully open gap at the step edge of the Ag island contradicts this explanation. Another explanation could be that the decoupling of the surface state of Ag(111) from the bulk hinders the proximity-induced superconductivity on the surface.

In this section, corrals are built using atom manipulation techniques. The surface state of Ag(111) can be confined within corrals to create systems with well-separated energy levels [126]. We use single Ag-atoms extracted from the substrate surface to build the corral walls, confining the Ag(111) surface state. This leads to energetically well-separated eigenmodes in the corral [127]. By doing so, we can simplify the problem to a single resonance level at E_F , effectively creating a quantum dot and investigating how it behaves in the presence of the underlying superconducting substrate. By resizing the corral in one dimension, we can tune the energetic locations of the eigenmodes. We look at spectroscopic measurements inside the corral in the low-energy regime around

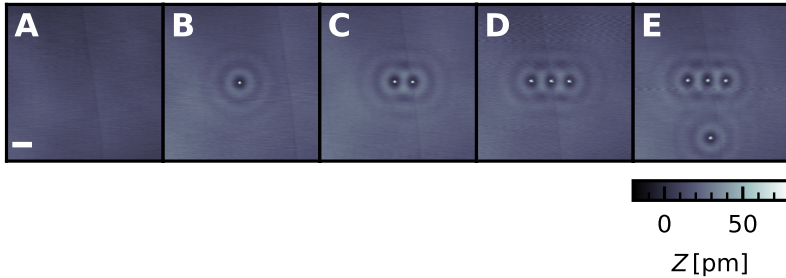


Figure 4.10: Extraction of single Ag atoms from Ag(111)/Nb(110). (A) Constant-current STM image of a clean Ag area. The white bar corresponds to 10 nm. (B-E) The same area after indenting the tip into the surface at different positions along the surface. A single adsorbate of similar apparent height is found after each indentation process. The tip was stabilized at the scanning parameters for the indentation and moved by -600 pm in the Z-direction towards the surface. Parameters: $I_{\text{set}} = 1$ nA, $V_{\text{bias}} = 15$ mV.

the superconducting gap. Note that the terms (quantum) corral and quantum dot (QD) will be used interchangeably throughout this chapter.

Extraction of single Ag-atoms

In the first step, single Ag-atoms have been gathered on the surface to build the quantum corrals. On the Ag(111) surface, this can be done by controlled dipping of the tip into the sample to coat the tip with Ag-atoms and, another time, to drop some of the atoms again [128]. The amount of atoms dropped is dependent on the crashing depth. We follow the procedure described by Ref.

[129]. This can result in one of the two scenarios:

1. Extract Ag-atoms from the surface, which are then bound to the tip. After this process, a vacant spot is usually observed where the tip has been dipped.
2. A single adatom on the surface is left behind (as shown in Figure 4.10).

The second scenario is explained by the tip being coated with Ag in a previous dipping process and dropping a single Ag-atom onto the surface. In the constant-current images of Figure 4.10, we see an object created with an apparent height of 80 nm. With this method, we can reliably produce single atoms, which can be used to build quantum corrals.

Spectroscopy measurements on quantum dots

To construct the quantum corrals, we used lateral atom manipulation of the Ag-atoms with tunneling resistances of $R \approx 100 \text{ k}\Omega$ (see example in Figure 4.11A). We built a rectangular corral with a width of $L_y = 9.1 \text{ nm}$ and a length of $L_x = 24.0 \text{ nm}$. The atoms were positioned with an interatomic distance of approximately 1.5 nm. An additional wall layer was added to the corral to reduce the transparency of the corral walls to the surface state waves. The length L_x of the corral can be tuned by moving one of the walls, as shown in panel (C), where the upper wall atoms were moved downwards, as depicted by the arrow. As indicated by the labels, the new corral has the same width L_y as the one in (A), but the

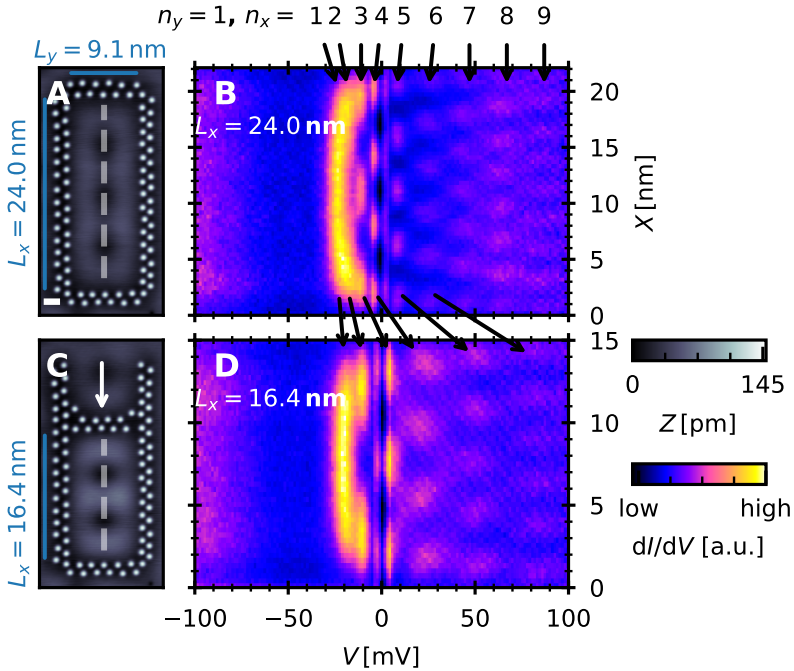


Figure 4.11: Spectroscopic line profiles for corrals of different sizes. (A) Constant-current STM image of a Ag corral with $L_x = 24$ nm. (B) Spectroscopic line profile along the dashed vertical line marked in panel (A). The arrows on the top mark the energetic positions of respective eigenmodes. The white line corresponds to 1.5 nm. (C) Constant-current STM image of a Ag corral with $L_x = 16.4$ nm. The arrow indicates the shift of the upper wall. (D) Spectroscopic line profile along the dashed vertical line marked in panel (C). QD eigenmodes with $n_y = 1$ and n_x , as indicated by the arrows at the top, are observed. As the black arrows illustrate, their energy shifts when L_x changes. Parameters: $I_{\text{set}} = 1$ nA, $V_{\text{bias}} = 5$ mV (A,C), $I_{\text{stab}} = 2$ nA, $V_{\text{stab}} = -100$ mV, $V_{\text{mod}} = 2.0$ mV (B,D).

4 Proximity induced superconductivity in artificial quantum dots: experimental discovery of Machida-Shibata states

length changed to $L_x = 16.4$ nm.

Spectroscopic line profiles were measured along the central line inside the corral, as depicted by the grey dashed lines in panels (A) and (C). The respective spectroscopic line profiles for the corrals in (A/C) are presented in the panels on the right (B/D).

In panel (B), we observe an increased dI/dV signal at low V , which decreases to a lower level and forms a low signal plateau between $V = -70$ mV and $V = -30$ mV. At $V = -22$ mV, a large peak in the dI/dV signal spans the entire corral. As we increase the energy, this peak, initially distributed over the whole corral, separates into two maxima. A large spatial overlap between the two resonances makes it hard to discern them as separate quantum states. The next resonance with three maxima appears at $V_{\text{bias}} \approx -10$ mV. At higher voltages, a resonance with an increasing number of maxima appears. For each mode, we can define a number n_x , which refers to the number of maxima we can count along the X -direction. The energetic position and n_x numbers are indicated by arrows.

The spectroscopic line profile through the smaller corral shown in panel (D) also reveals the quantized resonances with maxima along the X direction. We match the resonances in (B) with the ones in (D) by counting the number of maxima. This is indicated by the black arrows connecting the resonances in (B) with those in (D). Comparing the energetic positions, we see that the energy intervals between the modes become larger as we decrease the corral size. This results in a shift of the modes of the smaller corral to higher energies. Additionally, we observe that the resonances

in (D) have a larger energy linewidth than the ones in (B). The linewidth or lifetime broadening of the resonance, which we will refer to as Γ , gives insight into the coupling between the observed resonances in the corral and the bulk electron states via the relation:

$$\Gamma \propto V^2 \quad (4.2)$$

Therefore, we can assume that we get a stronger coupling between surface and bulk when corral sizes are decreased. This observation will be investigated more rigorously later in this chapter.

To map the spatial distribution of the resonances, we measured dI/dV -maps of the corral's interior at V_{bias} corresponding to the eigenmode's energy. Figure 4.12 shows the spatial pattern of the $L_x = 16.4$ nm corral's eigenmodes. In panel (A), a constant-current image of the corral is presented, with the orange box illustrating the area where the dI/dV -maps were acquired. Panels (B-L) display those maps taken at energies ($E = eV$) between -18 meV and 16 meV. The maps show that the interior of the corral forms patterns that resemble the solution of a particle-in-a-box problem. Panel (B) shows the $(n_x, n_y) = (1,1)$ -eigenmode, where n_x counts the number of maxima in the X - and n_y the number of maxima in the Y -direction. It transitions to the $(2, 1)$ -mode in panel (C). Panels (D) and (E) were taken at bias voltages inside the gap and show the $(3, 1)$ -mode. In panels (F-H), a mixture between the $(3, 1)$ - and the $(1, 2)$ -mode is observed. Panel (I) resembles a $(1, 2)$ -state and panels (J-L) resemble different mixtures of $(4, 1)$ - and $(2, 2)$ -states (see comparison to a particle-in-a-box model below).

Most interestingly, we can see states appearing at energies inside

4 Proximity induced superconductivity in artificial quantum dots: experimental discovery of Machida-Shibata states

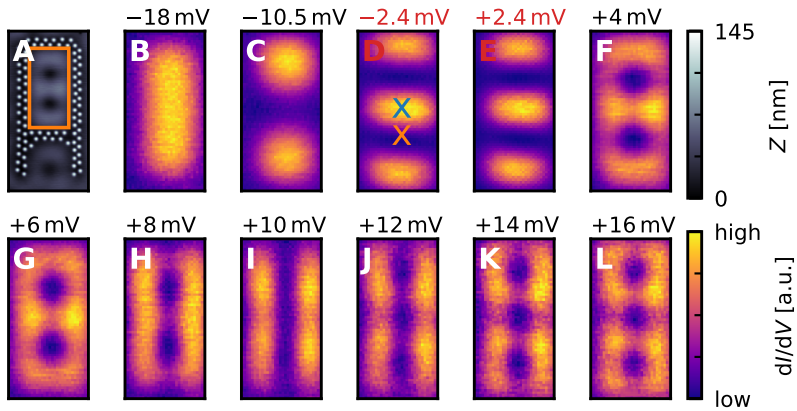


Figure 4.12: Constant-height dI/dV -maps of corral eigenmodes. (A) Constant-current STM image of the corral (also shown in Fig. 4.11C, but mirrored along the horizontal axis). The orange box depicts the area of the dI/dV -maps presented in panels (B-L), which has a size of $15 \text{ nm} \times 5 \text{ nm}$. (B-L) Constant-height dI/dV -maps of the corral's interior measured at the bias voltages indicated by the respective labels above the panel. The measurements in panels (D, E) were taken at the energy of the in-gap peaks shown in Figure 4.13. Parameters: $I_{\text{set}} = 1 \text{ nA}$, $V_{\text{bias}} = 5 \text{ mV}$ (A), $I_{\text{stab}} = 1 \text{ nA}$, $V_{\text{mod}} = 0.5 \text{ mV}$, feedback: off (B-L).

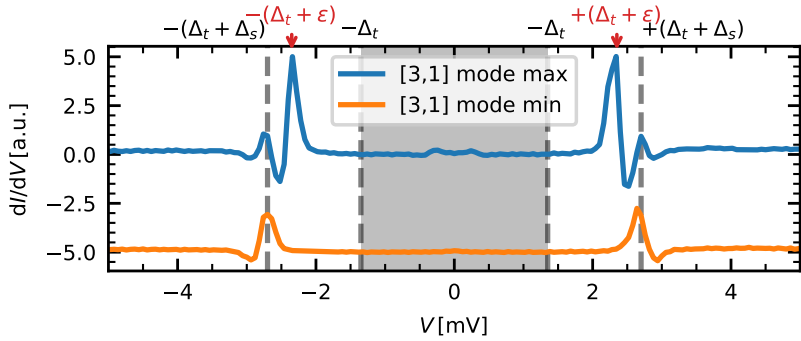


Figure 4.13: Bias spectroscopy at different locations in the corral. The spectra were taken on the maximum (blue) and minimum (orange) of the (3,1) eigenmode. In Figure 4.12 (D), these positions are marked with an "x" with the color corresponding to the spectrum. The bias value corresponding to the tip's superconducting gap $V_t = \frac{\Delta_t}{e}$ and the bias value corresponding to the sum of the tip and the sample gap $V = \pm \frac{\Delta_t + \Delta_s}{e}$ with the proximity-induced Ag bulk gap Δ_s are marked by dashed lines, respectively. In-gap states appear at energies $\pm(\Delta_t + \epsilon)$, marked by red arrows. Parameters: $I_{\text{stab}} = 4 \text{ nA}$, $V_{\text{stab}} = 15 \text{ mV}$, $V_{\text{mod}} = 50 \text{ } \mu\text{V}$.

4 Proximity induced superconductivity in artificial quantum dots: experimental discovery of Machida-Shibata states

the superconducting gap. To gain more insight into the states shown in Figure 4.12D/E, we acquire bias spectroscopy measurements at different locations of the corral as depicted by the crosses in panel (D). We take measurements on the (3,1)-eigenmode's LDOS maximum (blue) and minimum (orange). We focus on the low-energy regime around the superconducting gap. Figure 4.13 displays both measurements. The measurement taken on the (3,1)-maximum (minimum) is depicted by the blue (orange) curve. The energetic locations of $\pm\Delta_t$ and $\pm(\Delta_t + \Delta_s)$ are marked by the grey dashed lines. The region between the $\pm\Delta_t$ is greyed out. The bias spectroscopy measurement acquired at the corral's minimum exhibits a clean SIS-junction. Conversely, the measurement obtained at the maximum reveals an additional pair of peaks at $\pm(\Delta_t + \varepsilon)$.

We interpret the resonances that have been observed in the spectroscopic line profiles of Figure 4.11 as well as in the maps in Figure 4.12 as the eigenmodes of the quantum corral, which result from the lateral confinement of the Ag(111) surface state. Here, the surface state electrons behave like particle-in-a-box states, where the corral walls serve as potential wells. The oscillation we can see as a function of X represents a standing electron wave. When the confinement conditions are altered by resizing the corral, the states of the corral shift in energy. These eigenstates exhibit an energetic spacing that varies as a function of the corral size. Spatial mapping of these eigenstates reveals identifiable patterns characterized by the number of maxima present (see the comparison to a particle-in-a-box model below).

The fact that the (3,1)-mode in the corral shown in Figures 4.12

and 4.13 displays sharp coherence peaks with a smaller separation than those of the substrate indicates that the superconductivity is also proximitized into the quantum corral eigenmode which will be investigated later on.

Particle-in-a-box model

To simulate the observed corral eigenmodes, we implement the particle-in-a-box model assuming a box with a rectangular shape and hard walls, following the analysis procedure used in Ref. [47].

The solution to this problem is given by the product between two wavefunctions (one for each dimension):

$$\Psi(n_x, n_y) = \Psi_x(n_x) \times \Psi_y(n_y) \quad (4.3)$$

with

$$\Psi(n_j) = \sqrt{2/(L_j - \delta_j)} \times \begin{cases} \sin(\pi n_j / (L_j - \delta_j) \times j), & \text{for even } n_j \\ \cos(\pi n_j / (L_j - \delta_j) \times j), & \text{for odd } n_j \end{cases} \quad (4.4)$$

where $j \in \{x, y\}$ refers to the coordinate, n_x (n_y) refers to the quantum number in x (y), and L_j is the length of the corral in the respective direction j . The length we measure in the topography is not necessarily the length that the scattering electrons experience. To account for that, the parameter δ_j is introduced, which can be seen as a renormalization parameter for the length.

4 Proximity induced superconductivity in artificial quantum dots: experimental discovery of Machida-Shibata states

The eigenenergies of the wavefunctions in Eq. 4.3 are given by:

$$E(n_x, n_y) = \frac{\hbar^2}{2m_{\text{eff}}} \left[\left(\frac{\pi n_x}{(L_x - \delta_x)} \right)^2 + \left(\frac{\pi n_y}{(L_y - \delta_y)} \right)^2 \right] + E_0. \quad (4.5)$$

with the effective mass of the surface state electron m_{eff} and the surface band offset E_0 .

With this Eq. 4.5, we can now calculate the energy of any eigenmode inside the rectangular corral for a given length L_x and width L_y .

To get the spatial distribution of the LDOS inside of the corral, we can use the following equation:

$$\text{LDOS}(E) = \sum_{n_x, n_y} \frac{|\Psi(n_x, n_y)|^2}{1 + (E - E(n_x, n_y))^2 / \Gamma^2}, \quad (4.6)$$

which represents a summation of the contributions stemming from the eigenfunctions of different quantum numbers n_x and n_y weighted by Lorentzians to account for the experimental energy resolution and lifetime of the eigenmodes.

The results of this simulation can be seen in Figure 4.14, which show a very good agreement with the modes in Figure 4.12.

Tuning of QD eigenstates

We have seen that the eigenmodes of the QDs can be tuned in energy and linewidth by varying the dimensions of the corral. To

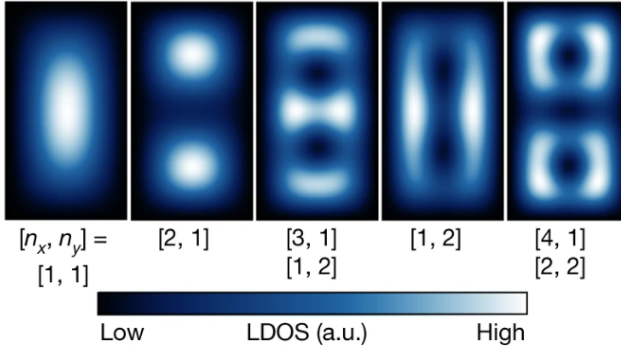


Figure 4.14: Particle in a box simulation. Simulations of the LDOS for the corral are shown in Figure 4.12 corresponding to the measurements shown in panels (B, C, G, H, L)

explore the relationship between the discovered superconducting in-gap states of Figure 4.13 and the energetic position of the QD states, we adjust these energies by resizing the corral in one direction.

In Figure 4.15, we can see the spectroscopic line profiles for corrals of sizes $L_x = 20.5$ nm, 19.5 nm, 17.4 nm, and 15.6 nm. In panels (A, C, E, G), we observe the bias voltage region spanning -15 mV to 15 mV, revealing the eigenmodes of the corral as a function of their energetic position. For instance, in panel (A), the (2,1)-eigenmode at ≈ -13 mV is identifiable from the number of maxima it exhibits as a function of X . Additionally, the (3,1)-eigenmode, at 3.5 mV indicated by the arrow, approaches the superconducting gap. As the corral length decreases in panels (C, E, G), all the modes shift to higher energies. The figure illustrates the scenario where the (3,1)-eigenmode of the corral

4 Proximity induced superconductivity in artificial quantum dots: experimental discovery of Machida-Shibata states

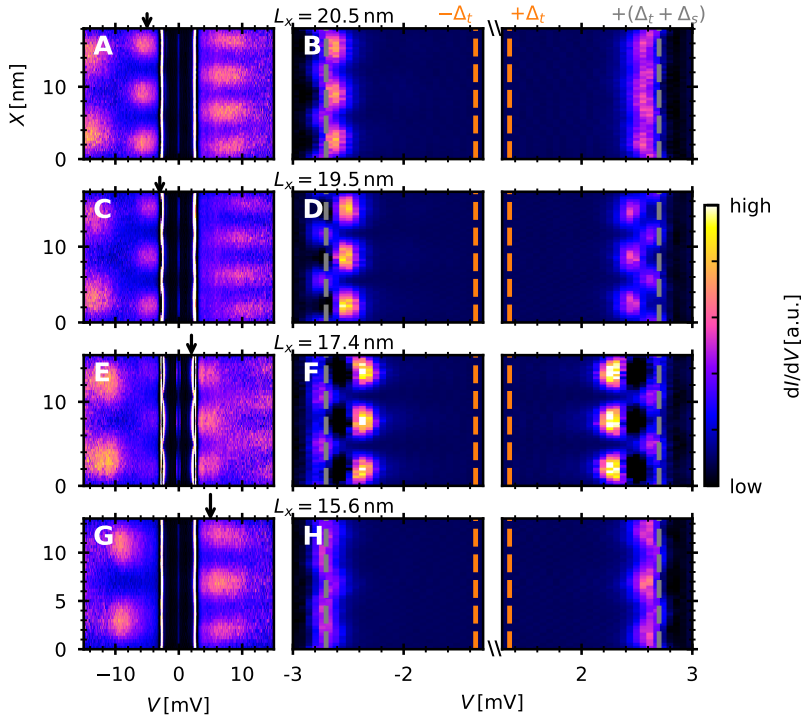


Figure 4.15: Spectroscopic line profiles measured on corrals of different lengths. (A, C, E, G) The spectroscopic line profiles were measured along the central longitudinal axis inside of the corral (see Figure 4.11) with the lengths indicated by the label in the top right corner. The arrow on the top side of the panel indicates the energetic position of the corral's (3,1)-eigenmode. (B, D, F, H) Zoom-in on the spectrum shown in the respective panel on the left. The spectra were cut in between $-\Delta_t$ and $+\Delta_t$. Parameters: $I_{\text{stab}} = 4 \text{ nA}$, $V_{\text{stab}} = 15 \text{ mV}$, $V_{\text{mod}} = 50 \mu\text{V}$.

shifts from negative V_{bias} to positive V_{bias} (see arrows). Particularly noteworthy is the observation for $L_x = 19.5$ nm (C), where the (3,1)-eigenmode moves into the gap. Subsequently, in panels (E) and (G), the (3,1)-eigenmode begins to exit the gap, eventually emerging on the positive side. Examining the superconducting gap region in panels (B, D, F, and H), we notice the appearance of an in-gap state oscillating in intensity as a function of X (see panel (B)). As the eigenmode approaches 0 mV, the in-gap state shifts further into the gap (panels (D, E)). Conversely, the in-gap state migrates towards the coherence peaks as the eigenmode exits the gap (panel (H)). An additional observation is the asymmetry between state intensities, evident in panels (B) and (D), where the intensity of the state on the negative bias side outweighs its counterpart on the positive bias side. However, in the scenario where the eigenmode exits the gap (H), the intensity of the peak on the positive bias side dominates.

We extend our investigation to encompass the complete range of corrals with lengths spanning from $L_x = 3$ nm to 24 nm. After taking the spectroscopic line profile along the corral's central longitudinal axis, we average the spectra along the position X . The resulting averaged spectroscopic line profiles for each corral are illustrated in the waterfall plot depicted in Figure 4.16. This plot portrays the averaged line profiles' evolution as a corral length function L_x . The eigenmodes, identifiable as local LDOS maxima, progressively traverse from the negative to the positive bias side as the corral length decreases and crosses E_F . Furthermore, each time one of the eigenmodes crosses the gap, a pair of in-gap states migrates into the gap. Notably, the energy of this in-gap state pair

4 Proximity induced superconductivity in artificial quantum dots: experimental discovery of Machida-Shibata states

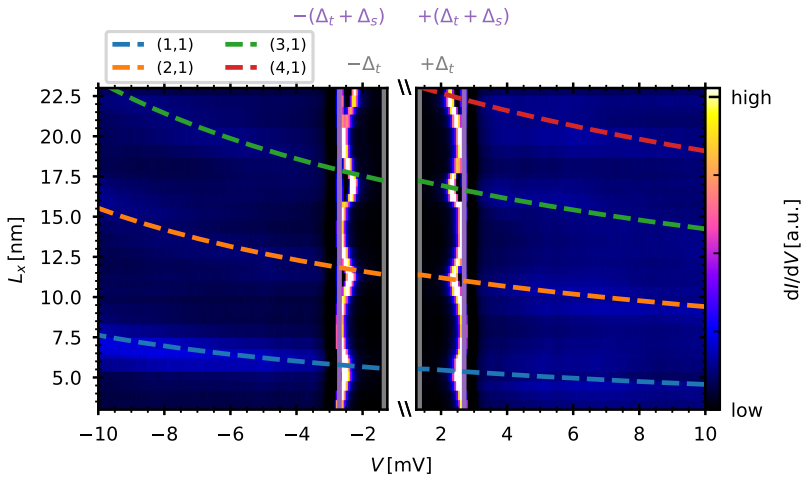


Figure 4.16: Averaged spectroscopic line profiles as a function of L_x . Evolution of averaged dI/dV spectra from dI/dV line profiles measured along the central longitudinal axis of different QDs (see dashed grey lines in Figure 4.11) as a function of L_x . The dashed colored lines mark the evolution of the eigenmodes with $n_y = 1$ and $n_x = 1, 2, 3, 4$ obtained from fitting the dI/dV spectra at energies outside the gap. Fitting parameters: $\delta_x = -0.28$ nm, $L_y = 9.1$ nm, $E_0 = -26.4$ meV and $m_{\text{eff}} = 0.58m_e$

attains a local energy minimum when the eigenmode aligns exactly with E_F , as explained below.

The evolution of the QD eigenmode energy as a function of L_x can be simulated by applying the particle-in-a-box model. We do this for L_x between 3 nm and 23 nm as presented in Figure 4.16. The evolutions of the individual eigenmode energies ($E = eV$) of L_x are depicted as dashed lines, with each color corresponding to a specific eigenmode. The fitting parameters $\delta_x = -0.28$ nm, $L_y = 9.1$ nm, $E_0 = -26.4$ meV and $m_{\text{eff}} = 0.58m_e$ were chosen to be the same for each mode. Due to the use of a superconducting tip, the spectral features are shifted by the tip gap. We account for this by shifting the calculated values for V by $+\Delta_t/e$ for positive values and $-\Delta_t/e$ for negative values. In the experimental data, the LDOS is gapped out between $\pm(\Delta_t + \Delta_s)$. Therefore, the eigenmodes also disappear as they reach the gap. However, with the theoretically fitted parameters, we can extrapolate the evolution of the eigenmodes even for energetic values inside of the superconducting gap. Therefore, we can gauge the value for L_x at which the eigenmode would have been directly at E_F .

The comparison between the experimental and theoretical eigenmode energies shows that the energy of the eigenmodes can indeed be described by a relation $E \propto \frac{1}{L_x^2}$. We can see the same behavior as observed in the in-gap states in Figure 4.15. When an eigenmode moves through the gap, the in-gap states move away from the coherence peak further into the gap. When the eigenmode reaches exactly E_F , the in-gap state energy reaches a minimal value, ε_{min} . Furthermore, the value of ε_{min} seems to decrease

for increasing n_x .

QD eigenmode lifetime and energy

From the overlay of the theoretically modeled data on the experimental results described above, we have seen that the energetic evolution of the eigenmodes as a function of corral size can be described by a particle-in-a-box model. Furthermore, we have seen that ϵ_{\min} decreases as we shift eigenmodes of increasing n_x through the gap. Already in the discussion of Figure 4.11, we have seen that the energetical linewidth Γ of the eigenmodes outside the gap decreases with increasing L_x . In the following, we will extend the analysis to extract Γ and the energies of the eigenmodes more accurately.

We start by disassembling the signals in the spectroscopic line profiles to analyze the eigenmode-specific contributions. We take a discrete Fourier Transform of each spectroscopic line profile (like the ones shown in Figure 4.15) along the position X . This way, we are left with signals for each eigenmode, where only the contribution of the n th eigenmode can be seen, while the others are filtered out. The result can be seen in Figure 4.17 for the first and the second and in Figure 4.18 for the third and the fourth component of the FFT. Here, we can see that each time an eigenmode with the respective number of maxima appears in the data, the FFT signals show a peak. All of the eigenmodes represented by peaks in their component-specific FFTs shift as a function of the corral length. The FFT-filtered line shapes outside of the gap region are used to

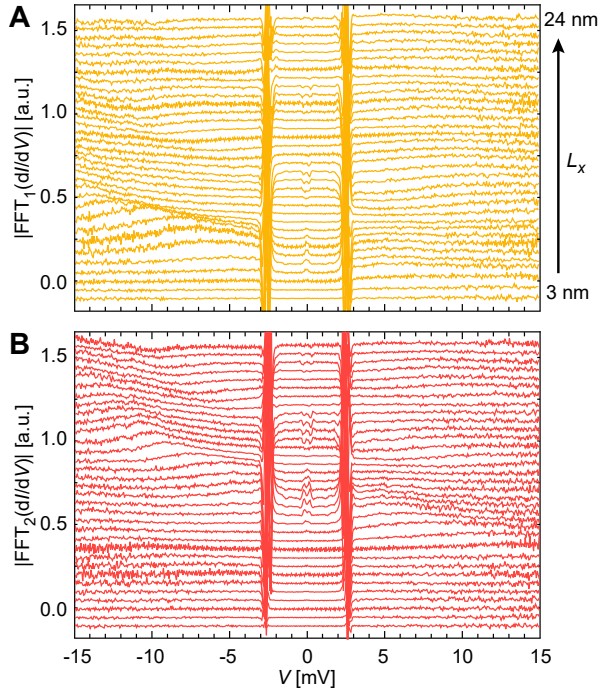


Figure 4.17: First and second component of the Fourier transform for different L_x . (A) First component of the FFT signal. (B) Second component of the FFT signal. An increasing offset along the y-axis was added to the curves for better visibility. As indicated by the arrow labeled by L_x , the curves are ordered by their respective L_x .

4 Proximity induced superconductivity in artificial quantum dots: experimental discovery of Machida-Shibata states

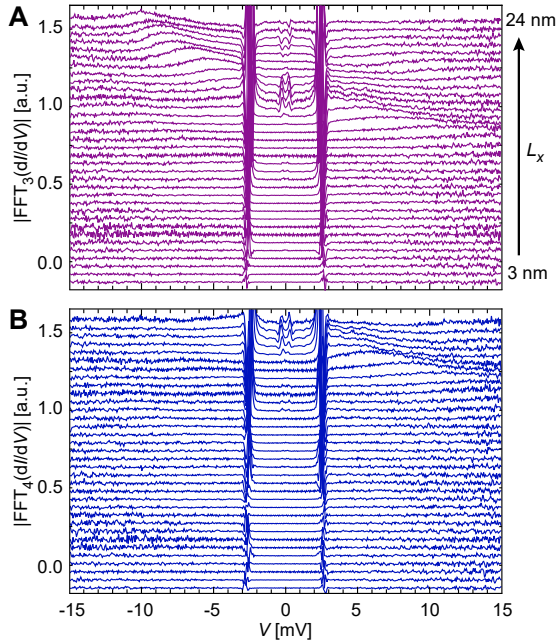


Figure 4.18: Third and fourth component of the Fourier transform for different L_x . (A) Third component of the FFT signal. (B) Fourth component of the FFT signal. An increasing offset along the y-axis was added to the curves for better visibility. As indicated by the arrow labeled by L_x , the curves are ordered by their respective L_x .

extract the bias voltage V (or energies $E = eV$) and the linewidths Γ of the eigenmodes by fitting the peaks with a Lorentzian function:

$$\left| \text{FFT}_n \left(\frac{dI}{dV}(x) \right) \right| (E) = A_0 + \frac{A_1}{1 + \left(\frac{(E-E_r)^2}{\Gamma^2} \right)} \quad (4.7)$$

with A_1 being the intensity of the peak, E_r the resonance energy, Γ the broadening of the peak and A_0 the energy independent contribution to the LDOS. Figure 4.19 shows an example of this fit, where the peak of the second and third eigenmodes are fitted for the $L_x = 14.9$ nm corral. The Lorentzian fit cannot be done for the energetic region around E_F because the eigenmode gets gapped out here. Figure 4.20 shows the result for Γ for all the spectroscopic line profiles and FFT components. Here, we can see that overall Γ gets smaller as we get to higher eigenmode quantum numbers, at least if we restrict our analysis to a constant bias region between -10 mV and 5 mV. This can be rationalized by the corrals getting larger for higher n_x eigenmodes. For larger corrals, the eigenmode electrons will reside for a longer time inside the corral until they scatter in the wall if we assume that wall scattering is the only decoherence process. Therefore, the lifetime increases for larger n_x , and Γ decreases. The weighted averages of the determined Γ values shown by the dashed horizontal lines in Figure 4.21 will be used later in Figure 4.21 for the comparison to the resonance scattering model. The eigenenergies extracted by the fitting procedure are shown in Figure 4.21. We compare the fitted values calculated with the particle-in-a-box model (Eq. 4.5) to the extracted data. The dashed lines represent the theoretical values, while the squares indicate the experimentally acquired data.

4 Proximity induced superconductivity in artificial quantum dots: experimental discovery of Machida-Shibata states

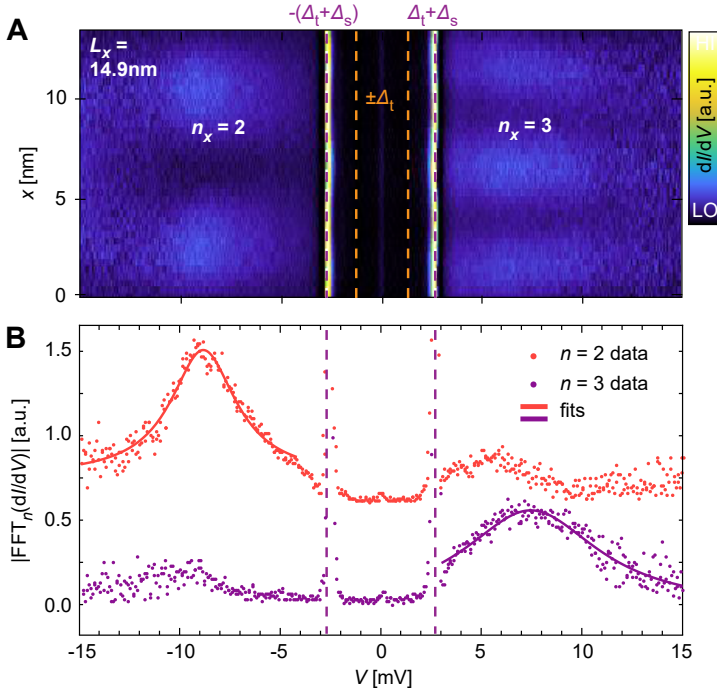


Figure 4.19: Example showing the fitting for the eigenmode. (A) Spectroscopic line profile of the $L_x = 14.9$ nm corral with the $n_x = 2$ eigenmode on the negative bias side and the $n_x = 3$ eigenmode on the positive bias side outside of the superconducting gap. (B) Lorentzian fit of the $n_x = 2$ and the $n_x = 3$ eigenmode for the respective component of the FFT of the spectroscopic line profile shown in (A).

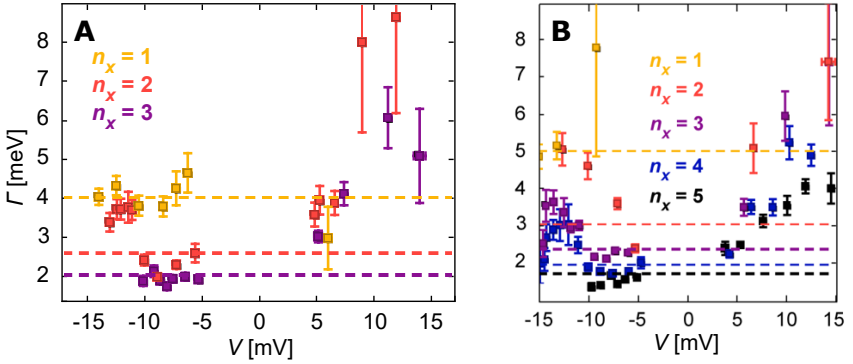


Figure 4.20: Extracted line widths of the corrals' eigenmodes. (A) Linewidth Γ of the eigenmodes extracted by Lorentzian fits from the spectroscopic line profiles as described in the text. The colors represent the n_x of the eigenmode. The dashed lines indicate the weighted average of the values from the same eigenmode. (B) Same as (A) but extracted from a different set of corrals as described in supplementary note 3 of Ref. [117].

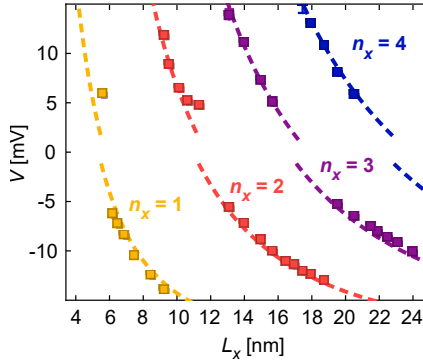


Figure 4.21: Extracted eigenenergies of the eigenmodes. Eigenenergies or their voltages $V = \frac{E_R}{e}$ extracted from the spectroscopic line profiles as a function of L_x . The dashed line represents the fit to the particle-in-a-box model described above.

4 Proximity induced superconductivity in artificial quantum dots: experimental discovery of Machida-Shibata states

We see that the data follows the $V \propto \frac{1}{L_x^2}$ behavior, which we have already seen in Figure 4.16.

Superconductivity in QDs

Next, we analyze the in-gap states of the corrals. As described in the previous section, the in-gap states change in energy and intensity when L_x changes. We use a Gaussian function to fit the in-gap states:

$$-\text{Re} \left[\text{FFT}_n \left(\frac{dI}{dV}(x) \right) \right] (E) = A_\epsilon \cdot e^{-\frac{(E-(\Delta_S+\epsilon))^2}{\gamma^2}} \quad (4.8)$$

where A_ϵ is the peak's intensity, ϵ is the energy of the in-gap state and γ is a broadening parameter.

Figure 4.22 shows an example of that. In panel (A), we can see the spectroscopic line profile of the $L_x = 17.4$ nm corral. On the negative bias side, we can see the $n_x = 2$ mode. On the positive bias side, we can see the $n_x = 4$ mode. Around the superconducting gap, one can see parts of the $n_x = 3$ mode. The in-gap states show a spatial LDOS distribution with three maxima like the $n_x = 3$ eigenmode. The column-wise discrete FFT is shown in panel (B), indicated by the black points. We use Eq. 4.8 to fit the in-gap states (red line).

The extracted values for ϵ are shown in Figure 4.23 as a function of the corral length. The colors correspond to the eigenmode that the spatial distribution of the in-gap state resembles. We can see that ϵ for each of the eigenmode follows a dip-shaped behavior,

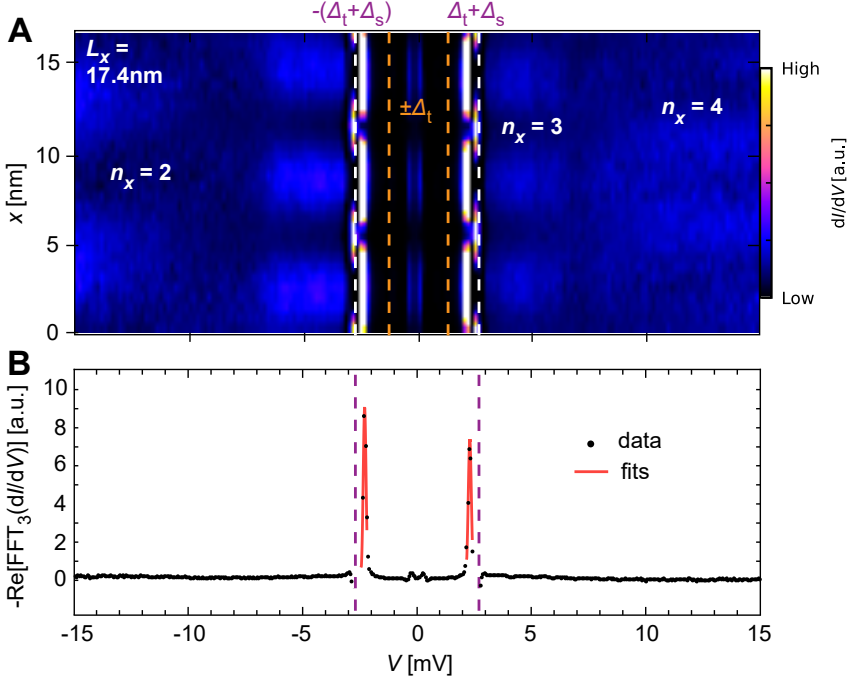


Figure 4.22: Example of in-gap state fitting. (A) Spectroscopic line profile taken along the central longitudinal axis of the $L_x = 17.4$ nm corral. Δ_t is indicated by the orange line. (B) Negative real part of the third FFT component of the line profile in (A) is depicted by the black line. The in-gap peaks of the data are fitted by a Gaussian fit (see Eq. 4.8 to determine their peak heights A_ϵ and energies ϵ (see also supplementary material of Ref. [117] for more details on the fitting procedure). From the peak heights, Θ_B (see Eq. 4.19) can be calculated. The results are presented in Figures 4.29 for Θ_B and 4.23 for ϵ .

4 Proximity induced superconductivity in artificial quantum dots: experimental discovery of Machida-Shibata states

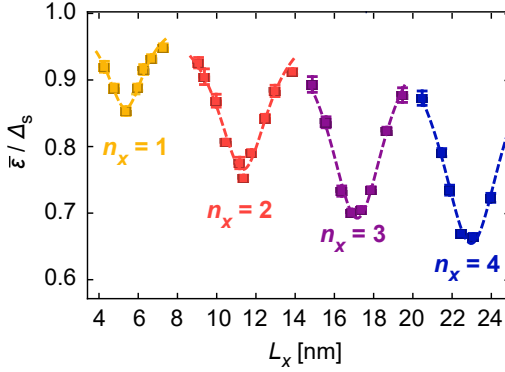


Figure 4.23: Averaged energies of the in-gap peaks. Energies $\bar{\epsilon}$ (average absolute value of the respective positive and negative peak energies) of the in-gap states in QDs of varying length L_x extracted from a series of fits. The colored labels denote the corresponding quantum numbers n_x of the relevant eigenmodes. Dashed lines show the data's respective fits.

which we can be described by:

$$\bar{\epsilon}(L_x) = \Delta_s \left(1 - \frac{1 - \epsilon_{\min}}{1 + \frac{(L_x - L_{\epsilon, \min})^2}{s^2}} \right), \quad (4.9)$$

where ϵ_{\min} is the minimal energy, $L_{\epsilon, \min}$ is the length at which the in-gap state reaches that minimum, and s is the width of the dip. The fits are depicted as dashed lines in Figure 4.23 and are well aligned with the experimental values. The fitted minimal energies ϵ_{\min} are used for the plot in Figure 4.28 below for comparison to the resonance scattering model.

Furthermore, we can use the intensities extracted from the peak fitting to calculate the Bogoliubov angle, representing the particle-

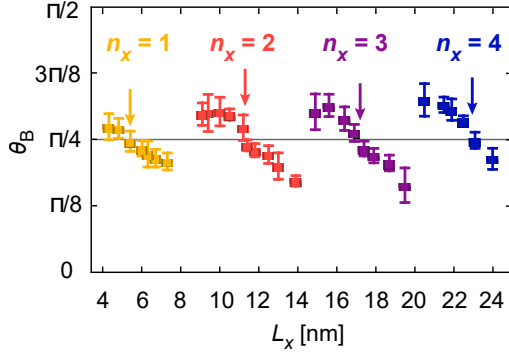


Figure 4.24: Particle-hole asymmetry. Bogoliubov angle θ_B of the in-gap states extracted from fits as in Figure 4.22. The colored arrows mark the lengths for which the in-gap state has a minimal energy $\bar{\varepsilon} \approx \varepsilon_{\min}$.

hole asymmetry between the particle-hole pair of peaks at ε_+ and ε_- inside the gap:

$$\theta_B = \arctan(\sqrt{|u|^2/|v|^2}) = \arctan(\sqrt{A_{\varepsilon_+}/A_{\varepsilon_-}}) \quad (4.10)$$

The result is displayed in Figure 4.24. Here θ_B is shown as a function of L_x . The grey line marks the value for θ_B , where the particle-hole peaks are symmetric in intensity. The correspondence to a certain eigenmode is again indicated by color. The arrows mark corral lengths L_x at which the energetic position of the in-gap state reaches its minimum (see Figure 4.23). We can see that in those cases, the peaks become particle-hole symmetric in intensity. For $L_x < L_{\varepsilon, \min}$, the resonances get an electron-like character, while for $L_x > L_{\varepsilon, \min}$, the resonance gets a hole-like character. We see this behavior consistently for each mode.

4.3 Machida-Shibata theory on resonance scattering and superconductors

The appearance of in-gap states in a nonmagnetic system we investigated is unusual. To understand this, one must know that the in-gap states appearing in STM experiments so far could always be traced back to one of the two following origins. The in-gap states have a magnetic origin in the first kind of system. Here, the incorporation of magnetic impurities leads to the formation of YSR-states (see also Section 2.2.4) [130]. However, this is not the case for our system. The sample only consists of a noble metal (Ag) and a Nb-substrate, which we investigate with a Nb tip. Each component has been characterized throughout the experiments, showing no indications of magnetism. The other explanation for in-gap states involves non-magnetic defects in unconventional superconductors [131]. As we know, Nb is a conventional s-wave superconductor. Nb and Ag have a comparably small Rashba SOC [40, 132]. Since this is one of the main ingredients for spin-triplet pairing, it would be hard to imagine how these two materials could lead to unconventional superconductivity induced into the surface state of Ag(111).

Resonance scattering model

The explanation of the observed in-gap states brings us back to the work developed by Kazushige Machida and Fumiaki Shibata and published in 1972 on resonance scattering in superconductors

[133]. This theoretical work deals with the case where a single spin-degenerate resonance mode is coupled to a superconductor. Machida and Shibata state that the Hamiltonian of such a system can be solved by a particle-hole symmetric pair of states, which appears inside the gap of the superconductor. The Hamiltonian describing this system is given by:

$$\begin{aligned}
 \mathcal{H} = & \underbrace{\sum_{\mathbf{k},\sigma} \varepsilon_{\mathbf{k}} c_{\mathbf{k},\sigma}^{\dagger} c_{\mathbf{k},\sigma}}_{\text{1. electron-dispersion}} - \underbrace{\Delta_s \sum_{\mathbf{k}} (c_{\mathbf{k},\uparrow}^{\dagger} c_{-\mathbf{k},\downarrow}^{\dagger} + c_{-\mathbf{k},\downarrow} c_{\mathbf{k},\uparrow})}_{\text{2. s-wave pairing}} \\
 & + \underbrace{\sum_{\sigma} E_r d_{\sigma}^{\dagger} d_{\sigma}}_{\text{3. Res. eigenmode}} + \underbrace{\sum_{\mathbf{k},\sigma} V (c_{\mathbf{k},\sigma}^{\dagger} d_{\sigma} + d_{\sigma}^{\dagger} c_{\mathbf{k},\sigma})}_{\text{4. Res.-SC coupling}} \quad (4.11)
 \end{aligned}$$

Here, $c_{\mathbf{k},\sigma}^{\dagger}$ ($c_{\mathbf{k},\sigma}$) refers to the creation (annihilation) operator of the electron band of the superconductor, d_{σ}^{\dagger} (d_{σ}) refers to the creation (annihilation) operator of the quantum dot, the spins are denoted by $\sigma \in \{\uparrow, \downarrow\}$, $\varepsilon_{\mathbf{k}}$ refers to the average electron dispersion relation of the superconductor, Δ_s is the order parameter of the superconductor and $V \propto \sqrt{\Gamma}$ refers to the coupling strength between the superconductor and the quantum dot. In Eq. 4.11, the first two are the usual terms to describe a conventional BCS-type superconductor. The third term represents a quantum dot with discretized spin-degenerate energy levels. The last term describes the coupling between the superconductor and the quantum dot. \hbar is set to 1. Unlike in the model from Ref. [133], the Eq. 4.11 assumes that $V(\mathbf{k}) = V = \text{const.}$. This is verified by the fact that we have a

4 Proximity induced superconductivity in artificial quantum dots: experimental discovery of Machida-Shibata states

perfectly localized resonance state inside of our quantum corral.

For simplicity, the Nb-substrate and the Ag-bulk are treated as one system. With the Nb inducing proximitized s-wave superconductivity into the Ag bulk, this coupled system is simplified as "superconducting" Ag. In our system, the coupling between the superconductor and the quantum dot is mediated by the scattering of the surface state at impurities such as the corral walls, which leads to a finite coupling between the surface state and the bulk of the Ag. We use this Hamiltonian to calculate the LDOS of our system. By using the Green's function approach, we end up with the following expression for the LDOS (for more details on the calculation, please refer to the methods section in Ref. [117]):

$$\text{LDOS}(E) = -\frac{2}{\pi} \text{Im} \left[\frac{\omega + E_r + \frac{\Gamma\omega}{\sqrt{\Delta_s^2 - \omega^2}}}{\omega^2 \left(1 + \frac{2\Gamma}{\sqrt{\Delta_s^2 - \omega^2}} \right) - E_r^2 - \Gamma^2} \right]. \quad (4.12)$$

Here, $\omega = E + i\delta E$, with δE being a small parameter that accounts for the finite energy broadening observed in the experimental data. The coupling parameter V that is part of Eq. 4.11 is now implicitly reflected by $\Gamma \propto V^2$.

Coupling strength dependence

From the experiment, we have seen that in-gap states appear as soon as a resonance is shifted through the superconducting gap. From Figure 4.28, we see a relation between the energetic posi-

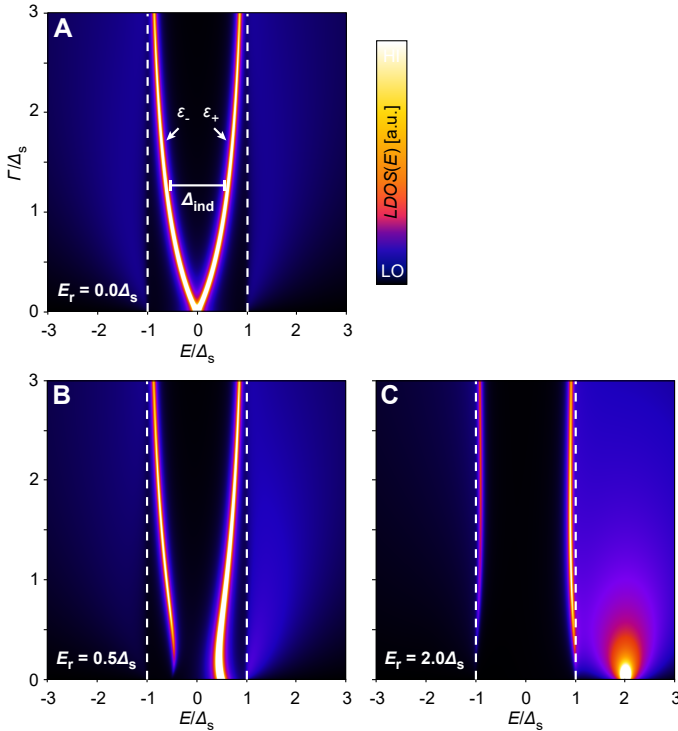


Figure 4.25: Machida-Shibata states for different coupling parameters. (A) Energy-dependent local electron density of states $LDOS(E)$ of a single localized level at energy E_r coupled to a superconducting bath with the parameter Δ_s . The coupling strength $\Gamma \propto V^2$ and $E_r = 0\Delta_s$. The induced gap Δ_{ind} and the energies of the in-gap states $\pm\epsilon$ are marked. (B) Same as panel (A) but for $E_r = 0.5\Delta_s$. (C), Same as panel (A) but for $E_r = 2.0\Delta_s$. An energetic broadening of $\delta E = 0.03\Delta_s$ has been added in all panels.

4 Proximity induced superconductivity in artificial quantum dots: experimental discovery of Machida-Shibata states

tion of the resonance (E_r) and the coupling. To explore this, we simulate the LDOS of the superconducting gap for different couplings with the E_r fixed. The result is shown in Figure 4.25. Here, we did that simulation for three cases of a fixed E_r . In (A), we see the case for a resonance mode being tuned to E_F . The dashed lines mark the superconducting gap of the substrate Δ_s . We normalized Γ on the y-axis and E (energetic variable of the spectrum) by the value of the superconducting gap of the substrate Δ_s . The outer tails of the resonances can be seen in the regions outside of the gap. We can see that a pair of in-gap states appear for finite couplings, which are marked by ε_{\pm} . From now on, we will label these in-gap peaks as Machida-Shibata state (MSS). When Γ is increased, the states shift to the edges of the gap until they reach the Δ_s value. We name the gap between these in-gap states the induced gap (Δ_{ind}). Later, we will explore how this induced gap can be understood.

When E_r is slightly shifted away from E_F , as shown in panel (B), already at zero coupling, we can see that a MSS appears at finite energies. Furthermore, we see a particle-hole asymmetry in the MSS-pair for small couplings. The negative bias peak's intensity is much lower than that of its particle-hole partner on the positive side of the gap. This asymmetry decreases with increasing Γ .

In panel (C), we have the case for a resonance outside the gap. We can see that the in-gap states barely move into the gap regardless of the coupling strength between the QD and the bulk. A strong particle-hole asymmetry can be found for the MSS, in which the electron-like part has a much higher intensity than the hole-like

part.

Resonance energy dependence

Next, we calculated the LDOS signal for the superconducting gap as a function of the resonance energy. This is presented in Figure 4.26 for different couplings between the quantum dot and the superconducting substrate.

On the y-axis, we see the energy of the quantum dot eigenmode. We calculate the eigenmode's resulting gap spectrum for each energy setting, with the applied bias energy voltage on the x-axis and the LDOS represented by color. We plotted the cases with minimal coupling between QD and bath (A), intermediate coupling (B), and strong coupling (C). The dashed lines depict the gap size of the substrate. The energy values are normalized by Δ_S . In each of these plots, we can see the eigenmode of the QD appearing as a peak outside of the gap. In our model, the coupling to the superconducting substrate is given by the linewidth of the resonance state. This is why, for small coupling, the regions outside of the superconducting gap show the eigenmode as a sharp peak. So, in the case of (A), this sharp resonance shifts through E_F .

For energies outside the superconducting gap, we see a resonance that shifts in energy. When the resonance shifts into the superconducting gap, we can observe an in-gap state continuing the shift of the resonance. The in-gap state shows a negligibly small gap since we assumed a finite but minimal coupling.

4 Proximity induced superconductivity in artificial quantum dots: experimental discovery of Machida-Shibata states

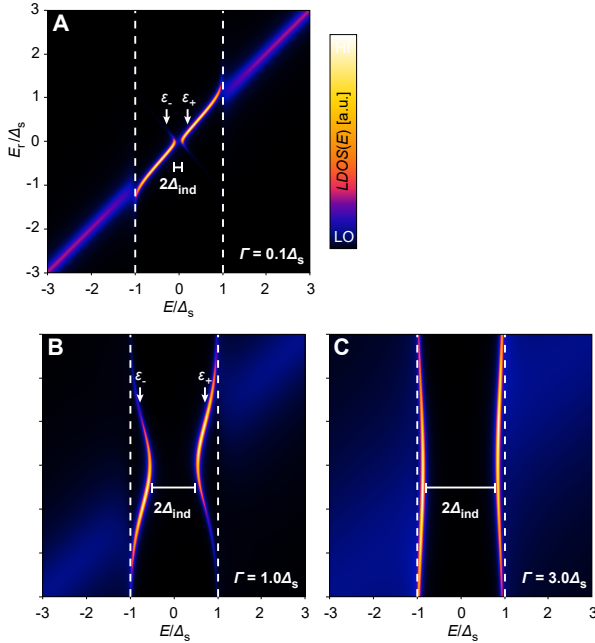


Figure 4.26: Machida-Shibata states for different coupling parameters. LDOS of a quantum corral with a spin-degenerate eigenmode shifting through E_F while coupled to a superconductor for (A) negligible, (B) intermediate and (C) strong coupling between the resonance and the superconductor.

In the next panel in (B), we increased Γ to have the same magnitude as the order parameter of the superconductor. As a result of the increased scattering, the eigenmode's linewidth has increased compared to panel (A). This time, we can see a particle-hole asymmetric pair of in-gap states when we shift the resonance into the superconducting gap. As the eigenmode moves towards E_F , the energy of the in-gap states decreases. Furthermore, we can see that the asymmetry in the intensity of the in-gap states reduces. We start with an intensity of the negative side peak, which is much larger than its particle-hole partner. When the eigenmode approaches E_F , this asymmetry decreases. Eventually, the eigenmode reaches E_F . This is where the energy of the in-gap-state pair reaches a minimum. We see a gap between the peaks, called $2\Delta_{\text{ind}}$. The intensity asymmetry between the in-gap states has gone to zero. When the eigenmode crosses the Fermi energy and reaches the positive bias side, the peaks move towards the coherence peaks again. The intensity asymmetry now becomes larger again. However, now, we see the opposite behavior. The peak on the positive bias side is larger than its particle-hole partner. In the last panel (C), we look at the case where the coupling is much stronger than Δ_s . As expected, the linewidth of the resonance increased. Differently from panel (B), we can barely see in-gap states appearing. The induced gap is almost the same as the substrate gap. Similar to the previous case, we can see the evolution in the asymmetry of the in-gap states.

Effective low-energy model

To gain more insight into the Hamiltonian in Eq. 4.11, we perform a Schrieffer-Wolff-Transformation. This way, we will be able to judge whether the gap between the MSS described above can be regarded as induced superconductivity in the corral eigenmode. The Schrieffer-Wolff-Transformation gives us an effective low-energy theory when the energetic position of the QD eigenmode is located inside the gap of the superconductor. The transformed Hamiltonian is given by:

$$\mathcal{H}' = e^S \mathcal{H} e^{-S} = \mathcal{H}'_D + \mathcal{H}'_{SC} + \mathcal{O}(V^3). \quad (4.13)$$

The new low-energy physics of our coupled system is given by

$$\mathcal{H}'_D = \sum_{\sigma} (E_r + E_{\text{shift}}) d_{\sigma}^{\dagger} d_{\sigma} - \Delta_{\text{ind}} (d_{\uparrow}^{\dagger} d_{\downarrow}^{\dagger} + d_{\downarrow} d_{\uparrow}), \quad (4.14)$$

with the new gap induced into the surface state

$$\Delta_{\text{ind}} \approx \Gamma \frac{\Delta_s}{\sqrt{\Delta_s^2 - E_r^2}} \quad (4.15)$$

and the shift in the chemical potential

$$E_{\text{shift}} \approx -E_r \frac{\Delta_{\text{ind}}}{\Delta_s}. \quad (4.16)$$

For more details on the derivation, please refer to the methods section in the Ref. [117]. The resulting Hamiltonian resembles the BCS-Hamiltonian, with the first term expressing a typical elec-

tronic dispersion term and the second term acting as a pairing term. The lowest excitation of the system is $\varepsilon_{min} = \pm\Delta_{ind}$. So, for a system with weak electron correlations ($U = 0$), ε_{min} can be seen as the superconducting gap parameter of the QD system.

Comparison to experiment

In the following, we will compare the result of the resonance scattering model described at the beginning of Section 4.3 with the experimental data. In the same way, as we did for the results in Figure 4.26, we simulate the SC gap spectra for a specific eigenmode passing through the gap. Here, we used the linewidth that we extracted from the experimental data. The results are shown in Figure 4.27, where we can see a very good resemblance between theory and experiment.

We use Eq. 4.12 to calculate ε_{min} as a function of Γ and compare it with the experimental data that we extracted before. The comparison is shown in Figure 4.28. The data points from the experiment are well described by the expression deduced from our effective low-energy theory. The experimental and theoretical values approach Δ_s when the coupling to the bulk increases.

Next, we compare the particle-hole asymmetry for experiment and theory. To get particle and hole weights we first calculate the eigenenergies of the MSS for a specific eigenmode from the effective low-energy model:

$$\varepsilon = \pm \sqrt{E_r^2(1 - \Delta_{ind}/\Delta_s)^2 + \Delta_{ind}^2}, \quad (4.17)$$

4 Proximity induced superconductivity in artificial quantum dots: experimental discovery of Machida-Shibata states

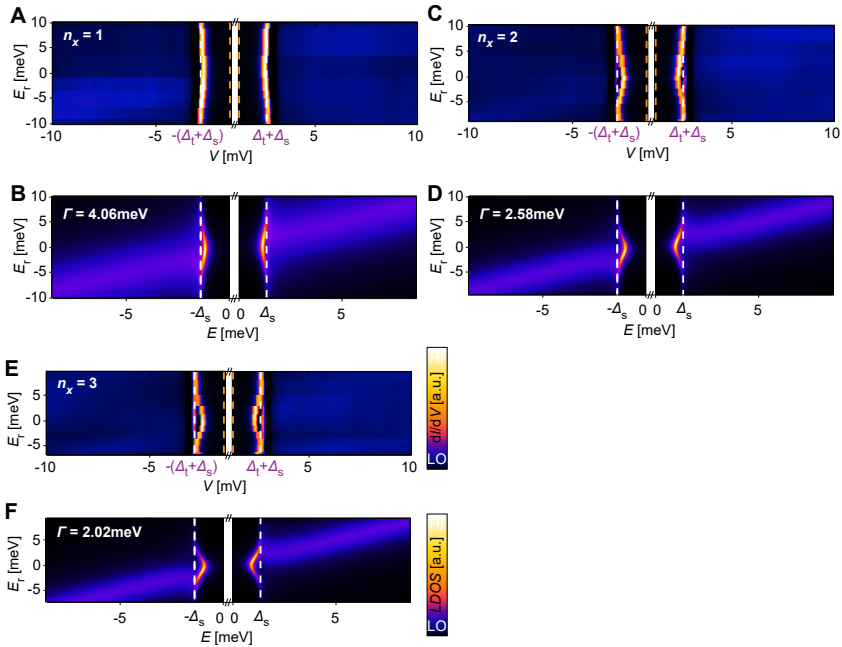


Figure 4.27: Dependence of MSS energy on the localized energy level E_r for individual QD eigenmodes: Comparison of the experiment and theory. (A) Evolution of averaged dI/dV spectra from dI/dV line profiles measured along the central longitudinal axis of different QDs as a function of the localized level energy E_r of the $n_x = 1$ resonance. The value of E_r has been extrapolated from inserting the known QD length into the fit function Eq. 4.5 for $E_r(L_x)$. (B) Energy-dependent local electron density of states LDOS(E) of a single localized level at energy E_r coupled to a superconducting bath with the parameter $\Delta_s = 1.35$ meV. The coupling strength Γ is set to 4.06 meV, motivated by the average experimental linewidth of the $n_x = 1$ resonances. (C, D) Same as panels (A) and (B) but for the $n_x = 2$ resonances and $\Gamma = 2.58$ meV. (E, F) Same as panels (A) and (B) but for the $n_x = 3$ resonances and $\Gamma = 2.02$ meV. For all theoretical panels, an energetic broadening of $\delta E = 0.08$ meV is included corresponding to the experimental energy resolution.

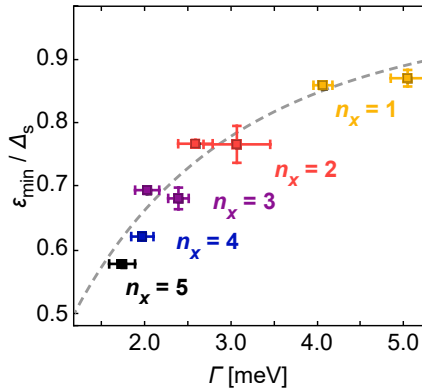


Figure 4.28: MSS energy as a function of the QD linewidth. Linewidths Γ of different QD eigenmodes extracted from fitting data from different QDs to Lorentzian peaks at energies outside the gap. These are compared with the minimal energies of the MSS found when $E_r \approx 0$ (error bars are standard deviations extracted from fitting the data). The dashed grey line is the expected theoretical relation for a spin-degenerate level coupled to a superconducting bath from Eq. 4.12.

4 Proximity induced superconductivity in artificial quantum dots: experimental discovery of Machida-Shibata states

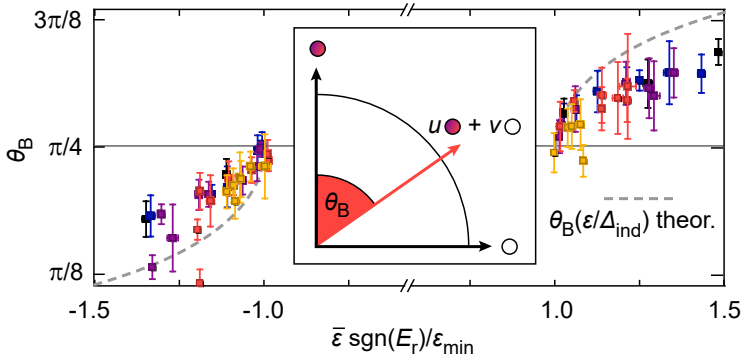


Figure 4.29: Particle-hole mixture of the in-gap states. Bogoliubov angle θ_B of the MSS with different mean energies normalized to their minimal energies ϵ_{\min} . All error bars are standard deviations extracted from data fitting. The dashed grey lines represent the expected relationship for Bogoliubov quasiparticles with an induced gap of $\Delta_{\text{ind}} = \epsilon_{\min}$ as derived from the effective Hamiltonian in Eq. 4.19. Inset: Bogoliubov quasiparticles are coherent combinations of electrons (filled circle) and holes (empty circle). The Bogoliubov angle θ_B of a quasiparticle quantifies the amount of particle-hole mixing.

With that, we can calculate the hole weight $|v|^2$:

$$|v|^2 = \frac{1}{2} - \frac{E_r \left(1 - \frac{\Delta_{\text{ind}}}{\Delta_s}\right)}{2\varepsilon} = \frac{1}{2} - \frac{\sqrt{\varepsilon^2 - \Delta_{\text{ind}}^2}}{2\varepsilon}. \quad (4.18)$$

With these values, we can get a function that describes the Bogoliubov angle Θ_B as a function of the eigenenergy:

$$\theta_B(\varepsilon) = \arctan(\sqrt{|u|^2/|v|^2}) = \arctan \left(\sqrt{\frac{1 + \sqrt{\varepsilon^2 - \Delta_{\text{ind}}^2}/\varepsilon}{1 - \sqrt{\varepsilon^2 - \Delta_{\text{ind}}^2}/\varepsilon}} \right). \quad (4.19)$$

The comparison between the normalized experimental values for all the eigenmodes and the simulated results can be seen in Figure 4.29. We see that the effective low-energy model describes the particle-hole asymmetry of the observed in-gap states reasonably well. This substantiates our identification of the observed in-gap states as MSSs, which are the coherence peaks related with the proximity-superconductivity of the quantum corral.

4.4 Conclusion

This chapter demonstrates the experimental discovery of the theoretically predicted Machida-Shibata states. To do this, we created corrals by confining the surface state of Ag(111) inside a rectangular bottom-up fabricated cage. With the different quantized eigenmodes of the surface state, this object is similar to a spin-degenerate quantum dot. We have seen that the eigenmodes of this quantum dot can be shifted in energy by resizing the quantum corral. When we tune the energy of an eigenmode toward the Fermi energy, we can observe that a pair of in-gap peaks appears inside the superconducting gap. By acquiring 2D spectroscopy maps at the energy of these energy peaks, we see that the spatial distribution of this excitation has the same shape as the eigenmode that we tuned toward E_F . We acquired a whole set of spectroscopy measurements for different lengths of the corral. We could shift the energies of the individual eigenmodes in and out of the gap one after the other. We can describe these observed peaks by the model from Machida and Shibata developed 50 years ago, which predicts the occurrence of in-gap states for a system where a spin degenerate resonance mode is coupled to a superconducting bath. We use this model to calculate the expected gap spectra with a resonance mode shifting through the superconducting gap for different couplings. From our calculation, we see that for a superconducting bath coupled to a quantum dot, where the coupling strength energy scale is in the range of the gap energy, a pair of in-gap states moves in and out of the gap as the resonance shifts through the gap. We conclude that the model describes our

observation very well.

In STM experiments, the appearance of subgap states is usually brought into conjunction with magnetism or the appearance of unconventional superconductivity. We have shown that a third option, the Machida-Shibata state, occurs when a sharp resonance is energetically positioned inside the superconducting gap. The reason why this has not yet been experimentally observed is that to get these in-gap states, the coupling to the superconductor has to be strong enough so that the resonance mode can scatter with the superconductor but not too strong because that would lead to an energy of the in-gap state comparable to the substrate coherence peak. With Ag(111), we have the exact amount of coupling to see these MSSs. This also explains why we only saw a gap Δ_{ind} in the corral eigenmode, while for the extended terraces, Δ_{ind} was almost zero. In the spectroscopic data taken on the clear terraces, we saw the superposition of many of those states, leading to a gap almost fully populated with in-gap states, the MSSs [125].

5 Realization of the YSR quantum mirage

In this chapter, we continue our work on the Ag(111) islands grown on Nb(110) and extend the studies by introducing single Fe-atoms. Magnetism would be the next ingredient for the creation of a topological superconductor. The interaction between the Fe-atoms' magnetism and the Ag-substrate's proximity-induced superconductivity leads to YSR-states. We will see how the coupling of a Fe-atom to a corral eigenmode (similar to the ones we investigated in the previous chapter) can lead to in-gap excitations at the YSR-energy of the atom, which extend throughout the corral. By using rectangular corrals, we conduct experiments similar to the ones in the previous chapter, where we tune the corral eigenmodes in energy by tuning them in size. This way, we can understand the relationship between the energetic positions of the corral eigenmodes and the intensity of the YSR-states. Finally, we will extend the studies to corrals with multiple magnetic impurities inside as well as in the corral walls. Large parts of the results presented in this chapter have been written up in:

Khai That Ton, Chang Xu, Lucas Schneider, Ioannis Ioannidis, Thore Posske, Roland Wiesendanger, Dirk Morr and Jens Wiebe

Non-local detection of coherent Yu-Shiba-Rusinov quantum projections

arXiv:2410.16054 [cond-mat.supr-con] (2024),

which is currently under review for publication.

Experimental and theoretical work sharing

Dr. Lucas Schneider and I obtained and analyzed the experimental results in this chapter. I analyzed the data using self-written Python scripts. Chang Xu from the group of Prof. Dirk Morr from the University of Illinois at Chicago did the real-space simulations on the elliptical and rectangular corrals. Ioannis Ioannidis calculated the analytical results from the effective model under the supervision of Dr. Thore Posske.

Introduction

In the field of topological quantum computation, the read-out mechanism in implementation proposals often involves the use of quantum dots. To read out the state of MZMs, the quantum state can be coupled to the eigenmode of a quantum dot [24, 134–137]. The basic idea is that the MZM projects its quantum state onto the quan-

tum dot, which, on the one hand, makes it easier to detect the MZM and, on the other hand, leads to less perturbation, which otherwise might lead to decoherence of the quantum state. To investigate how quantum dots can be coupled to spins on surfaces, the basic ingredients of the spin-chain platform and the surface state of noble metal surfaces become interesting. As the last chapter shows, quantum dots/quantum corrals can be created by confining the Ag(111) surface state inside a cage made atom by atom. These corral states can be coupled to an impurity placed inside of the corral to project the impurity's properties to a different location inside of the corral. Such a projection of a quantum state is widely known as a quantum mirage [138], and it was experimentally realized for a Kondo impurity [139], which was coupled to an atom-by-atom built quantum dot by confining the surface state of Cu(111). Apart from that, Ag(111) based corral experiments have been reported in Ref. [140], where the quantum mirage is used to create logical gates, and Ref. [141], where the corral is used as a tool to distinguish between Kondo-[142] and Spinaron-impurities [143–145] from each other.

On the side of the theory, multiple works predict the occurrence of mirages based on quantum properties such as molecular vibrational modes [146], spin-excitations [147], resonance modes which are energetically located at E_F [148–150] or YSR-states [64, 151]. Since the first experimental realization of a quantum mirage involved an elliptical corral, where the atoms were located on the focal points (FPs), it has been debated whether the shape and the position of the impurity inside the corral play an important role in the occurrence. However, it has been theoretically concluded that

mirages are not limited to elliptical corrals and that the Kondo impurity is not required to be placed on one of the foci [152, 153]. In this chapter, I will present our work on implementing and investigating YSR-mirages induced inside a QD built atom-by-atom on a superconducting Ag(111) surface.

5.1 YSR-states of Fe on Ag(111)/Nb(110)

This section examines the superconducting properties of a single Fe-atom on the Ag(111)/Nb(110) surface.

Fe-atom deposition

We deposit single Fe-atoms onto the cold Ag(111) surface grown on Nb(110) (see Chapter 4 on the characterization of the substrate). For the experiments presented in this chapter, we used the same island as in Chapter 4 (see Figure 5.1A). The island has a thickness of ≈ 12 nm corresponding to ≈ 48 MLs. A comparison between the surface before (panel (B)) and after Fe-deposition (panel (C)) shows additional objects on the surface. We can identify these as Fe-atoms. In a direct comparison between the Fe and Ag-atoms (panel (D)), the apparent height and extent in the $x - y$ directions of both atom species strongly resemble each other.

YSR-states induced on Ag(111)/Nb(110)

As known from Chapter 4, Ag(111) surface states can alter the superconducting gap spectrum on the surface by inducing MSSs. To mitigate this effect, we encapsulate the Fe-atom within a double-walled quantum corral constructed from individual Ag-atoms (see Figure 5.2A). This can quench possible contributions from a MSS, by pushing the lowest lying energy mode of the Ag(111) surface state up in energy, far away from the region around E_F . The

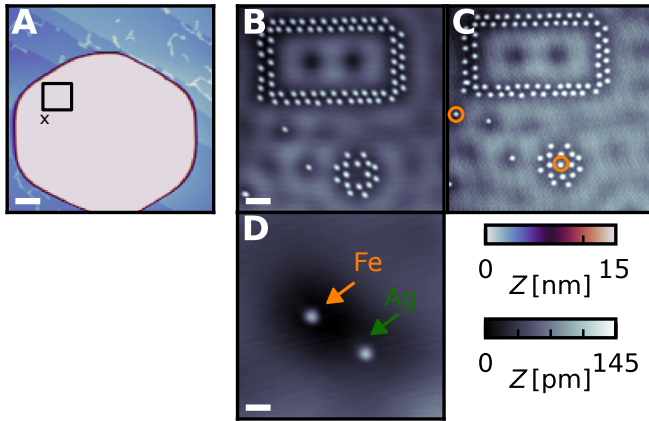


Figure 5.1: Deposition of single Fe-atoms. (A) Constant-current STM overview image of the island (same measurement as in 4.6A). The white line corresponds to 20 nm. The black square indicates the location of the measurements shown in panels (B) and (C), while the cross indicates the location of the measurement shown in (D). (C, B) Constant-current STM images of the Ag(111) surface before (A) and after Fe-atom deposition, where the lower Fe-atom was put into the corral by atom manipulation (B). The line in (B) corresponds to a length of 3 nm. (D) Constant-current STM image showing an Fe- and a Ag-atom on a smaller scale. The white line corresponds to 1 nm. Parameters: $V_{\text{bias}} = 5 \text{ mV}$, $I_{\text{set}} = 1 \text{ nA}$.

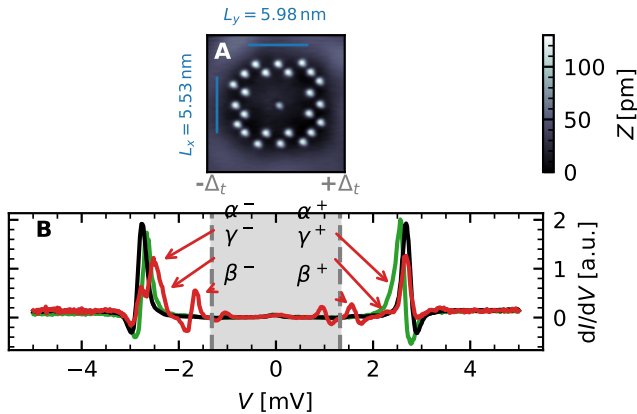


Figure 5.2: Pristine YSR-states of the Fe-atom. (A) Constant-current STM image of a single Fe-atom in the center of an Ag-corrals of dimensions $L_x = 5.53 \text{ nm}$ and $L_y = 5.98 \text{ nm}$. L_x and L_y are the distances between the inner rows of Ag-atoms. (B) dI/dV spectra taken on the Fe-atom (red) shown in (A), a free Ag-atom (green), and a substrate region (black) where the Ag(111) surface state has been expelled by assembling Ag-atoms close to each other. Parameters: $V_{\text{bias}} = 5 \text{ mV}$, $I_{\text{set}} = 1 \text{ nA}$ (A); $V_{\text{stab}} = 5 \text{ mV}$, $I_{\text{stab}} = 1 \text{ nA}$, $V_{\text{mod}} = 20 \mu\text{V}$ (for Fe and Ag) and $V_{\text{mod}} = 50 \mu\text{V}$ (for the substrate) (B).

double walls are meant to prevent the surface state modes outside the corral from leaking into the interior. With dimensions of $L_x = 5.53$ nm and $L_y = 5.98$ nm, we expect that the energetically lowest lying surface state mode ($n = (1,1)$) is located outside of the gap regime as shown in Figure 4.16.

Even the energetically lowest eigenmode of the corral lies above E_F , ensuring it does not interfere with the measurement of the in-gap spectrum of the Fe-atom. This setup enables us to measure the spectrum of the Fe-atom without the contribution of the surface state, providing insight into what we refer to as the Fe-atom's *pristine* YSR-states. The spectrum obtained from the Fe-atom in the center of the corral is depicted by the red curve in Figure 5.2B. We can compare it to the spectrum obtained from the pristine surface (black) inside a small corral of Ag-atoms. The Ag substrate's lowest surface state mode in this corral is also shifted to higher energies due to confinement. Consequently, the substrate spectrum only exhibits the dGSJ coherence peaks at the boundaries of the superconducting gap. The spectrum taken on a free Ag-atom (green) is similar to the substrate spectrum, with the only difference being the enhanced signal appearing near the coherence peaks, which can be explained by the MSS states of the free substrate.

Both spectra were obtained using a superconducting tip with a tip gap value of $\Delta_t = 1.32$ meV. The positive and negative tip gap values are indicated in the plot by the gray dashed lines. Comparing this spectrum to the one obtained from the Fe-atom reveals additional shoulders or peaks distinct from the dGSJ coherence

peaks. These peaks occur in pairs and exhibit symmetry in the bias voltage. We label these states as $\alpha^{+/-}$, $\beta^{+/-}$, and $\gamma^{+/-}$, where the notions "-" and "+" indicate whether the feature is on the negative or positive bias side.

In total, we identify three pairs of states appearing at $\beta^{+/-} = \pm 1.67$ meV, $\gamma^{+/-} = \pm 2.32$ meV, and $\alpha^{+/-} = \pm 2.46$ meV, each exhibiting varying intensities. The α^- states exhibit the highest intensity, whereas its partner, α^+ , is scarcely visible, appearing as a shoulder on the positive bias side of the coherence peak. The $\beta^{+/-}$ states are discernible as they are energetically well-separated from other in-gap features. The intensity of β^- is about twice as large as its partner. The $\gamma^{+/-}$ states have the lowest intensities. While γ^+ is observable as a small peak, γ^- manifests as a shoulder of the α^- peak.

The constant-contour dI/dV -maps captured at bias voltages corresponding to these in-gap states offer insights into the spatial distributions of the in-gap states. In Figure 5.3, these maps are displayed for the β^- (B), β^+ (C), α^- (D), and γ^+ (E) states. Panel (A) shows the corresponding topographic data. The $\beta^{+/-}$ -states exhibit triangular-shaped distributions with reduced intensity at the center. Notably, the triangle points downward for the β^- state and upward for the β^+ state. The β^- state has a considerably larger intensity. In contrast, the α^- state displays a circular-shaped distribution. Finally, the γ^- state manifests another upward-pointing triangular-shaped distribution with larger spatial extent than the other peaks.

Since the in-gap states observed on the Fe-atom do not manifest

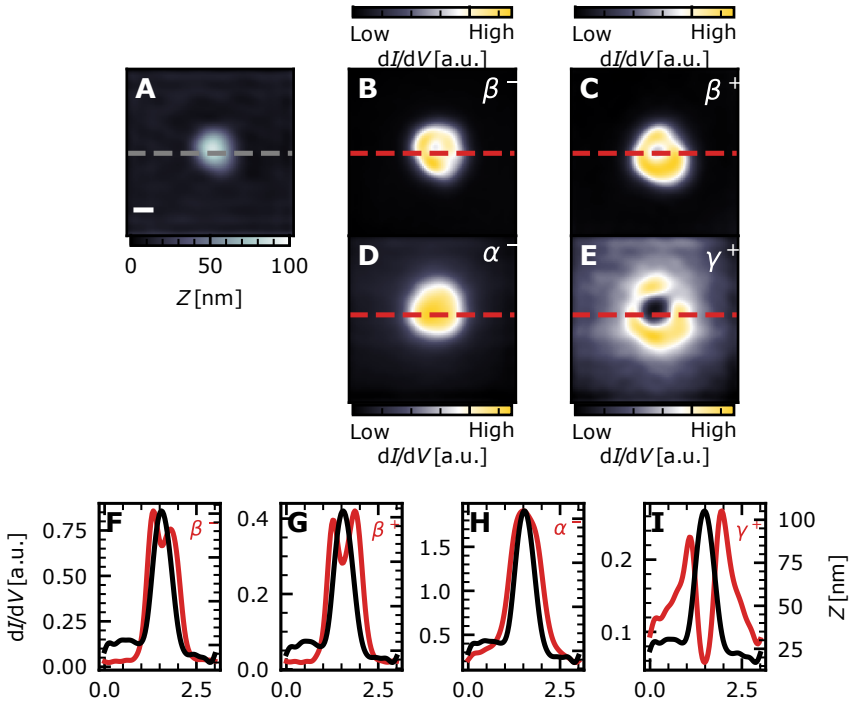


Figure 5.3: Pristine YSR-states of the Fe-atom. (A) Constant-current STM image of the Fe-atom inside of the corral from Figure 5.2A. (B-E) Constant-contour dI/dV -maps of the Fe-atom in panel (A) taken at the approximate V_{bias} -value of the β^- -peak (B), β^+ -peak (C), α^- -peak (D), γ^- -peak (E), as marked in Figure 5.2B. (F-I) Line cuts through the topography (black line) are depicted in (A) by the grey dashed line, and the constant contour maps (red line) are depicted by the red lines in (B-E) for the respective YSR-states as indicated by the red labels. Parameters: $V_{\text{bias}} = 5$ mV, $I_{\text{set}} = 1$ nA (A); $V_{\text{stab}} = 5$ mV, $I_{\text{stab}} = 1$ nA, $V_{\text{mod}} = 100$ μ V (B-E), and $V_{\text{bias}} = -1.61$ mV (B), 1.61 mV (C), -2.46 mV (D), 2.32 mV (E).

on the Ag-atoms, we infer that the peaks in the Fe-spectrum are caused by YSR-states. The YSR-states are induced by the hybridization between the 3d orbitals of the Fe-atom and the underlying superconducting substrate. The excitations' 3-fold symmetric spatial distribution can be attributed to the underlying hollow adsorption site of Fe on the Ag(111) surface, which exhibits a 3-fold symmetry. This leads to a 3-fold symmetric crystal field influencing the electronic states of the substrate. The number of YSR-state pairs correlates strongly with the number of non-degenerate 3d orbitals of the Fe-atom [154]. For the 3-fold symmetry, the d_{xy} and $d_{x^2-y^2}$ orbitals are nearly degenerate, and the same applies to the d_{xz} and d_{yz} orbitals. Therefore, we are left with three non-degenerate orbitals interacting with the superconducting bath, explaining the three observed pairs of YSR-states. Furthermore, considering the intensities of the YSR-pairs, we can assign the different YSR-states to their respective orbitals. The α state, with its high intensity and centrally distributed LDOS, likely corresponds to the d_z^2 orbital, exhibiting lobes pointing into the z direction. With the second-largest intensities, the β states correspond to the d_{xz} and d_{yz} orbitals. In contrast, the γ states are assigned to the d_{xy} and the $d_{x^2-y^2}$ orbitals, exhibiting the smallest signals in the Z-direction. Comparing the dI/dV -maps with the topography of the Fe-atom, we see that the Fe YSR-states are all strongly localized around the Fe-atom. Their lateral extent is only slightly larger than the radius of the topographic width of the Fe-atom, which is further quantified by comparing the line cuts shown in Figure 5.3 (F-I).

The α - and γ -states are energetically located near the coherence peaks, while the β -states are further inside the gap. This makes

5 Realization of the YSR quantum mirage

the β -states more favorable for experiments with the quantum corral as they are less likely to be overshadowed by either the coherence peak or the MSS close to the gap edge. Hence, we will primarily focus on the β -states for the experiments presented throughout this chapter.

5.2 YSR-mirage effect in elliptical corrals

In this section, we use the knowledge from the last section to potentially create a YSR-mirage. Similar to the experimental work reported in Ref. [139] we build an elliptical corral. To understand the effect that the magnetic impurity has on the corral eigenmode, we first place a non-magnetic impurity inside the corral and then a magnetic impurity and compare both cases.

Building elliptical corrals with impurities

From the previous chapter, we know that the energy of the corral eigenmodes can be influenced by the corral's geometry and size. We used this knowledge to design a corral with its $(3, 1)$ -eigenmode ($n_x = 3, n_y = 1$) tuned to E_F , which can be seen in Figure 5.4A. Note that, strictly speaking, elliptical corrals have different quantum numbers compared to rectangular ones. However, for the sake of simplicity, we use the assignment $(3, 1)$ in order to refer to a state that has three lobes along the major and one along the minor axis. The quantum corral has a major axis length $a = 18.2$ nm and a minor axis length $b = 13.3$ nm. Additionally, we placed either a non-magnetic impurity (Ag-atom) or a magnetic impurity (Fe-atom) inside the corral at exactly the same lattice site. The constant-current images display the topographies of the corrals without an impurity (A), with a Ag-atom (B) and an Fe-atom (C). We conducted bias-spectroscopy measurements for each corral at the impurity position and the lower FP, marked

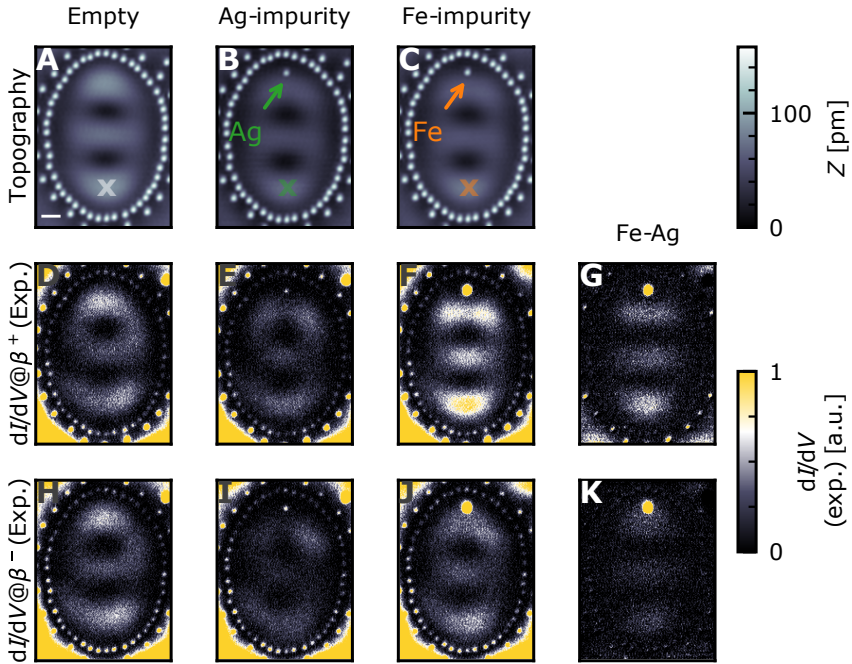


Figure 5.4: YSR quantum mirage in an elliptical quantum corral. (A) Constant-current STM images of an empty double-wall corral assembled from Ag-atoms (major axis length $a = 18.20$ nm, minor axis length $b = 13.30$ nm, eccentricity $e = \sqrt{1 - \frac{b^2}{a^2}} = 0.68$, separation of foci $2ea = 24.85$ nm). The "x" at the bottom marks the lower FP of the corral. The white line corresponds to 3 nm. (B, C) Same as in (A) but with a Ag-atom (B)/ Fe-atom (C) placed inside the corral at the same locations. (D-F) Constant-height dI/dV -maps of the corral without impurity (D), with Ag-impurity (E) and Fe-impurity (F) taken at the energy of the β^+ -state. For each measurement, the tip was stabilized on the same Ag-atom located on the outer wall. (G) Difference map between the data in (E) and (F). (H-J) Same as in (D-F) but taken at β^- -energy for the empty corral (H), corral with the Ag-impurity (I), and corral with the Fe-impurity (J). (K) Same as in (G) but between (J) and (I). Parameters: $V_{\text{bias}} = -5$ mV, $I_{\text{set}} = 1$ nA (A-C), $V_{\text{bias}} = 1.67$ mV (D-F), $V_{\text{bias}} = -1.67$ mV (H-J), $V_{\text{stab}} = -5$ mV, $I_{\text{stab}} = 1$ nA, $V_{\text{mod}} = 100$ μ V (D-F, H-J).

by the "x" in the constant-current images (see Figure 5.5). Additionally, we acquired constant-height dI/dV -maps at the β^+ and β^- energies for each corral (Figure 5.4). We stabilized the tip on the same outer wall Ag-atom for all measurements to ensure reproducibility between the measurements for the different cases. The constant-height dI/dV -measurements are depicted in panels (D) (empty corral), (E) (Ag-atom), and (F) (Fe-atom). The dI/dV -measurement inside the empty corral reveals a very faint signal in the corral's interior. Although weak, the signal suggests the presence of the (3,1)-eigenmode. In the measurement with the Ag-atom inside the corral, the overall intensity of the signal inside the corral slightly decreases compared to the empty corral measurement. Upon examining the measurement with the Fe-atom inside the corral, a notable signal appears at the Fe-atom's position, attributed to the β^+ YSR-state of the Fe-atom. More intriguingly also, the signal inside the corral undergoes a drastic increase. We observe the (3,1)-eigenmode of the corral within it. The differences between the two corrals with the Ag-atom and with the Fe-atom become evident when we subtract the image for the non-magnetic impurity Ag from the one with the magnetic impurity Fe. Overall, the difference map displays a (3,1)-eigenmode. Furthermore, an increased intensity maximum can be observed around the lower FP of the corral. A similar effect can be seen for the measurement taken at the β^- -energy. However, while the dI/dV -map of the empty corral (panel (I)) and the corral with the Ag-impurities (panel (J)) are comparable to the measurements taken at the energy of β^+ , the intensities of the measurements taken for the corral with the Fe-impurity are much smaller for the

β^- than for the β^+ energy. The difference gets even more evident when comparing the subtracted maps in (G) and (K), where the β^- case shows a faint signal but with the same shape as in the β^+ case. At this point, we can already conclude that due to the Fe-impurity with its YSR-states, a state at the same energy is excited in the quantum corral, which has a spatial shape that is very similar to the quantum corral eigenmode of the empty corral. To investigate whether this excited state has the same energy as the $\beta^{+/-}$ YSR-states of the pristine Fe, we take bias-spectroscopy measurements at the impurity positions and near the lower FPs, as marked by arrows and the "x" in panels (A-C) in Figure 5.4 with the same stabilization procedure as for the dI/dV -maps. A comparison between the bias-spectroscopy data taken for the different corrals (empty, Ag-impurity, Fe-impurity) can be seen in Figure 5.5. Panel (A) shows the measurements of the Ag (Fe)-impurity atoms as green (orange) lines. The values of $\pm\Delta_t$ are indicated by the dashed lines with the respective label on the top. The interval between $\pm\Delta_t$ is greyed out. The measurement performed on the Ag-atom is similar to what we observed in Figure 5.2. At $V_{\text{bias}} \approx \pm 2.77$ mV, the peak can be assigned to the dGSJ-state. At $V_{\text{bias}} \approx \pm 2.4$ mV, we can see the next pair of peaks and assign them to the MSS. There are no additional in-gap states. The Fe-atom (orange line) spectroscopy data shows additional peaks compared to the Ag spectrum. The dGSJ and the Machida-Shibata (MS)-peaks on the negative bias side overlap and are difficult to discern. On the positive bias side, we can see two well-separated peaks. However, the MS-peak in the Fe spectrum is shifted to slightly lower energies than the Ag spectrum. The $\gamma^{+/-}$ and $\alpha^{+/-}$

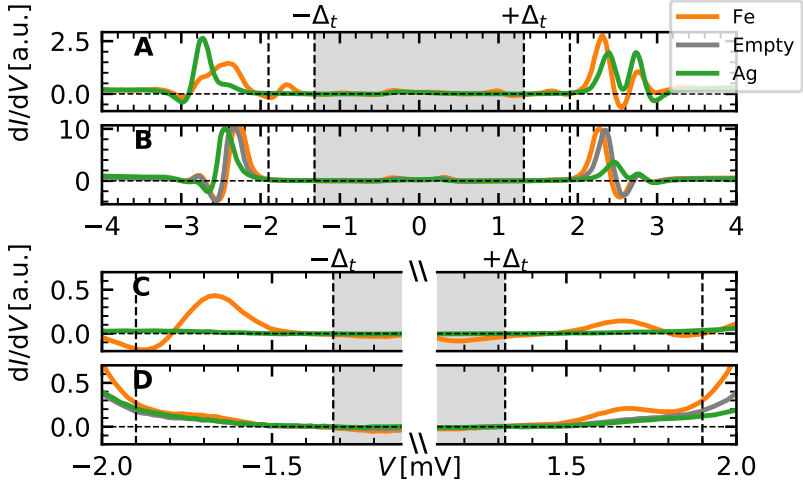


Figure 5.5: Bias-spectroscopy measurements inside the corral with and without impurities. (A) Bias-spectroscopy measurement performed on the impurities placed in the corrals. The green line depicts the measurement on the Ag-atom in Figure 5.4B, while the orange line refers to the one on the Fe-atom in Figure 5.4C. (B) Bias-spectroscopy measurement performed on the empty spot of the corrals in Figure 5.4(A-C) as marked by the "x" in the respective constant-current images. The orange line refers to the empty spot in the corral with the Fe-impurity (Figure 5.4C), the green line refers to the spot in the corral with the Ag-impurity (Figure 5.4B), and the grey line refers to the spot in the empty corral (Figure 5.4A). (C) Zoom-in of the spectra shown in (A) on the bias regions around the $\beta^{+/-}$ -states. (D) Zoom-in of the spectra shown in (B) on the bias regions around the $\beta^{+/-}$ -states. Parameters: $V_{\text{stab}} = -5$ mV, $I_{\text{stab}} = 1$ nA, $V_{\text{mod}} = 50$ μ V.

YSR-states of the Fe-atom that we saw for the pristine Fe in Figure 5.2B are overshadowed by the MS-peaks. Most importantly, the last pair of peaks appears at $V_{\text{bias}} = \pm 1.67$ mV, where the peak on the negative bias side shows about twice as large intensity as its positive bias partner. This becomes more evident when we zoom in on the V_{bias} intervals around the $\beta^{+/-}$ -peaks shown in panel (C). The dashed lines indicate the intervals around the respective $\beta^{+/-}$ -peaks. For better visibility, we cut parts of the greyed area between $-\Delta_t$ and $+\Delta_t$. While the $\beta^{+/-}$ YSR-peaks are clearly visible on the Fe-atom, the spectrum taken on the Ag-atom in this bias voltage range is featureless.

Next, we compare the measurements taken at the empty FP of the corrals (at the "x"-marks in Figure 5.4(A-C)) for the different corrals. The spectra are shown in Figure 5.5B. We can see that the MS-peaks (≈ 2.4 mV) are much more prominent this time compared to the rest of the features, such as the dGSJ-peaks. This is not surprising since we know that the MSSs are caused by the LDOS of the corral eigenmode. At the impurity location, this eigenmode is scattered, which leads to a decreased surface state LDOS. Consequently, the MSS intensity is smaller on the impurity than on an empty spot inside the corral. In contrast, the V_{bias} -values of the MS-peaks for the spectra measured on the atom and on the empty FP of the same corral are identical. For the measurement in the empty corral, we see that the position of the MSSs appears at lower energies when compared to the MS-peak of the corrals with impurity. The different V_{bias} -values of the MSSs can be explained by different scattering conditions because of the additional impurity in the non-empty corrals, which leads to an energetic shift of

the corral's eigenmodes.

Due to the large intensity of the MSSs in panel (B), the regions further inside the superconducting gap around the $\beta^{+/-}$ -states look flat. However, if we zoom in on these regions (see panel (D)) with the same scales on the x- and the y-axis as in panel (C), clear peaks at the energy of the $\beta^{+/-}$ YSR-state can be observed. Surprisingly, the spectrum taken at the empty focus of the corral with the Fe-impurity shows peaks at the $\beta^{+/-}$ bias voltages, which are absent in the spectra of the corral with the Ag-impurity and the empty corral. Interestingly, the intensity of the negative bias side peak is smaller than its particle-hole partner on the positive bias side, which is the opposite of what can be observed on the Fe-impurity (panel (C)). The fact that we can see enhanced spectral intensities at $\beta^{+/-}$ energy inside the corral containing the Fe-impurity, which can neither be observed for the Ag-impurity nor the empty corral, strongly suggests that this effect is induced by the YSR-state of the pristine Fe. Another argument for a magnetism-related effect is that the in-gap states at the empty focus have the same linewidth as the Fe-atom's YSR-state. At the same time, the spatial distribution of the spectral intensity mirrors the corral's eigenmode, which is currently tuned near E_F . The spatial extent in the x and y directions of the YSR-states of the pristine Fe-atom is less than 0.85 nm, as observed in the constant contour maps of the pristine Fe YSR-states (Figure 5.3). This rules out the possibility that the extended in-gap state we observe throughout the corral is due to a long-range tail of the YSR-state. The resemblance of the spatial pattern of the in-gap state to the (3, 1)-eigenmode of the corral, coupled with its energetic alignment with the YSR-state energies,

strongly suggests that this in-gap state arises from hybridization between the magnetic impurity's YSR-state and the corral's eigenmode. This hybrid state was baptized mirage for the Kondo case [139]. We, therefore, refer to it as YSR quantum mirage in the following.

Impurity position dependence

Next, we investigate the same corral with the impurity placed in different locations inside the corral to see how this affects the YSR quantum mirage we observed. We choose two different cases. In the first case, we place the impurity inside one of the ellipse's FPs. In the second case, we put the impurity far away from any FP of the ellipse. As for the measurements above, we compare the corrals with a magnetic and a non-magnetic impurity.

The first corral can be seen in Figure 5.6 with an Fe-atom (A) and a Ag-atom (D) placed approximately on the upper FP (FP1) as marked by "x." Corresponding dI/dV -maps are shown in the rows beneath for β^+ (Fe: (B), Ag: (E)) and β^- (Fe: (C), Ag: (F)) and the subtracted maps between the Fe and Ag measurement in panel (G) for β^+ and panel (H) for β^- . When we compare the measurements in (B) and (E), we can see that the LDOS inside of the Fe-corral is very similar to the Ag-corral. This is accentuated in the difference map in (G), where no signal can be seen apart from the YSR-state of the Fe-atom. In the measurements at β^- (panel (H)), the difference between Fe and Ag is slightly more significant but still very weak.

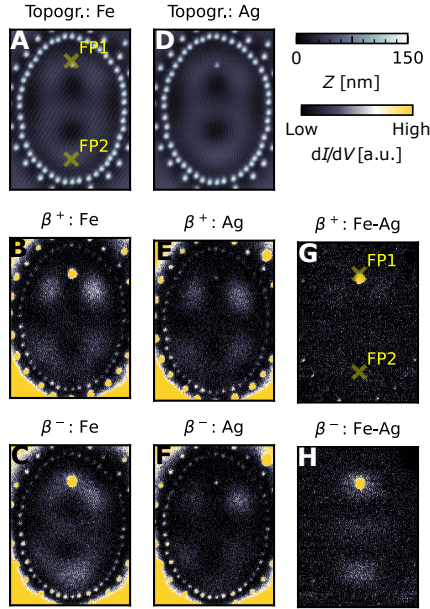


Figure 5.6: YSR quantum mirage in the elliptical corral for an impurity close to a FP. (A, D) Constant-current STM images with the Fe-atom (A)/Ag-atom (D) placed slightly below the upper FP ("FP1"). The lower FP is indexed by "FP2". Dimensions of the ellipse are the same as in Figure 5.4. (B, C) Constant-height dI/dV -maps of the corral in (A) taken, as indicated, at the biases of the YSR-state V_{β^+} (B) and V_{β^-} (C). (E, F) Same as (B) and (C) but for the corral in (D). (G, H) Difference of the constant-height dI/dV maps of the corral with Fe and the corral with Ag-atom (Fe-Ag) for β^+ (G) and β^- (H). Parameters: $V_{\text{bias}} = -5$ mV, $I_{\text{set}} = 1$ nA (A, D), $V_{\text{bias}} = 1.67$ mV (B, E), $V_{\text{bias}} = -1.67$ mV (C, F), $V_{\text{stab}} = -5$ mV, $I_{\text{stab}} = 1$ nA, $V_{\text{mod}} = 100$ μ V (B, C, E, F).

5 Realization of the YSR quantum mirage

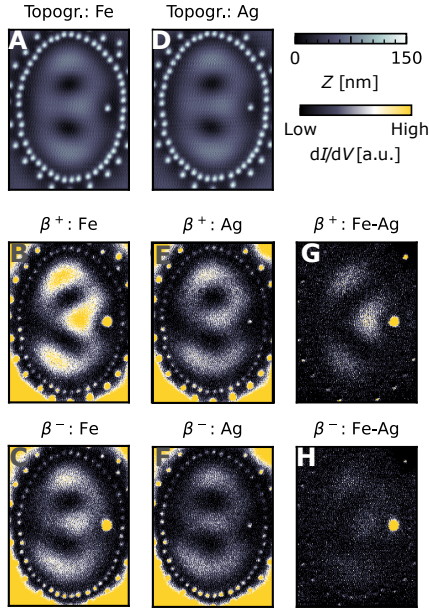


Figure 5.7: YSR quantum mirage in the elliptical corral for an impurity placed far away from the FP. (A, D) Constant-current STM images with the Fe-atom (A)/Ag-atom (D) placed completely off any FP. Dimensions of the ellipse are the same as in Figure 5.4. (B, C) Constant-height dI/dV -maps of the corral in (A) taken, as indicated, at the biases of the YSR-state V_{β^+} (B) and V_{β^-} (C). (E, F) Same as (B) and (C) but for the corral in (D). (G, H) Difference of the constant-height dI/dV maps of the corral with the Fe and the corral with the Ag-atom (Fe-Ag) for β^+ (G) and β^- (H). Parameters: $V_{\text{bias}} = -5$ mV, $I_{\text{set}} = 1$ nA (A, D), $V_{\text{bias}} = 1.67$ mV (B, E), $V_{\text{bias}} = -1.67$ mV (C, F), $V_{\text{stab}} = -5$ mV, $I_{\text{stab}} = 1$ nA, $V_{\text{mod}} = 100$ μ V (B, C, E, F).

In the second case, we place the impurity far away from both of the FPs as shown in Figure 5.7, with the topographies in the first row (Fe: (A), Ag: (D)), the dI/dV -map at V_{β^+} in the second row (Fe: (B), Ag: (E)) and the dI/dV -map at V_{β^-} in the last row (Fe: (C), Ag: (F)). When comparing (B) and (E), we can see that the corral with the Fe has a strongly enhanced LDOS. The difference map in (G) confirms that this is the case. However, this time, the eigenmode's shape is strongly distorted compared to the eigenmodes we saw in Figure 5.4. The intensity of the YSR quantum mirage is again much weaker for the bias voltage of β^- compared to the β^+ measurement.

We can conclude that the intensity of the YSR-mirage depends on the impurity's location with respect to the lobes of the quantum corral eigenmode. Different from the Kondo mirage in corrals, which confine the Cu(111) surface states [139], we do not find that the YSR-mirage is only restricted to positions close to the FPs of the ellipse. Also, the intensity of the YSR-mirage is not strongly localized on the empty FP, which is in contrast to what was described in [139]. We conclude that the YSR-mirage we observe is more accurately described by a quantum rather than by a classical model.

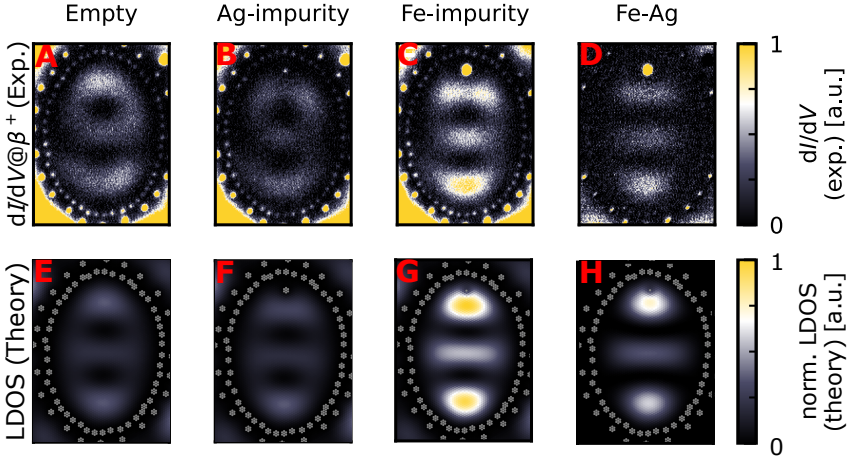


Figure 5.8: Comparison of experiment and simulated LDOS of elliptic corrals. (A) Same as Figure 5.4D. (B) Same as 5.4E. (C) Same as Figure 5.4F. (D) Same as Figure 5.4G. (E) Simulated LDOS of empty Ag corral comparable to data shown in (A). (F) Simulated LDOS of the corral with Ag-impurity comparable to data shown in (B). (G) Simulated LDOS of the corral with Fe-impurity comparable to data shown in (C). (H) Difference maps between data in (G) and (F).

Theoretical model for YSR-projection

To gain more insight into the effect, we model our results with the following Hamiltonian:

$$\hat{H} = \hat{H}_{\text{bulk}} + \hat{H}_{\text{surf}} + \hat{H}_{\text{adatom}} + \hat{H}_{\text{corral}} \quad (5.1)$$

With this model, the spatial distribution of the LDOS is calculated for the corrals shown in Figure 5.4. The result can be seen in Figure 5.8. The computed LDOS agrees quite well with the experimen-

tal data, further solidifying that our results can be interpreted as a YSR quantum mirage. Importantly, the model assumes that the Fe spin is mostly coupled to the bulk Ag-states, while the coupling to the surface state is assumed to be negligible. Thereby, the energy of the $\beta^{+/-}$ YSR-state on the Fe and of the YSR-mirage are essentially always the same, independent of the coupling of the $\beta^{+/-}$ state to the corral eigenmode. This is consistent with the experiment, as we can see in Figure 5.5C and Figure 5.2B that the energies of the YSR-state of the pristine Fe, of the Fe in the corral, and of the YSR quantum mirage are largely the same.

5.3 Tuning YSR-mirages in rectangular corrals

In the last section, we saw that coupling a magnetic impurity to the eigenmode of a corral can lead to the projection of that state mediated through surface-bulk scattering into the eigenmode. The scattering conditions inside the corral strongly depend on the position of the embedded impurity because it influences (i) the overlap of the Fe spin with the corral eigenmode as well as (ii) the energetic position of the eigenmode.

With these results, an intriguing question arises regarding how the mirage varies with the quantum numbers of the eigenmode and how it behaves as we tune these eigenmodes across E_F . We employ the same methodology as in Chapter 4 to address this. To this end, we utilize rectangular corrals and adjust the energetic positions of the corral eigenmode by resizing them. This enables us to shift the corral's different eigenmodes across E_F and observe the mirage's behavior. By rescaling the corral in one dimension and shifting the wall on one side, we can efficiently alter the corral's properties with minimal atomic rearrangement. This saves time during the rescaling process and maintains consistent boundary conditions for most atoms, thus streamlining the experimental procedure.

YSR-mirage in rectangular corrals

We initiate our measurements with the corrals depicted in Figure 5.9, featuring a width of $L_y = 9.1$ nm and a length of $L_x =$

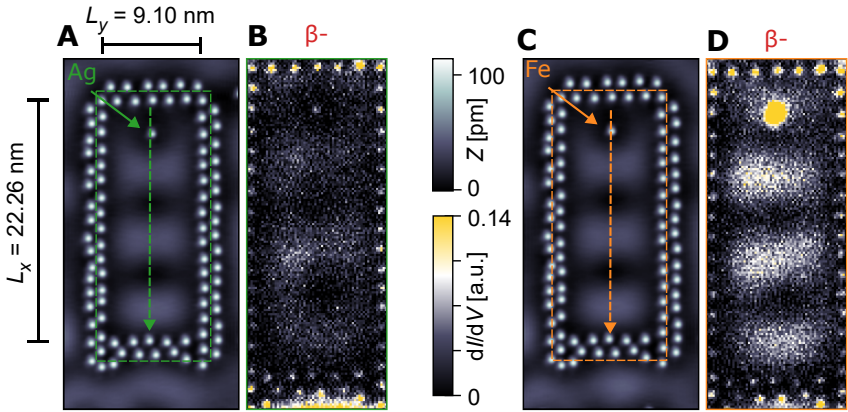


Figure 5.9: YSR quantum mirage in a rectangular quantum corral. (A) Constant-current STM images of a Ag-coral ($L_x = 22.26$ nm, $L_y = 9.1$ nm) with a Ag-atom placed in the topmost quarter (Fourier-filtered). (B) Constant-height dI/dV -maps taken inside the corral of (A) at the β^- -energy. (C) Same as in (A) but with an Fe-impurity placed at the same location as the Ag inside of the corral. (D) Same as in (B) but taken in the corral with the Fe-atom shown in (C). Parameters: $V_{\text{bias}} = -5$ mV, $I_{\text{set}} = 1$ nA (A, C) $V_{\text{bias}} = -1.68$ mV, $V_{\text{stab}} = -5$ mV, $I_{\text{stab}} = 1$ nA, $V_{\text{mod}} = 100$ μ V (B, D).

22.26 nm. After placing the impurity atom into the upper quarter of the corral, we obtain the respective constant-current STM image in panel (A) for a non-magnetic Ag-atom and in panel (D) for an Fe-atom replacing the Ag-atom at the same location. Following the procedure used for the elliptical corrals, we conduct constant-contour dI/dV -measurements at bias voltages corresponding to $\beta^{+/-}$, with the tip stabilized above the same Ag-atom located in the outer wall of the corral. The resulting maps taken at β^- are displayed in panel (B) for the corral with the Ag-impurity and panel (D) for the corral with the Fe-atom. Similar to what has been observed in Section 5.2, introducing the Fe-atom leads to an enhanced LDOS at the $\beta^{+/-}$ -bias voltage, which has the same spatial shape as the $(4, 1)$ corral eigenmode. Furthermore, subtle differences are noted in the spatial LDOS distributions of the magnetic corrals between the maps obtained at β^- and β^+ . While the measurement in (E) displays a $(4, 1)$ -eigenmode, the pattern in (F) resembles a $(3, 1)$ -eigenmode.

The YSR quantum mirage is also evident in spectroscopic line profiles measured along the central vertical axis inside the corral (see Figure 5.10). The spectroscopic line profile measured inside the corral with the Ag-atom is shown in panel (A), with the redundant area between $-\Delta_t$ and $+\Delta_t$ greyed out. Across the line profile, a pair of in-gap states near the gap edge, oscillating in intensity as a function of position X , can be observed, corresponding to the quantum corrals' MSSs. However, no additional in-gap states are apparent throughout the corral. This observation differs from the measurement inside the corral with the Fe-impurity (panel (B)). In the spectroscopic line profile, the YSR quantum mirage at β^+ / β^-

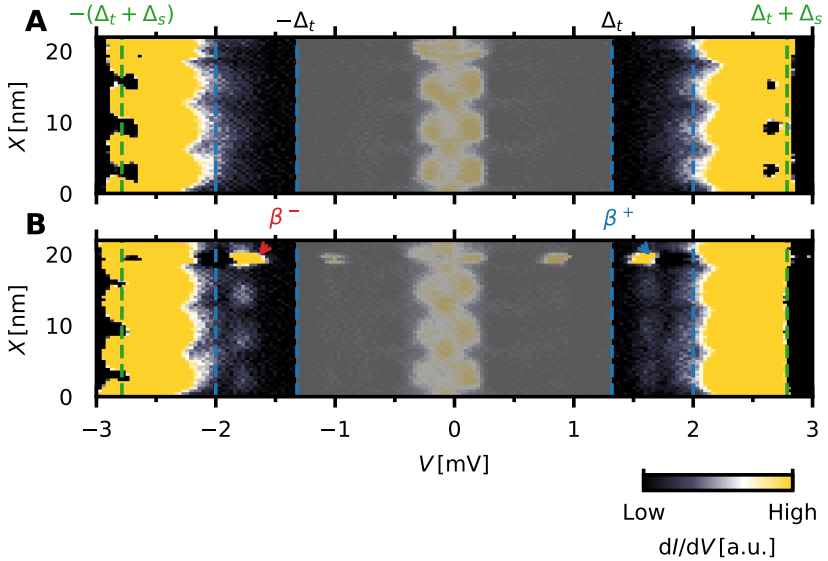


Figure 5.10: Spectroscopic line profiles taken inside the rectangular corrals with Ag- or Fe-atoms. (A) dI/dV line profile taken inside of the corral in Figure 5.9A along the central vertical line. The greyed-out area indicates the region between $-\Delta_t$ and $+\Delta_t$. The blue dashed lines correspond to the ones in Figure 5.11. **(B)** Same as (A) but taken inside of the corral in Figure 5.9C. The energetic location of the $\beta^{+/-}$ -states are marked by the arrow with the respective labels. Parameters: $I_{\text{stab}} = 1$ nA, $V_{\text{stab}} = -5$ mV, $V_{\text{mod}} = 50$ μ V.

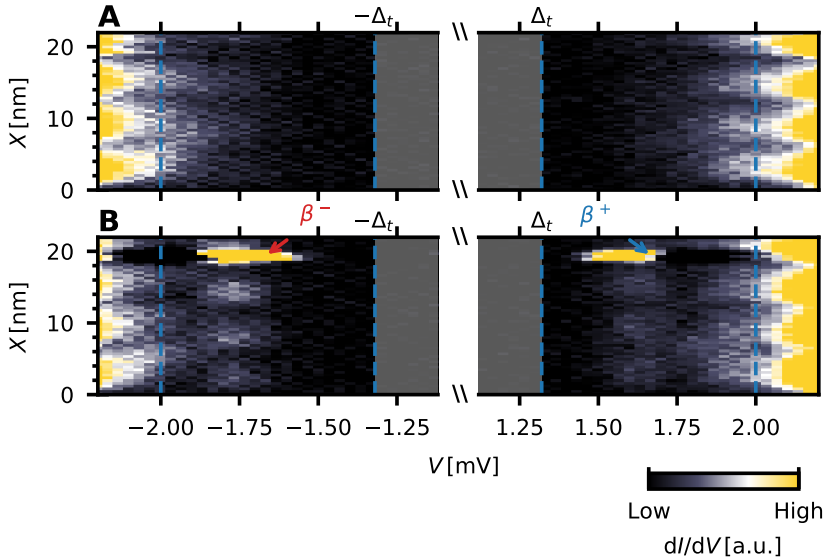


Figure 5.11: Spectroscopic line profile zoom on the bias range of the $\beta^{+/-}$ YSR-states. (A) Zoom-in on the line profile shown in Figure 5.10A with the Ag-atom at V_{bias} corresponding to $\beta^{+/-}$ YSR-states indicated by the blue dashed lines in Figure 5.10A. **(B)** Same as in (A) but for the measurement shown in Figure 5.9B with the Fe-atom. The red and blue arrows indicate V_{bias} of the β^- and β^+ YSR-states. Parameters: $V_{\text{stab}} = -5$ mV, $I_{\text{stab}} = 1$ nA, $V_{\text{mod}} = 50$ μ V.

is visible in between the blue dashed lines.

A zoom into the areas around the $\beta^{+/-}$ energies, as depicted by the blue dashed lines in both panels, can be seen in Figure 5.11. Panel (A) shows the zoom for the corral with the Ag-atom. The plot reveals the decaying tails of the MSSs. Aside from the MSS, no other in-gap states are observed. Contrastingly, the zoom into the measurement taken inside of the corral with the Fe-impurity in (B) shows clear peaks at the location of the Fe-atom ($X \approx 20$ nm), which are marked by the arrows labeled as β^- and β^+ . Furthermore, the YSR quantum mirage appears throughout the corral at $\beta^{+/-}$, oscillating as a function of position. For β^- , this oscillation features three maxima, with another overshadowing the YSR peak of the Fe-atom. On the β^+ energy, a similar pattern with comparable linewidth is evident. When we compare the intensities of the β^- and β^+ mirage, we see that, in contrast to the mirage in the elliptical corral where the β^+ mirage had the higher intensity (Figure 5.4F, J, and Figure 5.5D), here in the rectangular corral the β^- mirage has a larger intensity. This effect will be more closely investigated in the next sections.

Tuning the corral length

To explore how the YSR-mirage correlates with the corral's eigenmodes, we tune the corral size in one dimension, similar to the approach in Chapter 4. This manipulation enables us to adjust the energy eigenmodes, thereby allowing us to observe the behavior of the YSR-mirage as an eigenmode traverses E_F .

We vary the corral's length (L_x) in the x direction, generating corrals ranging from $L_x = 4.7$ nm to $L_x = 24.1$ nm. For all the measurements that require stabilizing the tip, we consistently stabilize above the same Ag-atom located in the outer wall of the corral. Constant-height dI/dV -maps are taken at the voltage of the $\beta^{+/-}$ state.

The outcome is depicted in Figure 5.12 for the maps taken at β^- and in Figure 5.13 for those taken at β^+ . We observe changes in the corrals' eigenmodes as we manipulate their size. Moreover, the intensity of the YSR-mirages oscillates in response to these variations. For the mirages, whose oscillation begins/ends between two of the displayed corrals, we use the mean length between the respective corrals to approximate the beginning/end length of the mirage oscillation. To exemplify this, let us focus on the maps taken at β^- for corrals with L_x ranging from 24.1 nm to 20.3 nm. For the 24.1 nm corral, we observe a YSR-mirage displaying the (4, 1)-mode with moderate intensity. As we decrease L_x to 23.9 nm, the YSR-mirage still manifests as the (4, 1)-eigenmode, but its intensity increases. With a continued decrease of the corral's size, the mirage progressively fades until it becomes scarcely

5.3 Tuning YSR-mirages in rectangular corrals

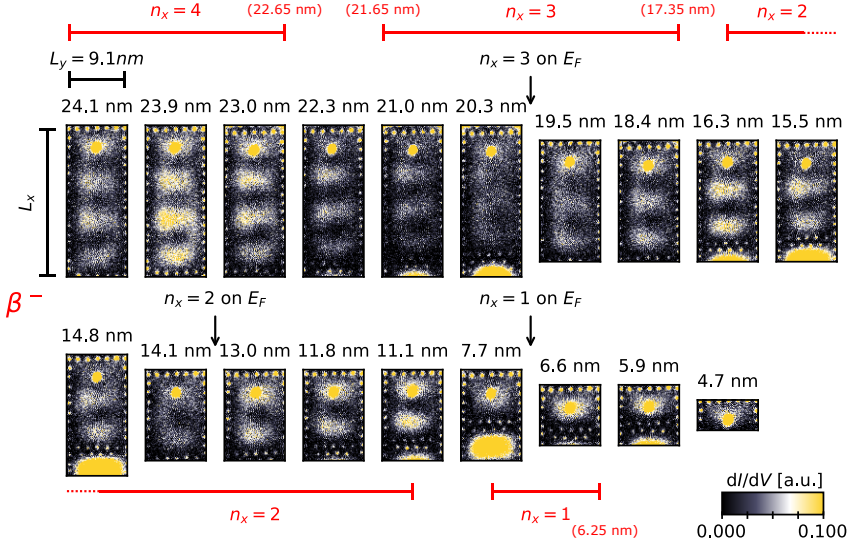


Figure 5.12: β^- -YSR quantum mirages of all rectangular corrals. Constant-height dI/dV -maps taken inside all corrals at the bias of the β^- state. The lengths L_x are indicated above each panel, and the widths are constant $L_y = 9.1$ nm. The black arrows with annotation ($n_x = 3, 2, 1$ on E_F) mark the lengths L_x for which the respective eigenmode crosses E_F according to the fit described later in the text. The red horizontal bars with annotations $n_x = 4, 3, 2, 1$ mark the L_x range, over which the β^- quantum mirages with the according quantum number are high in intensity. For bars ending or beginning between two corrals, we calculate the mean length of the corrals and assign this value to the beginning/end of the bar. Parameters: $V_{\text{bias}} = -1.67$ mV, $V_{\text{stab}} = -5$ mV, $I_{\text{stab}} = 1$ nA, $V_{\text{mod}} = 100$ μ V

5 Realization of the YSR quantum mirage

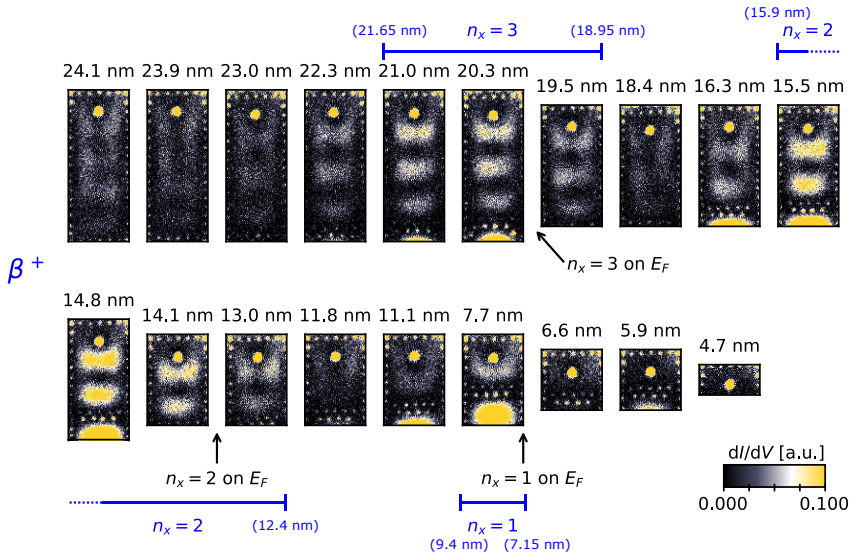


Figure 5.13: β^+ -YSR quantum mirages of all rectangular corrals. Same as in Figure 5.12 but taken at V_{bias} of the β^+ -state. The blue horizontal bars with annotations $n_x = 3, 2, 1$ mark the L_x range, over which the β^+ quantum mirages with the indicated quantum number have a high intensity. Parameters: $V_{\text{bias}} = 1.67$ mV, $V_{\text{stab}} = -5$ mV, $I_{\text{stab}} = 1$ nA, $V_{\text{mod}} = 100$ μ V.

distinguishable from the noise, as evident in the $L_x = 20.3$ nm corral. Moving on to the next corral ($L_x = 19.5$ nm), we already see the (3, 1)-mode emerging, repeating the oscillation in intensity as we transition to smaller corrals. This oscillating intensity behavior accompanying the transition between different eigenmodes persists throughout the entire set.

Upon comparing the YSR-mirage intensities of the different corrals, we can approximate the corral size at which a specific eigenmode has considerable intensity in its YSR-mirage, as indicated by the red bars above the dI/dV -maps. The n_y quantum number of the eigenmode remains constant at 1, while n_x varies between $n_x = \{4, 3, 2, 1\}$. We, therefore, in short, denote the different eigenmodes by the n_x quantum number. For the $n_x = 4$ mode, the YSR-mirage intensity peaks between $L_x = 24.1$ nm and $L_x = 22.65$ nm. For $n_x = 3$, it peaks between $L_x = 21.65$ nm and $L_x = 17.35$ nm, for $n_x = 2$ between $L_x = 16.3$ nm and $L_x = 11.1$ nm, and for $n_x = 1$ between $L_x = 7.7$ nm and $L_x = 6.25$ nm. Similarly, we analyze the maps taken at β^+ energies (Figure 5.13). For $n_x = 3$, the maximum intensity of the quantum mirage occurs between $L_x = 21.65$ nm and $L_x = 18.95$ nm, for $n_x = 2$ between $L_x = 15.9$ nm and $L_x = 12.4$ nm, and for $n_x = 1$ between $L_x = 9.4$ nm and $L_x = 7.15$ nm. Comparing the results for β^- with those taken at β^+ , we observe that the YSR-mirage of an eigenmode always appears at β^+ first (for longer corrals than for β^-) before appearing at β^- . For instance, the $n_x = 3$ mode's β^+ -mirage peaks in intensity between 21.65 nm and 18.95 nm, while for β^- , the peak occurs later, between 21.65 nm and 17.35 nm. This leads to a particle-hole intensity asymmetry oscillation of the

quantum mirage, which will be investigated in detail in section 5.4. We also use the theoretical model presented in Section 5.2 to compare three representative cases of the corrals with the simulation (see Figure 5.14). The first case shows the $L_x = 16.29$ nm corral (panel (A)). Here, the β^- -mirage reaches a maximum in intensity (panel (D)), displaying the $(2, 1)$ -eigenmode, while the intensity of the β^+ -mirage is very weak. The simulations for this case (J, M) agree well with the measurements. The next corral ($L_x = 20.27$ nm) displays a case where the β^+ -mirage reaches a maximum showing the $(3, 1)$ -eigenmode. At the same time, the β^- -mirage has a small intensity, agreeing well with the respective theoretical data (K, N). In the last corral ($L_x = 23.91$ nm) shown in panel (C), again the β^- mirage reaches a maximum, showing the $(4, 1)$ -eigenmode, while the β^+ mirage is barely visible which agrees with the theoretical data in panels (L, O).

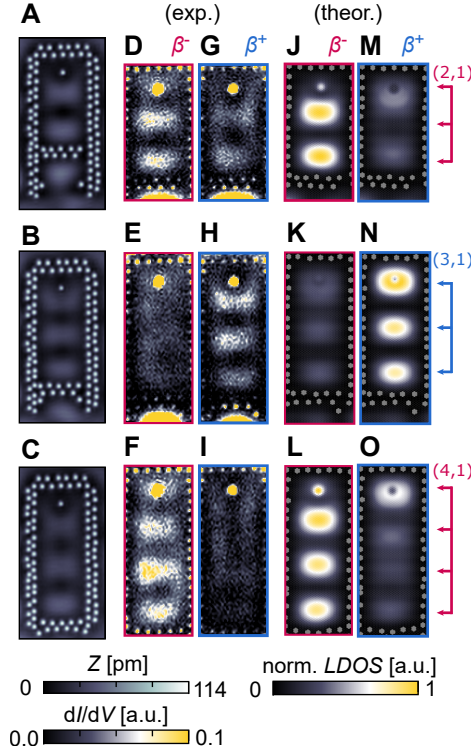


Figure 5.14: Particle-hole asymmetry oscillation of the YSR quantum mirage intensity. (A-C) Constant-current STM images of Ag-corrals, including an Fe-atom at the top, with constant widths $L_y = 9.1$ nm and different lengths $L_x = 16.29$ nm (A), 20.27 nm (B), and 23.91 nm (C). (D-F) Experimental constant-height dI/dV -maps taken inside the corrals of (A-C) at the V_{bias} of β^- . (G-I) Same as in (D-F) but taken at the V_{bias} of β^+ . (J-O) Simulated LDOS maps taken inside the corrals of (A-C) at the energy of β^{\pm} as indicated by the colored frame (red: β^- , blue: β^+). The arrows on the right indicate the positions of respective eigenmodes' maxima. Parameters: $V_{\text{bias}} = -5$ mV, $I_{\text{set}} = 1$ nA (A-C), $V_{\text{bias}} = -1.67$ mV (D-F), $V_{\text{bias}} = 1.67$ mV (G-I), $V_{\text{stab}} = -5$ mV, $I_{\text{stab}} = 1$ nA, $V_{\text{mod}} = 100$ μ V (D-I).

5.4 Oscillations in the YSR-mirage intensity

In this part of the chapter, we aim to delve deeper into the oscillatory behavior of the YSR-mirages. We first model the eigenmode as we did in Section 4.2 for the empty Ag-corrals. Next, we extract the intensity values of the YSR-mirages by fitting the dI/dV -maps for $\beta^{+/-}$. We can then compare the oscillations of the amplitudes with the evolution of the corral eigenmodes.

Determination of the corral eigenmodes

We measured spectroscopic line profiles for each corral along the central line of the corrals to further elucidate this oscillating behavior.

As a first step, we measure L_x of the corral defined by the distance between the inner wall at the top and the inner wall at the bottom (see Figure 5.15).

Second, we average the spectroscopic line profile taken for each corral over the coordinate x , excluding measurements taken on the Fe-atom and its immediate vicinity ($r = 0.85$ nm, see Figure 5.15), focusing solely on the YSR-mirage contribution. Next, we stack the averaged measurements to create a waterfall plot with energies on the x -axis and the corral length on the y -axis.

The result can be seen in Figure 5.16. The panels display various V_{bias} and intensity scales to highlight particular spectral features. panel (A) features scales suitable for distinctly observing the gap

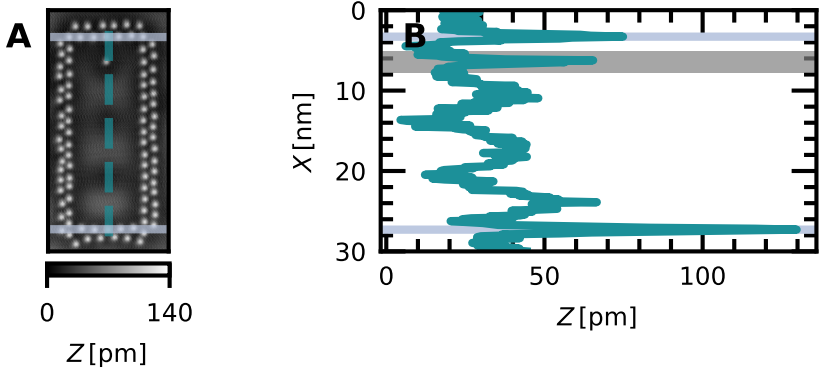


Figure 5.15: Extracting the corral length. (A) Constant-current STM image of a rectangular corral with $L_x = 23.91$ nm, where the light blue lines indicate how the length of the corral is measured. The turquoise dashed line corresponds to the line profile shown in panel (B). (B) Line profile along the central vertical axis inside of the corral shown in panel (A). The grey area around the position of the atom accounts for the mask, which is used to exclude the YSR-impurity from the spectroscopic line profiles when extracting the YSR-mirage (see Figure 5.18).

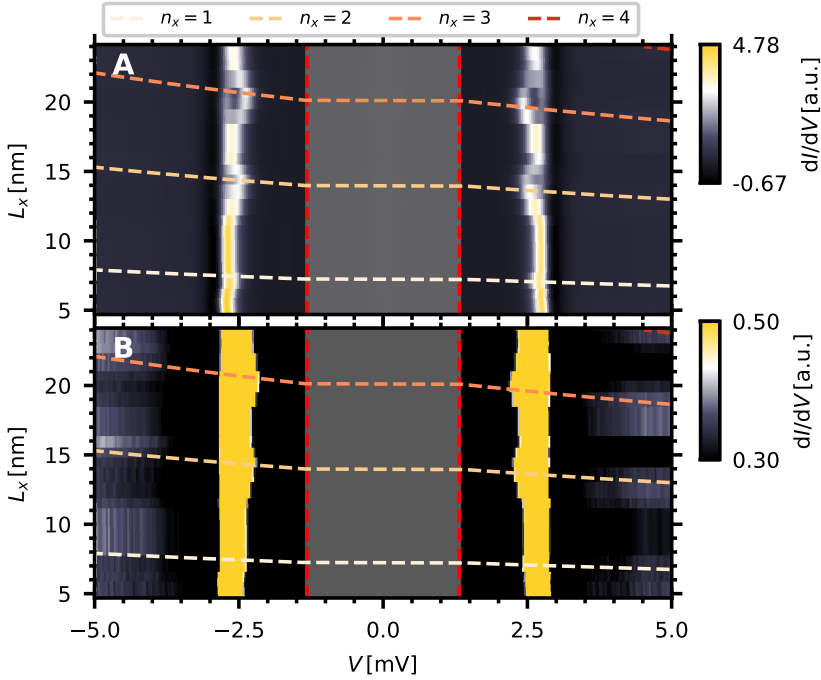


Figure 5.16: Determination of the L_x -dependent corral eigenenergies. (A, B) Averaged dI/dV spectra taken inside all corrals with the Fe-impurities as a function of L_x . Each line represents the average of a corral's spectroscopic line profile taken along x , where the region with a radius of $r < 0.85$ nm around the Fe-atom is excluded (see Figure 5.15). The color scale has been optimized to accentuate the MSSs (A) and the corral eigenmodes outside the gap region (B). The colored, diagonal lines show the L_x -dependent evolution of the eigenmode energies with $(n_x, n_y) = (1, 1), (2, 1), (3, 1), (4, 1)$ obtained from fitting the corral eigenmodes at energies outside the gap. Fit parameters: $\delta_x = 1.4$ nm ($n_x = 1$), 2.3 nm ($n_x = 2$), 2.6 nm ($n_x = 3$), 2.4 nm ($n_x = 4$), and $\delta_y = -0.28$ nm, $E_0 = -26.4$ meV, $m_{\text{eff}} = 0.58m_e$.

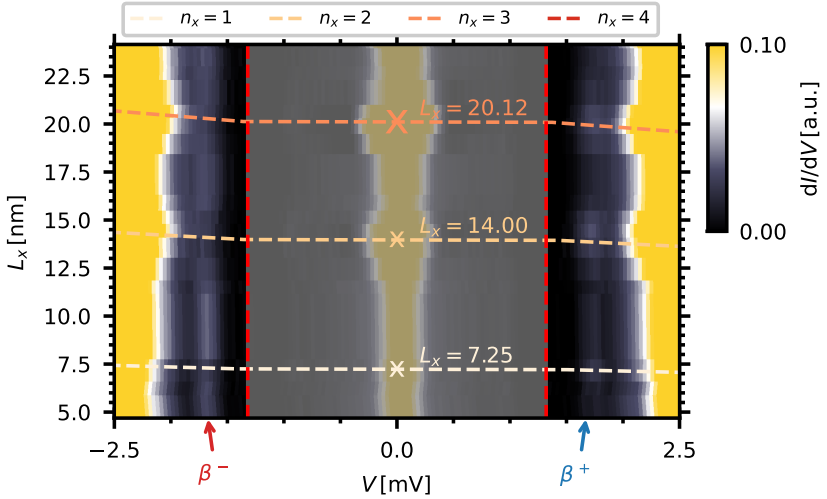


Figure 5.17: Zoom on YSR-mirage spectrum as a function of L_x . The same measurement as shown in Figure 5.16 but with V_{bias} range and the color scale accentuating the YSR-mirage features. The energetic positions of the $\beta^{+/-}$ mirages are indicated by the bottom labels. The evolution of the eigenmodes is depicted by the horizontal lines, where the labeled "x" at $V = 0$ mV indicate the L_x at which the respective mode is positioned at E_F . The values were approximated by reading out the L_x at which the oscillation of the MSS reaches a local energy minimum (Figure 5.16A).

region. Besides the coherence peaks, which remain constant for each corral length, a pair of in-gap states oscillates in energy and intensity, representing the MSS. We'll leverage these states to estimate the energetic position of the corrals' eigenmodes.

panel (B) focuses on the regions outside the gap, where broad resonances appear at energies beyond the gap, shifting as a function of corral length. On the negative bias side, we recognize three maxima ($L_x = 22$ nm, 16.29 nm, 9 nm), and on the positive bias side, we also observe three maxima ($L_x = 18$ nm, 13 nm, 6 nm).

As a first step of the analysis, we need to know at which energy an eigenmode is located for a given corral length. It is crucial to tell when a certain corral eigenmode shifts through the superconducting gap and E_F . To do that, we use the particle-in-a-box model from Eq.4.5 to simulate the evolution of the corral eigenmodes in Figure 5.16 as a function of V_{bias} and the length of the corral L_x .

Apart from the impurity inside the corral and the precise positions of the Ag-atoms forming the moving wall, the rectangular corrals in this chapter and the one we used in Chapter 4 are identical. For this reason, we can reuse most of the fit parameters in Section 4.2. The parameters $E_0 = -26.4$ meV and $m_{\text{eff}} = 0.58m_e$ are solely associated with the underlying Ag island and can thus be reused without modification. Furthermore, δ_y represents an effective corral shortening, accounting for increased scattering in the Y -direction. In our case, the impurity is located in Y -direction close to the upper wall, resulting in a relatively weak influence on the width y all over the corral length. For this reason, we approximate δ_y of the impurity corral by the value we used for the

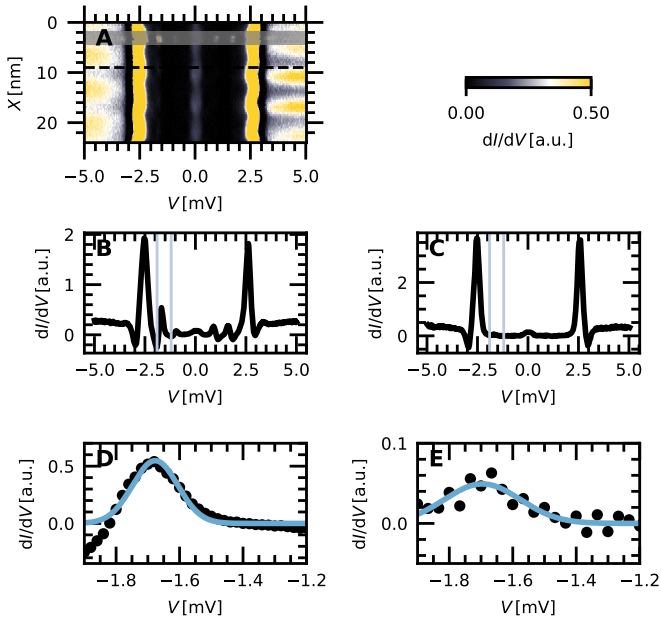


Figure 5.18: Extraction of the YSR-mirage energy and quantum number. (A) Example of a spectroscopic line profile taken along the central vertical axis inside of the corral shown in Figure 5.15A ($L_x = 23.91$ nm) with the greyed-out area depicting the data around the Fe-atom, which is excluded before extracting the YSR-mirage. The black dashed line illustrates the position of the line cut shown in (C). (B) Bias-spectroscopy measurement taken at the position of the Fe-atom (grey area in (A)). The light blue lines depict the area of the zoom around β^- shown in (D). (C) Bias-spectroscopy measurement taken at the position depicted by the dashed line in (A). The light blue lines depict the area of the zoom around β^- shown in (E). (D) Zoom-in on the measurement shown in (B) with a Gaussian fit (blue line) of the β^- peak. (E) Same as (D) but for data in (C) with a Gaussian fit of the β^- mirage. Parameters: same as in Figure 5.10.

empty corral $\delta_y = -0.28$ nm. In the x -direction, however, the impurity effectively acts as an additional wall atom, causing a shortening of the corral in L_x , taken into account by the parameter δ_x . Later in the text, I will describe how we obtain a value for δ_x . To extract the eigenmode's quantum number n_x , we can examine the spectroscopic line profile measurements, where the intensity is plotted as a function of energy and position, as depicted in Figure 5.18. By analyzing this measurement, we can determine n_x . We count the maxima observed at a specific energy outside the gap. For example, the corral eigenmode with three maxima along the x -direction ($n_x = 3$) manifests in the $L_x = 23.91$ nm corral of Figure 5.18A with significant intensity outside the gap at negative $V_{\text{bias}} = -4.5$ mV, while the corral eigenmode with four maxima along the x -direction ($n_x = 4$) is still visible at position $V_{\text{bias}} = 4.5$ meV.

With a similar analysis, we can, therefore, assign the intensities at ± 4.5 meV of the $L_x = 20.98$ nm data in Figure 5.16B to the $n_x = 3$ and $n_x = 4$ eigenmodes (see orange and red dashed lines). By a similar analysis of the spectroscopic line profiles, we can identify the other peaks outside the gap to other eigenmodes as shown by the yellow and white dashed lines in Figure 5.16B.

With these peaks outside the gap from the line-averaged spectroscopic line profile alone, we cannot fit the whole evolution of the eigenmode. Therefore, we utilize the MSS appearing in Figure 5.16A to determine the points for fitting the line. The energy of the MSS is linked to the energetic distance between an eigenmode and E_F (see Section 4.2). Using this information, we interpolate L_x

at which a certain eigenmode crosses E_F . This is given by the corral length in Figure 5.16A, at which the MSS is maximally split off from the coherence peak (see horizontally running parts of the dashed lines in Figure 5.16A). This way, we obtain sufficient points to fit Eq. 4.5 to the data in Figure 5.16. Finally, we vary the value of δ_x until the curves intersect their supposed values. This yields the following parameters for the respective modes that pass through E_F : $\delta_{x,n_x=1} = 1.4$ nm, $\delta_{x,n_x=2} = 2.3$ nm, $\delta_{x,n_x=3} = 2.6$ nm and $\delta_{x,n_x=4} = 2.4$ nm. Figure 5.16 depicts the fit results as dashed lines.

Using these fitted eigenmode energies of the states $n_x = 1, 2, 3, 4$, we can now focus on the YSR-mirage. Figure 5.17 focuses on the energetic positions around $\beta^{+/-}$. Consistent with the dI/dV -maps, a pair of peaks appears at $\beta^{+/-}$, attributed to the YSR-mirage. Additionally, these peaks oscillate in intensity with corral length.

Similar to the dI/dV -map data in Figure 5.12 and 5.13, the analysis of the spectroscopic line profiles in Figure 5.17 show the following trend. Whenever an eigenmode crosses E_F , the β^+ mirage spectral intensity has a maximum, while the β^- mirage has a minimum. At the same time, the energies of the $\beta^{+/-}$ mirage seem unaffected and stay at the bias voltage of the $\beta^{+/-}$ YSR-state of the pristine Fe. This will be investigated in more detail in the following.

Extraction of YSR-mirage energies

We analyze the spectroscopic line profiles with the procedure described in the following example to extract energies of the $\beta^{+/-}$ Fe mirages as a function of corral length L_x .

First, we take the spectroscopic line profile of the corral as shown exemplarily in Figure 5.18A, locate the position of the Fe-atom from the height-profile measurement and exclude an interval of about ± 1.5 nm around the Fe-atom's position (see grey area in panel (A)). We apply this mask to the spectral data to separate the contribution of the pristine YSR-states from the YSR-mirage. The pristine YSR-state data is then used to determine the bias offset. As shown in (B), we zoom into the $\beta^{+/-}$ -peak. We apply a Gaussian fit over this peak (see panel (D)). This way, we can determine a value V_{bias} corresponding to the peak. Then, the offset can be calculated by:

$$\Delta V = \frac{V_{\beta^+} + V_{\beta^-}}{2}. \quad (5.2)$$

We correct all the remaining values in the spectroscopic line profile by the offset and apply the same Gaussian fitting procedure (see panels (C) and (E)). The points are omitted if a fit does not converge (e.g., for positions around a nodal line of the mirage). Finally, all the extracted V_{bias} are averaged and weighed by the errors of the individual Gaussian fits. This leads to the average energies of the β^- - and β^+ -mirages for the respective corral length L_x .

The result of this procedure is shown in Figure 5.19. As supposed before, the energies of the $\beta^{+/-}$ -mirages show minimal variations.

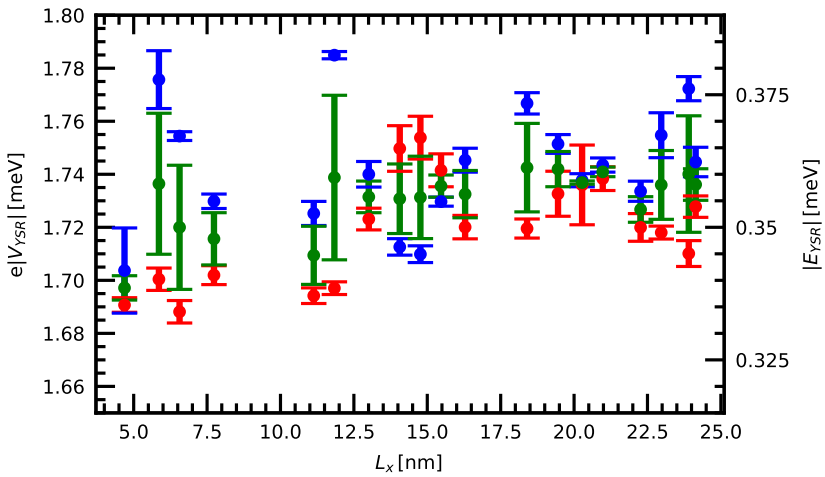


Figure 5.19: Energies of the YSR-mirages. Energies of the β^- - (red), β^+ -mirage (blue), and the average of both (green) extracted from the fitting procedure exemplified in Figure 5.18 as a function of the corral length L_x .

5 Realization of the YSR quantum mirage

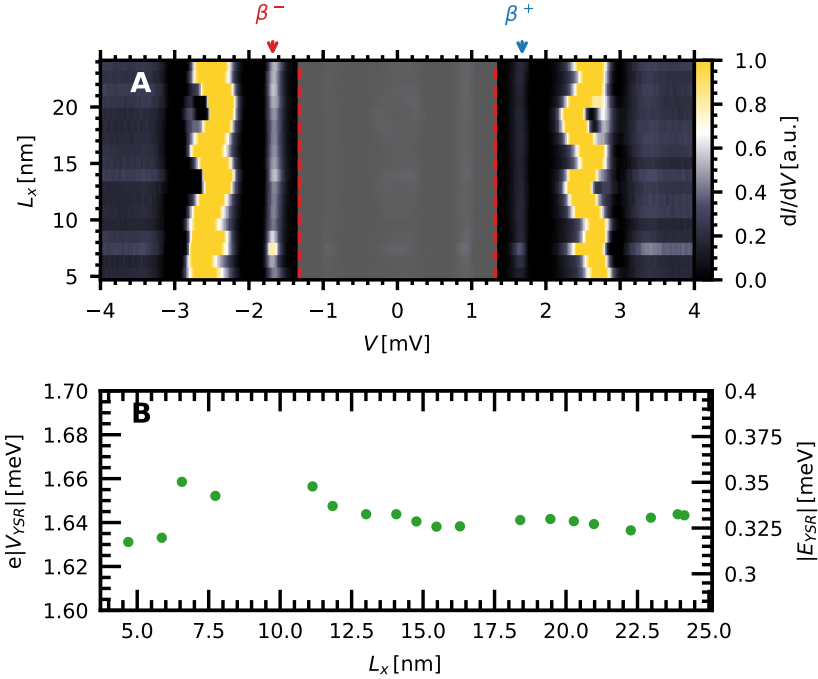


Figure 5.20: Bias-spectroscopy measured on the Fe-impurity in the corral. (A) Bias-spectroscopy measurements taken on the single Fe-atom inside the corrals shown in Figures 5.12 and 5.13. The tip was stabilized on the same Ag-atom inside of the corral wall. (B) YSR-state energy extracted by fitting the YSR-peaks in (A) as explained in Figure 5.18 and averaging the values for β^+ and β^- . Parameters: $V_{\text{stab}} = -5$ mV, $I_{\text{stab}} = 1$ nA, $V_{\text{mod}} = 50$ μ V, feedback: off (A).

Interestingly, when we compare these to the energies extracted from pristine YSR-states (± 1.67 meV), we only see a small deviation from each other (≈ 80 μ eV).

On the other hand, to see whether the presence of the corral eigenmode influences the YSR-states of the impurity, we can look at the spectra taken on the Fe-atom inside the corral. In Figure 5.20A, these spectra are depicted as a function of the corral length. We can see that the MSS located next to the coherence peaks oscillates in energy as a function of L_x whenever an eigenmode traverses the gap, similar to the findings in Chapter 4. More interestingly, the $\beta^{+/-}$ states marked by the respective labels on the top are constant in energy as a function of L_x . In panel (B), the YSR-energy extracted from a Gaussian fit is displayed. The plot shows that the variations in the energy are in the order of $\lesssim 0.03$ meV, which is even smaller than our energy resolution limited by $V_{\text{mod}} = 50$ μ eV. Therefore, we conclude that the direct coupling between the corral eigenmode and the YSR-state of the Fe is negligible or below our energy resolution.

This behavior indicates that the spins residing in the $3d$ -orbitals of the Fe-atom, forming the YSR-states, are mainly coupled to the Ag bulk states and not so strongly to the Ag(111) surface state, which is responsible for the corral eigenmodes. This is different from what has been assumed in Ref. [151], where a strong coupling between the impurity spin and the substrate's surface state would lead to a significant variation in YSR-energy. Therefore, it was already assumed in the model described in Section 5.2 that the direct coupling of the Fe spin to the surface state is negligible.

Moving Impurity

Another way of proving that there is no direct interaction between the Fe-atoms' spins and the surface state of Ag(111) is to move the Fe-atom along the corral and probe its YSR-states. As seen in Section 5.2 for the elliptical corrals, moving the impurity inside the corral leads to different scattering conditions and shifts the corral eigenmodes in energy. Here, we investigate this behavior more systematically.

To this end, we use a rectangular corral with $L_x = 24.1$ nm and $L_y = 9.1$ nm (same as in Figures 5.12/5.13) with an Fe-impurity inside. As depicted in Figure 5.21, we move the Fe-impurity along the central longitudinal axis of the corral from the top wall to the center of the corral. We define the distance ΔX as the distance between the impurity and the atoms of the inner top wall, and vary Δx between 2 nm and 12.5 nm. We measure the spectrum on the Fe-atom and the empty spot depicted by the gray circle at the bottom for each corral.

The result can be seen in Figure 5.22 for the Fe-atom in panel (A) and the empty spot in panel (B). The color scale is adjusted to show the coherence peaks and the MSS features. The labels indicate the β^- - and β^+ -states.

As we move the Fe-atom toward the center of the corral, we can see in the "empty spot" measurement (panel (B)) that the MSS shifts further into the gap. The MSS energies reach a local minimum for $\Delta x = 4.4$ nm. Furthermore, a strong particle-hole asymmetry of the MS-peak occurs from $\Delta X = 2$ nm to 5 nm, where the

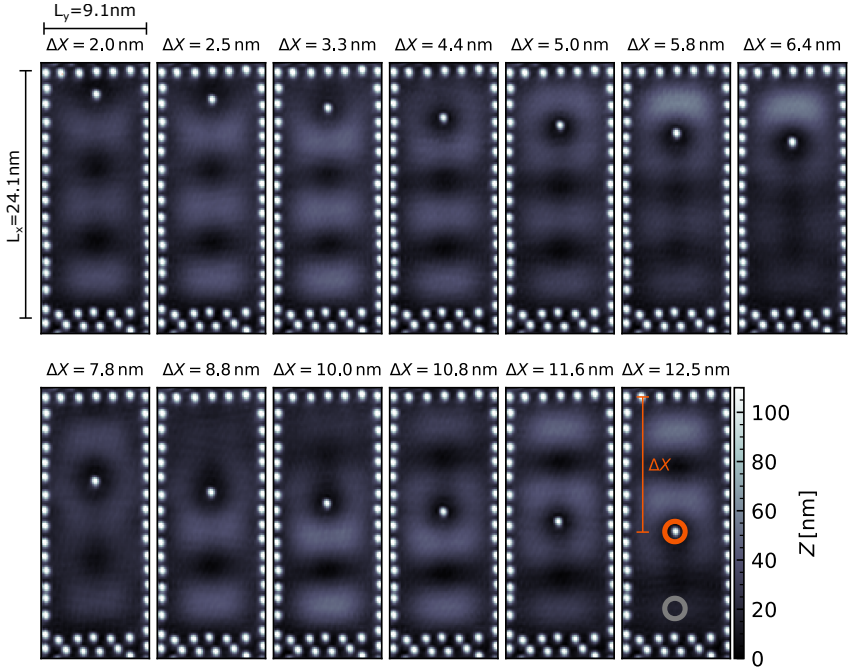


Figure 5.21: Rectangular corral with an Fe-impurity on different positions. Constant-current STM image of the rectangular corral with the Fe-atom moving along the corral's central axis. Δx is the distance between the upper wall and the impurity, as depicted in the last panel. The orange circle marks the position of the Fe-impurity, and the grey circle depicts the location we define as *empty spot*. Parameters: $I_{\text{set}} = 1$ nm, $V_{\text{bias}} = -5$ mV.

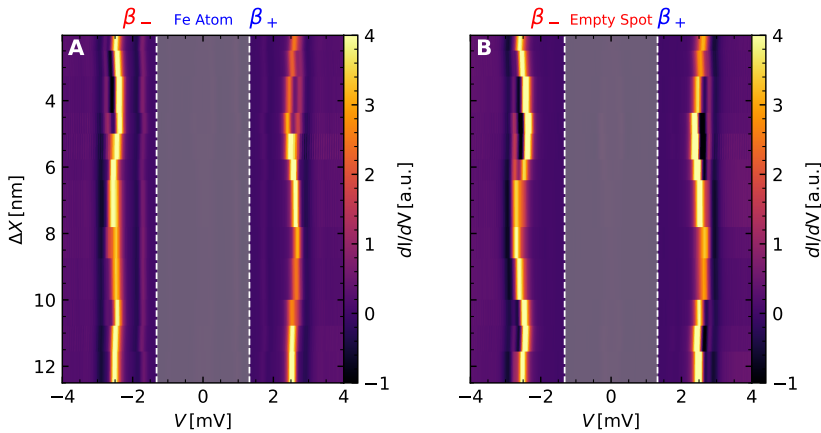


Figure 5.22: Spectra taken inside of the corral as a function of impurity position. (A) Bias-spectroscopy measurement performed on the Fe-atom (see Figure 5.21, orange circle) as a function of the distance between atom and upper corral wall Δx as depicted in the same Figure. The label on the top marks the voltages of the $\beta^{+/-}$ -state. The white dashed lines mark the values between $-\Delta_t$ and $+\Delta_t$. (B) Same as (A) but taken on the empty spot as depicted in Figure 5.21 by the grey circle. Parameters: $V_{\text{stab}} = -5$ mV, $I_{\text{stab}} = 1$ nA, $V_{\text{mod}} = 50$ μ V, feedback: off.

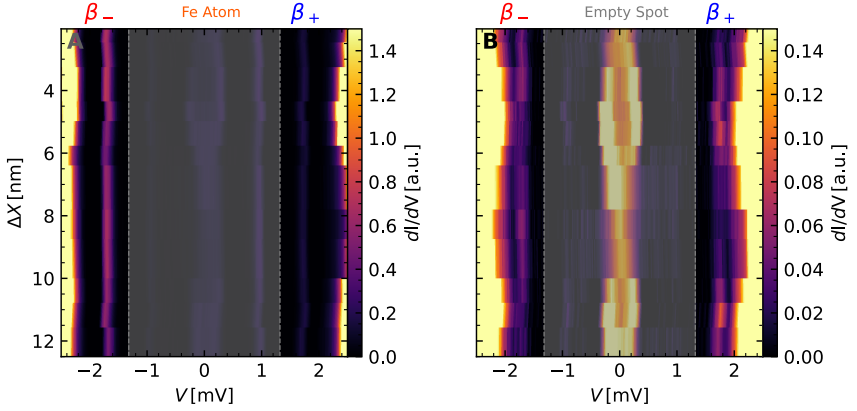


Figure 5.23: Spectra taken inside of the corral as a function of impurity position (color scale adjusted) (A, B) same as Figure 5.22 but with the color scale and V_{bias} range adjusted to accentuate the YSR-states (A) and -mirages (B).

peak on the negative bias side is much more intense than the one on the positive bias side. At 5 nm this asymmetry is reversed. For the corrals at $\Delta X = 10.8$ nm or 11.6 nm, another local minimum of the MSS energy seems to occur. However, due to the limited energy resolution, the MSS is hard to discern from the coherence peak.

For the Fe spot presented in panel (A), the MSS behaves similarly to that in the empty spot (B). However, the separation between MSS and the coherence peak is much less apparent. For the first oscillation, we can see the particle-hole asymmetry of the MSS behaves the same as for the measurement in panel (B).

Next, we zoom in on the β YSR-state and YSR-mirage features

shown in Figure 5.23. Panel (A) shows the measurements on the Fe. Similar to Figure 5.20A, the energies of both β -states stay constant. The same applies to the particle-hole asymmetry, where β^- is always larger in intensity than β^+ . In panel (B), we can see the measurement on the empty spot. The respective labels at the top of the figure mark the voltages of the β -mirages. Like in the observations in Figure 5.17, the YSR-mirages are constant in energy but oscillate in intensity. For β^- , we see peaks in intensity at $\Delta X = 3.3$ nm and 8 nm, while β^+ has peaks at 5.8 nm and 11.6 nm where the β^- -mirage has minima in intensity.

We can interpret the results qualitatively with the knowledge we gained from the previous parts: Apart from the magnetic scattering, the Fe-impurity also induces Coulomb scattering (like the Ag-atoms) [155]. This way, the Fe-atom can be seen as another wall to the surface state eigenmodes. However, the wall must be treated as relatively transparent since it is only one atom. As we move the Fe-atom, we mimic a scenario where we move the upper wall towards the center of the corral, which, on the other hand, tunes the eigenmodes of the corrals in energy. The MSS, visible in Figure 5.22B, can be used to get insights into the evolution of the corral eigenmodes as a function of ΔX . One example can be seen between $\Delta X = 2$ nm and 8.8 nm. The evolution of the MSS asymmetry in Figure 5.22 implies that a mode moves from negative to positive V_{bias} and crosses E_F at $\Delta X = 4.4$ nm.

At this corral length, the β^+ -mirage has maximum intensity (Figure 5.23, and the β^- -mirage has maximum intensity. The same can be observed around $\Delta X \approx 11$ nm. Overall, the evolution of

the mirage intensity with eigenmode energy is consistent with the previous experiment using corrals of different lengths.

Amplitudes of the YSR-mirages

Finally, we analyze the intensity oscillation of the mirages quantitatively ($\beta^- > \beta^+$ to $\beta^+ > \beta^-$), which is the same as in Figure 4.16 whenever an eigenmode crosses E_F . We take the constant-height dI/dV -maps that we obtained at the voltage of the $\beta^{+/-}$ state (Figure 5.12, 5.13) and fit the data as I will describe in the following.

As a first step (see Figure 5.24), we cut out the interior rectangular-shaped area of the corral, restricted by the inner wall atoms. We also exclude an area around the Fe-atom, as shown in Figure 5.24, to exclude the contribution coming from the YSR-state of the Fe-atom. With this area cut out, we average over the y -coordinate and end up with a line representing the y -averaged YSR-mirage intensity in the corral. In the next step, we proceed to fit the line using a sinusoidal fit, which is given by:

$$\psi(x) = A \sin(kx + \Phi) + \psi_0, \quad (5.3)$$

with the amplitude A , the wavevector k , the phase shift Φ and an offset ψ_0 . The fitted value A is what we extract as the intensity value for each corral. For the corrals smaller than 11.13 nm, no reasonable fits could be done for the β^- -mirage due to the lack of data points after the cutout. We omit these measurements from the analysis. The same applies to corrals smaller than 13.01 nm in

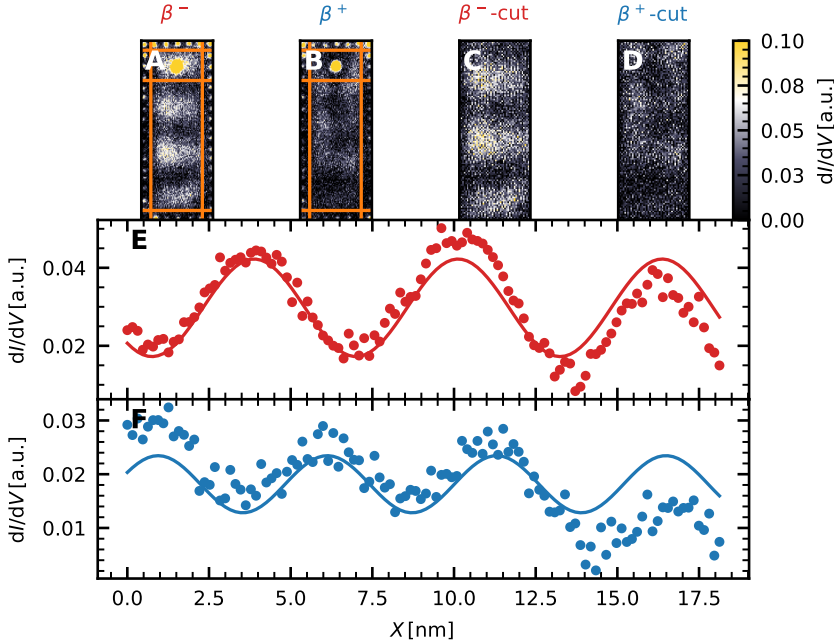


Figure 5.24: Extraction of the YSR-mirage amplitude. (A,B) Constant-height dI/dV -map of the $L_x = 23.9$ nm corral with the Fe-impurity at β^-/β^+ (A/B) energy. The orange lines depict how the cutout is done, as shown in (C/D). The same measurement is shown in Figure 5.12/5.13. (C/D) Area which is cut out for further analysis as depicted in (A/B). (E) Data from the cut in (C) averaged along the width of the dataset as a function of x and depicted by the points. The line represents a sinusoidal fit (see equation 5.3) of the data points. (F) Same as in (E) but for the data in (D) for β^+ .

the case of the β^+ -mirage.

The extracted values for the β^- and β^+ YSR-mirage intensities can be seen in Figure 5.25 in panel (A) alongside the values extracted from the theoretical model described in Section 5.2 in panel (B). The values corresponding to the β^+ (β^-) are shown in blue (red). The energetic positions of the corral eigenmodes, extrapolated by the particle-in-the-box model, are depicted by the color gradient in the background and the schematic at the top of the plot. The border where the color changes from blue to red represents the L_x at which the eigenmode is crossing E_F from positive to negative energy. By comparing the data in Figure 5.25 with the dI/dV -maps in Figures 5.12 and 5.13, we can match the intensity maxima with the dI/dV -maps.

In the experimental data shown in Figure 5.25, we see for the β^+ -mirage that the value reaches an intensity maximum when a corral eigenmode is shifted through E_F . The maximum of β^+ for both eigenmode cases ((3,1) and (2,1)) appears when the corresponding eigenmode is near to E_F according to the extrapolated values (shading from blue to red). We see a different behavior if we look at the oscillations of the intensity of the β^- -mirage. Each time an eigenmode is crossing E_F , the intensity of the mirage decreases. For the corral lengths, where an eigenmode is tuned to E_F , the β^- -mirage reaches a minimum. The maxima appear when the eigenmode is tuned out of the gap. The same qualitative behavior can be seen for the theoretical values of the mirage intensities (see panel (B)). Here, however, the maxima of β^+ mirages are systematically shifted to smaller corral lengths, which indicates that

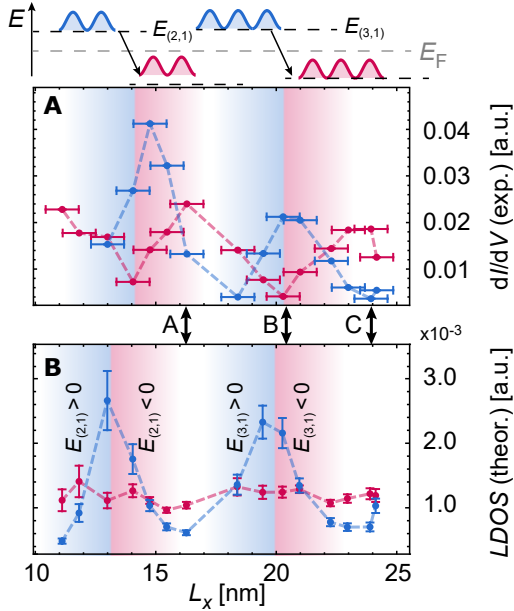


Figure 5.25: Intensity oscillation of the YSR quantum mirage. (A) Experimental and (B) simulated intensities of the β^- (red) and β^+ (blue) YSR quantum mirages as a function of corral length L_x extracted from corrals of lengths $L_x = 4.7$ nm to $L_x = 24.1$ nm as described in the text. The schematic on the top and the colored background depict the relative position of the corral eigenmode with respect to E_F (blue eigenmode energy $> E_F$, red eigenmode energy $< E_F$). The arrows in the schematic indicate the L_x at which the indicated eigenmode is crossing E_F . The double arrows underneath panel (A) indicate the lengths of the corrals shown in Figure 5.14.

the corral eigenmodes cross E_F for slightly shorter L_x in the simulation compared to the experiment. This might indicate that the Coulomb repulsion of the Fe-atom on the corral eigenmode is not accurately considered in the model. Most importantly, in both the experiment and the simulation, the YSR-mirage intensity oscillations result in an inversion of the particle-hole intensity of the mirage with respect to that of the pristine β^- YSR-state of the Fe. While for the pristine Fe YSR-state, β^- has always larger intensity compared to β^+ , this is reversed in the mirage whenever a corral eigenmode crosses E_F .

Effective model and analytical results

In order to rationalize the experimentally observed oscillation in the YSR-mirage intensities and the particle-hole inversion, we take the same model used in Section 4.3 and extend it by an additional term to describe the YSR-impurity:

$$\begin{aligned}
 H_M &= H_{\text{MSS}} + H_{\text{YSR}} + H_{\text{SC}}, \\
 H_{\text{SC}} &= \sum_{\mathbf{k}, \sigma} \epsilon_{\mathbf{k}} c_{\mathbf{k}, \sigma}^\dagger c_{\mathbf{k}, \sigma} - \Delta \sum_{\mathbf{k}} \left(c_{\mathbf{k}\uparrow}^\dagger c_{-\mathbf{k}\downarrow}^\dagger + c_{-\mathbf{k}\downarrow} c_{\mathbf{k}\uparrow} \right), \\
 H_{\text{YSR}} &= \sum_{\sigma} (\sigma J + U) \tilde{d}_{\sigma}^\dagger \tilde{d}_{\sigma} + \sum_{\mathbf{k}, \sigma} \tilde{V}(\mathbf{k}) c_{\mathbf{k}, \sigma}^\dagger \tilde{d}_{\sigma} + \tilde{V}^*(\mathbf{k}) \tilde{d}_{\sigma}^\dagger c_{\mathbf{k}, \sigma}, \\
 H_{\text{MSS}} &= E_R \sum_{\sigma} d_{\sigma}^\dagger d_{\sigma} + \sum_{\mathbf{k}, \sigma} V(\mathbf{k}) c_{\mathbf{k}, \sigma}^\dagger d_{\sigma} + V^*(\mathbf{k}) d_{\sigma}^\dagger c_{\mathbf{k}, \sigma}.
 \end{aligned} \tag{5.4}$$

Here, the operators d_{σ} and \tilde{d}_{σ} refer to the non-magnetic and the magnetic level, respectively, and $\epsilon_{\mathbf{k}} = \frac{\mathbf{k}^2}{2m} - E_F$ is the dispersion

relation of the 3D bulk superconductor with Fermi energy E_F . The coupling constants $V(\mathbf{k}) = V$ and $\tilde{V}(\mathbf{k}) = \tilde{V}e^{i\mathbf{k}\mathbf{R}}$ describe a corral state localized at the origin and a magnetic level located at position \mathbf{R} , respectively.

To picture what that model means, I will briefly explain each part of the Hamiltonian. The parts of the Hamiltonian H_{SC} and H_{MSS} are the terms that we have already treated in the previous chapter (Section 4.3). These two terms describe a superconductor (H_{SC}) and a resonance mode coupled to that superconductor (H_{MSS}). The new term H_{YSR} describes a magnetic resonance \tilde{d}_σ , which is coupled to the spin of a magnetic impurity given by the first part in H_{YSR} . The second part in H_{YSR} describes the coupling between the magnetic state and the corral resonance. The coupling constant in this case is given by $\tilde{V}(\mathbf{k}) = \tilde{V}e^{i\mathbf{k}\mathbf{R}}$. The coupling depends on an artificial distance between the YSR-impurity and the superconductor. Since this is a 0D model, it does not consider any corral geometry. This model can give us a very basic explanation of the origin of the intensity oscillating in the mirage that we observe in the experiment. Using the Greens function approach, we can calculate the LDOS of the YSR-mirage in the case of a corral eigenmode shifting through the superconducting gap by changing E_R . This way, we can simulate how the YSR-mirage intensity behaves when a corral eigenmode shifts through the superconducting gap.

The result is shown in Figure 5.26. Here, the YSR-mirage intensities are depicted as colored lines for the β^- (red) and the β^+ (blue) states, which evolve as a function of the corral eigenmode energy E_R normalized by Δ . The x -axis is reversed and runs from posi-

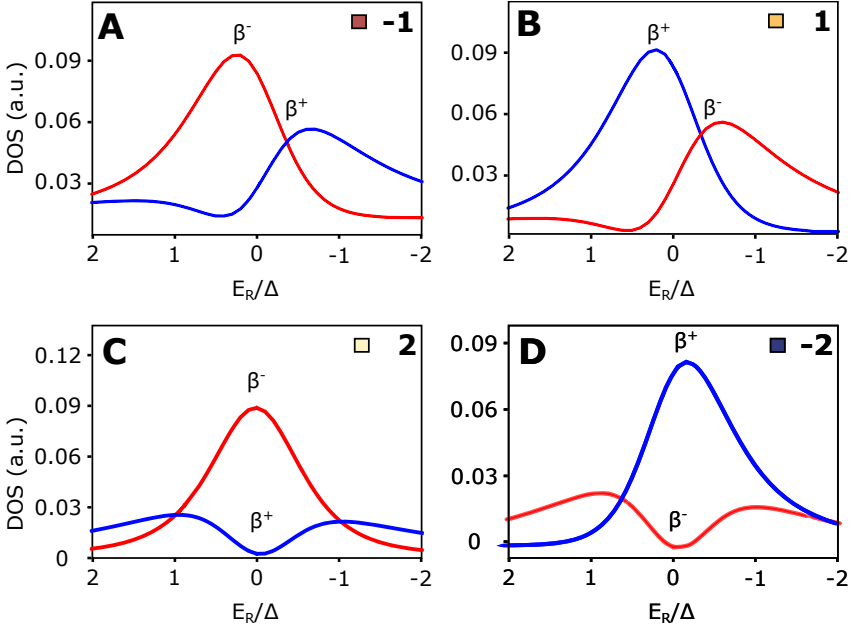


Figure 5.26: Evolution of the YSR-mirage intensity for different parameters. (A) YSR-mirage intensities of β^- (red) and β^+ (blue) as a function of the corral eigenmode's energy E_R normalized by the sample's superconducting gap Δ . The plot shows an example of the single crossing mirage, where the β^- -state peaks first while β^+ has a minimum (labeled as "-1"). (B) Same as (A) but for parameters such that the behavior is inverted. The plot shows an example of the single crossing mirage, where the β^+ -state peaks first and the β^- has a minimum (labeled as "1"). (C(D)) Same as (A(B)) but for different parameters such that the mirage shows the shape we label as double-crossing, with the β^- - (β^+)-mirage exhibiting a maximum exactly where the eigenmode crosses E_F while β^+ (β^-) has a minimum (labeled as "+2" ("-2")). Simulation parameters: $\frac{J}{\Delta} = 26$ (A), $\frac{J}{\Delta} = 24$ (B), $\frac{U}{\Delta} = 1$ (A, B), $\frac{J}{\Delta} = 44$, $\frac{U}{\Delta} = 35$ (C), $\frac{J}{\Delta} = 33$, $\frac{U}{\Delta} = 12$ (D), $R = 4.1$ nm (A-D).

tive to negative E_R . This depiction corresponds to the case where the length of the corral L_x is increased, starting with small L_x on the left and ending with large L_x on the right (see Figure 5.25). Depending on the parameter sets, we get results that are qualitatively different from each other. We label these cases by "-1", "1", "-2" and "2". The origin of the label choice will be evident later.

I will start the description of this Figure with the "-1"-case (Figure 5.26A). For large E_R , both mirages show very low intensities. However, the more we shift E_R towards 0, the more the mirage intensities deviate from each other. β^- increases, while β^+ decreases in intensity. Right before E_R reaches E_F , β^- reaches a maximum and β^+ a minimum. After that, the β^- intensity decreases drastically, while β^+ increases in intensity when E_R is shifted off E_F towards negative energies, and β^+ peaks in intensity.

Interestingly, we can achieve the opposing behavior by increasing the magnetic coupling J between the impurity and the superconducting substrate while keeping the remaining parameters the same. Note that this case corresponds to tuning the pristine impurity YSR-state through the quantum phase transition (QPT) [156].

The result can be seen in (B). When we compare these results to (A), we see that the curves for $\beta^{+/-}$ have been exchanged. Apart from that, the evolution of the YSR-mirage intensities resembles that of the "-1"-case. Both mirage intensities peak as a function of E_R , where the peaks appear at different values for E_R . This time, β^+ reaches its peak before β^- .

For larger values of J , we get the behavior as shown in panels

(C) and (D). Here, we see that the β^- (C) or β^+ (D)-mirage intensity shows a maximum right where the corral eigenmode crosses E_F , while the β^+ (C) and the β^- (D) mirage intensities show a minimum. Since, for this case, the curves for the different mirages show two crossings, we refer to this case as "double-crossing" cases "2" and "-2". Accordingly, we will refer to the cases in (A) and (B) as "single-crossing" cases. The labeling of the cases reflects whether the mirage has one or two crossings and whether the β^- ("-") or the β^+ ("+") part has the overall maximum first. Overall, we can see that the case "-2" in Figure 5.26D resembles both the experiment as well as the simulations in Figure 5.25. With these classifications, we can simulate the mirages for different parameter sets of J and U to understand better how these phases are related to the parameter sets.

In Figure 5.27, the phase space of the model is depicted for different parameters of R as functions of E_N and U . The black lines correspond to the parameter set at which the resulting YSR-state would be located at the coherence peak, whereas the red line corresponds to the parameters at which the bare YSR-state of the impurity crosses E_F , which is often referred to as a QPT. The phase space is separated into four quadrants for $R = 4.1$ nm. For large values of U , we see that the mirage can either be in the "2"-phase or the "-2"-phase depending on whether the YSR-states are located before or after the QPT, which is determined by J . For smaller U up to large negative values of U , the system either exhibits the "1"- or the "-1"-phase. The small arrow connects the two parameter sets referring to the calculations from Figure 5.26. We can see that Figure 5.26A corresponds to a case where the YSR-

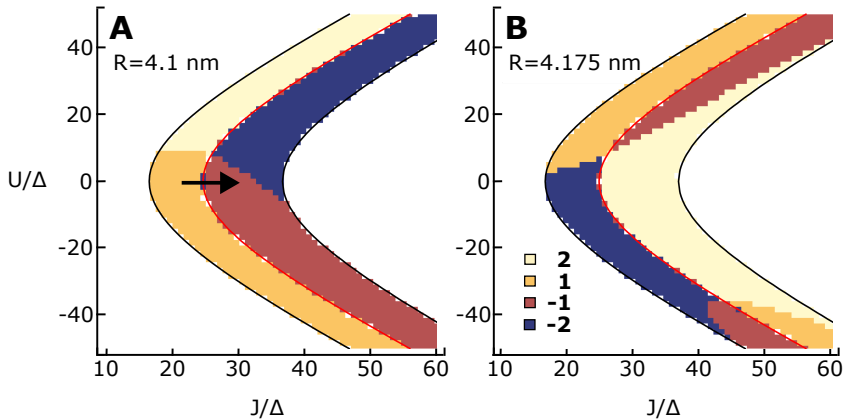


Figure 5.27: YSR-mirage phase diagram. (A) Simulated YSR-mirage phase diagram as a function of the Coulomb scattering U and the magnetic coupling J for different values of R . The individual colors correspond to the cases shown in Figure 5.26. The red lines correspond to the parameter sets, where the bare impurity YSR-state would cross E_F , which is often referred to as the QPT. The black lines correspond to the cases where the YSR-state is at the same energy as the coherence peak. The black arrow exemplifies two points in the phase space, which would lead to the same YSR-energy but are on different sides of the QPT. $R = 4.1$ nm. (B) Same as in (A) but with $R = 4.175$ nm.

impurity is before the QPT while Figure 5.26B reflects the case of the YSR-impurity after crossing the QPT.

The plot in Figure 5.27A suggests that by measuring the intensity oscillations of the YSR-mirage and assigning it to one of the cases (-2, -1, 1, 2), we can determine whether the YSR-mirage is before or after the QPT. Mirages of cases "2" and "1" would indicate a YSR-impurity before a QPT, and cases "-2" and "-1" to a YSR-impurity behind the QPT. Even though this is true for parameters in panel (A), panel (B) shows that the whole phase space changes for a different value of R such that an unambiguous correlation between QPT and YSR-mirage intensity behavior while the corral eigenmode crosses E_F does not exist. However, we can see that the model can reproduce the particle-hole inversion of the YSR-mirage intensity we observed in the experiment, which occurs whenever an eigenmode crosses E_F (see Figure 5.26D).

5.5 Multiple impurity corral

So far, we have only considered corrals with a single impurity. In this section, we will look at corrals with multiple impurities. One exciting aspect is that due to the coupling between the impurity and the eigenmode, we can potentially cause a long-range coupling between two atoms using the YSR-mirage [66]. Also very interesting is to see what happens to the YSR-mirage when the eigenmode is caused by scattering with corral walls made of Fe-atoms.

Elliptical corrals with multiple impurities

We use the elliptical corral from one of the previous Sections 5.2 for our experiments. The upper atom is placed at the same location as in Figure 5.4. In addition, we place another impurity into the lower half of the ellipse, symmetrical to the upper atom, concerning the horizontal half-axis.

In Figure 5.28A, we can see this for a corral with an Fe-atom on the top and a Ag-atom at the bottom called in the following *Fe-corral with Ag-impurity (1)*. For this corral, we record the dI/dV -maps taken at the voltages of the β^- (B) and β^+ (C) YSR-state. Similar to the cases discussed in Section 5.2, the Fe-atoms cause a YSR-mirage inside the corral. The shape resembles that in Figure 5.4. Crossing both impurities, we take a spectroscopic line profile through the corrals along the major axis (see panel (D)). The labeled arrows mark the YSR-states of the Fe-atom. We can see an

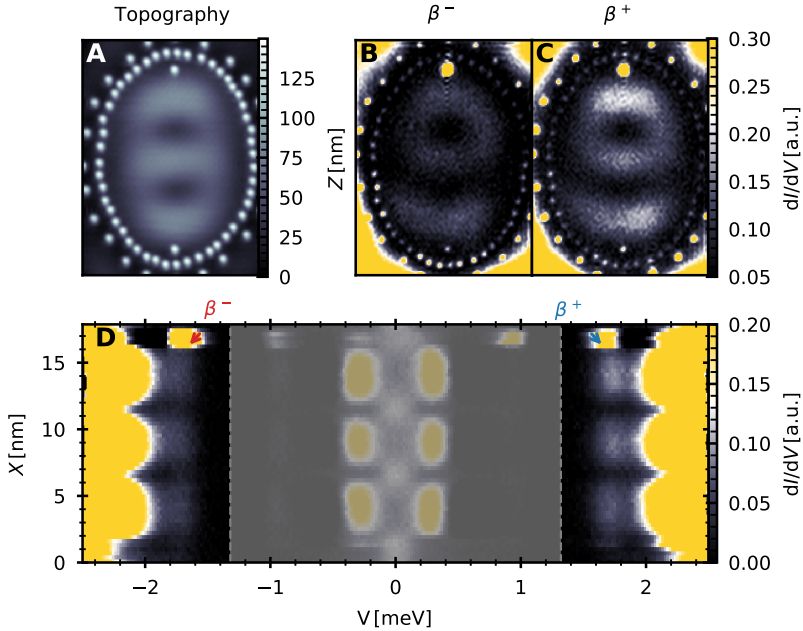


Figure 5.28: Elliptical corral with Fe and Ag-impurity (Fe-Ag-impurity corral (1)). (A) Constant-current measurement of the same elliptical corral as in Figure 5.4 but with a Fe-impurity at the top and a Ag-atom at the bottom. (B, C) Constant-height dI/dV -map of the corral shown in (A) taken at the voltage of the β^- -state (B) and the voltage of the β^+ -state (C). (D) Spectroscopic line profile taken along the major axis of the corral shown in (A). The greyed out area marks the V_{bias} -interval between $-\Delta_t$ and Δ_t . Parameters: $I_{\text{set}} = 1 \text{ nA}$, $V_{\text{bias}} = -5 \text{ mV}$ (A), $V_{\text{bias}} = -1.67 \text{ mV}$ (B), $V_{\text{bias}} = 1.67 \text{ mV}$ (C), $V_{\text{stab}} = -5 \text{ mV}$, $I_{\text{stab}} = 1 \text{ nA}$, $V_{\text{mod}} = 100 \text{ } \mu\text{V}$, feedback: off (B, C), $V_{\text{stab}} = -5 \text{ mV}$, $I_{\text{stab}} = 1 \text{ nA}$, $V_{\text{mod}} = 50 \text{ } \mu\text{V}$, feedback: on (D).

oscillating pattern appearing at the β voltages. At the position of the Ag-atom, no notable increase in the intensity at this energy can be found. Notably, there is again an inversion of the particle-hole asymmetry in the intensity of the mirage with respect to the pristine YSR-state of the Fe, i.e., the positive energy mirage has higher intensity compared to the negative counterpart.

In the next measurement, we replace the Ag-impurity with an Fe-atom (see Figure 5.29A, called *Fe-Fe-impurity corral (2)* in the following). The dI/dV -maps show an additional strong spectral intensity at the bottom of the corral at the location of the lower Fe-atom for the scan at β^- (B) and β^+ (C). When we compare the dI/dV -maps of this corral to the Fe-coral with the Ag-impurity (Figure 5.28), we see that the shapes of the LDOS signal inside of the corral are otherwise similar. However, in the core of the Fe-Fe-impurity corral (2) the intensity of the mirage β^+ is considerably increased. Still, in the cases of the Fe-coral with the Fe-impurity (2), the β^+ -mirage has a higher intensity compared to the β^- -mirage.

In the spectroscopic line profile in panel (D), we see the YSR-states of the atoms at both ends and the YSR-mirage between them. When we compare this to Figure 5.28D, we see, apart from the appearance of a YSR-state at the location of the atom, also here that the YSR-mirage intensity changes. The intensities are larger for the Fe-coral with the Fe-impurity.

In order to see whether there is an interaction between the Fe-impurities, we have to compare the spectra taken on the impurity atoms. In Figure 5.30, the single spectra taken on the impuri-

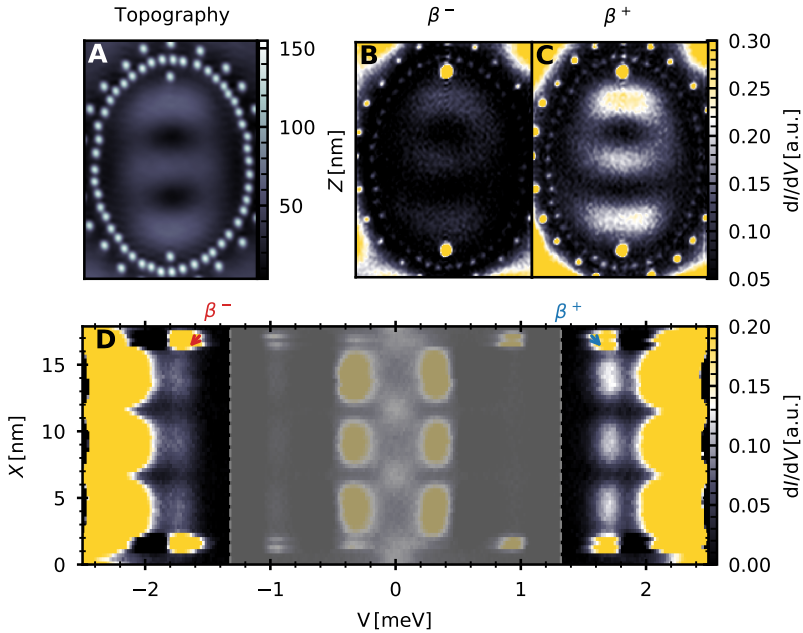


Figure 5.29: Elliptical corral with two Fe impurities (Fe-Ag-impurity corral (2)). (A) Same as in Figure 5.28 but with an Fe-atom at the top and the bottom inside of the corral. (B, C) Constant-height dI/dV -map of the corral shown in (A) taken at the voltages of the β^- (B) and β^+ (C) YSR-state. (D) Spectroscopic line profile taken along the major axis of the corral shown in (A). The greyed out area marks the V_{bias} -interval between $-\Delta_f$ and $-\Delta_f$. Parameters: $I_{\text{set}} = 1$ nA, $V_{\text{bias}} = -5$ mV (A), $V_{\text{bias}} = -1.67$ mV (B), $V_{\text{bias}} = 1.67$ mV (C), $V_{\text{stab}} = -5$ mV, $I_{\text{stab}} = 1$ nA, $V_{\text{mod}} = 100$ μ V, feedback: off (B, C), $V_{\text{stab}} = -5$ mV, $I_{\text{stab}} = 1$ nA, $V_{\text{mod}} = 50$ μ V, feedback: on (D).

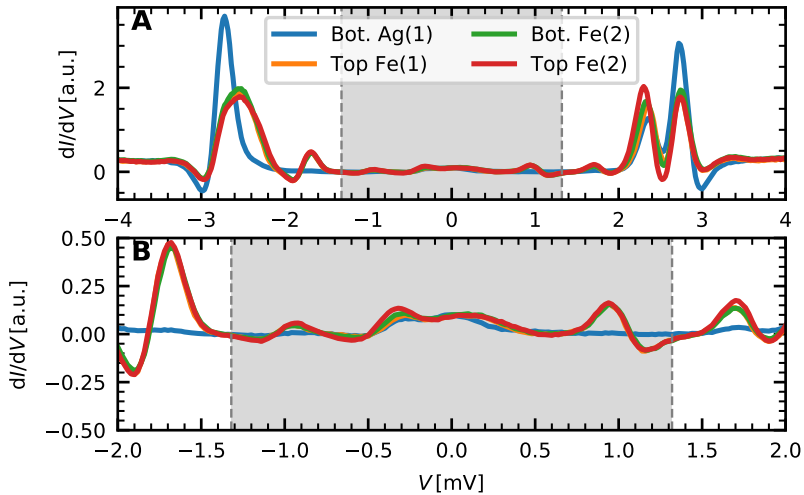


Figure 5.30: Bias spectroscopy measurement on impurities in corrals. (A) Bias-spectroscopy performed on the impurities inside of the elliptical corrals as shown in Figure 5.28 and 5.29. The indices (1, Fe-Ag-imp.) and (2, Fe-Fe-imp.) refer to the respective corrals. (B) Same as (A) but zoomed in on the $\beta^{+/-}$ -peaks. Parameters: $V_{\text{stab}} = -5$ mV, $I_{\text{stab}} = 1$ nA, $V_{\text{mod}} = 50$ μ V, feedback: off (stabilization on the same Ag-wall atom for all measurements).

ties of the Fe-Fe-impurity corral (2) and Fe-Ag-impurity corral are compared to each other. In panel (A), we can see the usual spectrum of the Ag-atom confined inside the corral, which has already been discussed in the previous sections. More interestingly, the Fe-atom spectra for the Fe-Fe-impurity corral (1) and the Fe-Ag-impurity corral (2) look very similar. For the $\beta^{+/-}$ -states far from the MSS, we can see in the zoom (panel (B)) that the Fe spectra on both corrals look almost identical. This proves that no additional interaction is induced by placing the two Fe-atoms inside the corral, as this would lead to a splitting or shifting of the YSR-peak.

An explanation for the negligible interaction of the Fe YSR-states via the quantum corral mirage is the aforementioned negligible coupling between the eigenmodes of the corral and the YSR-states (Section 5.4). As explained in this previous section, the coupling is indirect. Therefore, we would expect it to be weak. This contrasts with other works on YSR-mirages where the impurity state couples directly to the 2D surface state [151].

Fe-wall corrals

Our last experiment examines hybrid corrals we constructed from Ag- and Fe-atoms. We vary the corrals in size and investigate the YSR-mirages inside them to see whether there is a qualitative difference to the single Fe-impurity corrals investigated before. We start the experiment by constructing a rectangular corral (see Figure 5.31), where we place rows of Fe-atoms at the top and the bottom, forming the inner upper and the inner bottom wall of the

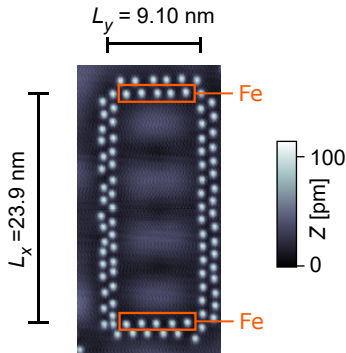


Figure 5.31: Topography of hybrid-wall corrals. Constant-current STM image of the hybrid corral. As depicted by the orange box, the inner wall atoms at the top and the bottom are made of Fe-atoms. To resize the corral, the lower wall is shifted upwards. Parameters: $I_{\text{set}} = 1 \text{ nA}$, $V_{\text{bias}} = -5 \text{ mV}$.

corral (as depicted by the orange boxes). The remaining walls are made from Ag-atoms. The example presented in Figure 5.31 shows a corral of $L_x = 23.9 \text{ nm}$ and $L_y = 9.1 \text{ nm}$.

For the experiment, we move the lower corral wall upwards to resize the corral, as can be seen in Figure 5.32. We measure the dI/dV -maps for each corral length at the voltages of the $\beta^{+/-}$ YSR-states. For the measurements, the tip is stabilized on the same Ag-atom located in the outer wall of the corral.

The maps taken at the β^- voltage can be seen in Figure 5.33. The panels of the Figure are labeled according to their L_x . As expected, we see strong intensity on the Fe-atoms at the corral's top and bottom boundary. The YSR-states of the Fe-atoms are locally separated and show no sign of hybridization. We see a standing wave

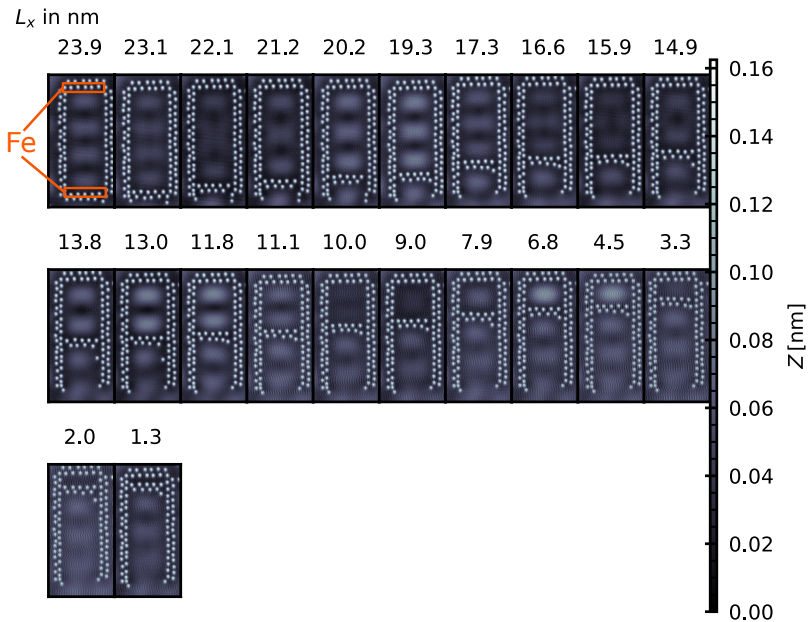


Figure 5.32: Hybrid-wall corral set. Constant-current STM images of hybrid corrals with different lengths L_x as indicated and $L_y = 9.1$ nm. Parameters: $I_{\text{set}} = 1$ nA, $V_{\text{bias}} = -5$ mV.

5 Realization of the YSR quantum mirage

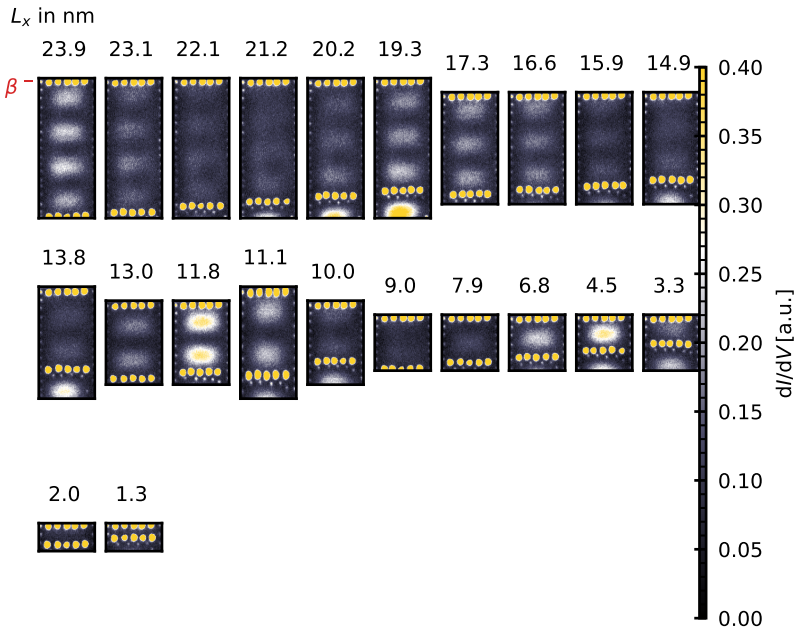


Figure 5.33: dI/dV -measurements at β^- voltage for hybrid corrals. Constant-height dI/dV -maps of the hybrid corrals shown in Figure 5.32 taken at the voltage of the β^- YSR-state. Parameters: $V_{\text{bias}} = -1.67$ mV, $V_{\text{stab}} = -5$ mV, $I_{\text{stab}} = 1$ nA, $V_{\text{mod}} = 100$ μ V.

Eigenmode	From L_x [nm]	To L_x [nm]
(4,1)	23.9	23.1
(3,1)	19.3	16.6
(2,1)	11.8	11.1
(1,1)	6.8	3.3

Table 5.1: Hybrid corral β^- -mirage lengths. Mirage quantum number and L_x -intervals at which they can be found in the corral; extracted from Figure 5.33.

pattern inside the corral, where the number of maxima along the x -direction varies between $n_x = \{4, 3, 2, 1, 0\}$ as we tune L_x . In contrast, n_y , the number of maxima along the y -direction stays constant at 1. Like in the case with the single Fe-impurity (Sections 5.3, 5.4), we can see that the intensity of the YSR-mirage oscillates as a function of L_x . From the measurements, we can read out the approximate L_x at which a specific eigenmode appears. The values are summarized in table 5.1:

Next, we analyze the dI/dV -maps, taken at the β^+ voltage (see Figure 5.34). Like in the β^- case, the wall atoms show YSR-states with a strong localization. Concerning the YSR-mirage, we can see the same eigenmodes ((4, 1), (3, 1), (2, 1) and (1, 1)) as for the β^- case and an oscillation in intensity. The eigenmodes and the lengths at which they appear are read out and summarized in table 5.2 like for the β^- maps. We can see that the YSR-mirage as a function of L_x shows the same behavior for β^- and β^+ . The correlation of maximum/minimum intensities of the β^- and β^+ mirages observed for the single impurity corrals in Section 5.4 cannot be observed for these corrals.

5 Realization of the YSR quantum mirage

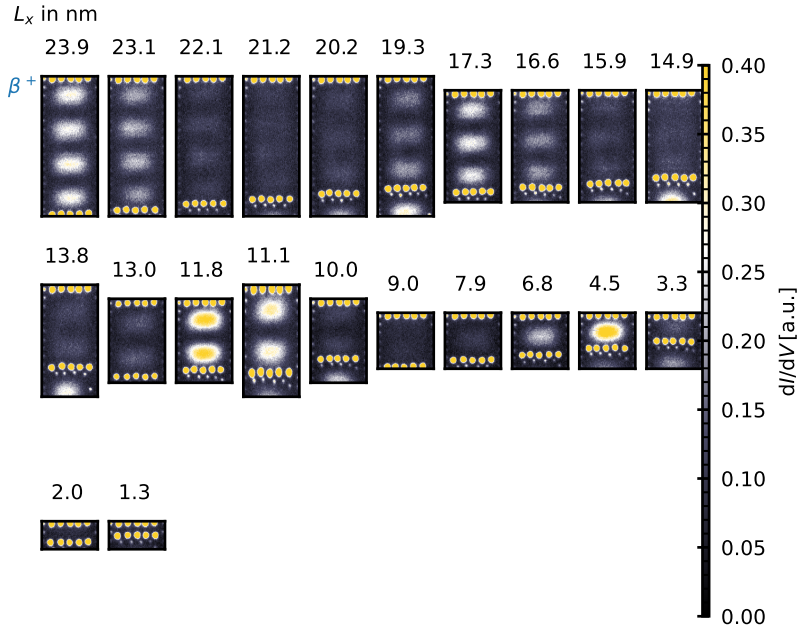


Figure 5.34: dI/dV -measurements at β^+ voltage for hybrid corrals. Constant-height dI/dV -maps of the hybrid corrals shown in Figure 5.32 taken at the voltage of the β^+ YSR-state. Parameters: $V_{\text{bias}} = 1.67$ mV, $V_{\text{stab}} = -5$ mV, $I_{\text{stab}} = 1$ nA, $V_{\text{mod}} = 100$ μ V.

Eigenmode	From L_x [nm]	To L_x [nm]
(4,1)	23.9	23.1
(3,1)	19.3	16.6
(2,1)	11.8	11.1
(1,1)	6.8	3.3

Table 5.2: Hybrid corral β^+ -mirage lengths. Mirage quantum numbers and L_x -intervals at which they can be found in the corral; extracted from Figure 5.34.

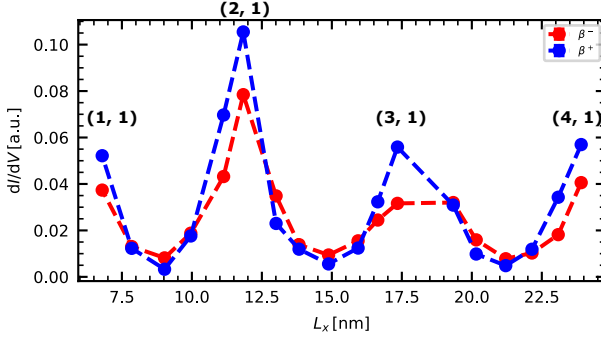


Figure 5.35: Intensity of the quantum mirages of all hybrid corrals as a function of L_x . The amplitude of the YSR-mirages inside the hybrid corrals was extracted with the same procedure described for the data in Figure 5.24. The labels correspond to the quantum numbers (n_x, n_y) of the mode and indicate the intensity maxima of the respective modes.

To quantify this observation, we use the same procedure demonstrated in Figure 5.3 to extract the intensity of the YSR-mirages for each corral. The result can be seen in Figure 5.35, where we compare the values extracted for β^- and β^+ . We can see that the intensities of both mirages oscillate with the same period ($\lambda \approx 6.5$ nm), as in the case of the single Fe-impurity corral (Figure 5.25). However, now, the maxima of both, the β^+ and β^- -mirages, appear for the same corral length. Note that for these corral lengths, the β^+ mirage still has a larger intensity compared to the β^- mirage. So, the particle-hole asymmetry of the mirage is still inverted with respect to that of the pristine Fe YSR-state. Interestingly, we see that these intensity maxima occur for shorter corral lengths (≈ 2.5 nm) compared to the single Fe-impurity corrals.

Most of the results of this experiment can be understood by applying the same explanation from the previous sections of this chapter. The appearance of the YSR-mirage results from an indirect coupling between the corral eigenmode and the YSR-impurity mediated via their interactions with the bulk. By resizing the corrals, we shift the corral eigenmodes in energy. The oscillatory behavior can be explained by the individual eigenmodes shifting through E_F . The 2.5 nm shift of the E_F crossings can be explained by a less effective Coulomb scattering of the Fe-atoms compared with the Ag-atoms. This is why the corral appears to be longer to the surface state electrons.

A significant remaining question for the single-impurity corral from Section 5.4 is the antiphasing between the mirages at β^- and β^+ . While the β^+ -mirages reached their intensity maximum, every time one of the corral eigenmodes is shifted through E_F , the β^- -mirage had a minimum there. The effective model we treated in Section 5.4 suggested that this effect was related to a particular set of parameters J , K , and R . However, this model is probably insufficient to describe the case of a hybrid corral involving multiple YSR-impurities.

5.6 Conclusion

In this chapter, we showed the first realization of the YSR-mirage inside of the atom-by-atom built quantum dot by positioning a magnetic impurity inside of it. The corrals show a long-range spectroscopic feature at the energy of the YSR-states of the mag-

netic impurity inside the superconducting gap, which can not be seen for a non-magnetic impurity. The occurrence of this effect is independent of the geometric shape of the corral [152, 153]. To investigate how the mirage is related to the energy of the corrals' eigenmodes, we built rectangular corrals and tuned the lengths, thereby shifting corral modes through the gap. The analysis shows that the YSR-mirages oscillate in intensity as a function of the corral length whenever an eigenmode crosses E_F . Interestingly, we can see that the mirage intensities show a peculiar behavior, where the positive energy mirage intensity always maximizes when the corral eigenmode crosses E_F , while the negative energy mirage minimizes. This leads to a particle-hole asymmetry inversion of the mirage intensities with respect to that of the pristine Fe YSR-states.

We explain the occurrence of the YSR-mirage by extending the MSS model from Chapter 4 with a magnetic interaction term, describing the YSR-states of the impurity. In this model, the spins of the magnetic impurity are mainly coupled to the bulk superconductor, inducing the YSR-states. The coupling to the corral eigenmode can be understood as a scattering of the YSR-states at the corral walls, connecting the impurity spins to the quantum corral eigenmodes indirectly. The corral eigenmode also scatters at the atom walls [157–160], leading to MSS [117].

The model can reproduce the intensity oscillations of the YSR-mirage between β^- and β^+ . Furthermore, it shows that the coincidence of maxima and minima in the β^+ and in the β^- mirage intensities can be switched to opposite behavior by varying

5 Realization of the YSR quantum mirage

the coupling between the impurity and substrate so that the YSR-states are driven through the quantum phase transition [155, 156, 161].

6 Bottom up constructed YSR-chains on a superconducting Rashba surface

This chapter deals with the growth and properties of a Rashba surface of $\text{BiAg}_2/\text{Ag}(111)$ grown on top of superconducting $\text{Nb}(110)$. We then continue with scattering experiments on the BiAg_2 surface. Finally, we will look at the proximitized superconductivity of the surface. Here, we investigate the last remaining ingredient of topological superconductivity, which is Rashba SOC, and will investigate it under the influence of proximity-superconductivity. Building on these findings, we explore the properties of magnetic adatoms adsorbed on the superconducting BiAg_2 surface alloy. We will begin by discussing the adsorption behavior of the magnetic atoms on the surface. This involves examining how the atoms interact with the surface and identifying the resulting YSR-states. Following this, we will investigate the behavior and properties of pairs of Fe-atoms on the surface, focusing on their interactions and the resulting hybridization of YSR-states. Subsequently, we will use atom manipulation techniques to construct chains of Fe-atoms. This will allow us to study the band formations within these chains. Notably, we observe that some of these chains exhibit end states. To understand these end states better, we perturb them using atoms adsorbed at different distances from the chain's ends and analyze the effects.

Experimental and theoretical work sharing

The experimental results in this chapter were measured by Dr. Lucas Schneider and myself. I analyzed the data by using self-written Python scripts.

Introduction

Rashba spin-orbit coupling is one of the main ingredients in creating topological superconductors [162, 163]. Even though Nb provides a substantial superconducting gap with a critical temperature T_c of 9.25 K, being the highest for any elemental superconductor, it has only a relatively weak SOC. Therefore, elemental superconductors exhibiting higher SOC due to their higher Z-numbers have been considered as well. This includes experiments on Ta [164, 165] ($T_c = 4.5$ K) or Re [27, 166] ($T_c = 1.7$ K). However, the problem with these substrates is that even though the SOC should be larger, the superconducting gap of these substrates is much smaller, which, on the other hand, cannot yield clear mini gap structures such as on Nb [29]. Pb is a heavy substrate with a comparably high T_c (7.2 K), but atoms cannot be manipulated on this surface. Therefore, the chains on the Pb surface must be created by depositing adatoms and rely on the self-assembling mechanisms [28, 34]. Another idea for increasing the SOC is to use substrates with significant superconducting gaps and depositing films with high SOC, which get superconducting properties by the proximity effect. Attempts have been reported using heavy-metal films [40, 167]. Another class of material known for its high SOC is the

so-called Rashba surface alloy. These materials are created by alloying a noble metal surface with a heavy element such as Bi or Pb [168]. The heavy element atoms replace every third atom on the surface of the noble metal. Even though the main motivation in this thesis is the use of the substrate for creating topological superconductors, Rashba SOC is a topic that is also relevant for a plethora of other fields of condensed matter physics like topological insulators [169, 170], spintronics [171, 172] and non-collinear magnetism [173, 174]. Therefore, the results from this chapter can also be used to progress the research in these directions.

6.1 Topographic and spectroscopic properties of BiAg₂ on Ag(111)/Nb(110)

This section uses the Ag(111) islands grown on Nb(110) to deposit Bi-atoms to create the BiAg₂ surface alloy. We characterize the surface by analyzing its topographic structure.

Growth modes of Bi on Ag(111)

For the growth of the BiAg₂ surface alloy, we use the sample preparation described in Chapter 4 as a starting point. The example in Figure 4.4 shows the growth of Stranski-Krastanov Ag islands on Nb(110) while the rest of the surface is covered by a Ag-wetting layer. The island thicknesses range from ≈ 5 nm to ≈ 30 nm (17 MLs-104 MLs). In order to create the surface alloy, we follow the preparation procedure described in Refs. [168, 175]. We deposit $\frac{1}{3}$ of a ML of Bi-atoms at room temperature ($T \approx 293$ K) onto the Ag(111) islands on Nb(110). Afterward, the sample is annealed at ≈ 375 K.

The outcome of this process is presented in Figure 6.1, which showcases the surface of a Ag(111) island on Nb(110) covered by Bi-atoms. Panel (A) displays an island with dimensions of $d_y \approx 560$ nm in the y -direction and $d_x \approx 560$ nm in the x -direction. The island's height, denoted as Z , relative to the wetting layer, is between 3.8 nm to 5 nm (13-17 MLs). The variation in height is a consequence of the island covering multiple step edges of the substrate underneath. Upon closer examination of the surface, as

6.1 Topographic and spectroscopic properties of BiAg₂ on Ag(111)/Nb(110)

depicted in (B), we discern two distinct growth modes on the islands. We label these phases as the "striped" phase and the "alloyed" phase.

Figure 6.2 shows a close-up image of both phases. Panel (A) presents a zoomed-in view of the alloyed phase. Here, we notice a hexagonal pattern of protrusions spanning the entire area. Panel (C), displaying the scan's FFT, supports this observation. In the FFT, six bright spots are visible around the center coordinates, each at a reciprocal distance of 5.69 nm^{-1} from the origin. Translated to real space, this pattern corresponds to a distance of $a = 175 \text{ pm}$. This observation can be compared to findings in previous studies [175], where it is explained that the hexagonal pattern we observe arises from the periodic arrangement of Bi-atoms within the alloy. Illustrated in panel (E), we depict the atomic lattice of the BiAg₂ alloy. Here, a Bi-atom replaces every 3rd atom of the Ag(111) lattice. This arrangement results in a superstructure where 6 Ag-atoms surround each Bi-atom. Due to the slightly larger radius of the Bi-atom (specific values can be found in Ref. [168]), it protrudes from the lattice in the Z -direction ($\Delta Z \approx 1.70 \text{ pm}$), as depicted in the upper part of the panel (E). The Bi-atoms form a lattice superstructure conforming to a $\sqrt{3} \times \sqrt{3}, R30^\circ$ pattern.

In examining the striped phase (panel (B)), we observe protrusions arranged in stripes along the $[1\bar{1}0]$ direction. These stripes appear approximately equidistant from each other. These characteristics are also evident in the FFT, shown in panel (D). Two bright spots appear, indicated by the arrows labeled "1". Furthermore, we see additional spots indicated by the circles labeled "2",

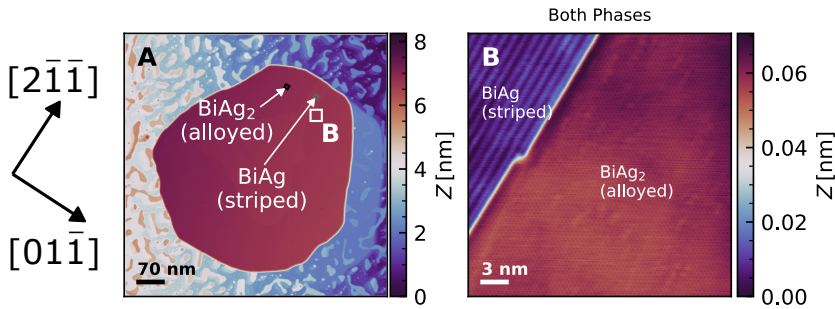


Figure 6.1: Different growth modes of BiAg₂: (A) Constant-current STM measurement of a Ag island on Nb(110) with a BiAg₂-alloyed surface. (B) Constant-current image of an area on the island from (A) showing the different growth modes of Bi on Ag. The cyan point marks the "striped" phase, while the black spot marks the alloyed phase (BiAg₂). Parameters: $I_{\text{set}} = 10 \text{ pA}$, $V_{\text{bias}} = 1 \text{ V}$ (A), $I_{\text{set}} = 1 \text{ nA}$, $V_{\text{bias}} = 500 \text{ mV}$ (B).

which hint toward shorter-ranged disorder along the line features. Similar structures have been reported in an earlier growth study for Bi on Ag(111) [176]. The structure is interpreted as the result of a dealloying process, which occurs when the amount of deposited Bi-atoms exceeds the number of atoms required to form the alloy.

Spectroscopy on BiAg₂

To verify whether the alloyed phase we obtained corresponds to the BiAg₂-alloy, we need to examine the surface's spectroscopic properties. This involves conducting bias-spectroscopy measurements on the surface. The results of these measurements are de-

6.1 Topographic and spectroscopic properties of BiAg₂ on Ag(111)/Nb(110)

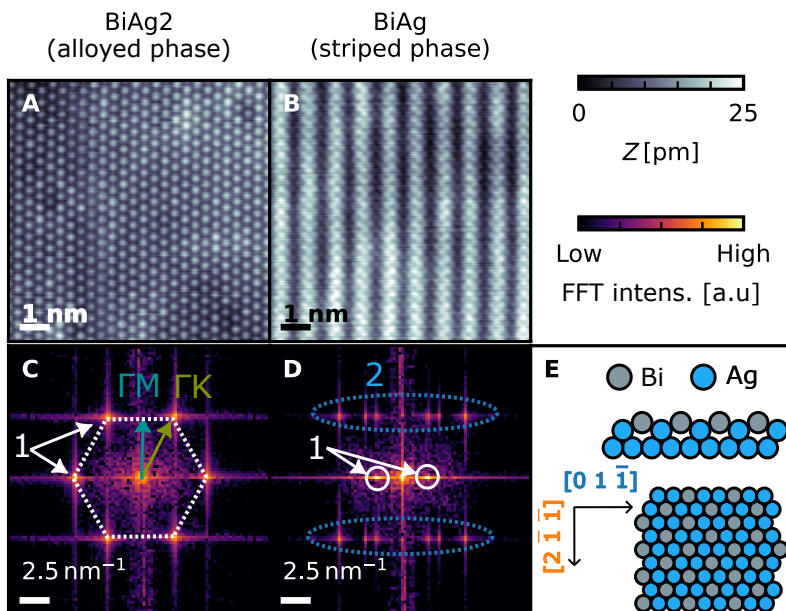


Figure 6.2: Different growth modes of BiAg₂: (A) Constant-current STM image of an area showing the alloyed phase and the striped phase (B) (taken at the locations marked in Figure 6.1A). (C) FFT of (A). The features marked by "1" are located at a reciprocal distance from the origin of $a_1 = 5.69 \text{ nm}^{-1}$ and form a hexagon (white dashed line). The directions of the Brillouin zone ΓM (blue) and ΓK (green) are given by the arrows. (D) FFT of (B). The characteristic features "1" and "2" are described in the text. (E) Schematics of the hexagonal lattice of BiAg₂ corresponding to the measurement showing the alloy from the side view (upper part) and top view (lower part). The arrows indicate the crystallographic orientations of the surface. Parameters: $I_{\text{set}} = 1 \text{ nA}$, $V_{\text{bias}} = 10 \text{ mV}$ (A, B).

6 Bottom up constructed YSR-chains on a superconducting Rashba surface

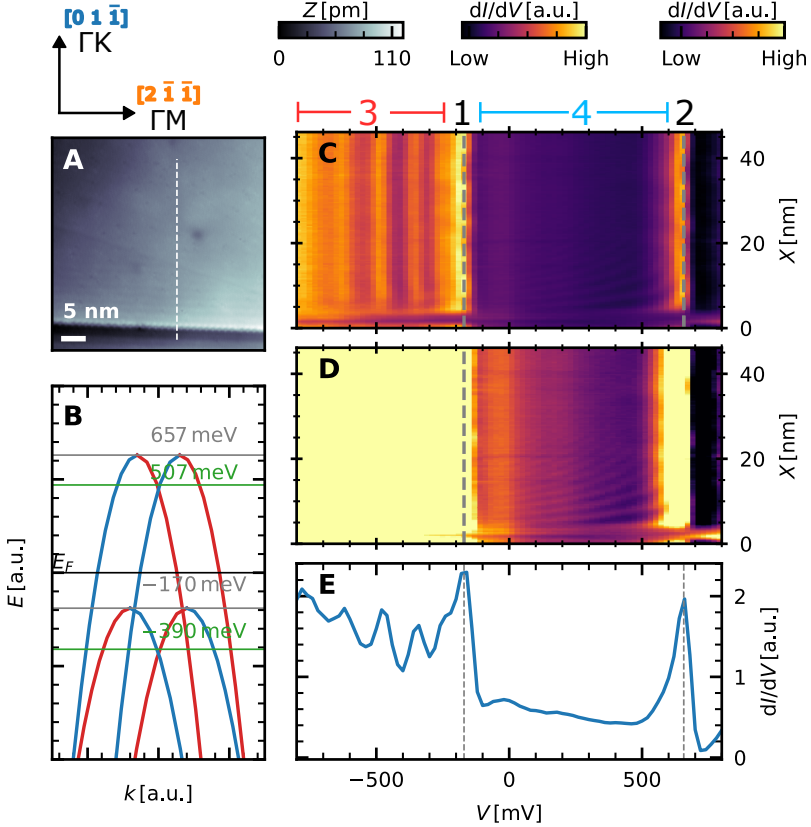


Figure 6.3: Spectroscopy on BiAg₂ surface: (A) Constant-current STM measurement of the BiAg₂-alloyed surface with line a defect. (B) Illustration of the BiAg₂ surface band dispersion as a function of k with blue and red depicting the different spin polarities of the bands (with the calculated spin topology taken from [177]). The grey lines mark the energies of the vHS. The green lines correspond to the Rashba energies of the respective bands $E_{R,1} = 507$ mV and $E_{R,3} = -390$ mV. (C, D) Spectroscopic line profile taken along the white dashed line in (A). The blue dashed lines at $V_1 = -170$ mV and $V_1 = 657$ mV mark the energetic positions of the vHSs, depicted in (B). (E) Bias spectroscopy taken above the line defect in (A). Parameters: $I_{\text{set}} = 1$ nA, $V_{\text{bias}} = 50$ mV (A), $I_{\text{stab}} = 0.8$ nA, $V_{\text{stab}} = 800$ mV, $V_{\text{mod}} = 20$ mV and feedback: on (C-E).

6.1 Topographic and spectroscopic properties of BiAg₂ on Ag(111)/Nb(110)

picted in Figure 6.3. Panel (A) displays the area's topography near a line defect of the island, which shows a peak-to-peak height difference of approximately 95 nm.

The spectroscopic line profile is presented in panel (C, D), with an example of a single-point spectrum on the terrace in panel (E). By comparing the direction of the line with the lattice structure, we extract that this measurement was taken along the ΓM -direction of the crystal [178]. The spectral data shows four distinct peak features. One can be found at -170 meV (1) and one at 657 meV (2). Both do not vary as a function of position X . Below the peak (1), we can find a series of equidistant peaks, which also do not vary as a function of X (3). Finally, there is a series between peaks (1) and (2), which shift in energy as a function of the position (see panel (D)) (4). Given that these peaks vanish upon reaching the line defect, their presence can be attributed to the sample rather than the tip.

Peaks (1) and (2) bear characteristic features consistent with spectra previously measured on the BiAg₂-alloy [168]. This phenomenon can be understood by considering the dispersion relation of the Rashba-split surface state, illustrated schematically in panel (B). The dispersion is made up of two pairs of Rashba-split bands. The first pair of bands is located at higher energies. The second pair of bands is located at lower energies entirely below E_F . Since the first pair encloses the second pair of bands, we refer to the first pair as *outer bands* and the second pair as *inner bands*. While the outer bands can be well-approximated by two shifted quadratic functions, the inner bands, in reality, have a much more complex

structure, as most recent works suggest [178]. Despite this difference, we can still use this simplified model to interpret the spectra in (C) and (E).

In k-space, we have a uniform distribution of electron states. If the parabolic dispersion relation is now Rashba-split in k-space, tunneling at the energetic positions of the band onset leads to a peak in the dI/dV -signal [175]. This way, we can read out the onsets of the pairs of subbands, which is at $E_{0,1} = 657$ meV for the outer bands and at $E_{0,2} = -170$ meV for the inner bands. These values are lower than the ones reported in the literature ($E_{0,1} = 731$ meV in Ref. [178], $E_{0,1} = 725$ meV in Ref. [179] and $E_{0,2} \approx -130$ meV [168] and $E_{0,2} \approx -110$ meV [179]). One possible explanation for this discrepancy could be a strain-related effect. When Ag(111)-islands are grown on the Nb(110) surface at elevated temperatures, thermal strain can be induced when the sample is cooled down due to different thermal expansion coefficients of Nb and Ag [124]. This strain can shift the band bottom of the Ag(111) surface state [107, 180–182]. In the same way, the surface state of BiAg₂ grown on Ag(111)/Nb(110) could be influenced by the strain in the Ag(111)-island, leading to a shift of the band edges compared to a BiAg₂ surface grown on a Ag(111) bulk crystal.

The remaining analysis and explanation of the series of peaks will be given in Section 6.3 for (3) and 6.2 for (4).

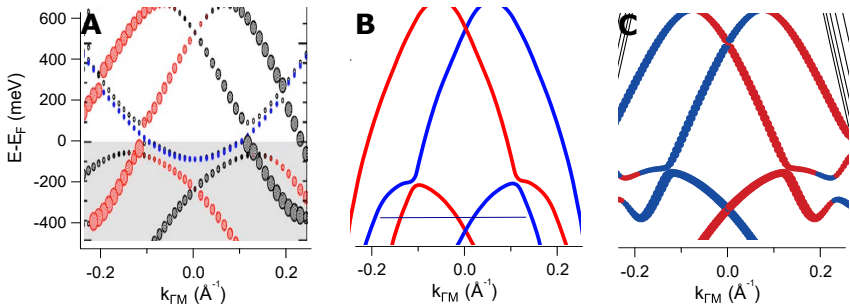


Figure 6.4: Rashba surface band structure according to different sources in literature: (A) Calculated BiAg₂ surface band structure taken and refined from [177]. The red and black colors depict the different directions of the spin-polarization. The blue line depicts the Ag-surface state band. (B) Proposed BiAg₂ surface band structure as proposed in [179]. (C) Calculated BiAg₂ surface band structure as reported in [178]. The blue and red colors depict the different spin-polarization directions.

6.2 Scattering patterns on the BiAg₂ surface

The series of peaks labeled as (4) in Figure 6.3C/D are the ones that we observed in the spectroscopic line profiles on the Ag(111) surface in Figure 4.6 in Chapter 4. These are similar to the Ag(111) peaks, originating from the QPI of the BiAg₂ surface state. This section will take a closer look at these QPI patterns.

Modelling the Rashba-split bands of BiAg₂

To understand the QPI patterns of the Rashba surface states, we will use a simple model for the Rashba-split surface bands. Figure 6.4 shows a selection of these proposed spin-polarized BiAg₂ dis-

persions reported in the literature. Starting with the first example in panel (A), we see that the surface band dispersion of BiAg₂ is mainly made out of two pairs of subbands, which are shifted in k . One pair has its onset at around 600 meV. These bands are the p_{xy} -type bands [183] and will be referred to as the *outer bands*. The other pair of subbands (sp_z) has its onset at around 100 meV and will be referred to as the *inner bands*. As we can see, the dispersion relation is not a classical Rashba-type dispersion relation. First, we can see that the parabolas are all turned upside down by a negative effective mass. In addition, we see that the spin polarization for each parabola changes the more we get to the maximum of the band. The next example in panel (B) shows another example of the BiAg₂ dispersion relation. Here, the split parabolas have a constant spin polarization. However, the bands show an avoided crossing at the intersection between the inner and outer bands. The last example in panel (C) again shows bands in which the spin-polarization changes. However, in this calculation, the bands show a more complex band shape for the inner bands, which is strongly distorted from a usual parabola. We will assume a surface band dispersion for our models like the one shown in (A). On the one hand, this simplifies the modeling as it can be done by just making use of quadratic functions, and on the other hand, there are results measured by angle-resolved photoemission spectroscopy (ARPES) that support the work in (A) [183].

The Hamiltonian referring to a system with Rashba-spin-orbit-interaction was already given in Chapter 2. For simplicity, we will assume that our system can be approximated by a quasi-free electron gas with Rashba interaction. As a result, the energy bands

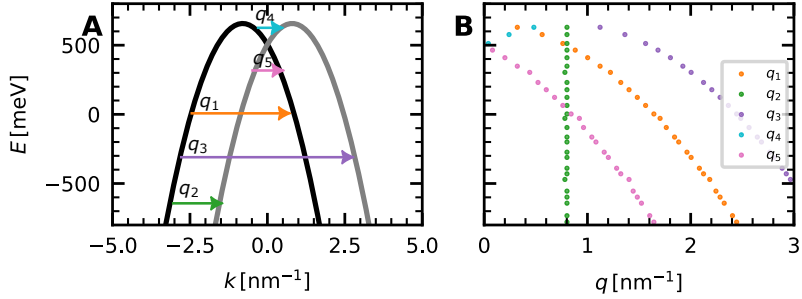


Figure 6.5: Rashba-split surface band model: (A) Dispersion relation of a Rashba-split quasi-free electron gas. (B) Scattering q_i vectors as a function of the energy calculated from the dispersion in (A). Simulation parameters: $m_1^* = -0.16m_e$, $k_{0,1} = 0.8 \text{ nm}^{-1}$, $E_0 = 0.657 \text{ eV}$.

are spin-split in the k -component. To understand the scattering patterns, we first approximate our system with the dispersion relation given by Equation 2.21. For the outer bands, we use $m_1^* = -0.16 \text{ meV}m_e$ and $k_{0,1} = 0.8 \text{ nm}^{-1}$ (taken from Ref. [178]). For the inner bands we used $m_2^* = -0.35 \text{ nm}^{-1}m_e$ and $k_{0,2} = 1.3 \text{ nm}$ (taken from Ref. [175]). $E_{0,1} = 0.657 \text{ eV}$ and $E_{0,2} = -0.170 \text{ eV}$ were determined by reading out the energetic position of van-Hove singularities (vHS₁ and vHS₂).

The result can be seen in Figure 6.5A. With the modeled dispersion relation, we can calculate the different scattering vectors by calculating the difference in k between the individual branches of the parabolas. When we do this for each energy value, we end up with the scattering vectors as a function of the energies seen in panel (B). We can use this as a first approximation to understand

our results for parabolically shaped dispersion relations. However, when it comes to the inner bands, which for our case start at $E \approx -170$ meV (see Figure 6.3), the bands deviate from the parabolic shape. This has been reported from experimental [178, 179] as well as theoretical side [177]. Note that the spin dependence of the scattering has been neglected so far.

Extracting scattering vectors from spectroscopic line profiles

We delve into a spectroscopic line profile's FFT, as depicted in Figure 6.6. By performing a FFT on the real space wave pattern of Figure 6.3C for each energy slice in the spectroscopic line profile, we can visualize the scattering processes observed in the QPI.

The resulting FFT signals, shown in Figure 6.6, are plotted against energy on the horizontal axis and the calculated scattering vector q on the vertical axis. Notably, a prominent scattering branch, indexed by q_1 , originates at the first Van-Hove singularity at $E_{0,1} = 657$ meV. However, after crossing $E = 0$, this branch either diminishes or vanishes entirely. Additionally, a less pronounced scattering branch, q_3 , emerges from the first Van-Hove singularity but is shifted in q compared to q_1 . Around $E \approx 450$ meV, another feature, which, however, does not show a clear dispersion, q_5 , manifests. Lastly, just below $E_{R,1}$, a feature denoted as q_4 , which has an inverted slope compared to q_1 and q_3 , is evident. Panel (B) displays the model outlined in section 6.2, where we utilize the energetic positions of the Van-Hove singularities from bias-spectroscopy measurements to determine the values for $E_{R,1}$

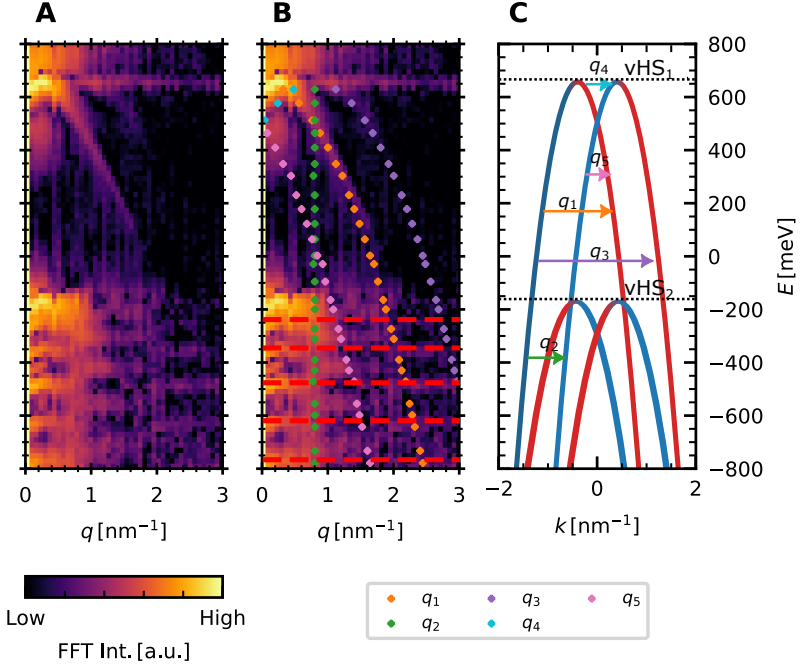


Figure 6.6: Electron scattering processes at a BiAg₂ line defect: (A) Fourier Transform of the spectroscopic line profile in Figure 6.3C. (B) Calculated scattering branches, plotted on top of the data of (A), obtained using the simple band structure model shown in (C). The scattering processes are shown as arrows in (C). Red lines depict the position of the series of peaks labeled as (3) in Figure 6.3. (C) Simplified band structure of BiAg₂. The k -splitted bands are modeled as quadratic functions. Simulation parameters: $m_1^* = -0.16m_e$, $k_{0,1} = 0.8 \text{ nm}^{-1}$ (taken from Ref. [178]), $m_2^* = -0.31m_e$, $k_{0,2} = 1.3 \text{ nm}^{-1}$ (taken from Ref. [175]), $E_{0,1} = 0.657 \text{ meV}$ and $E_{0,2} = -0.17 \text{ meV}$ extracted from 6.3E.

and $E_{R,2}$ and incorporate them into our model.

Analyzing the possible scattering vectors without presuming a specific spin texture of the bands reveals that a constant q -vector should displace the scattering vectors q_1 and q_3 . Assuming these scattering vectors correspond to what was marked in panel (A) as q_1 and q_3 enables us to determine the shift in q between these two parabolas, consequently yielding a value for the Rashba-splitting k_0 . Utilizing the theoretical values for the band structure, we compute the possible scattering vectors. Panel (B) displays the scattering vectors q_i as a function of energy overlaid on the data depicted in panel (A).

Comparing the experimental values with the theoretical ones reveals an astonishingly accurate similarity, at least for the scattering branches q_1 and q_3 . However, due to the complexity of the signals, it's challenging to discern anything meaningful for processes below E_F .

The scattering vector labeled q_2 might correspond to the continuous line of constant intensity observed for different energy values at $q = 0.8 \text{ nm}^{-1}$. Upon reviewing the scattering vectors, it becomes apparent that the most evident scattering processes are observed for q_1 ; q_3 is only observed in a very limited energy range below $E_{vHS,1}$, and q_5 only at E_{vHS} . The non-spin-flip scattering process q_2 is nearly nonexistent for energies between E_F and E_{vHS} .

This observation aligns with the one reported in [178], assuming the complex band structure. According to that interpretation, scattering processes in the q -direction involve a change of orbital an-

gular momentum at the step edges. This change requires the electrons to flip their spin to compensate for the altered orbital angular momentum, maintaining the conservation of total angular momentum.

Additionally, the report suggests that scattering processes may depend on the scattering direction. However, in the FFT of the spectroscopic line profile, we can only observe what is happening in one direction. To observe the direction dependence of the scattering patterns, we need to record 2D-QPI maps, as discussed in the next section.

Quasi-particle interference patterns on BiAg₂

As previously mentioned, spectroscopic maps of the surface provide valuable insights into the scattering behavior of the surface band electrons of the sample. This is illustrated in Figure 6.7 for three different energies. In panel (A), we observe the topography of the investigated area, which includes the edge of the island on the top and a line defect on the left side, serving as scattering centers for the QPI measurements. These objects are oriented perpendicular to each other, allowing for scattering processes from the x - and y -directions. Recording dI/dV -maps at different energies enables the acquisition of various scattering patterns, as depicted in panels (C-E). These panels demonstrate that the wavelengths of the scattering patterns increase with the energy. We perform a Fourier transform of these patterns to get more quantitative insights. Given the 6-fold symmetry of our sample, the resulting

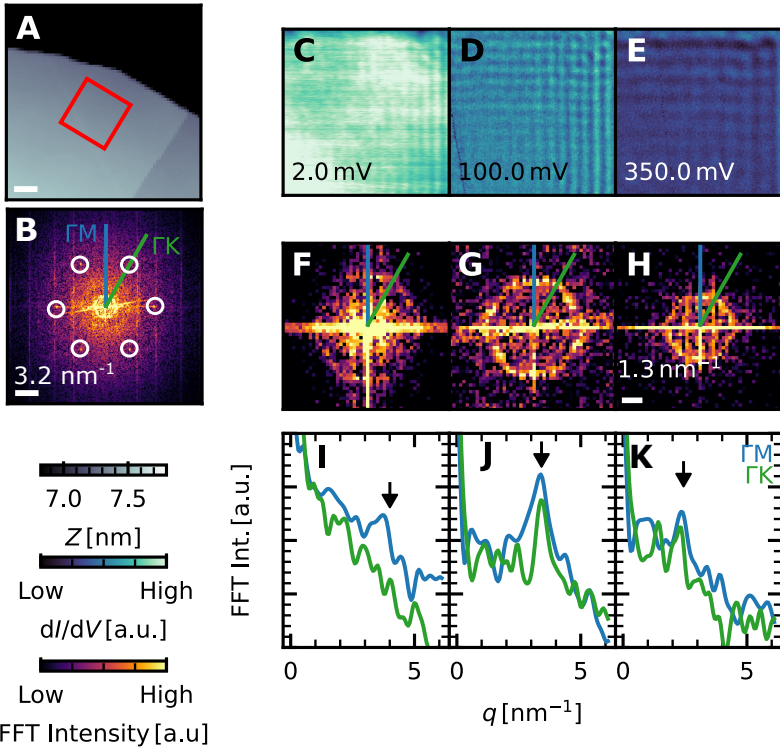


Figure 6.7: QPI on the BiAg₂ surface: (A) Constant-current STM measurement of the BiAg₂ island with the red square depicting the area in which the data shown in (C-E) was recorded. (B) FFT of the real space patterns shown in (D) on a large scale in k-space, showing the Bragg spots of the BiAg₂-lattice. (C-E) Constant-current dI/dV-maps showing the quasi-particle interference patterns. (F-H) Zoomed-in FFT of the real space patterns shown in (C-E). The color-coded, radial lines depict the position of the line cuts shown in panels (H-J). (I-K) Radial line cuts taken from the center point of the FFTs for different directions of the BZ (blue: ΓK and green: ΓM). The arrows correspond to the hexagonal feature seen in (F-H). Parameters: $V_{\text{bias}} = 2 \text{ mV}$ (B), 100 mV (C), 350 mV (D) and $I_{\text{set}} = 1 \text{ nA}$ (B-D)

FFT pattern should exhibit this exact symmetry. The directions of the k -space can be deduced from the Bragg spots of the FFT, as shown exemplarily in panel (B). This way, we can relate the BiAg₂ lattice orientation with the features of the QPI. To see these features, it is necessary to zoom in on the FFTs as shown in panels (E-G). Here, the FFTs of the data shown in (C-E) are presented. To increase the FFT quality, the data was first multiplied by a Hamming window before the FFT process [184]. This decreases the intensity of artifacts that occur due to finite-sized arrays. However, with this process, it was not possible to eliminate these artifacts completely, as we can see by the high-intensity lines along $q_x = 0$ and $q_y = 0$. The results for the FFT show a hexagonal pattern for panels (F-H). However, the size of the hexagon decreases as the energy increases. This can be seen even clearer in the line cuts shown in panels (I-K), where the black arrow indicates the position of this feature. The feature exists for both directions; however, the q value for this peak is slightly larger for the ΓK - than the ΓM -direction. These features in the FFT patterns correspond to scattering branches of the BiAg₂ surface alloy. Comparing this feature with the FFT of the spectroscopic line profile in Figure 6.6, we observe that the prominent hexagon corresponds to the scattering vector q_3 . Although additional features exist inside the hexagon, they are obscured by the oversaturated signal and are not discernible.

In Figure 6.8, I present the entire set of Fourier transformed dI/dV -maps recorded in the area depicted in Figure 6.7A at different energies. In contrast to the data presented in Figure 6.7, noticeable differences emerge across different bias voltages.

6 Bottom up constructed YSR-chains on a superconducting Rashba surface

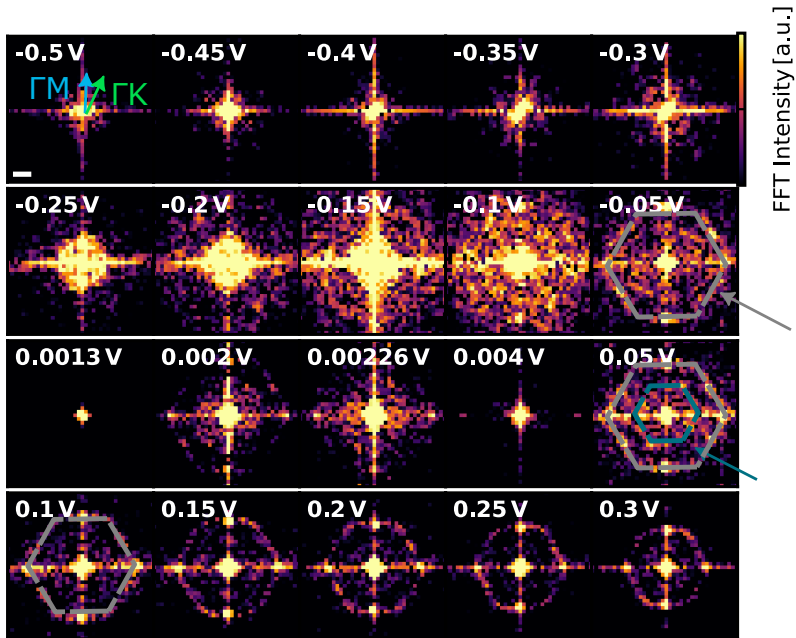


Figure 6.8: Complete set of FFT-QPI on BiAg₂: FFT of dI/dV -measurements performed within the area shown in Figure 6.7 for different energies. The scale bar in the first panel corresponds to 1 nm^{-1} . The colored hexagons correspond to and point out certain scattering features, which are described in the text.

At $V_{\text{bias}} = 50 \text{ mV}$, a ring-shaped or curved-out hexagon is evident (grey), with its edges converging towards the origin as the energy increases to $V = 300 \text{ mV}$. However, the distinct hexagonal pattern becomes progressively washed out. Conversely, identifying the hexagon or ring as a hexagonal feature becomes challenging at $V_{\text{bias}} = 0.05 \text{ V}$. Furthermore, at $V_{\text{bias}} = 0.05 \text{ V}$, an additional feature at smaller q -values ($q \approx 1.9 \text{ nm}^{-1}$) is apparent (teal), which could correspond to the scattering vector q_5 . The measurements obtained at $V_{\text{bias}} = 1.3 \text{ mV}$ and $V_{\text{bias}} = 2 \text{ mV}$ were conducted within the superconducting gap. We will discuss the superconductivity related observations as part of Section 6.4.

The features represented as hexagons in the reciprocal space indicate that the band structure of BiAg_2 is anisotropic. This effect, known as warping, has been reported in [179], as well as for similar systems such as BiCu_2 [185, 186].

6.3 Quantum well states

In this section, we take a closer look at the series of peaks that are labeled as (3) in Figure 6.3. In Figure 6.9A, the same bias-spectroscopy measurement as in Figure 6.3E is shown, but with arrows marking the energetic position of these peaks. The labels correspond to the index n of the peak. In panel (B), the peaks' V_{bias} values are plotted as a function of n . This plot shows that the peaks are equidistantly distributed on the V_{bias} -axis. This is further proven by the linear regression through these points. The spectrum shown here with the peak structure differs from the ones

6 Bottom up constructed YSR-chains on a superconducting Rashba surface

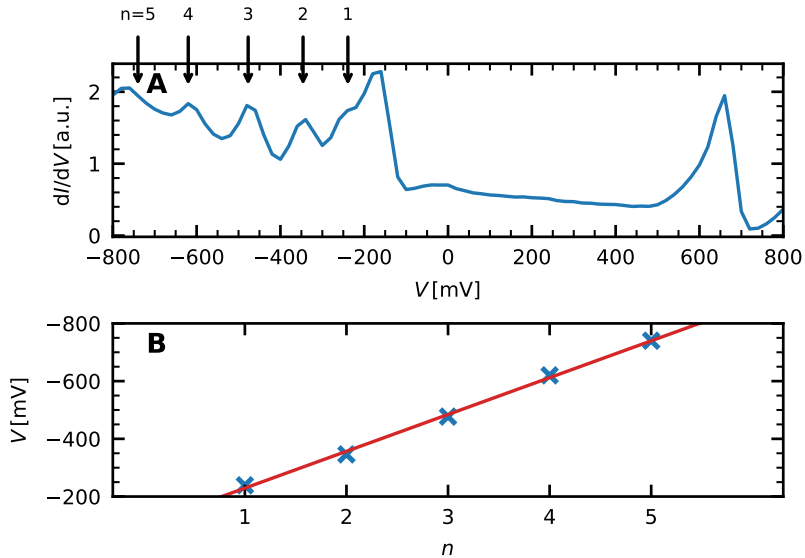


Figure 6.9: Spectroscopy on the BiAg₂ surface: (A) Same data as shown in Figure 6.3E with the labeled arrows depicting the positions of the peaks on the V_{bias} -axis. **(B)** V_{bias} -values of the peaks as a function of n (blue), read out from (A), with a linear regression (red). Fitting parameters: slope $m = -127.6 \pm 3.3 \text{ mV}$, intersection $V_0 = -101.6 \pm 11.0 \text{ mV}$ (B)

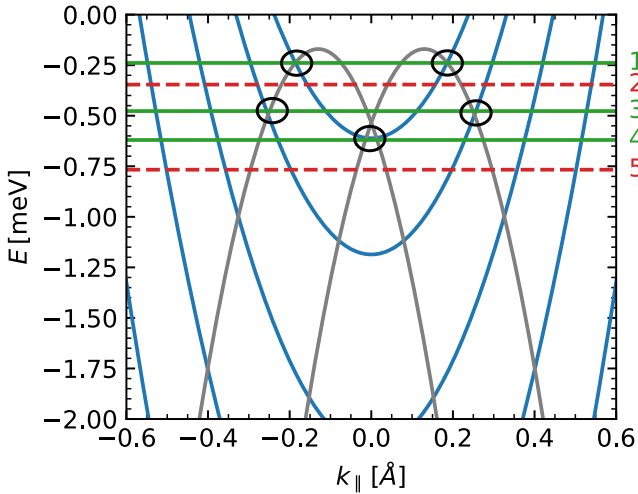


Figure 6.10: Intersection points between fitted QWS and Surface state dispersion: The quantum well state dispersion is depicted in blue, while the grey parabolas depict the dispersion of the inner BiAg₂ surface bands (see also Figure 6.3). The energetic position of the measured peaks (see Figure 6.9) are depicted as horizontal lines, where the green ones correspond to energies where an intersection between the QWS and the surface band can be found (black circles) and red corresponds to the ones where none is found. Simulation parameters: $m_{z,QWS}^* = -0.5m_e$ (taken from Ref. [187]), $d = 3.945$ nm, $E_{0,QWS} = -420$ meV. For the parameters of the surface state dispersion, see Figure 6.3.

reported in Refs. [178, 179].

Different from the cases of Refs. [178, 179], the underlying Ag(111) was grown as thin film [188, 189] on the Nb(110)-surface. For Ag thin films, QWSs can form inside the Ag-bulk along the z -direction [187, 190]. Here, the surface and the interface between the Ag and the underlying Nb(110)-substrate act as boundaries, and the bulk electrons of the Ag are reflected, forming standing waves. This confinement effect is similar to what we have seen in the corrals built on the Ag-surface; however, this confinement occurs naturally inside the Ag-bulk and goes along the z -direction instead of the xy -plane.

To model the energetic positions of these QWSs, we start with a similar approach described in Ref. [187]. Possible wavelengths of the QWSs λ_{QWS} are given by the quantization condition:

$$\lambda_{\text{QWS},z}n = d, \quad (6.1)$$

with the thickness of the Ag island d and an integer number n . We assume a quasi-free electron dispersion for the QWS, which is valid as the QWS appears inside the Ag bulk. We split the dispersion into a contribution coming from the movement of the electrons parallel to the surface and the movement perpendicular to it:

$$E_{\text{QWS}}^{(n)} = \frac{\hbar^2 k_{\parallel}^2}{2m_{\parallel}^*} + \frac{\hbar^2 k_z^2}{2m_{z,\text{QWS}}^* d^2} + E_0 \quad (6.2)$$

Here k_{\parallel}^2 refers to the k vector component and m_{\parallel}^* to the effective mass of the electrons moving parallel to the surface. k_z refers to

the k vector component and m_z^* to the effective mass along the z -direction, and E_0 refers to an energetic band offset. We use Eq. 6.1 to deduce an expression for k_z :

$$k_z = \frac{2\pi}{\lambda_{\text{QWS}}^z} = \frac{2\pi n}{d} \quad (6.3)$$

This can be plugged into Eq. 6.2:

$$E_{\text{QWS}}^{(n)} = \frac{\hbar^2 k_{\parallel}^2}{2m_{\parallel, \text{QWS}}^*} + \frac{(2\pi\hbar)^2 n^2}{2m_{z, \text{QWS}}^* d^2} + E_0 \quad (6.4)$$

With this formula, we can reproduce the QWSs reported in Ref. [187] for islands with a similar thickness (≈ 15 MLs). The results reported in this reference are based on ARPES-measurements, which refer to the binding energies. Therefore, the sign of the energy scale compared to our formalism is switched. For $m_{z, \text{QWS}}^*$ we take the value reported in [187]. For $m_{\parallel, \text{QWS}}^*$, we assume the same value as for the inner surface state bands. E_0 is fitted in such a way that the minimum of the QWS with $n = 1$ is at around -0.5 eV leading to $E_0 = -420$ meV. With the dispersion relation for the QWS, we can now compare this to the inner surface state bands of BiAg₂ and the energetic positions of the peaks from Figure 6.9. The results in Figure 6.10 show that some of the peaks (1,3 and 4) are located at energies, for which the surface bands and a QWS intersect, while for the peaks 2 and 5, we can not find any intersecting area between the surface state and the QWS.

As reported in Refs. [187, 190] the intersection between the (s, p_z)

type bands and the QWS leads to hybridization, opening up a gap in both bands. If this is true, this might be an explanation for the peaks since such a gap can lead to vHSs with an increased LDOS around the gap.

Furthermore, by looking closely at the energetic position of the peaks in Figure 6.3A/B, we can see that the series of equidistantly spaced peaks alternate slightly in energy as a function of q at $q \approx 0.8 \text{ nm}^{-1}$ and $\approx 1.9 \text{ nm}^{-1}$. This hints towards more physical phenomena that must be understood to fully explain the peak series' appearance.

6.4 Proximity induced superconductivity on BiAg₂

In this part of the chapter, we will examine the superconductivity proximitized in the BiAg₂ surface alloy.

As we saw in Chapter 4, the Ag islands should be thin enough to be proximitized by the superconductivity of the underlying Nb-substrate. As we learned, it is essential to distinguish between bulk and surface-state superconductivity. Even for islands with thicknesses well above the coherence length of Nb, superconductivity can still be induced on the surface if the island's interior is within the clean limit, allowing for ballistic electron transport to the surface [191].

Spectroscopy measurements at 4.2 K

In the preceding section, we observed that the LDOS on the surface, and consequently the scattering patterns, enormously diminish in intensity as we approach the low-energy bias region (see Figure 6.8). We focus on spectroscopy in the low-energy range around E_F to investigate the sample's superconductivity.

Interestingly, a scattering feature with a hexagonal shape is observable at $V_{\text{bias}} = 2$ mV. This observation is unexpected, as one would not anticipate states inside of the superconducting gap. Typically, such states would originate from YSR-states, which can be excluded in this scenario, as no magnetic impurities were deposited onto the sample. An alternative explanation could involve MSSs, akin to those observed in Chapter 4.

6 Bottom up constructed YSR-chains on a superconducting Rashba surface

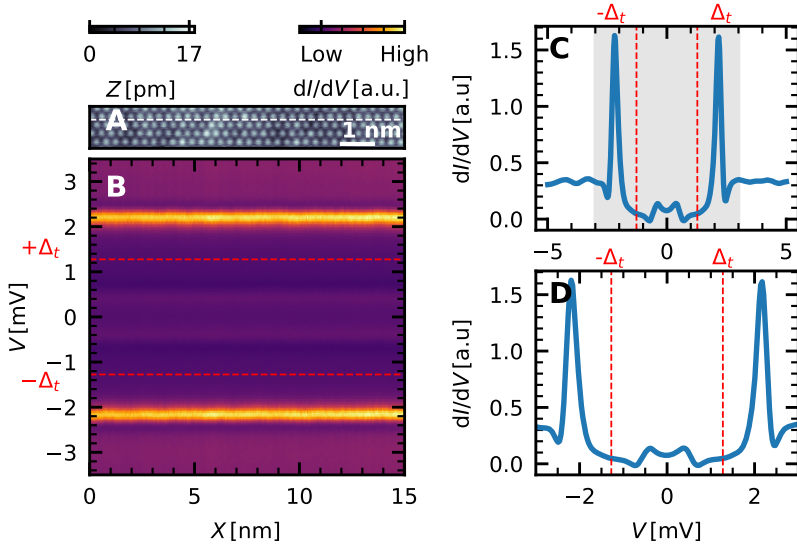


Figure 6.11: Proximitized superconductivity of BiAg₂ on Ag/Nb: (A) Constant-current STM measurement of BiAg₂ with the white dashed line depicting the location of the spectroscopic line profile in (B). (B) Spectroscopic line profile measured along the white dashed line in (A). The red-dashed lines depict the tip gap values. (C) Spectroscopic line profile averaged along the line of measurement shown in (B). The grey area depicts the bias range of the zoom-in shown in the panel below. The red dashed lines mark the tip gap value at $\pm\Delta_t = \pm 1.275$ meV. Parameters: $I_{\text{set}} = 500$ pA, $V_{\text{bias}} = 5$ mV (A), $I_{\text{stab}} = 500$ pA, $V_{\text{stab}} = 5$ mV, $V_{\text{mod}} = 200$ mV (B).

The spectroscopic data of the surface is shown for the energetic region around E_F in Figure 6.11. In panel (A), we see the region's topography. The topography shows no surface defects, and the surface shows a clear BiAg₂-lattice. The spectroscopic line profile in the area looks homogeneous for each point along the surface, as shown in (B). We observe two distinct peaks at ± 2.18 meV. Between those two peaks, the LDOS decreases drastically. Inside the gap around $V_{\text{bias}} = 0$ meV, two minor peaks appear at ± 0.37 meV. Since the spectroscopic line profile suggests that the measurements are homogeneous for each point over the whole line, we average over the whole line to get a more distinct look at the peak structure.

To interpret the gap spectrum, we consider that the gapped LDOS of the superconducting tip affects the spectrum. In that case, the outer peaks are interpreted as the dGSJ-states, which appear at $\pm(\Delta_t + \Delta_s)$. The inner peaks around $V_{\text{bias}} = 0$ meV are the thermal resonances discussed in 3.4. All the spectra were bias-offset corrected by reading out the coherence peaks caused by the dGSJ-states. We extracted the parameters for the tip gap and the sample gap by modeling the LDOS of the tip and the sample using two Dynes functions, as we did in the preceding chapters with Equation 3.9. We found the tip gap to be $\Delta_t = 1.28$ meV and the sample gap to be $\Delta_s = 0.90$ meV, which is about 60 % of the superconducting gap of Nb and 68 % of the NbO_x-gap that we extracted from the measurements in Chapter 4. The tip gap energy is depicted as red dashed lines in each spectroscopy measurement. The dGSJ-state can be read out at $\pm(\Delta_g + \Delta_s) = \pm 2.18$ meV.

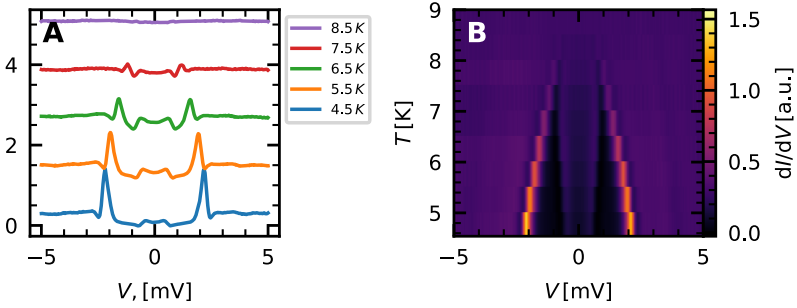


Figure 6.12: Temperature dependent point spectra taken on BiAg_2 on Ag/Nb(110) : (A) Bias-spectroscopy measurements on BiAg_2 on Ag/Nb for different temperatures, as stated in the legend. (B) Evolution of the bias-spectroscopy measurements with temperature T . Parameters: $I_{\text{stab}} = 1 \text{ nA}$, $V_{\text{stab}} = 10 \text{ mV}$, $V_{\text{mod}} = 100 \text{ } \mu\text{V}$, feedback: on.

We can see that even though there is a superconducting gap, the LDOS inside of the gap is not completely flat. This is in accordance with the dI/dV -maps shown in Figure 6.8 taken at energies inside the gap ($V_{\text{bias}} = 1.3 \text{ mV}$ and $V_{\text{bias}} = 2 \text{ mV}$), which show a finite signal even for energies inside the gap. With the knowledge of the interaction between surface states and a superconducting substrate from Chapter 4, these excitations could be caused by MSSs.

Temperature dependence of the sample gap

Another way to verify whether the gap observed in Figure 6.11 is due to the proximitized superconductivity from the underlying Nb-substrate is to examine the evolution of the gap with temper-

ature T . If the gap is due to proximitized superconductivity, we expect it to decrease as the temperature increases.

To investigate this, we performed bias-spectroscopy measurements on the BiAg₂ alloy at different temperatures. The results are shown in Figure 6.12. In panel (A), we can see the bias-spectroscopy data for different temperatures between $T = 4.54$ K and 9 K. At $T = 4.54$ K we see the coherence peaks at ± 2.18 meV. At $T = 6$ K we see the coherence peaks appearing at ± 1.77 meV. At $T = 7.5$ K, the peaks shift to ± 1.2 K. Finally, at $T = 9$ K, the peaks disappear almost entirely.

In panel (B), the evolution of the superconducting gap with temperature is displayed as a waterfall plot, illustrating how the spectral features change as the temperature increases. It becomes apparent that the outer peaks ($\pm\Delta_t + \Delta_s$) almost linearly decrease in energy as a function of temperature. However, the inner peaks as thermal resonances increase in energy as the temperature increases. Notably, this increase is not entirely linear.

We must consider that we are observing tunneling between two superconducting electrodes, both of which exhibit a superconducting LDOS influenced by temperature. As the temperature increases, both gaps will gradually close. The tip and the sample electrode do not have the same gap size. At low temperatures, we observe both gaps in our bias-spectroscopy measurements. As the temperature rises, both gaps gradually close. At a specific temperature (denoted as T_1), the gap of one electrode will be completely closed while the superconductivity in the other electrode remains. Consequently, we will only see the superconducting gap of the re-

6 Bottom up constructed YSR-chains on a superconducting Rashba surface

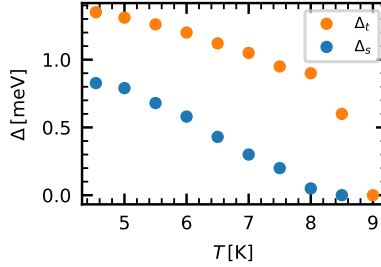


Figure 6.13: Δ_t and Δ_s as a function of T . Δ_t and Δ_s extracted from the bias-spectroscopy measurements shown in Figure 6.12 by fitting the spectrum with Eq. 3.8. Fitting parameters: $\gamma = 0.05 \text{ meV}$, $I_{0,t} = 0.5 \text{ m}^{-3} \text{ meV}^{-1}$, $I_{0,s} = 0.55 \text{ m}^{-3} \text{ meV}^{-1}$,

maining electrode closing as the temperature increases. This results in a kink in the superconducting gap's evolution as a function of temperature.

To quantify this, we can fit the spectra for each temperature with the model introduced in Chapter 3.4. This way, we can extract the values for the tip gap Δ_t and the sample gap Δ_s for each bias-spectroscopy measurement in the temperature-dependent data set. The result is shown in Figure 6.13. We can see that both gaps decrease with increasing temperature. Since Δ_s is smaller than Δ_t , Δ_s disappears first. Then, right below 9 K, also the superconducting gap Δ_t goes to zero. It should be noted that for these simulations, the superconducting electrodes are described by BCS-theory. However, this is not necessarily true for a sample, such as the BiAg₂ surface alloy, which has a strong SOC.

6.5 Single Fe-atoms on BiAg₂

In the previous sections, we demonstrated the successful growth of a Rashba material on a superconducting substrate. Specifically, we showed that the surface alloy grown on a Ag(111) surface atop Nb(110) exhibits a strong proximity effect. With what we have learned from the previous parts, we are finally ready to investigate a system that brings together all the components of topological superconductivity. With the use of atom manipulation techniques we can assemble the atomic structures atom-by-atom and tailor the interactions between them to our needs. In this section, we deposit Fe-atoms onto the BiAg₂ surface. We investigate the different adsorption sites of these Fe-atoms and look at their spectral properties.

To build a YSR-chain on the high SOC surface, it is necessary to find magnetic atoms that exhibit YSR-states, ideally far inside the gap. The energies of the YSR-states vary with the Fe adsorption sites. So, the first step to building Shiba-chains is to classify the YSR-states of the magnetic atoms.

Adsorption of individual Fe-atoms on BiAg₂

Individual Fe-atoms were deposited onto the BiAg₂ surface through cold deposition (see Figure 6.14). The distribution of the Fe-atoms appears statistically uniform across the surface. Upon examining the reference lattice of the substrate, we can identify two distinct adsorption sites for the Fe-atoms. The first adsorption site is illus-

6 Bottom up constructed YSR-chains on a superconducting Rashba surface

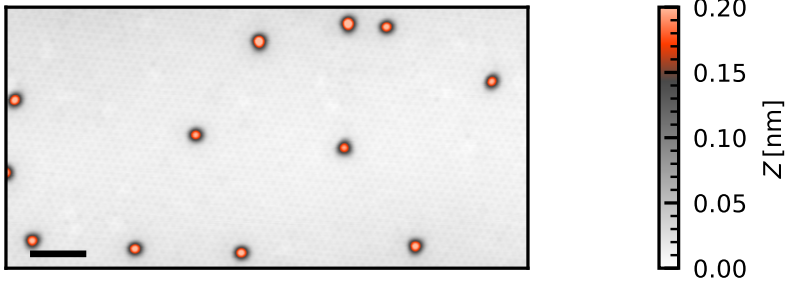


Figure 6.14: BiAg₂ surface after Fe deposition. The black line corresponds to 3 nm. Parameters: $I_{\text{set}} = 50 \text{ pA}$, $V_{\text{bias}} = 5 \text{ mV}$. Temperature during deposition was $< 10 \text{ K}$.

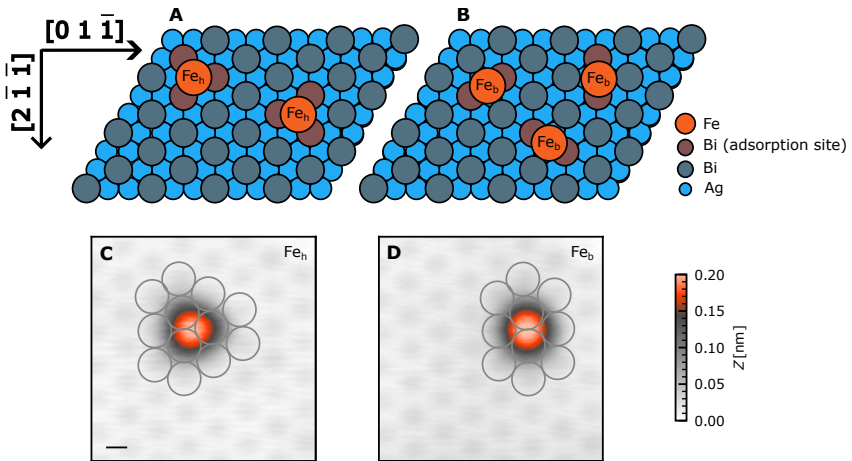


Figure 6.15: Schematic of Fe adsorption sites on BiAg₂ (A, B) Schematics showing Fe-atoms on the hollow adsorption site (Fe_h) (A) and on the bridge adsorption site (Fe_b) (B). (C, D) Constant-current STM images of an Fe-atom adsorbed on a hollow site (C) and a bridge site (D). The grey circles represent the Bi-lattice underneath. The black line corresponds to a length of 300 pm. Parameters: $I_{\text{set}} = 1 \text{ nA}$, $V_{\text{bias}} = 5 \text{ mV}$ (C, D).

trated in Figure 6.15A. The model shows that the Fe-atoms are adsorbed on a site, which is threefold coordinated by Bi-atoms. The underlying Bi-atoms form a triangle. As the schematic shows, we can reach that by two different configurations, with the triangle either pointing upwards or downwards. This configuration will be called the *hollow site* (Fe_h). The average height of the Fe-atoms at the hollow site is ≈ 176 pm, and the constant-current STM-image resembles a triangular shape.

The second type of adsorption site is depicted in Figure 6.15B, accompanied by its schematic. The Fe-atom resides on the connecting line between two Bi-atoms, i.e., it is twofold coordinated. The schematic drawing shows the three different possible orientations of this kind of site. We will refer to this site as the *bridge site* (Fe_b). The Fe-atoms at the bridge sites have an average height of ≈ 186 pm and resemble an elongated shape in the STM image.

At V_{bias} of approximately 5 mV and currents above 20 nA the Fe-atoms can be moved along the surface. By manipulating the atom on the surface, we found that Fe-atoms predominantly prefer the bridge sites: While positioning Fe-atoms onto the bridge sites is relatively straightforward, placing them onto the hollow sites requires multiple careful attempts and the adjustment of various parameters. Additionally, applying voltages of 1 V or higher can cause Fe-atoms initially located at the hollow sites to hop onto a bridge site.

6 Bottom up constructed YSR-chains on a superconducting Rashba surface

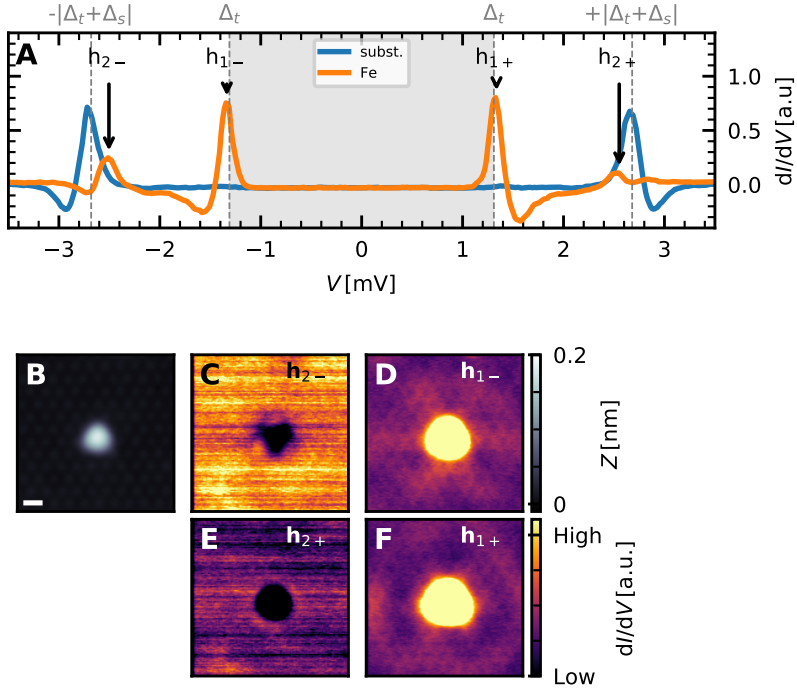


Figure 6.16: In-gap states of Fe-atoms adsorbed on hollow sites of BiAg₂ on Ag(111) on Nb(110): (A) Bias-spectroscopy measurement taken on Fe_h with different YSR-states marked by the arrows in comparison to a spectrum taken on the substrate. The white line corresponds to 500 pm. (B) Constant-current STM image of Fe_h. (C-F) Constant-contour maps taken on Fe_h at the respective energies of the YSR-peaks. Parameters: $I_{\text{stab}} = 1 \text{ nA}$, $V_{\text{stab}} = 6 \text{ mV}$, $V_{\text{mod}} = 20.0 \text{ } \mu\text{V}$, $T = 320 \text{ mK}$ (A), $I_{\text{set}} = 500 \text{ pA}$, $V_{\text{bias}} = 5 \text{ mV}$ (B), $V_{\text{stab}} = 5 \text{ mV}$, $I_{\text{stab}} = 500 \text{ pA}$, $V_{\text{mod}} = 20.0 \text{ } \mu\text{V}$ (C-F), $T = 320 \text{ mK}$.

Spectroscopy on Fe-atoms

Next, we investigate the spectral features of single Fe-atoms. First, we examine the spectrum taken on Fe_h, depicted in Figure 6.16A. The spectrum was measured with a superconducting tip, and the tip gap value was determined by fitting the gap spectrum with the model shown in Section 3.4 (see the detailed fit analysis below). The grey dashed lines in the spectrum indicate this tip gap energy. The orange line represents the measurement taken on the Fe-atom, while the blue line is a reference spectrum taken on the substrate of the same island. The plot focuses on the low-energy features of the spectra between -3 meV and 3 meV, highlighting the features within the superconducting gap.

A comparison of the two spectra reveals the presence of additional in-gap states within the superconducting gap of the spectrum taken on the Fe-atom. These peaks appear in symmetric pairs concerning energy. We observe two pairs of peaks in total, which we label as $h_{i,-/+}$, where $i = 1,2$ and the sign ($-/+$) indicates whether the peak is at a positive or negative bias voltage. The energetic positions of these peaks are summarized in Table 6.1. The most prominent pair ($h_{1,\pm}$) is located near the Fermi energy of the tip (± 1.31 meV). These peaks are nearly symmetric in intensity. The second pair of peaks ($h_{2,\pm}$) is located at a bias voltage of ± 2.56 meV, close to the coherence peak of the substrate at ± 2.68 meV. At first sight, this pair of peaks could be interpreted as a pair of coherence peaks, which is shifted in energy with respect to the substrate's coherence peaks. However, a closer inspection shows a strong particle-hole asymmetry for the pair of

6 Bottom up constructed YSR-chains on a superconducting Rashba surface

h_i	V_{bias}	E	E/Δ_s
$h_{1\pm}$	± 1.31 mV	0 meV	0.0 %
$h_{2\pm}$	± 2.56 mV	1.25 meV	0.91 %

Table 6.1: Extracted YSR-state V_{bias} and energies E of Fe_h .

peaks, which would be unusual for a pair of coherence peaks. For this reason, we interpret these as YSR-states. Since the coherence peak and h_2 are so close to each other, both are superimposed, making it hard to identify the coherence peak separately.

We obtained constant contour maps for each peak, shown in panels (C, D) for the negative energy side and (E, F) for the positive energy side. The maps for the $h_{2,\pm}$ peaks (C, E) are very noisy due to the strong overlap with the substrate's coherence peaks. However, a triangular-shaped structure is discernible. $h_{1,\pm}$ (E, H) shows that a sixfold symmetric ray structure originating from the atom's position is more clearly visible at negative than at positive bias.

The spectral properties of an Fe_b atom are depicted in Figure 6.17, with the topography of the atom shown in (B). Three pairs of in-gap peaks labeled as $b_{i,\pm}$ with $i = 1, 2, 3$ are observed (see energies of the peaks summarized in Table 6.2). The first pair, $b_{1,\pm}$, is located at $V = \pm 1.52$ mV. There is a slight asymmetry in peak heights, with the negative side peak slightly higher in intensity. The second pair ($b_{2,\pm}$) appears at $V = \pm 1.9$ mV. The negative bias side peak is slightly larger in intensity. Lastly, the $b_{3,\pm}$ peaks are located at $V = \pm 2.31$ mV. This pair exhibits a much smaller intensity than the others and a different asymmetry pattern: The

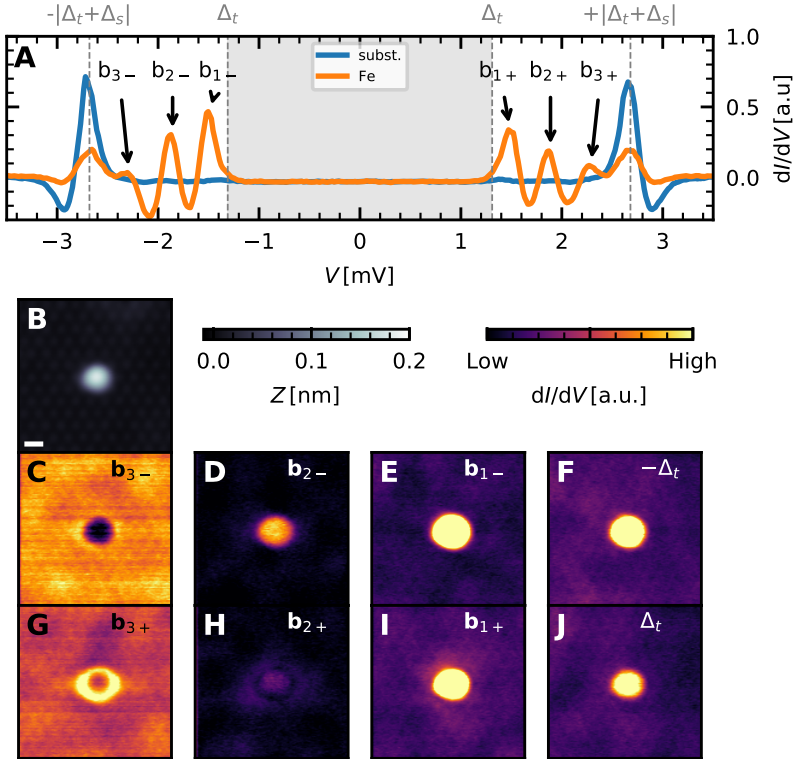


Figure 6.17: In-gap states of Fe-atoms adsorbed on bridge sites of BiAg₂ on Ag(111) on Nb(110): (A) Bias-spectroscopy measurement taken on Fe_b with different YSR-states marked by the arrows in comparison to a substrate spectrum. White line corresponds to 500 pm. Parameters: $I_{\text{stab}} = 1 \text{ nA}$, $V_{\text{stab}} = 6 \text{ mV}$, $V_{\text{mod}} = 20.0 \mu\text{V}$, $T = 320 \text{ mK}$ (B) Constant-current STM image of Fe_b. (C-J) Constant-contour maps taken on Fe_b at the respective energies of the YSR-peaks and $\pm\Delta_t$ (F, J). Parameters: $V_{\text{stab}} = 5 \text{ mV}$, $I_{\text{stab}} = 500 \text{ pA}$, $V_{\text{mod}} = 20.0 \mu\text{V}$.

b_i	V_{bias}	E	E/Δ_s
$b_1 \pm$	$\pm 1.52 \text{ mV}$	0.21 meV	0.15%
$b_2 \pm$	$\pm 1.9 \text{ mV}$	0.59 meV	0.43%
$b_3 \pm$	$\pm 2.31 \text{ mV}$	1 meV	0.73%

Table 6.2: Extracted YSR-state V_{bias} and energies E of Fe_b .

positive side peak is higher in intensity.

In panels (C-J), constant-contour maps taken at the energies of the peaks are shown, along with a map taken at the Fermi energy of the sample. The LDOS maps taken at the peak positions appear mostly oval-shaped. Around the atom, disordered wavy patterns are observed, as seen in panels (E, F, I, J). However, compared to Fe_h , these patterns appear somewhat random and much weaker in intensity.

The in-gap states observed in the spectra on the Fe-atoms can be attributed to YSR-states. These states arise from the interaction between the d-orbitals of the Fe-atom and the superconducting BiAg_2 substrate. The symmetry of the substrate influences the shape of the YSR-states [154]. For Fe_b , which occupies a twofold symmetric adsorption site, the short-range YSR-states exhibit twofold symmetric shapes. Conversely, Fe_h resides in a threefold symmetric adsorption site, resulting in a corresponding threefold symmetric wavefunction of the YSR-states. The orbitals of the magnetic impurity also influence the symmetry of the YSR-states. According to Ref. [154], the C_{3v} -symmetry of the Fe_h is expected to lead to degeneracies of the spin, yielding exactly three YSR-states. However, we only found two pairs of YSR-states in our case. One

possible explanation for this discrepancy could be that the intensity of the last pair of peaks is so small that it is buried below the signal of other peaks.

The spectra obtained on Fe_h, Fe_b, and the substrate were further analyzed using the model presented in Section 3.4. The LDOS of the tip and the sample are modeled as BCS-type gap spectra. Lorentzian peaks were added to the sample spectrum to model the in-gap states. This way, we extract the values for the tip and sample gap. The fitting results are depicted as red lines in Figure 6.18 with the substrate in panel (A), Fe_b in (B), and Fe_h in (C).

Please note that a comparison of the fit and the data in (A) shows a significant difference between the height of the fitted and measured coherence peaks. However, the fit is sufficient for our purpose as we are primarily interested in the values for Δ_t , Δ_s , $N_{0,t}$, $N_{0,t}$ and γ_{YSR} .

By fitting the spectra for the substrate and the Fe-atoms, we extract the gap values $\Delta_1 = 1.31$ meV and $\Delta_2 = 1.41$ meV.

To assign these gap values to either Δ_t or Δ_s , we did a measurement of the MARs, which occur as a result of the tunneling process between two superconducting electrodes (for more information, see Ref. [192]). To do that, the tip is stabilized above the substrate surface at low tunneling gap resistances (e.g., by increasing the stabilization current), and a bias spectroscopy measurement is performed. At sufficiently low tunneling gap resistances, additional in-gap peaks appear. Figure 6.19 shows such an example. We can see that additional in-gap features appear at $V_{\text{bias}} = 0$,

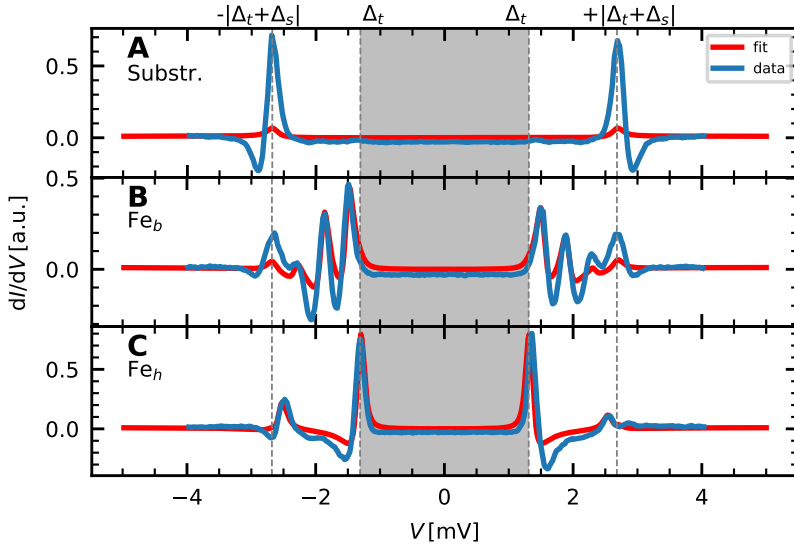


Figure 6.18: Fitted spectra taken on the Fe-atoms with different adsorption sites. (A) Bias-spectroscopy measurement taken on the substrate (blue) and the corresponding fit using the model as described in the text. (B) Same as (A) but for the spectrum of an Fe_h . (C) Same as (A) but for the spectrum of an Fe_b . The measured data is the same as in Figures 6.16A and 6.17A. Simulation parameters: $E_{b,\{1,2,3\}} = \pm 0.206 \text{ meV}, \pm 0.59 \text{ meV}, \pm 1 \text{ meV}$, $E_{h,\{1,2\}} = 0 \text{ meV}, \pm 1.247 \text{ meV}$, $\Delta_t = 1.31 \text{ meV}$, $\Delta_s = 1.37 \text{ meV}$, $\gamma_{\text{YSR}} = \gamma_{\text{SC}} = 0.05 \text{ meV}$, $N_{0,t} = N_{0,s} = 0.1 \text{ meV}^{-1}$, $T = 320 \text{ mK}$.

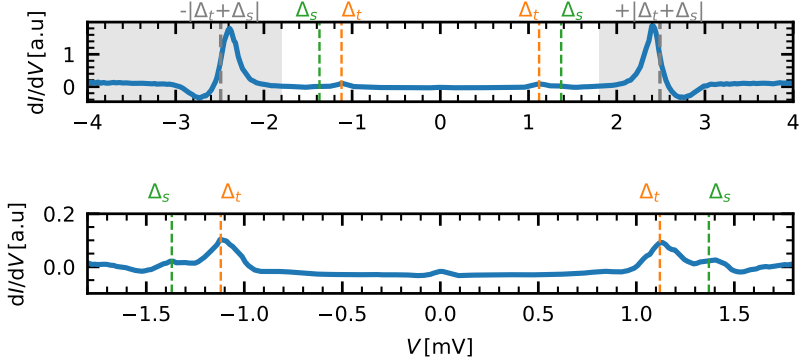


Figure 6.19: Measurement of MARs on BiAg₂. (A) Bias-spectroscopy measurement performed on the BiAg₂ substrate. (B) Same as (A) but zoomed on the V_{bias} -interval in (A), which is not greyed out. Parameters: $V_{\text{stab}} = 5 \text{ mV}$, $I_{\text{stab}} = 30 \text{ nA}$, $V_{\text{mod}} = 20.0 \text{ } \mu\text{V}$.

$V_{\text{bias}} = \pm 1.12 \text{ mV}$ and $V_{\text{bias}} = \pm 1.37 \text{ mV}$. As described in Ref. [192] the peak at $V_{\text{bias}} = 0$ can be assigned to Josephson tunneling processes [193]. The other pairs of peaks can be assigned to Δ_s or Δ_t . When we compare the measurement in Figure 6.19 to the results in Figure 6.18, one of the gap values is similar in both measurements, while the other differs. Taking into account that the measurements were taken on the same substrate but with different tips, we can now assign the features at $V_{\text{bias}} = \pm 1.37 \text{ mV}$ to Δ_s and the other one $V_{\text{bias}} = \pm 1.18 \text{ mV}$ in Figure 6.19 (or $V_{\text{bias}} = \pm 1.31 \text{ mV}$ in Figure 6.18) to Δ_t .

With the knowledge of the tip and sample gap values, we can extract the YSR-state energies of Fe_h and Fe_b , which can be found in tables 6.2 and 6.1.

6 Bottom up constructed YSR-chains on a superconducting Rashba surface

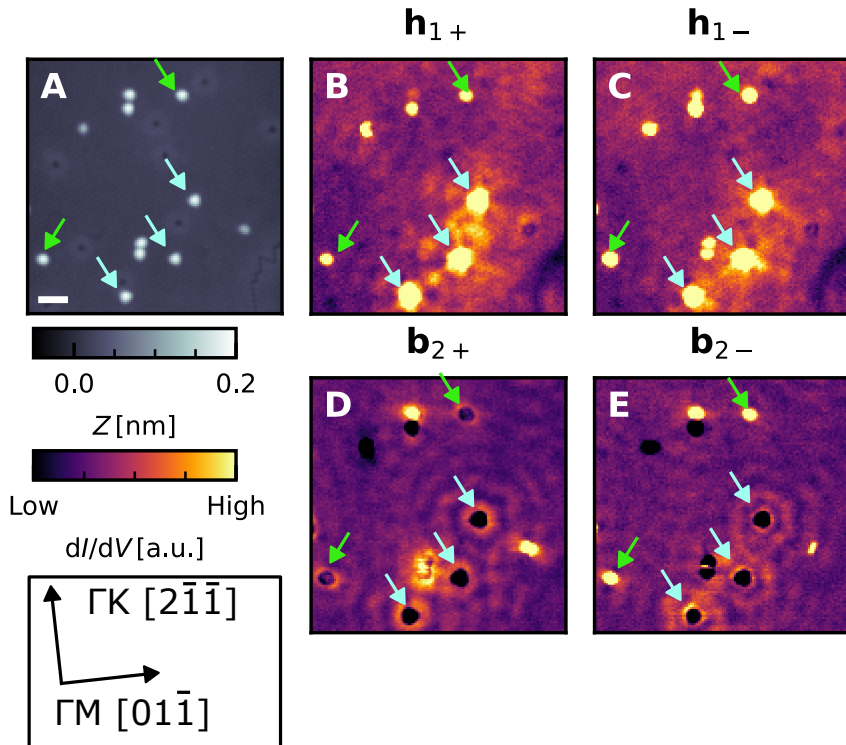


Figure 6.20: Long-range scattering patterns of YSR-states of Fe on BiAg₂ on Ag(111) on Nb(110). (A) Constant-current map of the BiAg₂ surface with adsorbed Fe-atoms. The white line corresponds to a length of 2 nm. Parameters: $I_{\text{set}} = 500 \text{ pA}$, $V_{\text{bias}} = 5 \text{ mV}$ (A), (B-E) Constant-contour maps at the corresponding YSR-energies as stated by the label in the top right corner. The arrows mark examples of Fe_h (cyan) and Fe_b (green). Parameters: $V_{\text{bias}} = 5 \text{ mV}$ (A), $V_{\text{bias}} = \pm 1.35 \text{ mV}$ (B/C), $\pm 1.92 \text{ mV}$ (D/E), $V_{\text{stab}} = 5 \text{ mV}$, $I_{\text{stab}} = 500 \text{ pA}$, $V_{\text{mod}} = 0.2 \text{ mV}$ (B-E).

Figure 6.20 presents constant-contour maps captured at various YSR-state energies extracted from the spectra. Panel (A) displays the topography of the investigated area. In panel (B/C), the constant-contour maps at energies $h_{1\pm}$ are shown, while the ones at energies $b_{2\pm}$ are shown in panels (D/E).

By inspecting the constant-contour maps, we can identify two types of objects that show similar behavior throughout each panel. The first type, marked by the blue arrows, shows strong long-range excitations on each map. Hexagonal-shaped scattering patterns originate from these Figure 6.20B and C. The wavelength of this oscillation along the ΓK -direction is estimated to be $\approx 1.88 \text{ nm}^{-1}$.

By comparing these objects to the YSR-states shown in Figure 6.16D/F, a strong resemblance to the YSR-states of Fe_h can be found. In contrast to that, the other group of objects that can be found, marked by the green arrows, shows very compact oval-shaped excitations, resembling the $h_{2\pm}$ states shown in Figure 6.17H/D. We, therefore, assign the long-ranged objects to Fe_h and the short-ranged ones to Fe_b . Please note that the strong scattering pattern on Fe_h at energies $b_{2\pm}$ might be an indication towards another pair of YSR-states of Fe_h that was not identified in Figure 6.16, due to its low intensity.

Typically, there are two ways to explain the appearance of long-ranged YSR-states. The first possibility is explained by a quasi-two-dimensional character of the superconductor to which the spins of the magnetic impurities couple, such as the one reported in Ref. [194]. The other explanation involves so-called quasi-particle-focussing effects along directions perpendicular to low-

curvature regions of the Fermi surface [67]. For our case, where the Fermi surface of Ag can be seen as sphere-shaped, the second effect can be neglected, and we can conclude that the long-range wavefunction indicates a coupling of the Fe_h to the BiAg_2 surface state. Nevertheless, it seems that the k -vector extracted for the oscillation pattern of the long-range YSR-state ($k = 1.88 \text{ nm}^{-1}$) is much larger than the Fermi wavenumbers of the BiAg_2 ($k_{F,1} = 0.44 \text{ nm}^{-1}$, $k_{F,2} = 1.22 \text{ nm}^{-1}$), which can be estimated by using the dispersion relation model in Figure 6.6C.

6.6 Hybridization between YSR-states on BiAg₂

In this part of the chapter, we examine the interaction between Fe-atoms. We manipulate atoms to place two Fe-atoms next to each other and measure their spectral properties through bias-spectroscopy measurements. By varying the distance between the atoms, we can observe changes in the spectroscopic features due to their interaction.

Distance dependent hybridization in Fe-pairs

When two atoms are placed near each other, their electron orbitals overlap and hybridize, splitting the atomic orbitals in energy and forming molecular orbitals. Typically, electrons form a bonding orbital, in which electrons have a high probability of being located between the atomic cores, and an antibonding orbital, where the electrons have zero probability of being located between the atomic cores. Similar behavior is observed for YSR-states of magnetic atoms coupled to a superconductor, which hybridize when placed near each other [68–70, 195–197]. However, it should be noted that for the case of spins with antiferromagnetic alignment and zero SOC, no splitting is expected for the YSR-states [70].

Please note that the measurements in this subsection were done in the SPECS setup (see Section 3.5.1) at $T = 4.2$ K and on a different sample as opposed to the spectra shown in the rest of this chapter, which were all measured in the 300 mK setup (see Section 3.5.2).

The effect of hybridization between two atoms is investigated in

6 Bottom up constructed YSR-chains on a superconducting Rashba surface

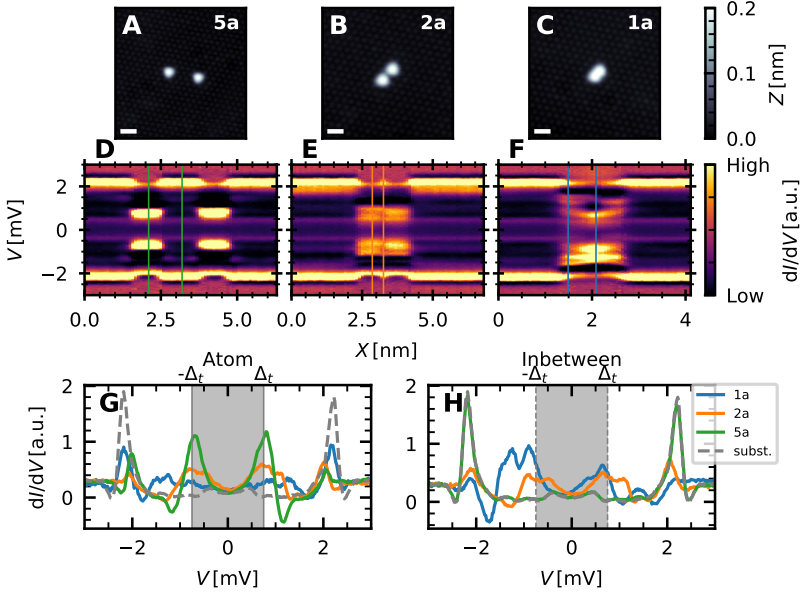


Figure 6.21: Hybridization between Fe_h for different interatomic distances (A-C) Constant-current STM image of atomic pairs for an interatomic distance of 5a (A), 2a (B) and 1a (C). The white line corresponds to 500 pm (A, B) and 1 nm in (C). (D-F) Spectroscopic line profiles taken through the atomic pairs as marked by the lines in the respective panel above. (G) Bias-spectroscopy measurement taken at the location of the atom as depicted by the color-coded lines in panels (D-F). (H) Bias-spectroscopy measurement taken at the location between the atoms as depicted by the color-coded solid lines in panels (D-F). Parameters: $V_{\text{bias}} = 5$ mV (A, C), $V_{\text{bias}} = -5$ mV (B), $I_{\text{set}} = 500$ pA (A-C), $I_{\text{stab}} = 500$ pA, $V_{\text{stab}} = 5$ mV, $V_{\text{mod}} = 50$ μ V (D-H), $T = 4.2$ K (A-H).

Figure 6.21. In this measurement set, we take a look at the Fe_h. Two atoms are placed next to each other at different inter-atomic distances of 5a (A), 2a (B), and 1a (C), where a refers to the distance between two neighboring lattice sites of the same kind and orientation. Usually, the manipulation only allows the creation of pairs down to a 2a distance. 1a-pairs, as presented here, can only be found in a self-assembled way right after deposition. We record a spectroscopic line profile for each pair that crosses both atoms, as shown in (D-F).

When comparing these measurements to the measurements shown in Figure 6.18 we consider that the higher temperature leads to thermal resonance peaks that occur at V_{bias} between $\pm\Delta_t$. In addition to that, the values of Δ_s and Δ_t differ from the measurements before. We also evaluate the data at the position of one of the atoms (panel (G)) and in between the atoms (panel (H)). In the spectroscopic line profile of the 5a chain, we see very prominently the h_1 -peak located at $\approx \pm 0.76$ mV. We look at the corresponding spectrum in panel (G), taken on the pair's left atom, to understand the spectroscopic features better. Comparing this to a single Fe_h (c.f. Figure 6.16A), we can not spot any significant difference. The spectrum taken in between the atoms (see panel (H) in green) is almost identical to the substrate spectrum (grey). Next, we look at the 2a-pair (B). The spectroscopic line profile along this adatom pair shows apparent differences from (D). The intensity of the h_1 -peak pair has decreased. The spectra in panels (E), (G), and (H) of the 2a-pair show a splitting of the h_1 -peak. Finally, we inspect the 1a-pair shown in panel (C). The corresponding spectroscopic line profile (F) shows an even stronger splitting of the h_1 -peak.

Also, the splitting increases at locations between the atoms of the pair. In the spectroscopy taken on the left atom of the pair (panel (G), blue curve), we can see a clear splitting on the negative bias side. To understand the splitting of the peaks, we model the gap spectrum by assuming the tunneling between two superconducting electrodes (see Section 3.4). In the first step, we model the superconducting spectrum taken on the substrate. This way, we can extract parameters such as the broadening parameter for the tunneling between the tip and substrate γ_{SC} , Δ_t , and Δ_s . This is presented in Figure 6.22A. In the next step, we model the spectrum of a free Fe_h -atom. The energetic positions of the YSR-states can be calculated by assuming the values in the last row of Table 6.1, which are the relative positions of the YSR-states concerning the sample gap. With the known values for the sample gap, we can calculate the energetic positions of the YSR-states. Each state is modeled by two Lorentzian functions with the same energy. Later in the text, it will be evident why we do this. This way, we end up with 8 Lorentzians in total, which are tuned in intensity I_i together with the other parameters (N_0 , γ_{YSR}) until the peaks show similarities in shape and broadening. For simplicity, we assume the same broadening for all the YSR-peaks. In any case, the states that are the most prominent ones are the h_1 -states. We model the pair spectra with these values fixed, adding a finite energy shift between the two Lorentzians at the same energy δ . This way, we can mimic the splitting or shifting of the YSR-states. With the assumption that the changes between the reference Fe_h spectrum and the spectrum of the paired Fe_h -atoms are mainly due to the interaction with the other pair atom, we reuse the val-

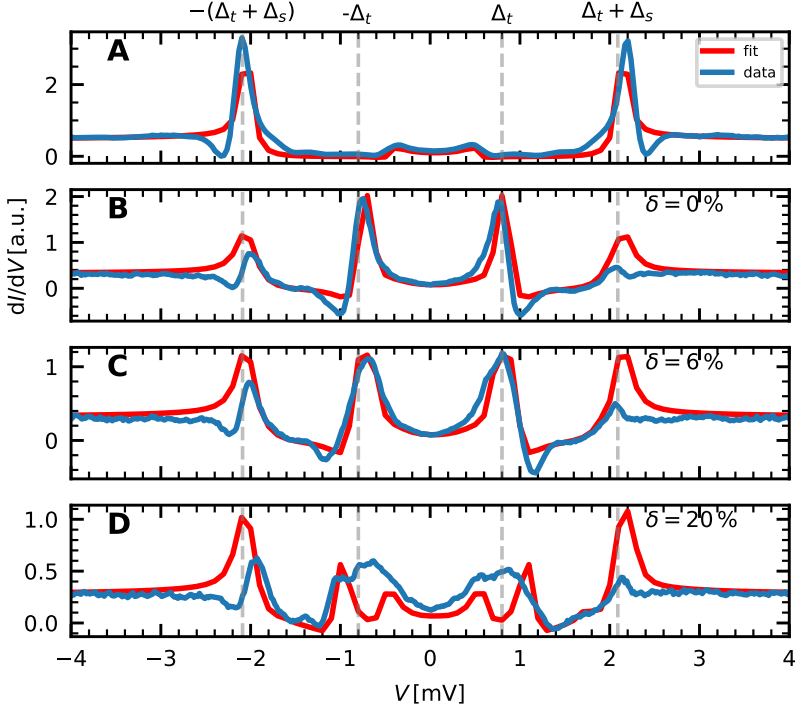


Figure 6.22: Modelling of the gap spectra for pairs of Fe_i . (A-D) Data and gap fit of substrate spectrum (A), single Fe_i (B), 5a-pair (C), and 2a-pair (D). Except for (B), the spectra are also shown in Figure 6.21G. Simulation parameters: $\delta = 6\%$ (C), 20% (D), $\Delta_t = 0.8$ meV, $\Delta_s = 1.29$ meV, $\gamma_{sc} = 0.055$ meV, $\gamma_{ysr} = 0.05$ meV, $E_{h_1} = 0$ and $E_{h_2} = 1.25$ meV (A-D). Measurement parameters: $V_{\text{stab}} = 5$ mV, $I_{\text{stab}} = 1$ nA, $V_{\text{mod}} = 50$ μ V (A, B); for (C, D) see description of Figure 6.21.

ues for γ_{SC} , γ_{YSR} , Δ_t and Δ_s from the free atom. To model the splitting of the YSR-states, the pairs of redundant Lorentzians with the same energy, which we used to model one YSR-peak before, are now shifted by a small V_{bias} value with respect to the energy of the unperturbed YSR-state consequently. For each YSR-peak, we now have one peak at $\epsilon_i + \delta\Delta_s$ and $\epsilon_i - \delta\Delta_s$, where ϵ_i corresponds to the unperturbed position of the peak i . Now, we vary the intensities of the peaks until we have an appropriate fit describing the splitted and shifted peaks of the pair spectra. We focus on capturing the overall linewidth of the peaks. The intensities are hard to catch. As we can see in the results in Figure 6.22, the fitted curves are not entirely identical. However, it gives us a rough indication of how large the splittings of the YSR-states are. We do this procedure for the 5a- and 2a-pairs. Due to the thermally excited peaks, the spectra become more complex. Despite the thermal peaks, the fitting method can be used for the 5a and the 2a-pair. We can find $\delta \approx 6\%$ for the 5a-pair and $\delta \approx 20\%$ for the 2a-pair, given as a percentage of Δ_s . For the 1a-pair, however, the spectrum becomes so complicated that finding an appropriate fit for the data is challenging, as we would have to consider an additional peak shift.

We do the same pair experiment for the bridge site atoms (see Figure 6.23). This set was measured with a different tip and sample preparation compared to Figure 6.21. Consequently, the gap values in both sets differ. As shown in panels (A-C), we perform the experiment again with interatomic distances of 5a (A), 4a (B), and 2a (C). The black arrow marks the fixed atom in (A). The spectra taken on the fixed atom are shown in panel (D). When we compare the different spectra, we can see slight variations in the intensities

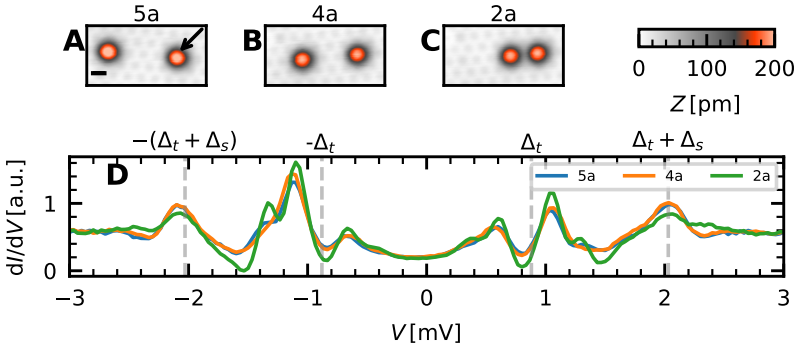


Figure 6.23: Spectra of Fe_b-pairs as function of interatomic distance (A-C) Constant-current measurements of Fe_b-pairs with an interatomic distance of 5a (A), 4a (B) and 2a (C). The arrow in (A) marks the fixed atom on which the bias-spectroscopy measurements in panel (D) were measured. The black line corresponds to a length of 400 pm (D) Bias-spectroscopy measurements on the fixed Fe_b for different interatomic distances of the Fe_b-pair. Parameters: $V_{\text{bias}} = -5$ mV, $I_{\text{set}} = 1$ nA (A-C), $V_{\text{stab}} = -5$ mV, $I_{\text{stab}} = 1$ nA, $V_{\text{mod}} = 50$ μ V (D), $\Delta_t = 0.88$ meV, $\Delta_s = 1.15$ meV (A-D)

6 Bottom up constructed YSR-chains on a superconducting Rashba surface

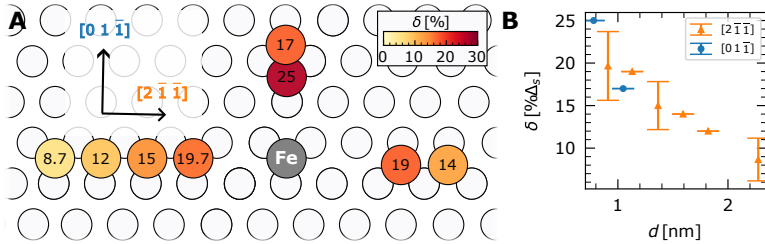


Figure 6.24: Splittings of the YSR-peaks of Fe_h -pairs as a function of distance and orientation. (A) The white circles represent the Bi-atoms of the underlying BiAg_2 substrate. The grey circle depicts the fixed Fe-atom, while the colored circles represent the relative positions of the other. The numbers indicate the fitted YSR-state splitting δ , which is induced on the fixed Fe_h for the respective relative orientation of the moving atom. The values were extracted as described in the text. The arrows depict the crystallographic direction $[198]$. (B) Direction-dependent splittings as a function of the interatomic distance.

of the peaks. However, when it comes to the peak positions, it looks as if there is no change as a function of the interatomic distance. Furthermore, there is no sign of peak broadening.

The absence of peak splittings in the Fe_b indicates a weak interaction between the Fe_b pairs. This is consistent with the strong localization of Fe_b YSR-states compared to Fe_h YSR-states (c.f. Figure 6.20). Due to this weak interaction strength, building chains from Fe_h -atoms should be more promising for forming YSR-bands than Fe_b -atoms. For this reason, we will focus on the Fe_h -atoms from here on.

We conduct the pair experiment with Fe_h for different distances and orientations of pairs with multiple tips and extract the split-

ting δ from the spectra described above. Some pair configurations were measured in various sets. We take the average of the fitted δ -values in these cases. Figure 6.24 sums up the extracted splittings. In (A), the grey circle depicts the position of the fixed Fe-atom. The colored circles represent the relative position of the other atom in the pair. The number and color represent the splittings of YSR-states extracted from the spectra measured on the fixed Fe-atom in each pair. We look at the splitting along the $[0\ 1\ \bar{1}]$ - and the $[2\ \bar{1}\ \bar{1}]$ -directions [198]. Panel (B) shows the splitting as a function of the interatomic distance between the atoms in each pair. The splitting increases for decreasing interatomic distances between the pair atoms along the $[2\ \bar{1}\ \bar{1}]$ -directions. We can even see a monotonic decrease in the splitting as a function of the distance. For the $[0\ 1\ \bar{1}]$ -direction, extracting more points to claim anything about the functional behavior would be necessary.

We investigated the interaction between Fe-atoms placed at different lattice sites and interatomic distances. To build magnetic chains on superconducting Rashba materials, which could potentially host topological superconductivity, we can use the insights gained from the Fe pair experiments to decide on the chain configuration. The interaction is weak for Fe_b atoms. Even at small distances of $2a$, the peak splittings are not notably strong. In particular, they are smaller than the separation of the YSR-states from E_F . Therefore, we do not expect that it is possible to realize YSR-bands from hybridized YSR-states of Fe_b atoms that cross E_F , which is required for the formation of topological SC bands. Fe_h pairs begin to interact at distances of approximately $3a$, with a notable increase in interaction for interatomic distances below that. For

the chains, strong hybridization is favorable. Building chains from Fe_h atoms with an interatomic distance of $1a$ would be ideal. However, manipulating atoms onto Fe_h adsorption sites is not easy. The closer the Fe_h atoms are brought to each other, the more difficult the placement onto hollow sites becomes. As the single Fe atoms get nearer, the probability that the atoms snap together and form a dimer increases. This process is not reversible and risks breaking the tip. Given these challenges, we found a good compromise by choosing $2a$ as the interatomic distance for building the chains.

6.7 YSR-chains on superconducting BiAg₂

In this section, we use the information on the interaction strength as a function of the distance from the previous section to build a YSR-chain. We perform spectroscopy measurements for different Fe chain lengths and temperatures to investigate the YSR-bands' properties toward topological superconductivity. We will focus on the chains along the $[2\bar{1}\bar{1}]$ -directions as their spectroscopic data shows the most interesting features. From the results of the last chapter, Fe chains with an interatomic distance of $1a$ along the $[01\bar{1}]$ -direction could also be interesting. However, these chains did not show symmetric zero energy states at the edges (see Section 6.7) and were already disqualified as candidates for chains hosting MZMs.

Building chains from Fe-atoms

The creation of the $2a$ chain can be seen in Figure 6.25. The chains are built along the $[2\bar{1}\bar{1}]$ -directions, which should lead to symmetric YSR-states on both ends of the chain due to the symmetry of the chain. In panel (A), topographic images show the chain built atom-by-atom. Atoms are added one by one to the chain from either the left or the right side. The chains are labeled by $\text{Fe}_{h,i}$ with i being the number of constituting atoms. The longest chain built this way is the $\text{Fe}_{h,11}$ chain, consisting of 11 Fe-atoms placed on hollow sites separated by $2a$. A model of the arrangement is presented in panel (B), showing the adsorbed atoms placed on the

6 Bottom up constructed YSR-chains on a superconducting Rashba surface

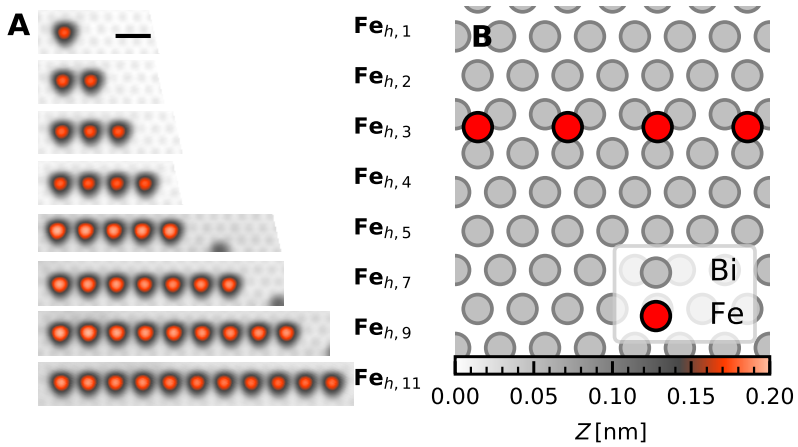


Figure 6.25: Atomic Fe chains with $2a$ interatomic distance along $[2\bar{1}\bar{1}]$. (A) Constant-current STM images of the Fe $2a$ chains for different numbers of atoms. The black line corresponds to 500 pm. (B) Sketch showing an example of a $Fe_{h,4}$ -chain (red) and the Bi-atoms (grey) of the underlying substrate. Parameters: $I_{\text{set}} = 500$ pA, $V_{\text{bias}} = 5$ mV.

Bi-atoms of the BiAg₂ substrate.

Spectroscopy on Fe_h chains

We performed a spectroscopic line profile measurement each time an atom was added to the chain. In Figure 6.26, results are shown for the Fe_{h,5}, Fe_{h,9} and Fe_{h,11} chains. Above the spectroscopic data, the corresponding topography measurement for each chain is displayed. The image size is scaled to match the x -axis positions in the spectroscopic line profile below, allowing for a direct comparison between spectroscopic signals and atomic positions within the chain. Already for the Fe_{h,5} chain, the h₁ YSR-state shows shifts and splittings due to interactions with other atoms in the chain. This effect increases towards the center atom of the chain. The magnitude of the splittings and shifts is symmetric around the center atom of the chain. However, on top of this systematic effect, there is an additional, unsystematic variation in the intensities of the spectral signal along the chain. For example, the outer peaks of the second and fourth atoms show differences in intensity. This unsystematic LDOS variation persists in longer chains, as seen in Fe_{h,9} and Fe_{h,11}. Additional excitations appear in between the split peaks. The atoms at the edges of the chains exhibit negligible splitting. The splitting/shifting increases for the second atom and saturates around the third or fourth atom. In this central region of the chain, it can be seen that the spectral intensities on each atom sometimes consist of more than two peaks in the energy range between $|\Delta_t + \Delta_s|$ and $|\Delta_t|$. This behavior is symmetric around the center atoms; for instance, the second atom

6 Bottom up constructed YSR-chains on a superconducting Rashba surface

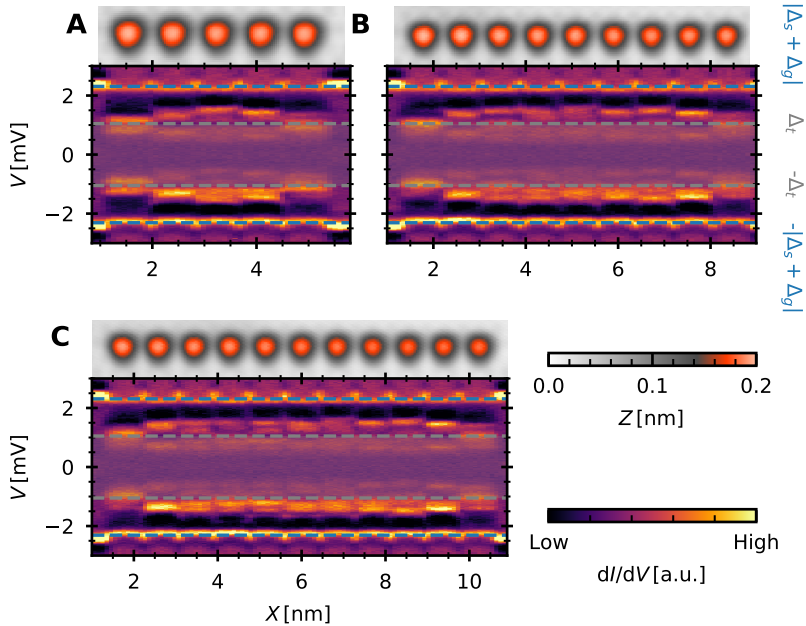


Figure 6.26: Spectroscopic line profile of the $\text{Fe}_{h,i}$ chain for different lengths (A) $\text{Fe}_{h,5}$ chain with the topography adjusted to the position coordinate x of the spectroscopic line profile shown below. The V_{bias} -values corresponding to $\pm\Delta_t$ are depicted by the grey, dashed lines (B) Same as (A) but for a $\text{Fe}_{h,9}$ chain. (C) Same as (A) but for a $\text{Fe}_{h,11}$ chain. The scans in panels (A-C) are the same as shown in Figure 6.25A. Parameters for spectroscopic line profiles: $I_{\text{stab}} = 500 \text{ pA}$, $V_{\text{stab}} = 5 \text{ mV}$, $V_{\text{mod}} = 20 \text{ } \mu\text{V}$, $T = 4.2 \text{ K}$.

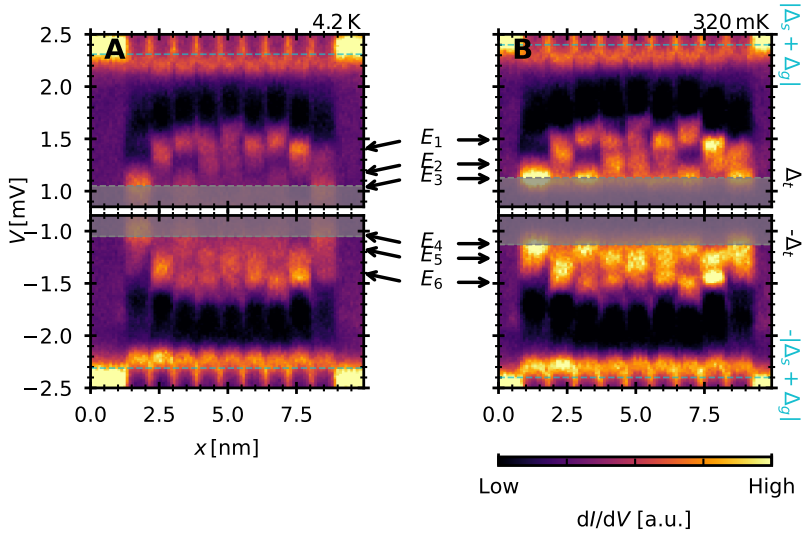


Figure 6.27: Spectroscopic line profile of $Fe_{h,9}$ chain at different temperatures. (A, B) Spectroscopic line profile through $Fe_{h,9}$ chain at 4.2 K (A) and 320 mK (B). The region between $\pm\Delta_f$ is cut out for better visibility. Parameters: $I_{\text{stab}} = 500$ pA, $V_{\text{stab}} = 5$ mV, $V_{\text{mod}} = 50$ μ V.

from the left end of the chain shows a similar splitting for the second atom from the right end. These measurements were taken at 4.2 K, meaning that thermal excitation processes contribute additional peaks, complicating the gap structure.

Temperature dependence of chain spectra

We, therefore, also conducted measurements at lower temperatures to get more insight into the YSR-band structure. Figure 6.27

shows a comparison between $\text{Fe}_{h,9}$ measurements at 4.2 K and 320 mK. Superconducting tips introduce redundancies in the spectra, necessitating a focus on relevant features by cutting the energy window between $-\Delta_t$ and Δ_t , similar to previous measurements. The cyan dashed lines indicate the positive and negative sum of the tip and sample gap. The grey lines mark the respective tip gap values. The labeled arrows E_1 to E_6 signify specific energy values and their corresponding positions in the measurements. By comparing both measurements, we make several observations. A slight increase in sample and tip gap values is observed from 4.2 K to 320 mK, when comparing the cyan lines with each other. In the 320 mK-measurement, the spectral features are more clearly resolved due to the increased tip gap. Moreover, the overall intensities of the in-gap states are increased. However, qualitatively, both measurements show a very similar behavior concerning the energies of the peaks in the spectra on the individual atoms. For example, for the third atom from the left and the right chain end, we can see a state at the tip gap energy and another at higher energy for the features on the positive bias side. These two states are well separated in terms of energy. We can see the same qualitative behavior for the same atom in the 320 mK-measurement; however, the gap between the peaks can be seen much more evident. This gap appearing at the third atom could be due to a nodal line of the confined quasi-particle state residing in the YSR-band around this energy.

Figure 6.28 presents a comparison of constant-contour maps of $\text{Fe}_{h,9}$ at the two different temperatures, focusing on the energies marked by the arrows in the spectroscopic line profiles in Figure

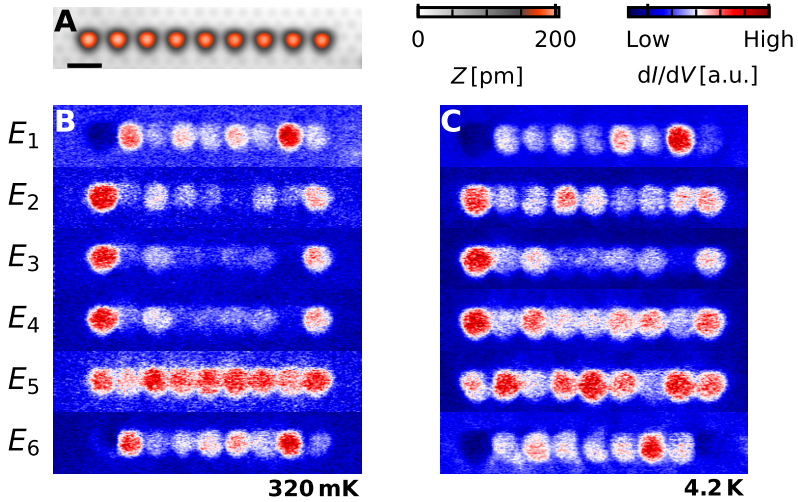


Figure 6.28: dI/dV -maps of the $\text{Fe}_{h,9}$ chain at energies marked in Figure 6.27 for different temperatures (A) Constant-current STM image of the $\text{Fe}_{h,9}$ chain. The black line corresponds to 1 nm (B, C) Constant-current maps measured at 320 mK (B) and 4.2 K (C). Parameters: $I_{\text{set}} = 500$ pA, $V_{\text{bias}} = 5$ mV (A), $V_{\text{bias}}^{E1,E6} = \pm 1.50$ mV, $V_{\text{bias}}^{E2,E5} = \pm 1.27$ mV, $V_{\text{bias}}^{E3,E4} = \pm 1.13$ mV (B), $V_{\text{bias}}^{E1,E6} = \pm 1.39$ mV, $V_{\text{bias}}^{E2,E5} = \pm 1.16$ mV, $V_{\text{bias}}^{E3,E4} = \pm 1.02$ mV (C), $V_{\text{stab}} = 5$ mV, $I_{\text{stab}} = 500$ pA, $V_{\text{mod}} = 20$ μ V (B, C).

6.27. Energies from the 4.2 K data were matched to the 320 mK data by normalizing the energy scales to the respective Δ_t . At E_1 , the dI/dV -maps for both temperatures show a signal distributed all over the chains, while the edge atoms exhibit almost vanishing intensity. A pattern is visible in the measurement, with the LDOS alternating between high and low for each atom. At 4.2 K, this alternating signal becomes more disordered, with varying intensities among the atoms. At E_2 , E_3 , and E_4 , the distinction between edge and bulk states is evident for the 320 mK, but not so clearly for the 4.2 K measurement. In the case of E_3 and E_4 , it is crucial to note that these maps are taken at Δ_t , i.e., at the Fermi energy of the sample. The measurements for E_5 at 320 mK show a mostly uniform intensity over the chain, while the 4.2 K data shows a more disordered pattern. The E_6 measurement at 320 mK, shows slightly more disorder compared to the 4.2 K measurement.

In summary, the measurements show that the spectra of atoms within the bulk of the chain change as more atoms are added, strongly indicating the formation of a YSR-band. The band has a width of about $500 \mu\text{eV}$ and shows intensity close to Δ_t , indicating that the band crosses E_F . This minigap that opened is the Δ_p that we referred to in the Kitaev model (see Section 2.4). However, there is no clear reopening of a minigap at Δ_t . Nevertheless, the spectroscopic line profiles and the dI/dV -maps show a strong spectral intensity at Δ_t , i.e., the sample's E_F , localized on the edge atoms. This intensity could hint towards a MZM.

There are multiple reasons to explain the absence of a minigap. The spectroscopic line profiles show that the in-gap states are still

quite localized on the atoms. The insufficient overlap between YSR-states may prevent a band with a large bandwidth. Also, there is disorder occurring in the chain due to electronic disorder of the substrate, which could suppress the formation of an ordered YSR-band.

Comparison of chains along different directions and with different interatomic distances

In Figure 6.29 Fe_h chains on BiAg_2 , of different orientations and different interatomic distances are shown (panels (A-C)). The measurements were taken on a different preparation compared to the chains shown in the last section. Through each chain, a spectroscopic line profile was recorded (panels (D-F)). For the 3a chain, we can see that the YSR-states of the constituent atoms are well separated from each other. The YSR-states are broadened as we get from the edges into the bulk. However, there is no evidence of a continuous band formation.

The chain shown in panel (B) is a $\text{Fe}_{h,9}$ chain with interatomic distances of $2a$ and is the same kind of chain that was discussed in sections 6.7 to 6.8. When we compare the spectroscopic data of this chain to the one shown in Figure 6.26, it seems as if the chain here shows less disorder in the YSR-states. However, this might also be due to a lower relative energy resolution. In this case $\Delta_s + \Delta_t = 2 \text{ meV}$, while the chain in Figure 6.26 is taken at $\Delta_s + \Delta_t = 2.3 \text{ meV}$ for 4.2 K. Therefore, it might also be that we are just measuring with a smaller energy resolution and, therefore,

6 Bottom up constructed YSR-chains on a superconducting Rashba surface

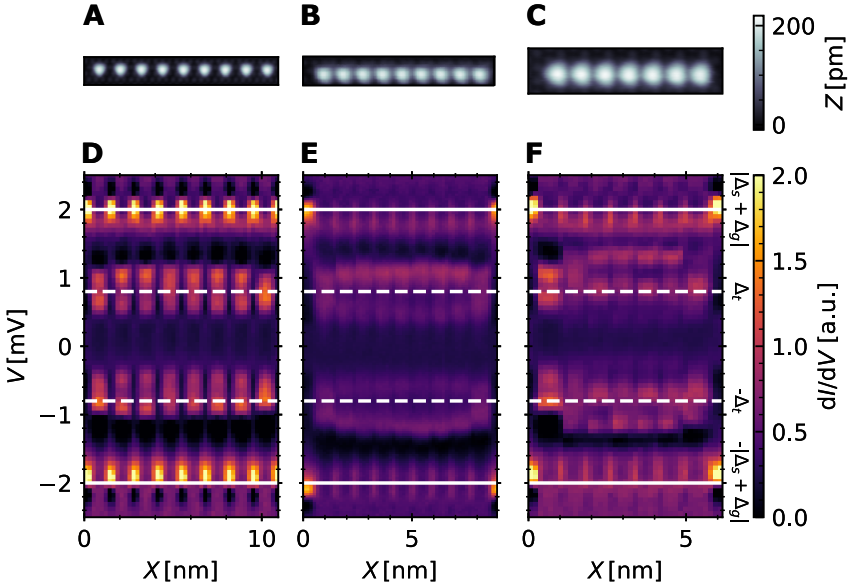


Figure 6.29: Further Fe_h chains on BiAg_2 . (A) $\text{Fe}_{h,9}$ chain with an interatomic distance of $3a$ along the $[2\bar{1}\bar{1}]$ direction. (B) $\text{Fe}_{h,9}$ chain with an interatomic distance of $2a$ along the $[2\bar{1}\bar{1}]$ direction. (C) $\text{Fe}_{h,7}$ chain with an interatomic distance of $1a$ along the $[01\bar{1}]$ direction. (D/E/F) Spectroscopic line profile along the chain shown in (A/B/C). The spectra were recorded with the same tip with $\Delta_t = 0.8$ meV and the same island with $\Delta_s = 1.2$ meV. Parameters: $I_{\text{set}} = 1$ nA, $V_{\text{bias}} = -5$ mV, (A-C), $I_{\text{stab}} = 1$ nA, $V_{\text{stab}} = -5$ mV, $V_{\text{mod}} = 50$ μV (D-F), $T = 4.2$ K.

cannot distinguish single features from each other.

The last chain shown in panel (C) is a $\text{Fe}_{n,7}$ chain built along the $[0\ 1\ \bar{1}]$ direction with an interatomic distance of $1a$. We can see that the YSR-states inside of the chain show a stronger splitting. However, we can also see a difference between the YSR-states on the left end of the chain and the YSR-states on the right. While the left end YSR-state shows an energy splitting, the right end seems to show none.

6.8 Perturbing the edge states of a YSR-chain

In this section, we probe the stability of the chain's end states, which were investigated in the previous section against local perturbation. To do this, we place another atom adsorbed near the chain's end. We vary the distance between the perturbing atom and the chain end atoms and measure the spectroscopic changes compared to the unperturbed chain.

The upcoming experiment has been designed to verify or falsify that the zero bias signal observed on the chain's ends is due to a topological edge state.

Expected outcomes for perturbed edge states

The procedure follows the method used in Ref. [39]. A chain was constructed using atom manipulation. To probe the chain's topological nature, the ends of the chains were perturbed by placing atoms of a different adsorption site next to one end of the chain. The possible outcomes of this experiment are depicted in Figure 6.30. The panels (A-D) depict the states of the YSR-chain as a function of energy E and position x , similar to the information that a spectroscopic line profile can provide for the different outcomes. The corresponding spectroscopic 2D maps taken at zero energy ($\pm\Delta_t$) are shown in the panels (E-H).

The grey boxes in (A-D) represent the YSR-band states of the chain. Due to the interaction with each other, the YSR-states of the atoms are split in energy. If the hybridization between the YSR-states is

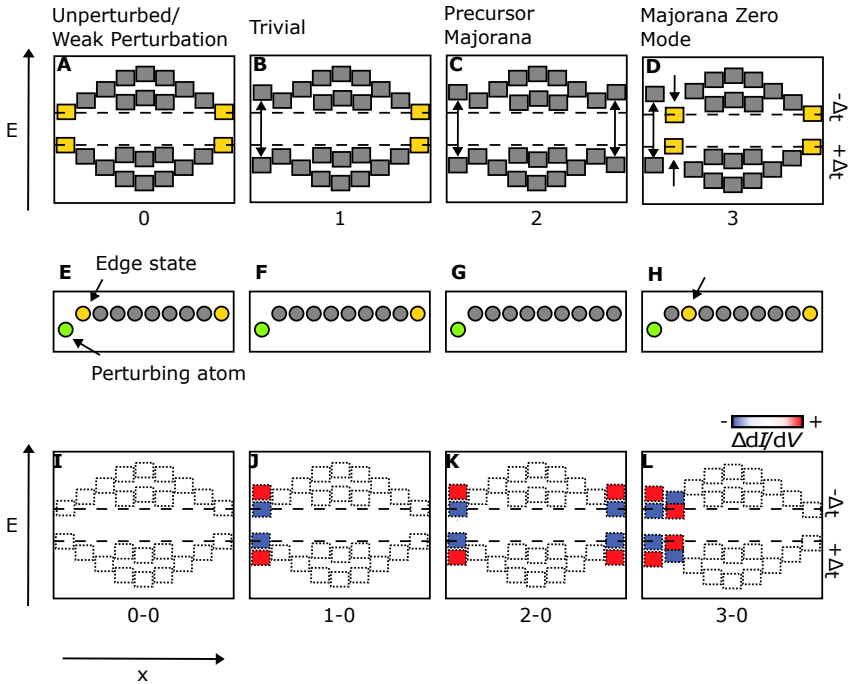


Figure 6.30: Schematics of the possible outcomes of the perturbation experiment (A) Schematic representation of the unperturbed YSR-band with edge-states at E_F as a function of energy and position. (B-D) Same as in (A) but with a perturbation on the left, showing the states' expected energy shifts for a chain with a trivial zero-bias edge state (B), with a PMZM at the end of the chain (C) and with a MZM at the end of the chain (D). (E-H) Illustration of the 2D zero-bias maps taken on the chain corresponding to the different cases, with the perturbing atom on the left end of the chain (green) and the zero-energy edge states depicted by yellow circles. (I-L) Difference maps of the unperturbed case (I), the trivial case (J), the precursor case (K), and the MZM case (L) subtracted by the unperturbed case (I).

strong enough, the YSR-states overlap and form band-like structures with some energy-dependent confined states illustrated in panel (A). For some YSR-bands, zero-energy edge states can form inside those bands. In the spectroscopic line profiles, these are detectable as states at $\pm\Delta_t$, located at the chain ends (yellow). The corresponding zero bias dI/dV maps (E) show them as intensity in the LDOS appearing at the chain ends (yellow). The chain can be perturbed on one of the ends to probe whether the states at the ends are topological or trivial. This perturbation is green in the 2D zero-bias maps (E-H).

The most basic case is when the perturbation is too weak to influence the YSR-states inside the chain. Here, the spectroscopy on the chain before and after the perturbation will look the same (A). The same applies to the zero-bias dI/dV map, where the LDOS on the edges stays the same (E). If the perturbation is strong enough, we can end up in one of the cases shown in panels (B-D). In the trivial case (panel (B)), where the edge state just consists of a local mode at the chain's end, which is not extended along the chain, the perturbation will lead to the edge state being split away from Δ_t , but only on the perturbed end. The rest of the chain stays mostly unaffected. In the 2D spectroscopy map shown in (F), we expect the zero-energy excitation on the left end of the chain to disappear while the edge state on the right end of the chain stays the same. Most importantly, we do not expect another zero-energy state to form somewhere close inside the chain. The next case illustrates the result for a PMZM (panel (C)). These states are characterized as non-local edge states with a strong overlap of the wave function of the parts of the MZM localized on the left and on the right

end. Consequently, these states can be destabilized and split away from Δ_t . However, due to the entanglement of the states at both ends, a perturbation on one end of the chain will have to cause the same to the other. In the 2D-spectroscopy map (G), the increased zero-bias LDOS will disappear on both ends. The last case demonstrates the expected outcome for MZMs. In this scenario, a perturbation weaker than the topological gap will shift the zero-bias spectral intensity on the perturbed atom to higher energy. However, the zero bias spectral intensity will now move to the side, e.g., towards the chain's bulk or also onto the perturbing atom at the perturbed end of the chain. In other words, the MZM moves further into the chain's bulk, as can also be seen in (H) (or onto the perturbing atom).

To better see the changes inside the chain, one can subtract the unperturbed spectra from the spectra of the perturbed chain. This will subtract out the same features for both cases and accentuate where states have appeared or disappeared due to the perturbation. This method makes it easier to detect shifts in the spectral intensity of the YSR-bands as edge modes. The panels (I-L) show the expected outcomes for the subtraction maps for the different cases. Since we subtract the unperturbed chain from the perturbed ones, negative values (blue) indicate the disappearance of a state, and positive values (red) indicate the appearance of a state. Panel (I) shows the difference map for a weak perturbation. In this case, the subtraction should show no difference signal. The trivial case (J) will lead to positive difference signals away from Δ_t and a negative signal at Δ_t for measurements at the perturbed chain end. The result for the PMZM case (panel (K)) is similar

to the trivial case in (J), with one difference. Instead of splitting the states only on the perturbed side, it splits them on both ends. Therefore, the signature in (J), which we see on the left, will be visible on both ends of the PMZM case. Finally, we have the expected outcome for the subtraction map in (L). Here, we can see that signals on the perturbed chain end are similar to panels (J, K); however, here, the atoms further inside of the chain show an increase in the difference signal at Δ_t , while the LDOS further away from Δ_t shows a more negative signal.

Perturbation arrangements

Figure 6.31 displays topographic images from the perturbation experiment. Each panel represents a different perturbation arrangement. The bottom part of each panel shows the constant-current STM image, while the top part provides the ball model of the atomic positions. The blue circles depict the perturbing atom. The perturbing atom is placed on the bridge site or buried next to the chain to introduce a perturbation without extending the chain with a YSR-state, which is slightly off the Fermi energy (c.f. Figure 6.17). panel (A) shows the unperturbed $\text{Fe}_{n,11}$ chain used for this experiment. Perturbations are applied to the left end of the chain. Different perturbation geometries are indexed for reference in the subsequent sections. The unperturbed case is indexed as "0". In the geometries labeled "1", "2," and "3," we placed the perturbing atom on bridge lattice sites in the lower left corner of the chain. Distances between the first chain atom and the perturbing atoms range between $d = 973$ pm (1) and 790 pm (2). For case 4, the

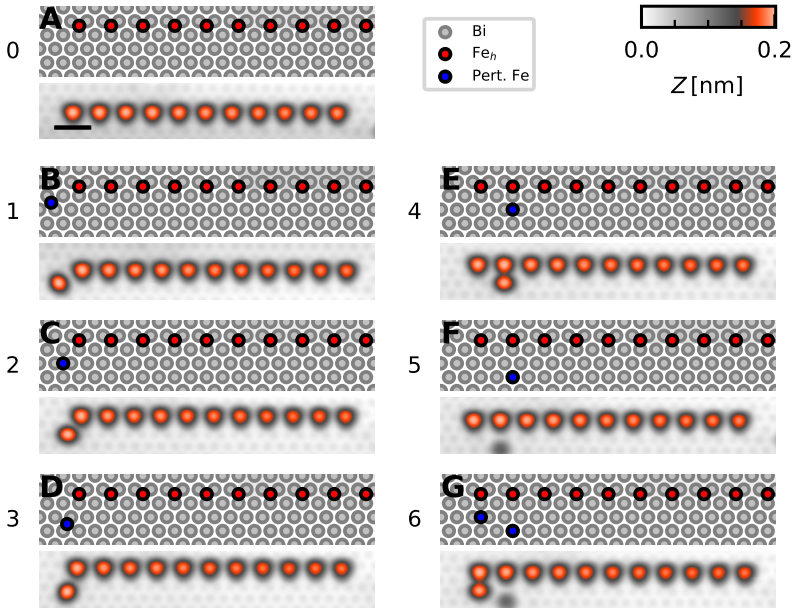


Figure 6.31: Perturbation experiment with $Fe_{h,11}$ (A) Constant-current STM image of the unperturbed $Fe_{h,11}$ chain (bottom) with a model depicting the adsorption sites of the Fe-atoms (top). The black line corresponds to a length of 1.2 nm. (B-E) Constant-current STM measurement of different perturbation constellations for the $Fe_{h,11}$ chain (bottom). The Fe_b atoms are placed near the chain's left end, as the schematics depict (top). The distances between the chain and the perturbing atom are 973 pm (B), 790 pm (C), 886 pm (D), 620 pm (E). (F) Same as (B-E) but with a subsurface impurity created from a Fe-atom beneath the second chain atom from the left. The distance between the chain and the defect is 1.038 nm. (G) Same as (F) but with an additional perturbing Fe_b atom below the first chain atom from the left. The distance between the chain and the defect is the same as in (F), and the distance between the chain and the perturbing atom is 620 pm. The cases are labeled by the numbers 1-6. Parameters: $I_{\text{set}} = 500$ pA, $V_{\text{bias}} = 5$ mV.

perturbing atom is placed below the second chain atom with a distance of $d = 620$ pm. In case 5, a subsurface defect is created below the second chain atom ($d = 1.038$ nm). In the last geometry (6), in addition to the same subsurface defect as in (5), an Fe_b atom is placed below the first chain atom ($d = 620$ pm).

2D spectroscopy maps at zero bias

Figure 6.32, shows the constant-contour maps taken at $\frac{\Delta_t}{e}$, i.e. at the samples E_F . Panel (A) displays the chain and the constant contour maps taken at Δ_t for the unperturbed chain and the individual perturbation geometries (B-G) as discussed in Figure 6.31. The labels 1-6 in the lower left of the panels assign the measurements to their respective perturbation case in Figure 6.31. The topography (A) and the constant-contour maps are scaled in lengths so that the positions of the atoms in (A) roughly correspond to the chain atoms' positions in panels (B-H). Each of these panels is split into two, where the left part shows the raw data, and the right part shows the data after being subtracted by the data of the unperturbed chain (A). Note that the perturbing atoms are now located next to the top end of the chain.

When we look at the perturbation cases 1 and 2 shown in panels (B and C), we see that both cases look very similar. The raw data, and even more the subtraction maps, show that the LDOS over the whole chain is smaller than in the unperturbed cases. Especially the edge state on the top side (with the arrow), where the perturbation atom has been placed, shows a decline in the LDOS.

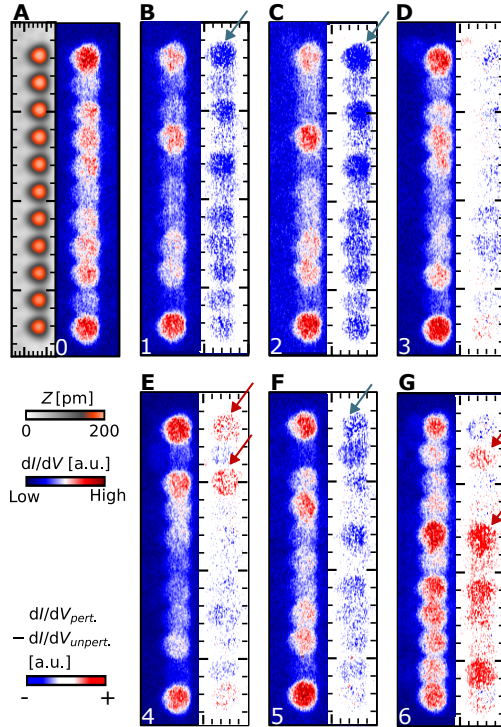


Figure 6.32: dI/dV maps corresponding to the sample's E_F of $\text{Fe}_{h,11}$ for different perturbation geometries (A) Constant-current STM images of (left) and constant-contour 2D-spectroscopy map (right) of the unperturbed $\text{Fe}_{h,11}$ taken at $\pm\Delta_t$. (B-H) Constant-contour 2D-spectroscopy maps taken at $-\Delta_t$ for the perturbed chains (left part) and the data subtracted by the unperturbed data (right part). The number labels correspond to the perturbation cases in Figure 6.31. The perturbation atom is placed at the chain end on the top. Please note that the color scale in the unsubtracted data in (F) was adjusted. Parameters: $I_{\text{set}} = 500 \text{ pA}$, $V_{\text{bias}} = 5 \text{ mV}$ (A, left), $V_{\text{stab}} = 5 \text{ mV}$, $I_{\text{stab}} = 500 \text{ pA}$, $V_{\text{bias}} = -\Delta_t$, $V_{\text{mod}} = 20 \mu\text{V}$, $T = 320 \text{ mK}$ (A, right, B-G).

Interestingly, from there on, every second atom (numbers 3 and 5) in the chain shows a more significant decrease in LDOS compared to the rest of the chain. We can not see any atom with an increased LDOS. The measurement for case 3 (panel D) shows almost no reaction to the perturbation atom. The difference between the perturbed and unperturbed chains is negligible for the perturbation geometry 4 shown in (E). As marked by the arrows, the first and the third atoms show a notable increase in their LDOS's. The dI/dV -signal on the other atoms only shows slight changes. Next, for case 5 in panel (F), the signals on atoms 1-3 (marked by the arrow) show a notable decrease in LDOS. Also, inside the chain on atoms 5 and 7, we can see a slight reduction in intensity. Significant changes in the chain spectrum can be seen in panel (G) (case 6). As marked by the upper red arrow in the difference map, the LDOS in the second atom increases slightly. More importantly, beginning from atom 5, a notable increase in the LDOS is detected. Atoms 5, 7, and 10 show the strongest increase.

By comparing the perturbed and unperturbed cases, we can classify the perturbation cases (1-6) and interpret the results according to the expected scenarios. First, let's examine case 3. Here, the changes with respect to the unperturbed chain are very small. Therefore, I conclude that this measurement indicates an example of a chain with a negligible disturbance.

Another interesting observation is that the measurement for case 3 shows very little to no perturbation effect in the chain, while cases 1 and 2 show a drastic change. It is not intuitively clear why the cases are so different. This can not be explained solely by the

distance between the perturbing atom and the chain because even though case 1 has the largest distance, it shows a similar LDOS change as case 2. As seen in Figure 6.17, the YSR-states have their elongated axis along the vector connecting the Bi-atoms, forming the bridge on which the Fe-atom is adsorbed. Therefore, in case 3, the YSR-state should be elongated towards the chain and show the most substantial perturbation in comparison to cases 1 and 2 (see Figure 6.31), but the opposite is observed. We conclude that the strength of the perturbation is not straightforwardly linked to the shape of the Fe_b YSR-state. In cases 1 (B) and 2 (C), the perturbation results in an overall decrease in the local density of states (LDOS). The edge state at the perturbed end exhibits the most significant decrease. The absence of any increase in the LDOS at any other chain atom suggests that the edge state was destroyed rather than being shifted further into the chain. This leaves us with either a trivial edge state or a PMZM inside the chain. To distinguish these two cases, one must examine the other chain end. To distinguish between these two cases, in the case of a PMZM, the other chain end must show a decrease in the LDOS of similar strengths as on the perturbed chain end. In the trivial case, the edge state on the unperturbed side would remain unchanged. Looking at the other chain end in panels (B) and (C), we observe decreased LDOS on the lower chain end. However, it is not as strong as on the upper chain end. Furthermore, the decrease is of the same magnitude as the overall LDOS decrease that occurs all over the chain. Case 5 in panel (F) is similar to cases 1 and 2, i.e., it shows a similar behavior as for panels (B) and (C). This perturbation experiment strongly suggests the trivial state scenario because only

the edge state on one end is disturbed, not the other. There is no increase in LDOS over the chain either. Cases 4 and 6 show increasing LDOS signals at multiple locations inside the chain. In panel (E), we see an increase in the LDOS on the first atom and further inside the chain on the third atom. If we interpret this observation as the edge state appearing further in the bulk of the chain, this would be evidence for a topological edge state. However, the measurement of case 6 (panel (G)) is again difficult to reconcile with the MZM scenario:

The slight decrease on the perturbed chain end and the slight increase of LDOS on the second atom look like what would happen for a MZM. However, the rise of LDOS throughout the unperturbed half of the chain, beginning with the fifth atom, is unexpected and cannot be explained by any of the cases from Figure 6.30.

In summary, from the zero bias-spectroscopy maps, we cannot find a coherent answer on whether the edge states appearing in the $\text{Fe}_{h,11}$ are of a topological or trivial nature. While some of the perturbation geometries (cases 1, 2, and 5) indicate that the edge states are trivial states or PMZMs, other geometries (cases 4 and 6) show features that could be interpreted as signatures of a topological edge state.

A general problem of the perturbation experiment via dI/dV -maps is that it is unclear which energies the spectral intensity at Δ_t are shifted after perturbation. E.g., an increased dI/dV -intensity in the map of Figure 6.32 may also result from off-zero energy modes, which are still detected by the measurement. To do a more

well-defined experiment, we performed a series of spectroscopic line profiles for all the perturbation geometries along the chains as sketched in Figure 6.30 (A-D) and (I-L).

Spectroscopic line profiles

The results of the spectroscopic line profile measurements are displayed in Figure 6.33. Similar to the previous measurements, the individual cases are identified by numbers ranging from 0 to 6, linking the spectroscopic line profiles to the perturbation geometries depicted in Figure 6.31. The measurement on the unperturbed chain is presented in panel (A). Panels (B-G) showcase the spectroscopic lines for the perturbed chains, with the number in the upper right corner corresponding to the labeled cases. Each panel includes the raw data (top) and a difference map (bottom) obtained by subtracting the unperturbed chain from the perturbed chain. The topographies of both measurements were compared to ensure that corresponding points were aligned.

We examine the subtracted maps to identify changes in the LDOS. In Figure 6.33, the blue areas represent the disappearance of a state after perturbation, while the red areas indicate the appearance of a state. This visual representation allows us to comprehend the entire spectroscopic behavior within the chain. Consequently, we can observe when a state transitions from one energy level to another. The grey dashed lines indicate $\pm\Delta_t$ corresponding to the sample's E_F . The unperturbed spectroscopic line profile (panel (A)) displays the zero-energy edge states at $\pm\Delta_t$. However, it

6 Bottom up constructed YSR-chains on a superconducting Rashba surface

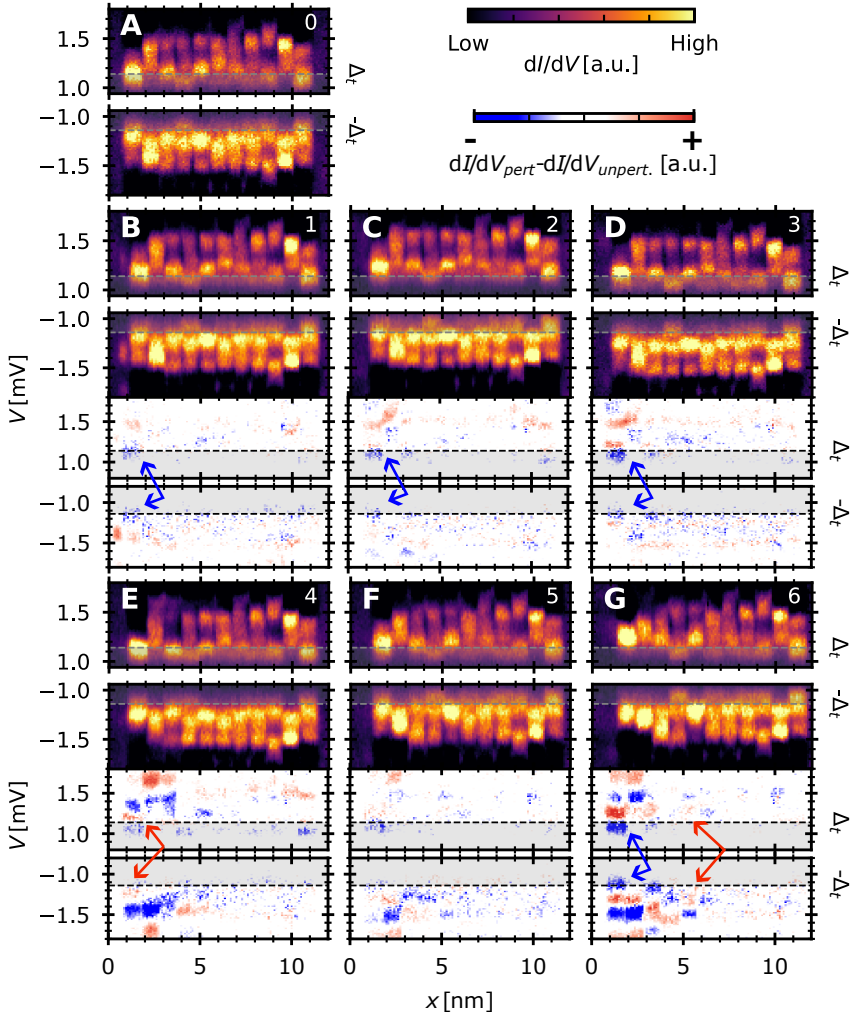


Figure 6.33: Spectroscopic line profiles for perturbed $\text{Fe}_{h,11}$ (A) Spectroscopic line profile of unperturbed $\text{Fe}_{h,11}$ (B-G) Spectroscopic line profiles of perturbed $\text{Fe}_{h,11}$ with the index in the top right corresponding to the different perturbation cases. Parameters: $I_{\text{stab}} = 500 \text{ pA}$, $V_{\text{stab}} = 5 \text{ mV}$, $V_{\text{mod}} = 50 \text{ } \mu\text{V}$ and $T = 320 \text{ mK}$.

is important to note that the zero-bias states are observed at the edges and with a smaller intensity inside the chain. When examining the difference maps in panels (B-D, F), we can observe that the edge states formerly located at zero Δ_t are shifted away from Δ_t on the perturbed chain end. The example in panel (D) clearly shows the state is shifted away to higher energies as indicated by the red signal just above $\pm\Delta_t$. In (B-D), these states are marked by the blue arrows. Looking at the rest of the chain, we can not see any clear appearance of a new state at $\pm\Delta_t$ further into the chain. The other side of the chain shows no clear signal change. This is consistent with the findings from Figure 6.32. In panel (E), we observe stronger changes. On the left end of the chain, we can see a shift of spectral intensity towards the Fermi energy. The shift to higher energies also affects the YSR-states of the second and third atoms. The most significant changes can be seen in panel (G). Here, the edge state on the left side moves away from E_F . The same applies to states on the second atom. On the fifth atom, marked by the red arrow, we observe an increase in spectral intensity, but it is located off the sample's E_F . Also, upon examining the raw spectroscopic line profile in (G), the state's energy, which is off from E_F , does not change, but its intensity increases.

There is also the possibility that the zero energy excitation is not wandering further into the chain but moving onto the perturbing atom. We can check this by looking for excitations on the perturbing atom at $\pm\Delta_t$. The spectra of the perturbing atoms for cases 1, 3-6 are shown in Figure 6.34. Please note that the measurement for perturbation case 2 is missing. Furthermore, the perturbing object for the perturbation case 5 is the buried subsurface defect. At first,

6 Bottom up constructed YSR-chains on a superconducting Rashba surface

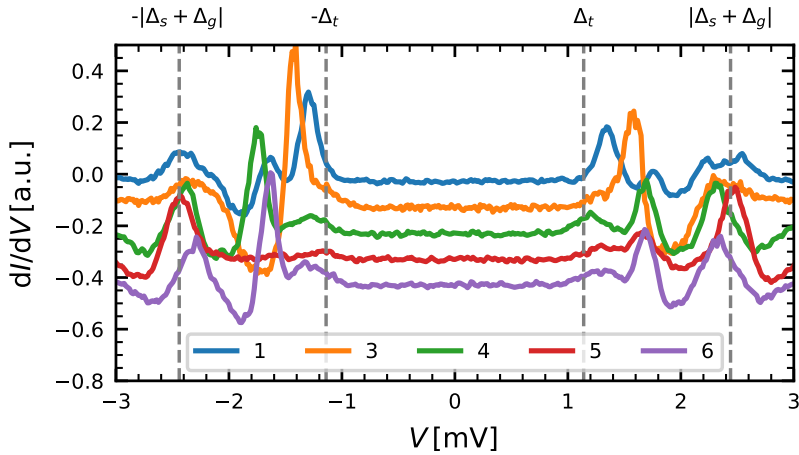


Figure 6.34: Bias spectroscopy measurements taken on the perturbing atoms: The measurements were taken on the perturbing Fe_b , with the indices corresponding to the perturbation cases shown in Figure 6.31. The red line, corresponding to the case 5, was taken on the buried atom Figure 6.31F. Note that the measurement for the perturbation case 2 is missing. Parameters: $I_{\text{stab}} = 500 \text{ pA}$, $V_{\text{stab}} = 5 \text{ mV}$, $V_{\text{mod}} = 50 \text{ } \mu\text{V}$ and $T = 320 \text{ mK}$.

the spectra for the cases look very different. This can be explained by the atom being adsorbed in different locations on the sample. We can also not exclude possible effects of local disorder in the substrate, either caused by defects below the surface or by a small surface distortion by the adsorption of the chain atoms itself. The measurement of case 6 might even indicate a small tip change, as seen from the deviation of the coherence peaks energetic position from the other measurements. The spectra measured on the perturbing Fe_b do not show any clear peak located at $\pm\Delta_t$. Therefore, we can exclude that the edge state of the chain moved onto the perturbing atom. For case 5, a minimal excitation can be seen $-\Delta_t$. However, compared to the other YSR-states, it is too small to draw any conclusions from this measurement.

6.9 Conclusion

In this chapter, we made use of the unique properties of thin epitaxially grown Ag(111) islands to create a Rashba alloy on top of Nb, the elemental superconductor with the highest T_c . By employing the QPI method, we not only confirmed the presence of the expected scattering pattern in our sample, as reported in other works but also found scattering branches that have not yet been reported. In addition, indications of quantum well states formed in the thin Ag films were seen. These quantum well states are expected to hybridize with the Rashba surface states [187, 190].

Furthermore, we analyzed the spectroscopic low-energy behavior and extracted a proximitized gap on the surface of about 60 % of

the gap of elemental Nb at a temperature of 4.52 K. We observed that the measured gap closes as the temperature inside the STM increases. We see a gap closing at around 8.5 K, a bit smaller than the T_c of Nb.

We then proceeded to deposit magnetic Fe-atoms onto the superconducting Rashba surface, aiming to investigate whether we can realize a topological superconductor. According to theory, this system would possess all the required ingredients for constructing a topological superconductor. We identified two adsorption sites for the Fe-atoms on the surface, labeling them as *hollow* and *bridge* site Fe.

Both types of Fe-atoms exhibit YSR-states, where the hollow site Fe-atoms were identified as most promising for building a topological superconductor for two reasons. Firstly, the Fe_h shows a YSR-state right at E_F , suggesting a higher likelihood of a YSR-band crossing the E_F when starting to hybridize along the chain. Secondly, this hollow site YSR-state exhibits a longer-range decay compared to Fe_b , which explains why pairs made out of Fe_h atoms show considerable shifts and splitting of their YSR-state already at quite long interatomic distances.

We arranged Fe_h atoms to form YSR-chains and observed a band-like structure forming along the chain, yielding edge states close to zero energy. However, the YSR-bands reveal no obvious mini-gap, i.e., if there is one, it has a width below our experimental energy resolution of $50 \mu\text{eV}$.

Several reasons might account for this. One potential issue could

be the local electronic disorder of the substrate, as evidenced by variations in intensity in the spectroscopic line profiles throughout the chain. This local disorder might hinder the formation of a clean minigap.

Another possible reason could be that the hybridization strength between the atoms is not sufficiently robust. The spectroscopic line profiles indicate that the YSR-states appear very localized on specific atoms, making it challenging to speak of a YSR-band compared to other systems that used artificially bottom-up fabricated YSR-states.

A third reason could be that the strong SOC in the Rashba surface state does not enter the YSR-bands, leading to a negligible size of a potential minigap.

7 Conclusion and outlook

In this thesis, I have demonstrated three main results. The first part shows the first experimental real-space investigation of Machida-Shibata states (MSSs), which gives us a better understanding of the mechanisms of proximity superconductivity in systems hosting surface states. These results state a difference between the superconductivity proximitized in a system's bulk and the one proximitized in the system's surface. Overall, the system behaves like a two-band superconductor with two different gaps: one for the bulk and one for the surface. This brings fundamental considerations to the design of the superconducting hybrid system. The second main result is the creation of a so-called Yu-Shiba-Rusinov (YSR) mirage, which demonstrates a coupling between the surface state mode of a quantum corral and a YSR-impurity. With this, a YSR-state can be projected over large distances inside the corral. This effect enables us to detect and measure YSR-based systems non-locally and without perturbing the YSR-state. When we think of the implementation of topological qubits, this effect can be used for reading out the qubit's states non-locally and non-evasively by coupling Majorana zero modes to a corral. The final result is the first demonstration of a potential system to create a topological superconductor based on Rashba-surface alloys. Rashba surface alloys are interesting materials due to their large spin-orbit coupling (SOC). Rashba SOC has become a fundamental building block in creating exotic states of matter [199]. Its use as an ingredient for topological superconductivity, as shown in this thesis, is only one of the many applications. The platform presented in

this thesis allows a detailed study of the interplay of strong spin-orbit interaction in conjunction with magnetism and proximitized superconductivity.

In this thesis, only simple artificial lattice systems, such as single quantum corrals or 1D chains, have been explored. However, to progress on this work's topics, one can consider building more complex atom-by-atom structures and study them under the influence of superconductivity.

Several works on creating artificial lattices on noble metal surfaces have been published in the last decade. Similar as in the present work, atoms have been arranged on a noble metal's (111) surface to create quantum states by confining the surface state. The examples range from the creation of an artificial graphene lattice [113] over the engineering of p-bands [112] to the design of a lattice with fractal geometry [200] or the realization of a Lieb lattice [111]. However, these ideas have only been realized in bulk noble metal systems and have not yet been studied under the influence of superconductivity. As we have shown, combining artificial lattices with proximity superconductivity can lead to the discovery of new exciting phenomena such as the MSSs. With this in mind, creating states with flat bands, such as the Lieb lattice, is particularly interesting. Flat band systems are known for strong electron-electron correlations, which can give rise to various exotic phenomena [201]. Combining strongly correlated states with proximity-superconductivity is particularly interesting due to their potential connection to unconventional superconductivity.

The above examples have all been built on a Cu(111) surface. Therefore, one could consider growing Cu(111) instead of Ag(111) on Nb(110) to build up on the existing works on noble metal surface artificial lattices. Furthermore, the studies on these proximitized complex artificial lattices could be studied in conjunction with magnetism by introducing magnetic atoms similar to our studies on the YSR-mirage.

For the superconducting BiAg₂, further studies could be done in the direction of corrals, as we did on the Ag(111) surface. Studies on BiCu₂ have shown that it is possible to create quantum corrals by confining the surface state of the Rashba surface alloy [186]. It would be interesting to see how the MSSs that we have learned about during this thesis interact with the Rashba SOC of the BiAg₂ surface state. Finally, one could also consider switching to similar Rashba surface alloys such as PbAg₂ or BiCu₂, which are similar in terms of preparation procedures but provide different surface band dispersions.

Bibliography

1. Feynman, R. P. Simulating physics with computers. *International Journal of Theoretical Physics* **21**, 467–488 (June 1982).
2. Grover, L. K. A fast quantum mechanical algorithm for database search. arXiv: 9605043 [quant-ph] (May 1996).
3. Harrow, A. W. & Montanaro, A. Quantum computational supremacy. *Nature* **549**, 203–209 (Sept. 2017).
4. Arute, F. *et al.* Quantum supremacy using a programmable superconducting processor. *Nature* **574**, 505–510 (Oct. 2019).
5. Wu, Y. *et al.* Strong Quantum Computational Advantage Using a Superconducting Quantum Processor. *Physical Review Letters* **127**, 180501 (Oct. 2021).
6. Madsen, L. S. *et al.* Quantum computational advantage with a programmable photonic processor. *Nature* **606**, 75–81 (June 2022).
7. Huang, H.-Y. *et al.* Quantum advantage in learning from experiments. *Science* **376**, 1182–1186 (June 2022).
8. Shor, P. W. Scheme for reducing decoherence in quantum computer memory. *Physical Review A* **52**, R2493–R2496 (Oct. 1995).
9. Chiaverini, J. *et al.* Realization of quantum error correction. *Nature* **432**, 602–605 (Dec. 2004).
10. Aoki, T. *et al.* Quantum error correction beyond qubits. *Nature Physics* **5**, 541–546 (Aug. 2009).

Bibliography

11. Suzuki, Y., Endo, S., Fujii, K. & Tokunaga, Y. Quantum Error Mitigation as a Universal Error Reduction Technique: Applications from the NISQ to the Fault-Tolerant Quantum Computing Eras. *PRX Quantum* **3**, 010345 (Mar. 2022).
12. Nayak, C., Simon, S. H., Stern, A., Freedman, M. & Das Sarma, S. Non-Abelian anyons and topological quantum computation. *Reviews of Modern Physics* **80**, 1083–1159. arXiv: 0707.1889 (Sept. 2008).
13. Freedman, M., Kitaev, A., Larsen, M. & Wang, Z. Topological quantum computation. *Bulletin of the American Mathematical Society* **40**, 31–38 (Oct. 2002).
14. Wilczek, F. Quantum Mechanics of Fractional-Spin Particles. *Physical Review Letters* **49**, 957–959 (Oct. 1982).
15. Kitaev, A. Y. Unpaired Majorana fermions in quantum wires. *Physics-Uspekhi* **44**, 131–136. arXiv: 0010440 [cond-mat] (Oct. 2001).
16. Fu, L. & Kane, C. L. Superconducting Proximity Effect and Majorana Fermions at the Surface of a Topological Insulator. *Physical Review Letters* **100**, 096407 (Mar. 2008).
17. Potter, A. C. & Lee, P. A. Topological superconductivity and Majorana fermions in metallic surface states. *Physical Review B - Condensed Matter and Materials Physics* **85**, 094516. arXiv: 1201.2176 (Mar. 2012).
18. Mourik, V. *et al.* Signatures of Majorana Fermions in Hybrid Superconductor-Semiconductor Nanowire Devices. *Science* **336**, 1003–1007 (May 2012).

19. Nadj-Perge, S., Drozdov, I. K., Bernevig, B. A. & Yazdani, A. Proposal for realizing Majorana fermions in chains of magnetic atoms on a superconductor. *Physical Review B* **88**, 020407 (July 2013).
20. Klinovaja, J. & Loss, D. Giant Spin-Orbit Interaction Due to Rotating Magnetic Fields in Graphene Nanoribbons. *Physical Review X* **3**, 011008 (Jan. 2013).
21. Braunecker, B. & Simon, P. Interplay between Classical Magnetic Moments and Superconductivity in Quantum One-Dimensional Conductors: Toward a Self-Sustained Topological Majorana Phase. *Physical Review Letters* **111**, 147202 (Oct. 2013).
22. Beenakker, C. W. Search for majorana fermions in superconductors. *Annual Review of Condensed Matter Physics* **4**, 113–136. arXiv: 1112.1950 (Apr. 2013).
23. Albrecht, S. M. *et al.* Exponential protection of zero modes in Majorana islands. *Nature* **531**, 206–209. arXiv: 1603.03217 (Mar. 2016).
24. Deng, M. T. *et al.* Majorana bound state in a coupled quantum-dot hybrid-nanowire system. *Science* **354**, 1557–1562 (Dec. 2016).
25. Lutchyn, R. M. *et al.* Majorana zero modes in superconductor–semiconductor heterostructures. *Nature Reviews Materials* **3**, 52–68 (May 2018).

26. Conte, R. L., Wiebe, J., Rachel, S., Morr, D. K. & Wiesendanger, R. *Magnet-superconductor hybrid quantum systems: a materials platform for topological superconductivity* 2024. arXiv: 2410.20177 [cond-mat.supr-con].
27. Kim, H. *et al.* Toward tailoring Majorana bound states in artificially constructed magnetic atom chains on elemental superconductors. *Science Advances* **4**, eaar5251 (May 2018).
28. Nadj-Perge, S. *et al.* Observation of Majorana fermions in ferromagnetic atomic chains on a superconductor. *Science* **346**, 602–607 (Oct. 2014).
29. Schneider, L. *et al.* Topological Shiba bands in artificial spin chains on superconductors. *Nature Physics* **17**, 943–948 (Aug. 2021).
30. Palacio-Morales, A. *et al.* Atomic-scale interface engineering of Majorana edge modes in a 2D magnet-superconductor hybrid system. *Science Advances* **5** (July 2019).
31. Bazarnik, M. *et al.* Antiferromagnetism-driven two-dimensional topological nodal-point superconductivity. *Nature Communications* **14**, 614 (Feb. 2023).
32. Soldini, M. O. *et al.* Two-dimensional Shiba lattices as a possible platform for crystalline topological superconductivity. *Nature Physics* **19**, 1848–1854 (Dec. 2023).
33. Sun, H.-H. *et al.* Majorana Zero Mode Detected with Spin Selective Andreev Reflection in the Vortex of a Topological Superconductor. *Physical Review Letters* **116**, 257003 (June 2016).

34. Ruby, M., Heinrich, B. W., Peng, Y., von Oppen, F. & Franke, K. J. Exploring a Proximity-Coupled Co Chain on Pb(110) as a Possible Majorana Platform. *Nano Letters* **17**, 4473–4477. arXiv: 1704.05756 (July 2017).
35. Jaeck, B. *et al.* Observation of a Majorana zero mode in a topologically protected edge channel. *Science* **364**, 1255–1259 (June 2019).
36. Manna, S. *et al.* Signature of a pair of Majorana zero modes in superconducting gold surface states. *Proceedings of the National Academy of Sciences* **117**, 8775–8782 (Apr. 2020).
37. Goedecke, J. J. *et al.* Correlation of Magnetism and Disordered Shiba Bands in Fe Monolayer Islands on Nb(110). *ACS Nano* **16**, 14066–14074 (Sept. 2022).
38. Schneider, L. *et al.* Precursors of Majorana modes and their length-dependent energy oscillations probed at both ends of atomic Shiba chains. *Nature Nanotechnology* **17**, 384–389. arXiv: 2104.11503 (Apr. 2022).
39. Schneider, L. *et al.* Probing the topologically trivial nature of end states in antiferromagnetic atomic chains on superconductors. *Nature Communications* **14**, 2742 (May 2023).
40. Beck, P. *et al.* Search for large topological gaps in atomic spin chains on proximitized superconducting heavy-metal layers. *Communications Physics* **6**, 83 (Apr. 2023).
41. Trivini, S. *et al.* Cooper Pair Excitation Mediated by a Molecular Quantum Spin on a Superconducting Proximitized Gold Film. *Physical Review Letters* **130**, 136004 (Mar. 2023).

Bibliography

42. Ashcroft, N. W. & Mermin, D. N. *Festkörperphysik 1072* (Oldenbourg Wissenschaftsverlag, 2007).
43. Kittel, C. & McEuen, P. *Introduction to Solid State Physics* (Wiley, 2018).
44. Shockley, W. On the Surface States Associated with a Periodic Potential. *Physical Review* **56**, 317–323 (Aug. 1939).
45. Mönch, W. *Semiconductor Surfaces and Interfaces* (Springer Berlin Heidelberg, Berlin, Heidelberg, 2001).
46. Heimann, P., Neddermeyer, H. & Roloff, H. F. Ultraviolet photoemission for intrinsic surface states of the noble metals. *Journal of Physics C: Solid State Physics* **10**, L17–L21 (Jan. 1977).
47. Crommie, M. F., Lutz, C. P. & Eigler, D. M. Imaging standing waves in a two-dimensional electron gas. *Nature* **363**, 524–527 (June 1993).
48. Hasegawa, Y. & Avouris, P. Direct observation of standing wave formation at surface steps using scanning tunneling spectroscopy. *Physical Review Letters* **71**, 1071–1074 (Aug. 1993).
49. Van Delft, D. & Kes, P. The discovery of superconductivity. *Physics Today* **63**, 38–43 (Sept. 2010).
50. Meissner, W. & Ochsenfeld, R. Ein neuer Effekt bei Eintritt der Supraleitfähigkeit. *Die Naturwissenschaften* **21**, 787–788 (Nov. 1933).
51. Bardeen, J., Cooper, L. N. & Schrieffer, J. R. Theory of Superconductivity. *Physical Review* **108**, 1175–1204 (Dec. 1957).

52. Czycholl, G. *Theoretische Festkörperphysik* (Springer Berlin Heidelberg, Berlin, Heidelberg, 2008).
53. Bogoljubov, N. N. On a new method in the theory of superconductivity. *Il Nuovo Cimento* **7**, 794–805 (Mar. 1958).
54. Valatin, J. G. Comments on the theory of superconductivity. *Il Nuovo Cimento* **7**, 843–857 (Mar. 1958).
55. Bergeret, F. S., Volkov, A. F. & Efetov, K. B. Odd triplet superconductivity and related phenomena in superconductor-ferromagnet structures. *Reviews of Modern Physics* **77**, 1321–1373 (Nov. 2005).
56. Yamazaki, H., Shannon, N. & Takagi, H. Interplay between superconductivity and ferromagnetism in epitaxial Nb(110)/Au(111)/Fe(110) trilayers. *Physical Review B* **73**, 094507 (Mar. 2006).
57. de Gennes, P. G. Boundary Effects in Superconductors. *Reviews of Modern Physics* **36**, 225–237 (Jan. 1964).
58. Buckel, W. & Kleiner, R. *Supraleitung: Grundlagen und Anwendungen* (Wiley, 2013).
59. De Gennes, P. & Saint-James, D. Elementary excitations in the vicinity of a normal metal-superconducting metal contact. *Physics Letters* **4**, 151–152 (Mar. 1963).
60. Ortuzar, J., Pascual, J. I., Bergeret, F. S. & Casalilla, M. A. Theory of a single magnetic impurity on a thin metal film in proximity to a superconductor. *Physical Review B* **108**, 024511 (July 2023).

61. Yu, L. Bound state in superconductors with paramagnetic impurities. *Acta Phys. Sin.* **21**, 75 (1968).
62. Shiba, H. Classical Spins in Superconductors. *Progress of Theoretical Physics* **40**, 435–451 (Sept. 1968).
63. Rusinov, A. I. Superconductivity near a paramagnetic impurity. *JETP Lett. (USSR) (Engl. Transl.)*, *9*: 85-7 (Jan. 20, 1969). **9** (1969).
64. Balatsky, A. V., Vekhter, I. & Zhu, J.-X. Impurity-induced states in conventional and unconventional superconductors. *Reviews of Modern Physics* **78**, 373–433 (May 2006).
65. Heinrich, B. W., Pascual, J. I. & Franke, K. J. Single magnetic adsorbates on s -wave superconductors. *Progress in Surface Science* **93**, 1–19 (Feb. 2018).
66. Ménard, G. C. *et al.* Coherent long-range magnetic bound states in a superconductor. *Nature Physics* **11**, 1013–1016 (Dec. 2015).
67. Kim, H., Rózsa, L., Schreyer, D., Simon, E. & Wiesendanger, R. Long-range focusing of magnetic bound states in superconducting lanthanum. *Nature Communications* **11**, 4573 (Sept. 2020).
68. Kezilebieke, S., Dvorak, M., Ojanen, T. & Liljeroth, P. Coupled Yu–Shiba–Rusinov States in Molecular Dimers on NbSe₂. *Nano Letters* **18**, 2311–2315. arXiv: 1701 . 03288 (Apr. 2018).
69. Ruby, M., Heinrich, B. W., Peng, Y., von Oppen, F. & Franke, K. J. Wave-Function Hybridization in Yu-Shiba-Rusinov Dimers. *Physical Review Letters* **120**, 156803 (Apr. 2018).

70. Beck, P. *et al.* Spin-orbit coupling induced splitting of Yu-Shiba-Rusinov states in antiferromagnetic dimers. *Nature Communications* **12**, 2040. arXiv: 2010.04031 (Apr. 2021).
71. Bihlmayer, G., Rader, O. & Winkler, R. Focus on the Rashba effect. *New Journal of Physics* **17**, 050202 (May 2015).
72. Michiardi, M. *et al.* Optical manipulation of Rashba-split 2-dimensional electron gas. *Nature Communications* **13**, 3096 (June 2022).
73. Zhai, Y. *et al.* Giant Rashba splitting in 2D organic-inorganic halide perovskites measured by transient spectroscopies. *Science Advances* **3** (July 2017).
74. Bernevig, B. A. & Hughes, T. L. *Topological Insulators and Topological Superconductors* 247 (Princeton University Press, Apr. 2013).
75. Majorana, E. Teoria simmetrica dell'elettrone e del positrone. *Il Nuovo Cimento* **14**, 171–184 (Apr. 1937).
76. Lado, J. L. *pyqula library*
77. Kitaev, A. Fault-tolerant quantum computation by anyons. *Annals of Physics* **303**, 2–30 (Jan. 2003).
78. Sau, J., Simon, S., Vishveshwara, S. & Williams, J. R. From anyons to Majoranas. *Nature Reviews Physics* **2**, 667–668. arXiv: 2103.14564 (Oct. 2020).
79. Sarma, S. D., Freedman, M. & Nayak, C. Majorana zero modes and topological quantum computation. *npj Quantum Information* **1**, 15001 (Oct. 2015).

Bibliography

80. Chatterjee, A. *et al.* *Semiconductor qubits in practice* Feb. 2021. arXiv: 2005.06564.
81. Kallin, C. & Berlinsky, A. J. Is Sr_2RuO_4 a chiral p-wave superconductor? *Journal of Physics: Condensed Matter* **21**, 164210 (Apr. 2009).
82. Huang, W. & Wang, Z. Possibility of mixed helical p-wave pairings in Sr_2RuO_4 . *Physical Review Research* **3**, L042002 (Oct. 2021).
83. Pientka, F., Glazman, L. I. & von Oppen, F. Topological superconducting phase in helical Shiba chains. *Physical Review B* **88**, 155420 (Oct. 2013).
84. Binnig, G., Rohrer, H., Gerber, C. & Weibel, E. Surface Studies by Scanning Tunneling Microscopy. *Physical Review Letters* **49**, 57–61 (July 1982).
85. Guo, H., Wang, Y., Du, S. & Gao, H.-J. High-resolution scanning tunneling microscopy imaging of $\text{Si}(1 \times 1)-7 \times 7$ structure and intrinsic molecular states. *Journal of Physics: Condensed Matter* **26**, 394001 (Oct. 2014).
86. Wiesendanger, R. *Scanning Probe Microscopy and Spectroscopy* (Cambridge University Press, Sept. 1994).
87. Chen, C. J. & Smith, W. F. Introduction to Scanning Tunneling Microscopy. *American Journal of Physics* **62**, 573–574 (June 1994).
88. Chen, W., Madhavan, V., Jamneala, T. & Crommie, M. F. *Scanning Tunneling Microscopy Observation of an Electronic Su-*

-
- perlattice at the Surface of Clean Gold* tech. rep. 7 (Feb. 1998), 1469–1472.
89. Esaki, L. Long Journey into Tunneling. *Science* **183**, 1149–1155 (Mar. 1974).
 90. Sonntag, A. *Magnetolectric Coupling and Thermally Driven Magnetization Dynamics Studied on the Atomic Scale* PhD thesis (Universität Hamburg, 2014), 113.
 91. Binnig, G. & Rohrer, H. Scanning tunneling microscopy. *Surface Science* **126**, 236–244 (Mar. 1983).
 92. Griffiths, D. J. & Schroeter, D. F. *Introduction to quantum mechanics* Third edition (Cambridge University Press, Cambridge ; New York, NY, 2018).
 93. Bardeen, J. Tunnelling from a Many-Particle Point of View. *Physical Review Letters* **6**, 57–59 (Jan. 1961).
 94. Tersoff, J. & Hamann, D. R. Theory and Application for the Scanning Tunneling Microscope. *Physical Review Letters* **50**, 1998–2001 (June 1983).
 95. Eigler, D. M. & Schweizer, E. K. Positioning single atoms with a scanning tunnelling microscope. *Nature* **344**, 524–526 (Apr. 1990).
 96. Stroscio, J. A. & Eigler, D. M. Atomic and Molecular Manipulation with the Scanning Tunneling Microscope. *Science* **254**, 1319–1326 (Nov. 1991).
 97. Griffiths, D. J. *Introduction to electrodynamics* (Pearson, 2013).

98. Pan, S. H., Hudson, E. W. & Davis, J. C. Vacuum tunneling of superconducting quasiparticles from atomically sharp scanning tunneling microscope tips. *Applied Physics Letters* **73**, 2992–2994 (Nov. 1998).
99. Löptien, P., Zhou, L., Khajetoorians, A. A., Wiebe, J. & Wiesendanger, R. Superconductivity of lanthanum revisited: enhanced critical temperature in the clean limit. *Journal of Physics: Condensed Matter* **26**, 425703 (Oct. 2014).
100. Wiebe, J. *et al.* A 300 mK ultra-high vacuum scanning tunneling microscope for spin-resolved spectroscopy at high energy resolution. *Review of Scientific Instruments* **75**, 4871–4879 (Nov. 2004).
101. Cornils, L. *STM investigations of superconductor hybrid systems: magnetic adatoms and chains on superconductors to thin superconducting films on topological insulators* PhD thesis (2019), 271.
102. Wiebe, J. *Aufbau einer 300mK-UHV-RTM-Anlage mit 14T-Magnet und Untersuchung eines stark ungeordneten zweidimensionalen Elektronensystems* PhD thesis (2003).
103. Eschrig, M. Spin-polarized supercurrents for spintronics: a review of current progress. *Reports on Progress in Physics* **78**, 104501 (Oct. 2015).
104. Zhang, R.-X., Cole, W. S., Wu, X. & Das Sarma, S. Higher-Order Topology and Nodal Topological Superconductivity in Fe(Se,Te) Heterostructures. *Physical Review Letters* **123**, 167001 (Oct. 2019).

105. Kezilebieke, S. *et al.* Topological superconductivity in a van der Waals heterostructure. *Nature* **588**, 424–428. arXiv: 2002.02141 (Dec. 2020).
106. Brüning, R. *et al.* The Non-collinear Path to Topological Superconductivity, 1–7. arXiv: 2405.14673 (May 2024).
107. Tomanic, T. *et al.* Local-strain mapping on Ag(111) islands on Nb(110). *Applied Physics Letters* **101**, 063111 (Aug. 2012).
108. Fölsch, S., Martínez-Blanco, J., Yang, J., Kanisawa, K. & Erwin, S. C. Quantum dots with single-atom precision. *Nature Nanotechnology* **9**, 505–508 (July 2014).
109. Drost, R., Ojanen, T., Harju, A. & Liljeroth, P. Topological states in engineered atomic lattices. *Nature Physics* **13**, 668–671 (July 2017).
110. Khajetoorians, A. A., Wegner, D., Otte, A. F. & Swart, I. Creating designer quantum states of matter atom-by-atom. *Nature Reviews Physics* **1**, 703–715 (Sept. 2019).
111. Slot, M. R. *et al.* Experimental realization and characterization of an electronic Lieb lattice. *Nature Physics* **13**, 672–676. arXiv: 1611.04641 (July 2017).
112. Slot, M. R. *et al.* p-Band Engineering in Artificial Electronic Lattices. *Physical Review X* **9**, 011009 (Jan. 2019).
113. Gomes, K. K., Mar, W., Ko, W., Guinea, F. & Manoharan, H. C. Designer Dirac fermions and topological phases in molecular graphene. *Nature* **483**, 306–310 (Mar. 2012).

Bibliography

114. Pan, Y., Yang, J., Erwin, S. C., Kanisawa, K. & Fölsch, S. Reconfigurable Quantum-Dot Molecules Created by Atom Manipulation. *Physical Review Letters* **115**, 076803 (Aug. 2015).
115. Sierda, E. *et al.* Quantum simulator to emulate lower-dimensional molecular structure. *Science* **380**, 1048–1052 (June 2023).
116. Odobesko, A. B. *et al.* Preparation and electronic properties of clean superconducting Nb(110) surfaces. *Physical Review B* **99**, 115437 (Mar. 2019).
117. Schneider, L. *et al.* Proximity superconductivity in atom-by-atom crafted quantum dots. *Nature* **621**, 60–65 (Sept. 2023).
118. Vaxevani, K. *et al.* Extending the Spin Excitation Lifetime of a Magnetic Molecule on a Proximitized Superconductor. *Nano Letters* **22**, 6075–6082 (Aug. 2022).
119. Stranski, I. N. & Krastanow, L. Zur Theorie der orientierten Ausscheidung von Ionenkristallen aufeinander. *Monatshefte für Chemie und verwandte Teile anderer Wissenschaften* **71**, 351–364 (1937).
120. Paniago, R., Matzdorf, R., Meister, G. & Goldmann, A. Temperature dependence of Shockley-type surface energy bands on Cu(111), Ag(111) and Au(111). *Surface Science* **336**, 113–122 (Aug. 1995).
121. Bürgi, L., Petersen, L., Brune, H. & Kern, K. Noble metal surface states: deviations from parabolic dispersion. *Surface Science* **447**, L157–L161 (Feb. 2000).

122. Grothe, S. *et al.* Quantifying Many-Body Effects by High-Resolution Fourier Transform Scanning Tunneling Spectroscopy. *Physical Review Letters* **111**, 246804 (Dec. 2013).
123. Li, J., Schneider, W.-D. & Berndt, R. Local density of states from spectroscopic scanning-tunneling-microscope images: Ag(111). *Physical Review B* **56**, 7656–7659 (Sept. 1997).
124. Tomanic, T., Schackert, M., Wulfhekel, W., Sürgers, C. & Löhneysen, H. V. Two-band superconductivity of bulk and surface states in Ag thin films on Nb. *Physical Review B* **94**, 220503. arXiv: 1506.06524 (Dec. 2016).
125. Schneider, L. *et al.* Scanning tunneling spectroscopy study of proximity superconductivity in finite-size quantized surface states. *Physical Review B* **110**, L100505 (Sept. 2024).
126. Crommie, M. F., Lutz, C. P. & Eigler, D. M. Confinement of electrons to quantum corrals on a metal surface. *Science* **262**, 218–220 (Oct. 1993).
127. Li, J., Schneider, W.-D., Berndt, R. & Crampin, S. Electron Confinement to Nanoscale Ag Islands on Ag(111): A Quantitative Study. *Physical Review Letters* **80**, 3332–3335 (Apr. 1998).
128. Hla, S.-W., Braun, K.-F., Iancu, V. & Deshpande, A. Single-Atom Extraction by Scanning Tunneling Microscope Tip Crash and Nanoscale Surface Engineering. *Nano Letters* **4**, 1997–2001 (Oct. 2004).

Bibliography

129. Limot, L., Kröger, J., Berndt, R., Garcia-Lekue, A. & Hofer, W. A. Atom Transfer and Single-Atom Contacts. *Physical Review Letters* **94**, 126102 (Apr. 2005).
130. Pan, S. H. *et al.* Imaging the effects of individual zinc impurity atoms on superconductivity in $\text{Bi}_2\text{Sr}_2\text{CaCu}_2\text{O}_{8+\delta}$. *Nature* **403**, 746–750 (Feb. 2000).
131. Yazdani, A., Howald, C. M., Lutz, C. P., Kapitulnik, A. & Eigler, D. M. Impurity-Induced Bound Excitations on the Surface of $\text{Bi}_2\text{Sr}_2\text{CaCu}_2\text{O}_8$. *Physical Review Letters* **83**, 176–179 (July 1999).
132. Nicolay, G., Reinert, F., Hühner, S. & Blaha, P. Spin-orbit splitting of the L-gap surface state on Au(111) and Ag(111). *Physical Review B* **65**, 033407 (Dec. 2001).
133. Machida, K. & Shibata, F. Bound States Due to Resonance Scattering in Superconductor. *Progress of Theoretical Physics* **47**, 1817–1823 (June 1972).
134. Gharavi, K., Hoving, D. & Baugh, J. Readout of Majorana parity states using a quantum dot. *Physical Review B* **94**, 155417 (Oct. 2016).
135. Plugge, S., Rasmussen, A., Egger, R. & Flensberg, K. Majorana box qubits. *New Journal of Physics* **19**, 012001 (Jan. 2017).
136. Karzig, T. *et al.* Scalable designs for quasiparticle-poisoning-protected topological quantum computation with Majorana zero modes. *Physical Review B* **95**, 235305 (June 2017).
137. Steiner, J. F. & von Oppen, F. Readout of Majorana qubits. *Physical Review Research* **2**, 033255 (Aug. 2020).

138. Fiete, G. A. & Heller, E. J. Colloquium : Theory of quantum corrals and quantum mirages. *Reviews of Modern Physics* **75**, 933–948 (July 2003).
139. Manoharan, H. C., Lutz, C. P. & Eigler, D. M. Quantum mirages formed by coherent projection of electronic structure. *Nature* **403**, 512–515 (Feb. 2000).
140. Li, Q. *et al.* Kondo-free mirages in elliptical quantum corrals. *Nature Communications* **11**, 1400 (Mar. 2020).
141. Aapro, M., Kipnis, A., Lado, J. L., Kezilebieke, S. & Liljeroth, P. Tuning spinaron and Kondo resonances via quantum confinement. *Physical Review B* **109**, 195415. arXiv: 2312.03364 [cond-mat.mes-hall] (May 2024).
142. Madhavan, V., Chen, W., Jamneala, T., Crommie, M. F. & Wingreen, N. S. Tunneling into a Single Magnetic Atom: Spectroscopic Evidence of the Kondo Resonance. *Science* **280**, 567–569 (Apr. 1998).
143. Bouaziz, J., Mendes Guimarães, F. S. & Lounis, S. A new view on the origin of zero-bias anomalies of Co atoms atop noble metal surfaces. *Nature Communications* **11**, 6112. arXiv: 2003.01746 (Nov. 2020).
144. Friedrich, F., Odobesko, A., Bouaziz, J., Lounis, S. & Bode, M. Evidence for spinarons in Co adatoms. *Nature Physics* **20**, 28–33 (Jan. 2024).
145. Noei, N. *et al.* Manipulating the Spin Orientation of Co Atoms Using Monatomic Cu Chains. *Nano Letters* **23**, 8988–8994 (Oct. 2023).

Bibliography

146. Gadzuk, J. W. & Plihal, M. Quantum mirages in scanning tunneling spectroscopy of Kondo adsorbates: Vibrational signatures. *Physical Review B* **68**, 235413 (Dec. 2003).
147. Fransson, J. & Balatsky, A. V. Imaging spin-inelastic Friedel oscillations emerging from magnetic impurities. *Physical Review B* **85**, 161401 (Apr. 2012).
148. Agam, O. & Schiller, A. Projecting the Kondo effect: theory of the quantum mirage. *Physical Review Letters* **86**, 484–487 (Jan. 2001).
149. Weissmann, M. & Bonadeo, H. A simple interpretation of quantum mirages. *Physica E: Low-dimensional Systems and Nanostructures* **10**, 544–548 (June 2001).
150. Hallberg, K., Correa, A. A. & Balseiro, C. A. Spectroscopic and Magnetic Mirages of Impurities in Nanoscopic Systems. *Physical Review Letters* **88**, 066802 (Jan. 2002).
151. Morr, D. K. & Stavropoulos, N. A. Quantum Corrals, Eigenmodes, and Quantum Mirages in s-Wave Superconductors. *Physical Review Letters* **92**, 107006. arXiv: 0304533 [cond-mat] (Mar. 2004).
152. Fiete, G. A. *et al.* Scattering Theory of Kondo Mirages and Observation of Single Kondo Atom Phase Shift. *Physical Review Letters* **86**, 2392–2395 (Mar. 2001).
153. Porras, D., Fernández-Rossier, J. & Tejedor, C. Microscopic theory for quantum mirages in quantum corrals. *Physical Review B* **63**, 155406 (Mar. 2001).

154. Ruby, M., Peng, Y., von Oppen, F., Heinrich, B. W. & Franke, K. J. Orbital Picture of Yu-Shiba-Rusinov Multiplets. *Physical Review Letters* **117**, 186801. arXiv: 1608.03457 (Oct. 2016).
155. Huang, H. *et al.* Quantum phase transitions and the role of impurity-substrate hybridization in Yu-Shiba-Rusinov states. *Communications Physics* **3**, 199 (Nov. 2020).
156. Franke, K. J., Schulze, G. & Pascual, J. I. Competition of Superconducting Phenomena and Kondo Screening at the Nanoscale. *Science* **332**, 940–944 (May 2011).
157. Knorr, N. *et al.* Long-range adsorbate interactions mediated by a two-dimensional electron gas. *Physical Review B* **65**, 115420 (Mar. 2002).
158. Bürgi, L., Jeandupeux, O., Hirstein, A., Brune, H. & Kern, K. Confinement of Surface State Electrons in Fabry-Pérot Resonators. *Physical Review Letters* **81**, 5370–5373 (Dec. 1998).
159. Hörmandinger, G. & Pendry, J. B. Interaction of surface states with rows of adsorbed atoms and other one-dimensional scatterers. *Physical Review B* **50**, 18607–18620 (Dec. 1994).
160. Crampin, S., Boon, M. H. & Inglesfield, J. E. Influence of Bulk States on Laterally Confined Surface State Electrons. *Physical Review Letters* **73**, 1015–1018 (Aug. 1994).
161. Hoffman, S., Klinovaja, J., Meng, T. & Loss, D. Impurity-induced quantum phase transitions and magnetic order in conventional superconductors: Competition between bound and quasiparticle states. *Physical Review B* **92**, 125422. arXiv: 1503.08762 (Sept. 2015).

Bibliography

162. Brydon, P. M. R., Das Sarma, S., Hui, H.-Y. & Sau, J. D. Topological Yu-Shiba-Rusinov chain from spin-orbit coupling. *Physical Review B* **91**, 064505 (Feb. 2015).
163. Park, K., Nyari, B., Laszloffy, A., Szunyogh, L. & Ujfalussy, B. Spin-polarized zero-bias peak from a single magnetic impurity at an s-wave superconductor: first-principles study. arXiv: 2109.05511 (Sept. 2021).
164. Beck, P., Schneider, L., Wiesendanger, R. & Wiebe, J. Effect of substrate spin-orbit coupling on the topological gap size of Shiba chains, arXiv:2205.10062 [cond-mat.supr-con]. arXiv: 2205.10062 (May 2022).
165. Beck, P., Schneider, L., Wiesendanger, R. & Wiebe, J. Systematic study of Mn atoms, artificial dimers, and chains on superconducting Ta(110). *Physical Review B* **107**, 024426 (Jan. 2023).
166. Schneider, L. *et al.* Controlling in-gap end states by linking nonmagnetic atoms and artificially-constructed spin chains on superconductors. *Nature Communications* **11**, 4707 (Sept. 2020).
167. Beck, P., Schneider, L., Bachmann, L., Wiebe, J. & Wiesendanger, R. Structural and superconducting properties of ultrathin Ir films on Nb(110). *Physical Review Materials* **6**, 024801 (Feb. 2022).
168. Ast, C. R. *et al.* Local detection of spin-orbit splitting by scanning tunneling spectroscopy. *Physical Review B - Condensed Matter and Materials Physics* **75**, 3–6 (2007).

169. Bernevig, B. A., Hughes, T. L. & Zhang, S.-C. Quantum Spin Hall Effect and Topological Phase Transition in HgTe Quantum Wells. *Science* **314**, 1757–1761 (Dec. 2006).
170. Knez, I., Du, R.-R. & Sullivan, G. Evidence for Helical Edge Modes in Inverted InAs/GaSb Quantum Wells. *Physical Review Letters* **107**, 136603 (Sept. 2011).
171. Chappert, C., Fert, A. & Van Dau, F. N. The emergence of spin electronics in data storage. *Nature Materials* **6**, 813–823 (Nov. 2007).
172. Jungwirth, T., Wunderlich, J. & Olejník, K. Spin Hall effect devices. *Nature Materials* **11**, 382–390 (May 2012).
173. Fert, A. & Levy, P. M. Role of Anisotropic Exchange Interactions in Determining the Properties of Spin-Glasses. *Physical Review Letters* **44**, 1538–1541 (June 1980).
174. Fert, A., Cros, V. & Sampaio, J. Skyrmions on the track. *Nature Nanotechnology* **8**, 152–156 (Mar. 2013).
175. Ast, C. R. *et al.* Giant Spin Splitting through Surface Alloying. *Physical Review Letters* **98**, 186807 (May 2007).
176. Zhang, K. H. L. *et al.* Observation of a surface alloying-to-dealloying transition during growth of Bi on Ag(111). *Physical Review B* **83**, 235418 (June 2011).
177. Bihlmayer, G., Blügel, S. & Chulkov, E. V. Enhanced Rashba spin-orbit splitting in BiAg (111) and PbAg (111) surface alloys from first principles. *Physical Review B - Condensed Matter and Materials Physics* **75**, 1–6 (2007).

Bibliography

178. Schirone, S. *et al.* Spin-Flip and Element-Sensitive Electron Scattering in the BiAg₂ Surface Alloy. *Physical Review Letters* **114**, 166801 (Apr. 2015).
179. El-Kareh, L., Sessi, P., Bathon, T. & Bode, M. Quantum interference mapping of rashba-split bloch states in Bi/Ag(111). *Physical Review Letters* **110**, 1–5 (2013).
180. Neuhold, G. & Horn, K. Depopulation of the Ag(111) Surface State Assigned to Strain in Epitaxial Films. *Physical Review Letters* **78**, 1327–1330 (Feb. 1997).
181. Sawa, K., Aoki, Y. & Hirayama, H. Thickness dependence of Shockley-type surface states of Ag(111) ultrathin films on Si(111)7x7 substrates. *Physical Review B* **80**, 035428 (July 2009).
182. Jiang, C.-S., Yu, H.-B., Wang, X.-D., Shih, C.-K. & Ebert, P. Scanning tunneling spectroscopy of quantum well and surface states of thin Ag films grown on GaAs(110). *Physical Review B* **64**, 235410 (Nov. 2001).
183. Noguchi, R. *et al.* Direct mapping of spin and orbital entangled wave functions under interband spin-orbit coupling of giant Rashba spin-split surface states. *Physical Review B* **95**, 041111 (Jan. 2017).
184. Podder, P., Zaman Khan, T., Haque Khan, M. & Muktaadir Rahman, M. Comparative Performance Analysis of Hamming, Hanning and Blackman Window. *International Journal of Computer Applications* **96**, 1–7 (June 2014).

185. Steinbrecher, M., Harutyunyan, H., Ast, C. R. & Wegner, D. Rashba-type spin splitting from interband scattering in quasiparticle interference maps. *Physical Review B* **87**, 245436 (June 2013).
186. Jolie, W. *et al.* Creating Tunable Quantum Corrals on a Rashba Surface Alloy. *ACS Nano* **16**, 4876–4883 (Mar. 2022).
187. He, K. *et al.* Spin Polarization of Quantum Well States in Ag Films Induced by the Rashba Effect at the Surface. *Physical Review Letters* **101**, 107604 (Sept. 2008).
188. Frantzeskakis, E. *et al.* Tunable Spin Gaps in a Quantum-Confined Geometry. *Physical Review Letters* **101**, 196805 (Nov. 2008).
189. Hirahara, T. *et al.* Manipulating quantum-well states by surface alloying: Pb on ultrathin Ag films. *Physical Review B* **78**, 035408 (July 2008).
190. He, K. *et al.* Direct Spectroscopic Evidence of Spin-Dependent Hybridization between Rashba-Split Surface States and Quantum-Well States. *Physical Review Letters* **104**, 156805 (Apr. 2010).
191. Schneider, L. *et al.* High-resolution spectroscopy of proximity superconductivity in finite-size quantized surface states, 1–11. arXiv: 2402.08895 (Feb. 2024).
192. Ternes, M. *et al.* Subgap structure in asymmetric superconducting tunnel junctions. *Physical Review B - Condensed Matter and Materials Physics* **74**, 3–6 (Oct. 2006).
193. Josephson, B. Possible new effects in superconductive tunnelling. *Physics Letters* **1**, 251–253 (July 1962).

194. Liebhaber, E. *et al.* Yu–Shiba–Rusinov states in the charge-density modulated superconductor NbSe₂. *Nano letters* **20**, 339–344 (2019).
195. Ding, H. *et al.* Tuning interactions between spins in a superconductor. *Proceedings of the National Academy of Sciences* **118**, e2024837118 (Apr. 2021).
196. Kamlapure, A., Cornils, L., Wiebe, J. & Wiesendanger, R. Engineering the spin couplings in atomically crafted spin chains on an elemental superconductor. *Nature Communications* **9**, 3253 (Aug. 2018).
197. Rütten, L. M. *et al.* Wave-function engineering on superconducting substrates: Chiral Yu-Shiba-Rusinov molecules. arXiv: 2404.16513 (Apr. 2024).
198. Kügel, J. *et al.* Reversible magnetic switching of high-spin molecules on a giant Rashba surface. *npj Quantum Materials* **3**, 53 (Oct. 2018).
199. Manchon, A., Koo, H. C., Nitta, J., Frolov, S. M. & Duine, R. A. New perspectives for Rashba spin–orbit coupling. *Nature Materials* **14**, 871–882 (Sept. 2015).
200. Kempkes, S. N. *et al.* Design and characterization of electrons in a fractal geometry. *Nature Physics* **15**, 127–131 (Feb. 2019).
201. Paschen, S. & Si, Q. Quantum phases driven by strong correlations. *Nature Reviews Physics* **3**, 9–26 (Dec. 2020).

Publications

1. K. T. Ton, C. Xu, L. Schneider, I. Ioannidis, T. Posske, R. Wiesendanger, D. Morr and J. Wiebe, *Non-local detection of coherent Yu-Shiba-Rusinov quantum projections* arXiv:2410.16054 [cond-mat.supr-con] (2024),
2. L. Schneider, C. von Bredow, H. Kim, K. T. Ton, T. Hänke, J. Wiebe and R. Wiesendanger, *Scanning tunneling spectroscopy study of proximity superconductivity in finite-size quantized surface states* Phys. Rev. B **110**, L100505 (2024)
3. L. Schneider, K. T. Ton, I. Ioannidis, J. Neuhaus-Steinmetz, T. Posske, R. Wiesendanger and J. Wiebe, *Proximity superconductivity in atom-by-atom crafted quantum dots* Nature **621**, 60–65 (2023)
4. J. Goedecke, L. Schneider, Y. Ma, K. T. Ton, D. Wang, J. Wiebe and R. Wiesendanger, *Correlation of Magnetism and Disordered Shiba Bands in Fe Monolayer Islands on Nb(110)* ACS Nano **16**, 14066–14074 (2022)
5. M. Steinbrecher, R. Rausch, K. T. Ton, J. Hermenau, A. A. Khajetoorians, M. Potthoff, R. Wiesendanger and J. Wiebe, *Non-collinear spin states in bottom-up fabricated atomic chains* Nature Communications **9**, 2853 (2018)

6. J. Hermenau, J. Ibañez-Azpiroz, C. Hübner, A. Sonntag, B. Baxevanis, K. T. Ton, M. Steinbrecher, A. A. Khajetoorians, M. dos Santos Dias, S. Blügel, R. Wiesendanger, S. Lounis and J. Wiebe, *A gateway towards non-collinear spin processing using three-atom magnets with strong substrate coupling* Nature Communications **8**, 642 (2017)

Acknowledgements

As I reach the end of this thesis, I want to express my gratitude to all the supervisors, mentors, colleagues, and especially the friends I have encountered during my time as a PhD student. Without their support, this work would not be what it is today. The results presented here would not have been nearly as impressive without the support I received.

First and foremost, I would like to express my gratitude to Prof. Roland Wiesendanger for allowing me to work on such an important topic within a fantastic group. He created an environment in which I could thrive and grow.

Additionally, I would like to thank Dr. Jens Wiebe, who provided me with invaluable guidance and supervision during my PhD studies. He is a leader I admire, and his heartfelt approach to leadership inspires me.

I want to express my gratitude to Dr. Lucas Schneider, one of the most brilliant individuals I have encountered in my career. His visionary thinking and innovative ideas, combined with a practical approach, have significantly contributed to the success of our scientific project.

I would also like to thank my labmates Christian von Bredow, Dr. Harim Jang, Dr. Julia Gödecke, and Bianca Schulz. I have always enjoyed working with all of you and continue to do so. Thank you for being such great teammates.

I would like to express my gratitude to the technicians and the He-

Acknowledgements

lium Team at the Campus Jungiusstrasse, especially Hajo Schröder and Michael Langer, who were always available whenever I needed assistance.

I thank my theory colleagues Thore Posske, Ioannis Ioannidis and Jannis Neuhaus-Steinmetz as well as Chang Xu and Dirk Morr from the University of Illinois in Chicago for the great collaboration and their valuable theory contributions to the publications presented in this thesis.

I thank Vishesh Saxena, Arturo Rodriguez, Dr. Eva Cortes del Rio, Arved Heilmann, Dr. Cody Friesen, Dr. Jonas Spethmann, Dr. Philip Beck, Tim Matthies, and Dr. Jinkyung Kim for captivating and thought-provoking conversations. Thanks for broadening my horizons by sharing your views with me. I will always remember the great times and discussions we had during our breaks (with or without coffee).

In general, I would like to thank the whole of Group R for making these past years such an enjoyable experience for me. I have always been happy and proud to be part of such an incredible scientific group.

In the end I want to thank all my friends and family for their unwavering support and motivation. I want to express my gratitude to my parents for nurturing my curious mind and inspiring me to continue learning new things since childhood and my brothers who have become anchors of mental support as we grow older. I thank all of the friends who accompanied me during the last couple of years, especially Nam Be, who has always been a source of

strength to me, and Dr. Alexander Ilin, who has been my friend and academic companion since day one of our physics studies.

Last but not least, I thank my wonderful girlfriend, Stephanie Dinh, who has been with me through the few lows and the many ups of this period of my life.

In the end, I thank you, the reader, for your interest in my work and the energy you have given to reading it.

Thank you, everyone, for the joy that you bring to my life. I dedicate the work and effort I have put into this thesis to you.